

**PHOTONIC, MAGNETIC AND METALLOMESOGENIC  
PROPERTIES OF Cu(II), Ni(II), Co(II), Fe(II) and Mn(II)/Mn(III)  
COMPLEXES WITH ALKYL CARBOXYLATES, SCHIFF  
BASES AND CYCLAM AS LIGANDS**

**YANTI YANA BINTI HALID**

**FACULTY OF SCIENCE  
UNIVERSITY OF MALAYA  
KUALA LUMPUR**

**2016**

**PHOTONIC, MAGNETIC AND METALLOMESOGENIC  
PROPERTIES OF Cu(II), Ni(II), Co(II), Fe(II) and  
Mn(II)/Mn(III) COMPLEXES WITH  
ALKYLCARBOXYLATES, SCHIFF BASES AND  
CYCLAM AS LIGANDS**

**YANTI YANA BINTI HALID**

**THESIS SUBMITTED IN FULLFILMENT OF THE  
REQUIREMENT FOR THE DEGREE OF DOCTOR OF  
PHILOSOPHY**

**FACULTY OF SCIENCE  
UNIVERSITY OF MALAYA  
KUALA LUMPUR**

**2016**

## ABSTRACT

The main objective of this research was to synthesis and study the photonic, magnetic and metallomesogenic properties of Cu(II), Ni(II), Co(II), Fe(II) and Mn(II)/Mn(III) with alkylcarboxylates, Schiff bases and cyclam as ligands. Three new Schiff bases (H<sub>2</sub>L1, H<sub>2</sub>L2 and H<sub>2</sub>L3) were successfully obtained from the condensation reactions of 1,8-diaminooctane with 2-hydroxybenzaldehyde, 2,4-dihydroxybenzaldehyde, and 3,5-di(*tert*-butyl)benzaldehyde, respectively. A total of twenty-two (22) complexes were successfully synthesised. The structures of these complexes were deduced from <sup>1</sup>H-NMR (for ligands), X-ray crystallography (for crystals), elemental analyses, FTIR and UV-visible spectroscopies, their band gap were determined from UV-visible, fluorescence spectroscopies and cyclic voltammetry, their room-temperature magnetic susceptibilities by the Gouy method and their thermal and mesomorphic properties by thermogravimetry (TG), optical polarizing microscopy (OPM) and differential scanning calorimetry (DSC). All Cu(II), Fe(II) and cyclam complexes were mononuclear, while all Ni(II), Co(II) and Mn(II)/Mn(III) complexes were dinuclear. The optical band gaps of these complexes were in the range of 0.31 eV to 3.61 eV and the lifetimes were in the range of 0.7 ns to 3.9 ns. All complexes were paramagnetic, and their decomposition temperatures were in the range of 134 °C to 301 °C. Finally, only [Mn<sub>2</sub>(R)<sub>2</sub>(L1)(H<sub>2</sub>O)<sub>4</sub>].2H<sub>2</sub>O, [Ni(R')(cyclam)]R'.4H<sub>2</sub>O and [Co(R')<sub>2</sub>(cyclam)].R'H, (where R = CH<sub>3</sub>COO and R' = CH<sub>3</sub>(CH<sub>2</sub>)<sub>14</sub>COO) were mesomorphic.

## ABSTRAK

Objektif utama kajian ini adalah untuk mensintesis dan mengkaji sifat-sifat fotonik, magnet dan mesogenik kompleks yang terbentuk daripada tindak balas Cu(II), Ni(II), Co(II), Fe(II) and Mn(II)/Mn(III) dengan alkilkarboksilat, bes Schiff dan siklam sebagai ligan. Tiga bes Schiff yang baru (H<sub>2</sub>L1, H<sub>2</sub>L2 dan H<sub>2</sub>L3) telah berjaya diperolehi daripada tindak balas kondensasi 1,8-diaminooktana dengan 2-hidroksibenzaldehid, 2,4-dihidroksibenzaldehid atau 3,5-di(tert-butyl)benzaldehyd. Sejumlah dua puluh dua (22) kompleks telah berjaya disintesis. Struktur kompleks ini telah dideduksikan daripada <sup>1</sup>H-NMR (untuk ligan), kristalografi sinar-X (untuk kristal), analisis unsur, spektrometri FTIR dan UV-vis, jalur optik dan electrokimia telah ditentukan dari spektrometri UV-vis, pendarfluor dan voltametri kitaran, sifat kerentanan magnet pada suhu bilik ditentukan melalui kaedah Gouy dan sifat terma dan mesomorfik melalui termogravimetri (TG), mikroskopi pengutuban optik (OPM) dan kalorimeter pembeza imbasan (DSC). Semua kompleks Cu(II), Fe(II) dan siklam adalah mononuklear, manakala semua kompleks Ni(II), Co(II) dan Mn(II)/Mn(III) adalah dinuklear. Jalur optik kompleks ini adalah dalam julat 0.31 eV ke 3.61 eV dan tempoh hayat kompleks adalah dalam julat 0.7 ns hingga 3.9 ns. Semua kompleks adalah paramagnetik, dan suhu penguraian adalah dalam julat 134 °C hingga 301 °C. Akhir sekali, hanya [Mn<sub>2</sub>(R)<sub>2</sub>(L1)(H<sub>2</sub>O)<sub>4</sub>].2H<sub>2</sub>O, [Ni(R')(cyclam)]R'.4H<sub>2</sub>O dan [Co(R')<sub>2</sub>(cyclam)].R'H, (R = CH<sub>3</sub>COO dan R' = CH<sub>3</sub>(CH<sub>2</sub>)<sub>14</sub>COO) adalah mesomorfik.

## ACKNOWLEDGEMENT

Foremost, thank you Allah S.W.T for giving me strength and good health in order to finish this research. I would like to express my sincere gratitude to my supervisor, Assoc. Prof. Dr Norbani Abdullah for her dedicated guidance and support throughout completing this project.

Also, during the period of this project, I would like to express my appreciation to all Inorganic Chemistry Research Laboratory members who have been very helpful and supportive in providing technical support and assistance for my work to the positive opinion given for me to complete my project, and many thanks for all staff in Chemistry Departments as well as in Faculty of Science, University of Malaya.

This project was financially supported by the scholarship from Ministry of Higher Education Malaysia (MyPhD), University of Malaya Postgraduate Research Grant (PG023-2013A) and High Impact Research Grant (UM.C/625/1/HIR/MOHE/05).

Last but not least, I would like to give my deepest gratitude to my beloved husband, Azlan Jalain, for his love, patience and understanding. Also, special thanks to my parents and parents-in-law for their encouragement and support.

## TABLE OF CONTENTS

Abstract	iii
Acknowledgement	v
Table of Contents	vi
List of Figures	xi
List of Tables	xix
List of Schemes	xx
List of Abbreviations	xxi
<b>CHAPTER 1: INTRODUCTION</b>	<b>1</b>
<b>CHAPTER 2: THEORY AND LITERATURE REVIEWS</b>	<b>6</b>
<b>2.1 Introduction</b>	<b>6</b>
<b>2.2 Schiff bases</b>	<b>6</b>
<b>2.3 Metal(II) complexes of Schiff bases: syntheses, chemical formulas and structures</b>	<b>9</b>
2.3.1 Copper(II) complexes of Schiff bases	9
2.3.2 Nickel(II) complexes of Schiff bases	13
2.3.3 Cobalt(II) complexes of Schiff bases	15
2.3.4 Iron(II) complexes of Schiff bases	17
2.3.5 Manganese(II) complexes of Schiff bases	19
<b>2.4 Cyclam and its metal carboxylate complexes</b>	<b>21</b>
<b>2.5 Band gap</b>	<b>24</b>
2.5.1 Absorption spectroscopy	26
2.5.2 Emission spectroscopy	28
2.5.3 Cyclic voltammetry	31
<b>2.6 Magnetisms</b>	<b>34</b>
<b>2.7 Metallomesogens</b>	<b>41</b>

<b>CHAPTER 3: EXPERIMENTAL</b>	49
<b>3.1 Introduction</b>	49
<b>3.2 Chemicals</b>	51
<b>3.3 Synthesis of Metal(II) Complexes of H<sub>2</sub>L1</b>	51
3.3.1 Step-wise synthesis	51
(a) H <sub>2</sub> L1	51
(b) Copper(II) complex	51
3.3.2 One-pot synthesis	52
(a) [Cu(L1)] <sub>2</sub> .H <sub>2</sub> O (1)	52
(b) [Ni <sub>2</sub> (CH <sub>3</sub> COO) <sub>2</sub> (L1)].3H <sub>2</sub> O (2)	52
(c) [Co <sub>2</sub> (CH <sub>3</sub> COO) <sub>2</sub> (L1)].2H <sub>2</sub> O (3)	52
(d) [Fe(CH <sub>3</sub> COO)(L1)] (4)	52
(e) [Mn <sub>2</sub> (CH <sub>3</sub> COO) <sub>4</sub> (L1)].5H <sub>2</sub> O (5)	53
<b>3.4 Synthesis of Metal(II) Complexes of H<sub>2</sub>L2</b>	53
3.4.1 Step-wise synthesis	53
(a) H <sub>2</sub> L2	53
(b) Copper(II) complex	53
3.4.2 One-pot synthesis	53
(a) [Cu(CH <sub>3</sub> COO)(HL2)(H <sub>2</sub> O)].H <sub>2</sub> O (6)	53
(b) [Ni <sub>2</sub> (CH <sub>3</sub> COO) <sub>2</sub> (L2)].4H <sub>2</sub> O (7)	54
(c) [Co <sub>2</sub> (CH <sub>3</sub> COO) <sub>2</sub> (L2)].H <sub>2</sub> O (8)	54
(e) [Fe(CH <sub>3</sub> COO)(HL2)].3H <sub>2</sub> O (9)	54
(d) [Mn(HL2) <sub>2</sub> (H <sub>2</sub> O) <sub>2</sub> ] (10)	54
<b>3.5 Synthesis of Metal(II) Complexes of H<sub>2</sub>L3</b>	55
3.5.1 Step-wise synthesis	55
(a) H <sub>2</sub> L3	55

(b) Copper(II) complex	55
3.5.2 One-pot synthesis	55
(a) [Cu(L3)] (11)	55
(b) [Ni(L3)] (12)	55
(c) [Co <sub>2</sub> (CH <sub>3</sub> COO) <sub>2</sub> (L3)].3H <sub>2</sub> O (13)	56
(d) [Fe(CH <sub>3</sub> COO)(HL3)(H <sub>2</sub> O) <sub>2</sub> ].3H <sub>2</sub> O (14)	56
(e) [Mn(HL3) <sub>2</sub> (H <sub>2</sub> O) <sub>2</sub> ] (15)	56
<b>3.6 Metal(II/III)-Palmitate-Cyclam Complexes</b>	56
(a) [Ni(CH <sub>3</sub> (CH <sub>2</sub> ) <sub>14</sub> COO)(cyclam)(H <sub>2</sub> O)].CH <sub>3</sub> (CH <sub>2</sub> ) <sub>14</sub> COO).4H <sub>2</sub> O (16)	56
(b) [Co(CH <sub>3</sub> (CH <sub>2</sub> ) <sub>14</sub> COO) <sub>2</sub> (cyclam)].CH <sub>3</sub> (CH <sub>2</sub> ) <sub>14</sub> COOH (17)	57
(c) [Fe(CH <sub>3</sub> (CH <sub>2</sub> ) <sub>14</sub> COO)(OH)(cyclam)].H <sub>2</sub> O.CH <sub>3</sub> CH <sub>2</sub> OH (18)	57
(d) [Mn(CH <sub>3</sub> (CH <sub>2</sub> ) <sub>14</sub> COO)(OH) <sub>2</sub> (NH <sub>3</sub> ) <sub>2</sub> (H <sub>2</sub> O)] (19)	57
<b>3.7 Mixed-Metal Complexes</b>	57
(a) [CuCo(CH <sub>3</sub> COO) <sub>2</sub> (HL1) <sub>2</sub> (H <sub>2</sub> O)] (20)	57
(b) [CuCo(CH <sub>3</sub> COO) <sub>2</sub> (L2)].2H <sub>2</sub> O (21)	57
(c) [CuCo(CH <sub>3</sub> COO) <sub>2</sub> (HL3) <sub>2</sub> ] (22)	58
<b>3.8 Instrumental Analyses</b>	58
3.8.1 Nuclear magnetic resonance spectroscopy	58
3.8.2 X-Ray Crystallography	58
3.8.3 Elemental analyses	58
3.8.4 FTIR-spectroscopy	59
3.8.5 Magnetic Susceptibility	59
3.8.6 UV-visible spectroscopy	59
3.8.7 Fluorescence spectroscopy	60
3.8.8 Cyclic voltammetry (CV)	60
3.8.9 Thermogravimetric analysis (TGA)	60

3.8.10	Differential scanning calorimetry (DSC)	61
3.8.11	Optical polarized microscopy (OPM)	61
<b>CHAPTER 4: RESULTS AND DISSCUSSION</b>		<b>62</b>
<b>4.1</b>	<b>Introduction</b>	<b>62</b>
<b>4.2</b>	<b>H<sub>2</sub>L1 and its Metal(II) Complexes</b>	<b>63</b>
4.2.1	H <sub>2</sub> L1	63
4.2.2	[Cu(L1)] <sub>2</sub> .H <sub>2</sub> O	66
4.2.3	[Ni <sub>2</sub> (CH <sub>3</sub> COO) <sub>2</sub> (L1)].3H <sub>2</sub> O	74
4.2.4	[Co <sub>2</sub> (CH <sub>3</sub> COO) <sub>2</sub> (L1)].2H <sub>2</sub> O	81
4.2.5	[Fe(CH <sub>3</sub> COO)(L1)]	88
4.2.6	[Mn <sub>2</sub> (CH <sub>3</sub> COO) <sub>4</sub> (L1)].5H <sub>2</sub> O	95
4.2.7	Summary	103
<b>4.3</b>	<b>H<sub>2</sub>L2 and its Metal(II) Complexes</b>	<b>105</b>
4.3.1	H <sub>2</sub> L2	105
4.3.2	[Cu(CH <sub>3</sub> COO)(HL2)(H <sub>2</sub> O)].H <sub>2</sub> O	107
4.3.3	[Ni <sub>2</sub> (CH <sub>3</sub> COO) <sub>2</sub> (L2)].4H <sub>2</sub> O	114
4.3.4	[Co <sub>2</sub> (CH <sub>3</sub> COO) <sub>2</sub> (L2)].H <sub>2</sub> O	118
4.3.5	[Fe(CH <sub>3</sub> COO)(HL2)].3H <sub>2</sub> O	121
4.3.6	[Mn(HL2) <sub>2</sub> (H <sub>2</sub> O) <sub>2</sub> ]	125
4.3.7	Summary	129
<b>4.4</b>	<b>H<sub>2</sub>L3 and its Metal(II) Complexes</b>	<b>131</b>
4.4.1	H <sub>2</sub> L3	131
4.4.2	[Cu(L3)]	134
4.4.3	[Ni(L3)]	142
4.4.4	[Co <sub>2</sub> (CH <sub>3</sub> COO) <sub>2</sub> (L3)].3H <sub>2</sub> O	148
4.4.5	[Fe(CH <sub>3</sub> COO)(HL3)(H <sub>2</sub> O) <sub>2</sub> ].3H <sub>2</sub> O	155

4.4.6	[Mn(HL3) <sub>2</sub> (H <sub>2</sub> O) <sub>2</sub> ]	160
4.4.7	Summary	167
<b>4.5</b>	<b>Cyclam and its Metal(II/III) Palmitate Complexes</b>	169
4.5.1	[Ni(CH <sub>3</sub> (CH <sub>2</sub> ) <sub>14</sub> COO)(cyclam)(H <sub>2</sub> O)](CH <sub>3</sub> (CH <sub>2</sub> ) <sub>14</sub> COO).4H <sub>2</sub> O	169
4.5.2	[Co(CH <sub>3</sub> (CH <sub>2</sub> ) <sub>14</sub> COO) <sub>2</sub> (cyclam)].CH <sub>3</sub> (CH <sub>2</sub> ) <sub>14</sub> COOH	176
4.5.3	[Fe(CH <sub>3</sub> (CH <sub>2</sub> ) <sub>14</sub> COO)(OH)(cyclam)].H <sub>2</sub> O.CH <sub>3</sub> CH <sub>2</sub> OH	184
4.5.4	[Mn(CH <sub>3</sub> (CH <sub>2</sub> ) <sub>14</sub> COO)(OH) <sub>2</sub> (NH <sub>3</sub> ) <sub>2</sub> (H <sub>2</sub> O)]	189
4.5.5	Summary	193
<b>4.6</b>	<b>Mixed-Metal Complexes</b>	195
4.6.1	[CuCo(CH <sub>3</sub> COO) <sub>2</sub> (HL1) <sub>2</sub> (H <sub>2</sub> O)]	195
4.6.2	[CuCo(CH <sub>3</sub> COO) <sub>2</sub> (L2)].2H <sub>2</sub> O	199
4.6.3	[CuCo(CH <sub>3</sub> COO) <sub>2</sub> (HL3) <sub>2</sub> ]	203
4.6.4	Summary	208
<b>CHAPTER 5: CONCLUSIONS AND SUGGESTIONS FOR FUTURE WORKS</b>		
5.1	Conclusions	210
5.2	Suggestions for Future Works	213
	<b>References</b>	214
	Appendices	

## LIST OF FIGURES

		Page
<b>Figure 1.1</b>	Structure of Re-Dian	1
<b>Figure 1.2</b>	Structure of cyclam	2
<b>Figure 2.1</b>	General structure of a Schiff base ( $R_1$ = hydrogen, alkyl or aryl, $R_2, R_3$ = alkyl or aryl)	6
<b>Figure 2.2</b>	Examples of Schiff bases	7
<b>Figure 2.3</b>	Molecular structures of crystalline Schiff bases	8
<b>Figure 2.4</b>	Molecular structure of [Cu(salabza)] [40]	10
<b>Figure 2.5</b>	Crystal structure of [Cu(Sal-6)] <sub>2</sub> [41]	11
<b>Figure 2.6</b>	Examples of Cu(II) complexes (a) [CuL <sub>6</sub> ]; (b) [Cu(L)Cl].Cl; and (c) [Cu(SAH)(H <sub>2</sub> O)]	12
<b>Figure 2.7</b>	Crystal structure of [Ni(HSalpn)(NCS)(H <sub>2</sub> O)].H <sub>2</sub> O [7]	13
<b>Figure 2.8</b>	Examples of Ni(II) complexes (a) [Ni(HPTP)Cl].H <sub>2</sub> O; and (b) [Ni(L) <sub>2</sub> (H <sub>2</sub> O) <sub>2</sub> ]; (c) [Ni(L) <sub>2</sub> ]	15
<b>Figure 2.9</b>	Crystal structure of [Co <sub>2</sub> (L)(H <sub>2</sub> O) <sub>2</sub> (CH <sub>3</sub> CO <sub>2</sub> ) <sub>2</sub> ](CH <sub>3</sub> CO <sub>2</sub> ) <sub>2</sub> [51]	16
<b>Figure 2.10</b>	Examples of Co(II) complexes (a) [Co(L) <sub>2</sub> (H <sub>2</sub> O) <sub>2</sub> ]; and (b) [Co(L)Cl]Cl	17
<b>Figure 2.11</b>	Crystal structure of [Fe(HL)](ClO <sub>4</sub> ) [53]	18
<b>Figure 2.12</b>	Proposed structure of [Fe <sub>2</sub> (OOC(CH <sub>2</sub> ) <sub>14</sub> CH <sub>3</sub> ) <sub>2</sub> (L3)(H <sub>2</sub> O) <sub>4</sub> ].2½H <sub>2</sub> O [55]	19
<b>Figure 2.13</b>	Crystal structure of [MnCl <sub>2</sub> (H <sub>2</sub> O)(L <sup>5</sup> )] [56]	20
<b>Figure 2.14</b>	Proposed structure of [Mn(L)(H <sub>2</sub> O) <sub>2</sub> ] [57]	21
<b>Figure 2.15</b>	Structure of cyclam	21
<b>Figure 2.16</b>	Molecular structure of [Cu(cyclam)(H <sub>2</sub> O) <sub>2</sub> ](CH <sub>3</sub> (CH <sub>2</sub> ) <sub>10</sub> CO <sub>2</sub> ) <sub>2</sub> .2H <sub>2</sub> O [70]	22
<b>Figure 2.17</b>	Crystal structure of [Cu(cyclam)(H <sub>2</sub> O) <sub>2</sub> ](C <sub>6</sub> H <sub>5</sub> COO) <sub>2</sub> .2H <sub>2</sub> O [71]	23
<b>Figure 2.18</b>	Crystal structure of [Ni(cyclam)(C <sub>6</sub> H <sub>5</sub> COO) <sub>2</sub> ] [71]	24
<b>Figure 2.19</b>	The formation of band	24
<b>Figure 2.20</b>	Comparison of the electronic band structures of (a) insulators; (b) semiconductors; and (c) conductors	25
<b>Figure 2.21</b>	Four types of electronic transition in molecules	26
<b>Figure 2.22</b>	UV-vis spectrum of TiO <sub>2</sub> [75]	27
<b>Figure 2.23</b>	Example of semiconductor materials	28

<b>Figure 2.24</b>	Jablonski energy diagram [78] (vibrational conversion; red: fluorescence; dark blue: intersystem crossing; purple: quenching; blue: non-radiative relaxation; orange: delayed fluorescence; pink: phosphorescence)	29
<b>Figure 2.25</b>	The Stokes shift of the excitation and emission spectra of a compounds	30
<b>Figure 2.26</b>	Photoluminescence spectrum of Pb nanopowder (red: excitation' blue: emission)	31
<b>Figure 2.27</b>	Typical cyclic voltammogram for a reversible electrochemical process	32
<b>Figure 2.28</b>	CV of [Cu(II)Cu(II)(R) <sub>3</sub> (RH) <sub>2</sub> L <sub>4</sub> ].CH <sub>3</sub> COCH <sub>3</sub> [83]	34
<b>Figure 2.29</b>	Energy level of the <i>d</i> -orbital in common stereochemistries: (a) tetrahedral; (b) free ion; (c) octahedral; and (d) square planar complexes	36
<b>Figure 2.30</b>	<i>d</i> -Orbital splitting for octahedral d <sup>6</sup> (a) high spin; and (b) low spin	37
<b>Figure 2.31</b>	Molecular structure of (a) [Cu(L)H <sub>2</sub> O] [45]; and (b) [Cu <sub>2</sub> (CH <sub>3</sub> (CH <sub>2</sub> ) <sub>12</sub> COO) <sub>4</sub> ] [84]	38
<b>Figure 2.32</b>	Molecular structure of [Co(L) <sub>2</sub> ] [42]	39
<b>Figure 2.33</b>	Molecular structure of (a) [Fe(L) <sub>2</sub> ](BF <sub>4</sub> ); (b) [Fe(OOC(CH <sub>2</sub> ) <sub>14</sub> CH <sub>3</sub> ) <sub>2</sub> (L)(H <sub>2</sub> O) <sub>2</sub> ] [55]	40
<b>Figure 2.34</b>	Molecular structure of (a) [Mn(L)H <sub>2</sub> O] [45]; and (b) [Mn(HPTP)Cl(H <sub>2</sub> O) <sub>2</sub> ] [49]	41
<b>Figure 2.35</b>	The average alignment of the molecules for solid, liquid crystal and liquid.	41
<b>Figure 2.36</b>	Example of metallomesogen: (a) calamitic; (b) discotic; and (c) polycatenar	42
<b>Figure 2.37</b>	Different phases of a liquid crystal	43
<b>Figure 2.38</b>	The nematic phase	43
<b>Figure 2.39</b>	The smectic phases	45
<b>Figure 2.40</b>	Columnar liquid crystal	45
<b>Figure 2.41</b>	X-ray structure of Ni-16opd [87]	47
<b>Figure 2.42</b>	Photomicrograph of Ni-16opd at 130 °C	47
<b>Figure 2.43</b>	(a) Molecular structure; and (b) TGA thermogram of Cu(II) complex [88]	48
<b>Figure 3.1</b>	Structural formulas of (a) H <sub>2</sub> L1; (b) H <sub>2</sub> L2; and (c) H <sub>2</sub> L3	49
<b>Figure 3.2</b>	Structural formulas of cyclam (1,4,8,11-tetraazacyclotetradecane)	50

<b>Figure 4.1</b>	Structural formula of H <sub>2</sub> L1	63
<b>Figure 4.2</b>	The FTIR spectrum of H <sub>2</sub> L1	64
<b>Figure 4.3</b>	The <sup>1</sup> H-NMR spectrum of H <sub>2</sub> L1	65
<b>Figure 4.4</b>	DSC scans for H <sub>2</sub> L1	66
<b>Figure 4.5</b>	A photomicrograph of H <sub>2</sub> L1 at 78 °C on cooling from <i>I</i>	66
<b>Figure 4.6</b>	FTIR spectra for <b>Complex 1</b> obtained from: (a) step-wise method, and (b) one-pot method	68
<b>Figure 4.7</b>	UV-visible spectrum of <b>Complex 1</b> in THF	69
<b>Figure 4.8</b>	Proposed structure for <b>Complex 1</b> (lattice H <sub>2</sub> O is omitted)	69
<b>Figure 4.9</b>	Fluorescence spectra for <b>Complex 1</b> after excitation at: (a) 298 nm, and (b) 688 nm	70
<b>Figure 4.10</b>	Fluorescence decay of <b>Complex 1</b> at $\lambda_{emission}$ (a) 342 nm, and (b) 697 nm	71
<b>Figure 4.11</b>	Cyclic voltammogram for <b>Complex 1</b>	72
<b>Figure 4.12</b>	TGA of <b>Complex 1</b>	73
<b>Figure 4.13</b>	DSC of <b>Complex 1</b>	73
<b>Figure 4.14</b>	Photomicrographs of <b>Complex 1</b> (a) on heating at 200 °C; and (b) on cooling at 154 °C	74
<b>Figure 4.15</b>	FTIR spectrum for <b>Complex 2</b>	75
<b>Figure 4.16</b>	UV-visible spectrum of <b>Complex 2</b>	75
<b>Figure 4.17</b>	Proposed structure for <b>Complex 2</b> (lattice H <sub>2</sub> O is omitted)	76
<b>Figure 4.18</b>	Fluorescence spectra of <b>Complex 2</b> after excitation at: (a) 325 nm, and (b) 411 nm	77
<b>Figure 4.19</b>	Fluorescence decay of <b>Complex 2</b> at $\lambda_{emission}$ (a) 360 nm, and (b) 419 nm	78
<b>Figure 4.20</b>	Cyclic voltammogram for <b>Complex 2</b>	79
<b>Figure 4.21</b>	TGA of <b>Complex 2</b>	80
<b>Figure 4.22</b>	DSC of <b>Complex 2</b>	81
<b>Figure 4.23</b>	Photomicrographs of <b>Complex 2</b> (a) on heating at 138 °C; (b) on heating at 227 °C; and (c) on cooling at 30 °C	81
<b>Figure 4.24</b>	FTIR spectrum for <b>Complex 3</b>	82
<b>Figure 4.25</b>	UV-visible spectrum of <b>Complex 3</b>	83
<b>Figure 4.26</b>	Fluorescence spectra of <b>Complex 3</b> after excitation at: (a) 362 nm, and (b) 611 nm	84
<b>Figure 4.27</b>	Fluorescence decay of <b>Complex 3</b> at $\lambda_{emission}$ , (a) 416 nm, and (b) 633 nm	85
<b>Figure 4.28</b>	Cyclic voltammogram for <b>Complex 3</b>	86
<b>Figure 4.29</b>	TGA of <b>Complex 3</b>	87

<b>Figure 4.30</b>	DSC of <b>Complex 3</b>	87
<b>Figure 4.31</b>	Photomicrographs of <b>Complex 3</b> : (a) on heating at 75.8 °C; (b) on heating at 133.5 °C; (c) on heating at 177.2 °C; (d) on heating at 198.3 °C; (e) on heating at 225 °C; (f) on cooling at 30 °C	88
<b>Figure 4.32</b>	FTIR spectrum for <b>Complex 4</b>	89
<b>Figure 4.33</b>	UV-visible spectrum of <b>Complex 4</b>	90
<b>Figure 4.34</b>	Proposed structure for <b>Complex 4</b>	90
<b>Figure 4.35</b>	Emission spectra of <b>Complex 4</b> after excitation at: (a) 322 nm, and (b) 502 nm	91
<b>Figure 4.36</b>	Fluorescence decay of <b>Complex 4</b> at $\lambda_{emission}$ , (a) 355 nm, and (b) 508 nm	92
<b>Figure 4.37</b>	Cyclic voltammogram for <b>Complex 4</b>	93
<b>Figure 4.38</b>	TGA of <b>Complex 4</b>	94
<b>Figure 4.39</b>	DSC of <b>Complex 4</b>	94
<b>Figure 4.40</b>	FTIR spectrum for <b>Complex 5</b>	96
<b>Figure 4.41</b>	UV-visible spectrum of <b>Complex 5</b>	96
<b>Figure 4.42</b>	Proposed structure for <b>Complex 5</b> (lattice H <sub>2</sub> O molecules are not shown)	97
<b>Figure 4.43</b>	Fluorescence spectra of <b>Complex 5</b> after excitation at: (a) 368 nm; and (b) 689 nm	98
<b>Figure 4.44</b>	Fluorescence decay of <b>Complex 5</b> at $\lambda_{emission}$ , (a) 410 nm, (b) 705 nm	99
<b>Figure 4.45</b>	Cyclic voltammogram for <b>Complex 5</b>	100
<b>Figure 4.46</b>	TGA of <b>Complex 5</b>	101
<b>Figure 4.47</b>	DSC of <b>Complex 5</b>	102
<b>Figure 4.48</b>	Photomicrographs of <b>Complex 5</b> on: (a) heating at 200 °C; and (b) cooling at 129 °C	102
<b>Figure 4.49</b>	Structural formula of H <sub>2</sub> L2	105
<b>Figure 4.50</b>	The FTIR spectrum of H <sub>2</sub> L2	106
<b>Figure 4.51</b>	The <sup>1</sup> H-NMR spectrum of H <sub>2</sub> L2	106
<b>Figure 4.52</b>	DSC of H <sub>2</sub> L2	107
<b>Figure 4.53</b>	FTIR spectrum of <b>Complex 6</b> : (a) step-wise method, and (b) one-pot method.	108
<b>Figure 4.54</b>	UV-visible spectrum of <b>Complex 6</b>	109
<b>Figure 4.55</b>	Proposed structure for <b>Complex 6</b> . Lattice H <sub>2</sub> O is not shown	109

<b>Figure 4.56</b>	Emission spectra of <b>Complex 6</b> after excitation at: (a) $\lambda = 438$ nm, and (b) $\lambda = 629$ nm.	110
<b>Figure 4.57</b>	Fluorescence decay of <b>Complex 6</b> at (a) $\lambda_{emission} = 501$ nm, and (b) $\lambda_{emission} = 632$ nm.	111
<b>Figure 4.58</b>	Cyclic voltammogram for <b>Complex 6</b>	112
<b>Figure 4.59</b>	TGA of <b>Complex 6</b>	113
<b>Figure 4.60</b>	DSC of <b>Complex 6</b>	113
<b>Figure 4.61</b>	FTIR spectrum for <b>Complex 7</b>	115
<b>Figure 4.62</b>	UV-visible spectrum of <b>Complex 7</b>	115
<b>Figure 4.63</b>	Proposed structure for <b>Complex 7</b> (lattice H <sub>2</sub> O molecules are omitted)	116
<b>Figure 4.64</b>	TGA of <b>Complex 7</b>	117
<b>Figure 4.65</b>	DSC of <b>Complex 7</b>	117
<b>Figure 4.66</b>	FTIR spectrum for <b>Complex 8</b>	119
<b>Figure 4.67</b>	UV-visible spectrum of <b>Complex 8</b>	119
<b>Figure 4.68</b>	TGA of <b>Complex 8</b>	120
<b>Figure 4.69</b>	DSC of <b>Complex 8</b>	121
<b>Figure 4.70</b>	FTIR spectrum for <b>Complex 9</b>	122
<b>Figure 4.71</b>	UV-visible spectrum of <b>Complex 9</b>	123
<b>Figure 4.72</b>	Proposed structure for <b>Complex 9</b> (lattice H <sub>2</sub> O is omitted)	123
<b>Figure 4.73</b>	TGA of <b>Complex 9</b>	124
<b>Figure 4.74</b>	DSC of <b>Complex 9</b>	125
<b>Figure 4.75</b>	FTIR spectrum for <b>Complex 10</b>	126
<b>Figure 4.76</b>	UV-visible spectrum of <b>Complex 10</b>	126
<b>Figure 4.77</b>	Proposed structure for <b>Complex 10</b>	127
<b>Figure 4.78</b>	TGA of <b>Complex 10</b>	128
<b>Figure 4.79</b>	DSC of <b>Complex 10</b>	128
<b>Figure 4.80</b>	The FTIR spectrum of H <sub>2</sub> L3	131
<b>Figure 4.81</b>	An ORTEP presentation of H <sub>2</sub> L3	132
<b>Figure 4.82</b>	The packing diagram viewed along the <i>c</i> -axis (H atoms are omitted for clarity).	132
<b>Figure 4.83</b>	DSC of H <sub>2</sub> L3	134
<b>Figure 4.84</b>	FTIR spectrum of <b>Complex 11</b> : (a) step-wise reaction, and (b) one-pot reaction	135
<b>Figure 4.85</b>	UV-visible spectrum of <b>Complex 11</b>	136
<b>Figure 4.86</b>	Proposed structure for <b>Complex 11</b>	137

<b>Figure 4.87</b>	Fluorescence spectra of <b>Complex 11</b> after excitation at: (a) 374 nm, and (b) 683 nm	138
<b>Figure 4.88</b>	Fluorescence decay of <b>Complex 11</b> after excitation at: (a) 465 nm, and (b) 689 nm	139
<b>Figure 4.89</b>	Cyclic voltammogram for <b>Complex 11</b>	140
<b>Figure 4.90</b>	TGA of <b>Complex 11</b>	141
<b>Figure 4.91</b>	DSC of <b>Complex 11</b>	141
<b>Figure 4.92</b>	FTIR spectrum for <b>Complex 12</b>	142
<b>Figure 4.93</b>	UV-visible spectrum of <b>Complex 12</b>	143
<b>Figure 4.94</b>	Proposed structure of <b>Complex 12</b>	143
<b>Figure 4.95</b>	Fluorescence spectra of <b>Complex 12</b> after excitation at: (a) 404 nm, and (b) 659 nm	144
<b>Figure 4.96</b>	Fluorescence decay of <b>Complex 12</b> at $\lambda_{emission}$ : (a) 425 nm, and (b) 662 nm	145
<b>Figure 4.97</b>	Cyclic voltammogram for <b>Complex 12</b>	146
<b>Figure 4.98</b>	TGA of <b>Complex 12</b>	147
<b>Figure 4.99</b>	DSC of <b>Complex 12</b>	147
<b>Figure 4.100</b>	FTIR spectrum for <b>Complex 13</b>	149
<b>Figure 4.101</b>	UV-visible spectrum of <b>Complex 13</b>	149
<b>Figure 4.102</b>	Proposed structure for <b>Complex 13</b> (lattice water molecules are omitted)	150
<b>Figure 4.103</b>	Fluorescence spectra of <b>Complex 13</b> after excitation at: (a) 372 nm, and (b) 574 nm	151
<b>Figure 4.104</b>	Fluorescence decay of <b>Complex 13</b> at $\lambda_{emission}$ (a) 410 nm, and (b) 592 nm	152
<b>Figure 4.105</b>	Cyclic voltammogram for <b>Complex 13</b>	153
<b>Figure 4.106</b>	TGA of <b>Complex 13</b>	154
<b>Figure 4.107</b>	DSC of <b>Complex 13</b>	154
<b>Figure 4.108</b>	FTIR spectrum for <b>Complex 14</b>	156
<b>Figure 4.109</b>	UV-visible spectrum of <b>Complex 14</b>	156
<b>Figure 4.110</b>	Proposed structure for <b>Complex 14</b> (lattice H <sub>2</sub> O molecules are not shown)	157
<b>Figure 4.111</b>	Fluorescence spectrum of <b>Complex 14</b> after excitation at 532 nm	157
<b>Figure 4.112</b>	Fluorescence decay of <b>Complex 14</b> at $\lambda_{emission} = 549$ nm	158
<b>Figure 4.113</b>	Cyclic voltammogram for <b>Complex 14</b>	158
<b>Figure 4.114</b>	TGA of <b>Complex 14</b>	159
<b>Figure 4.115</b>	DSC of <b>Complex 14</b>	160

<b>Figure 4.116</b>	FTIR spectrum for <b>Complex 15</b>	161
<b>Figure 4.117</b>	UV-visible spectrum of <b>Complex 15</b>	162
<b>Figure 4.118</b>	Proposed structure for <b>Complex 15</b>	162
<b>Figure 4.119</b>	Fluorescence spectra of <b>Complex 15</b> upon excitation at: (a) 416 nm, and (b) 704 nm	163
<b>Figure 4.120</b>	Fluorescence decay of <b>Complex 15</b> at $\lambda_{emission}$ : (a) 473 nm, and (b) 717 nm	164
<b>Figure 4.121</b>	Cyclic voltammogram for <b>Complex 15</b>	165
<b>Figure 4.122</b>	TGA of <b>Complex 15</b>	166
<b>Figure 4.123</b>	DSC of <b>Complex 15</b>	166
<b>Figure 4.124</b>	The FTIR spectrum of <b>Complex 16</b>	169
<b>Figure 4.125</b>	An ORTEP presentation of <b>Complex 16</b> along <i>b</i> -axis. The probability level was 30%.	170
<b>Figure 4.126</b>	The packing diagram viewed along the <i>b</i> -axis (H atoms are omitted for clarity).	170
<b>Figure 4.127</b>	UV-visible spectrum of <b>Complex 16</b>	173
<b>Figure 4.128</b>	Cyclic voltammogram of <b>Complex 16</b>	174
<b>Figure 4.129</b>	TGA trace of <b>Complex 16</b>	175
<b>Figure 4.130</b>	DSC of <b>Complex 16</b>	175
<b>Figure 4.131</b>	Photomicrograph of <b>Complex 16</b> on: (a) heating at 150 °C; and (b) cooling at 66.4 °C	176
<b>Figure 4.132</b>	The FTIR spectrum of <b>Complex 17</b>	177
<b>Figure 4.133</b>	An ORTEP presentation of <b>Complex 17</b> along <i>b</i> -axis. The probability level 50%.	178
<b>Figure 4.134</b>	The packing diagram of <b>Complex 17</b> , viewed along the <i>b</i> -axis (H atoms are omitted for clarity).	178
<b>Figure 4.135</b>	UV-visible spectrum of <b>Complex 17</b>	181
<b>Figure 4.136</b>	Cyclic voltammogram of <b>Complex 17</b>	182
<b>Figure 4.137</b>	TGA trace of <b>Complex 17</b>	183
<b>Figure 4.138</b>	DSC of <b>Complex 17</b>	183
<b>Figure 4.139</b>	Photomicrographs of <b>Complex 17</b> on: (a) heating at 122 °C; (b) cooling at 70.2 °C; and (c) further cooling at 61.0 °C	184
<b>Figure 4.140</b>	The FTIR spectrum of <b>Complex 18</b>	185
<b>Figure 4.141</b>	UV-visible spectrum of <b>Complex 18</b>	185
<b>Figure 4.142</b>	Proposed structure for <b>Complex 18</b> (lattice CH <sub>3</sub> CH <sub>2</sub> OH are omitted).	186
<b>Figure 4.143</b>	Cyclic voltammogram of <b>Complex 18</b>	187

<b>Figure 4.144</b>	TGA trace of Complex 18	188
<b>Figure 4.145</b>	DSC of Complex 18	188
<b>Figure 4.146</b>	The FTIR spectrum of Complex 19	190
<b>Figure 4.147</b>	UV-visible spectrum of Complex 19	190
<b>Figure 4.148</b>	Cyclic voltammogram of Complex 19	191
<b>Figure 4.149</b>	TGA trace of Complex 19	192
<b>Figure 4.150</b>	DSC of Complex 19	193
<b>Figure 4.151</b>	FTIR spectrum for Complex 20	196
<b>Figure 4.152</b>	UV-visible spectrum of Complex 20	196
<b>Figure 4.153</b>	Cyclic voltammogram for Complex 20	197
<b>Figure 4.154</b>	TGA of Complex 20	198
<b>Figure 4.155</b>	DSC of Complex 20	198
<b>Figure 4.156</b>	FTIR spectrum for Complex 21	200
<b>Figure 4.157</b>	UV-visible spectrum of Complex 21	200
<b>Figure 4.158</b>	Cyclic voltammogram for Complex 21	201
<b>Figure 4.159</b>	TGA of Complex 21	202
<b>Figure 4.160</b>	DSC of Complex 21	203
<b>Figure 4.161</b>	FTIR spectrum for Complex 22	204
<b>Figure 4.162</b>	UV-visible spectrum of Complex 22	205
<b>Figure 4.163</b>	Cyclic voltammogram for Complex 22	206
<b>Figure 4.164</b>	TGA of Complex 22	207
<b>Figure 4.165</b>	DSC of Complex 22	207
<b>Figure 4.166</b>	Photomicrograph of Complex 22: (a) on heating at 200 °C; and (b) on cooling at 62 °C	208
<b>Figure 5.1</b>	Structure formula of Schiff bases (a) H <sub>2</sub> L1, (b) H <sub>2</sub> L2 and (c) H <sub>2</sub> L3	210

## LIST OF TABLES

		Page
<b>Table 2.1</b>	Fluorescence lifetime ( $\tau$ ) for various dyes	31
<b>Table 2.2</b>	DSC data of complex Ni-16opd	48
<b>Table 3.1</b>	Chemicals used in this project	51
<b>Table 4.1</b>	The $^1\text{H-NMR}$ data (in ppm) and peak assignment for $\text{H}_2\text{L1}$	65
<b>Table 4.2</b>	DSC data for <b>Complex 5</b>	101
<b>Table 4.3</b>	Analytical results for metal(II) complexes of $\text{H}_2\text{L1}$	104
<b>Table 4.4</b>	The $^1\text{H-NMR}$ data and peak assignment for $\text{H}_2\text{L2}$	106
<b>Table 4.5</b>	Analytical results for metal(II) complexes of $\text{H}_2\text{L2}$	130
<b>Table 4.6</b>	Crystal data and structure refinement for $\text{H}_2\text{L3}$	133
<b>Table 4.7</b>	Selected bond lengths ( $\text{\AA}$ ) and angles ( $^\circ$ ) for $\text{H}_2\text{L3}$	133
<b>Table 4.8</b>	Hydrogen bonds for $\text{H}_2\text{L3}$ ( $\text{\AA}$ and $^\circ$ ).	134
<b>Table 4.9</b>	Analytical results for metal(II) complexes of $\text{H}_2\text{L3}$	168
<b>Table 4.10</b>	Crystal data and structure refinement for <b>Complex 16</b>	171
<b>Table 4.11</b>	Selected bond lengths ( $\text{\AA}$ ) and angles ( $^\circ$ ) for <b>Complex 16</b>	172
<b>Table 4.12</b>	Crystal data and structure refinement for <b>Complex 17</b>	179
<b>Table 4.13</b>	Selected bond lengths ( $\text{\AA}$ ) and angles ( $^\circ$ ) for <b>Complex 17</b> .	180
<b>Table 4.14</b>	Analytical results for metal(II) complexes of cyclam	194
<b>Table 4.15</b>	Analytical results for heterometallic complexes	209
<b>Table 5.1</b>	Chemical formulae of complexes	211

## LIST OF SCHEMES

	Page
<b>Scheme 1.1</b> (a) Homometallic complexes <b>1 – 19</b> (M = Cu(II), Ni(II), Co(II), Fe(II), Mn(II)/(III); and (b) heterometallic complexes <b>20 – 22</b>	3
<b>Scheme 2.1</b> General equation for the synthesis of a Schiff base	6
<b>Scheme 4.1</b> (a) Homometallic complexes <b>1 – 19</b> (M = Cu(II), Ni(II), Co(II), Fe(II), Mn(II); and (b) heterometallic complexes <b>20 - 22</b>	63
<b>Scheme 4.2</b> Synthetic steps for <b>Complex 1</b>	66

University of Malaya

## LIST OF ABBREVIATIONS

<b>CV</b>	Cyclic voltammetry
<b>DSC</b>	Differential scanning calorimetry
<b>OPM</b>	Optical polarizing microscopy
<b>TGA</b>	Thermogravimetric analysis

University of Malaya

## CHAPTER 1: INTRODUCTION

Metallomesogens are metal-containing liquid crystals. Liquid crystals exhibit the characteristics of both the solid and liquid states. In addition, metallomesogens of first-row transition metal ions with one or more unpaired electrons are potential magnetic and semiconductor materials. Various semiconductor based on both molecular and polymeric materials have been reported. The majority of organic semiconductors reported to date demonstrate power conversion efficiencies of less than 1% [1]. In order to design an efficient organic semiconductor, it is imperative that the efficiency in the dissociation of excitons and the charge transport process should be improved, by lowering the band gap. The ability to tune the band gap is becoming increasingly important for developing highly efficient solar cells and transparent conducting oxides. For example, Wong *et al.* [2] have reported the fabrication of photovoltaic cells using chlorotricarbonylrhenium(I) bis(phenylimino)acenaphthene (Re-DIAN) (**Figure 1.1**) as the photosensitizer. The band gap for this complex was 2.0 eV.

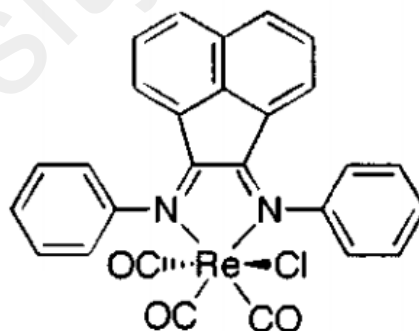


**Figure 1.1** Structure of Re-Dian

Due to the presence of the transition metal atom, an efficient spin-orbit coupling would favour intersystem crossing, which leads to the formation of long-lived triplet excited states. It is therefore envisaged that after photoexcitation, the exciton formed may have a longer lifetime so that subsequent exciton dissociation process is favoured.

Metal complexes derived from salicyldiimine Schiff bases are the most extensively studied metallomesogens. Schiff bases are synthesised from the condensation of amino compounds with carbonyl compounds. Schiff base ligands can be coordinated to transition metal ions via azomethine nitrogen. The strength of the azomethine group is insufficient to form a stable complexes. Hence, the present of functional group, preferably hydroxyl group as substituent, is nearly enough to permit formation of more stable complexes [3]. The salen type Schiff bases complexes are most extensively studied topic in coordination chemistry [4-8]. They also play important role in magnetism and have some interesting applications, such as in catalytic oxidation-reduction processes [4,9,10], metal-containing liquid-crystalline polymers [4,11], and as dye and fluorescent agents [12].

Cyclam (**Figure 1.2**) is a macrocyclic ligand able to bind strongly to many transition metal ions. It is an easily functionalised ligand and exhibits enhanced structural stabilities, since the metal ion is firmly held within its cavity. Functionalization of the parent macrocycle has opened new directions in fields ranging from fundamental coordination chemistry [13], diagnostic and nuclear medicine [14-16] to waste water treatment [17-19].

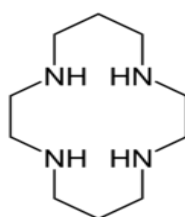
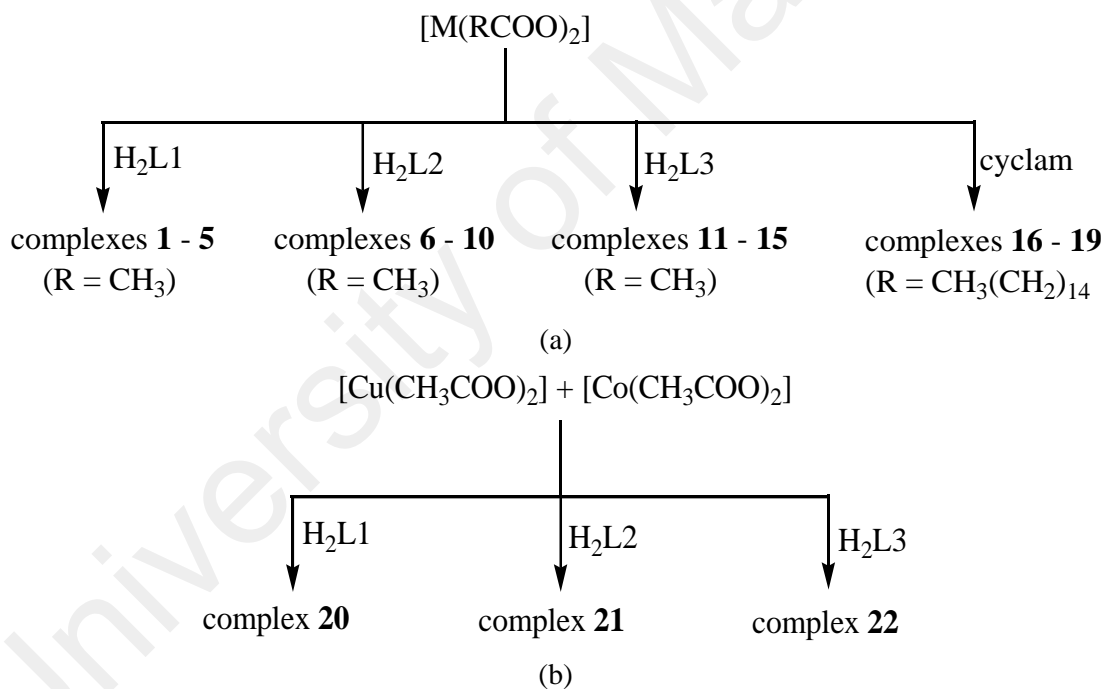


**Figure 1.2** Structure of cyclam

Hence, this research was focused on the synthesis and characterization of Cu(II), Ni(II), Co(II), Fe(II) and Mn(II)/Mn(III) with anionic ligands from Schiff bases, and alkylcarboxylato and cyclam as co-ligands. Photonic, magnetic and metallomesogenic properties of these complexes were studied.

A total of twenty two (22) complexes were successfully prepared and characterised. For homometallic complexes of Cu(II), Ni(II), Co(II), Fe(II) and Mn(II), the ligands were anions of three Schiff bases ( $H_2L1$ ,  $H_2L2$  and  $H_2L3$ ) formed from the condensation reactions of 1,8-diaminooctane with 2-hydroxybenzaldehyde, 2,4-dihydroxybenzaldehyde, and 3,5-di(*tert*-butyl)benzaldehyde, respectively. In addition, four homometallic complexes were synthesized from the reaction of cyclam with  $[M(CH_3(CH_2)_{14}COO)_2]$ , where  $M = Ni(II)$ ,  $Co(II)$ ,  $Fe(II)$  and  $Mn(II)$ . For the heterometallic complexes, three complexes were synthesized from the reactions of  $H_2L1$ ,  $H_2L2$ , and  $H_2L3$  with a mixture of  $[Cu(CH_3COO)_2]$  and  $[Co(CH_3COO)_2]$ . These are shown in **Scheme 1.1**.



**Scheme 1.1** (a) Homometallic complexes **1 – 19** ( $M = Cu(II)$ ,  $Ni(II)$ ,  $Co(II)$ ,  $Fe(II)$ ,  $Mn(II)$ ); and (b) heterometallic complexes **20 – 22**

These materials were characterised by  $^1H$ -NMR (for ligands), X-ray crystallography (for crystals), elemental analyses, FTIR, UV-visible and fluorescence spectroscopies, cyclic voltammetry, room-temperature magnetic susceptibilities by the

Gouy method, thermogravimetry (TG), optical polarizing microscopy (OPM) and differential scanning calorimetry (DSC).

The findings of this research were accepted for publication in ISI journals and were presented in regional and international conference and seminar (**Appendices 2-5**), as listed below.

1. Norbani Abdullah, Suhana Mohd Said, Yanti Yana Halid, Naimah Sharmin, Siti Amira Mat Hussin, Nik Muhd Jazli Nik Ibrahim, Nurul Atikah Safiin, Nurul Shafinaz Anuar. *Complexes of Nickel(II) Carboxylates With Pyridine and Cyclam: Crystal Structures, Mesomorphisms and Thermoelectrical Properties*, J. Coord. Chem. (accepted on 26 May 2016).
2. Norbani Abdullah, Yanti Yana Halid, Tee Jia Ti, Afiq Azil *Crystal Structures and Mesomorphic Properties of Schiff Base Homologs and Derivative, and Magnetic Properties of their Dimeric and Dinuclear Copper(II) Complexes*. *Mol. Cryst. Liq. Cryst.*, Vol. 624, No. 1, 132-143, 2016
3. Yanti Yana Halid and Norbani Abdullah. *Synthesis and Characterization of Cu(II) and Co(II) Complexes of a Schiff Base Ligand as Potential Spintronics and Low Band Gap Photonic Materials*. The Fourth International Conference for Young Chemists, 2013, Pulau Pinang (Oral presentation).
4. Yanti Yana Halid and Norbani Abdullah, *Synthesis and Characterization of Cu(II) and Co(II) Complexes as Spintronic and Low Band-Gap Photonic Materials [M(CH<sub>3</sub>COO)<sub>x</sub>(C<sub>22</sub>H<sub>26</sub>N<sub>2</sub>O<sub>4</sub>)<sub>x</sub>(H<sub>2</sub>O)<sub>x</sub>*. International Conference of Ionic Liquid, 2013, Langkawi (Oral presentation).

This thesis contains five chapters. **Chapter 2** presents the theory and literature review of Schiff bases and cyclam complexes with focused on structural elucidation by <sup>1</sup>H-NMR (for ligands), X-ray crystallography (for crystals), elemental analyses, FTIR and UV-visible spectroscopy, followed by band gap and magnetic, thermal and liquid crystalline

properties. **Chapter 3** contains the experimental methods used in the syntheses and the techniques of instrumental analyses. **Chapter 4** presents the results and discussion, and finally, **Chapter 5** presents the conclusions and suggestions for future works. A list of references and appendices are included at the end of this thesis.

University of Malaya

## CHAPTER 2: THEORY AND LITERATURE REVIEW

### 2.1 Introduction

The main focus of this research project was to synthesize and characterize homometallic and heterometallic complexes with alkylcarboxylate ion, Schiff bases and cyclam as ligands. These complexes were designed as molecular magnetic and/or low band gap metallomesogenic materials. Accordingly, this chapter presents literature reports, theory and basic concepts relevant to this project.

### 2.2 Schiff bases

Schiff bases (**Figure 2.1**) are a group of organic compounds containing an imine group ( $\text{R}-\text{C}=\text{N}-$ ), either secondary ketimines or secondary aldimines, and also known as azomethines. These compounds are named after a German chemist, Hugo Schiff [20].

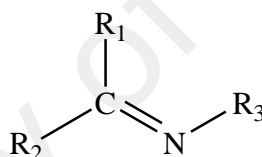
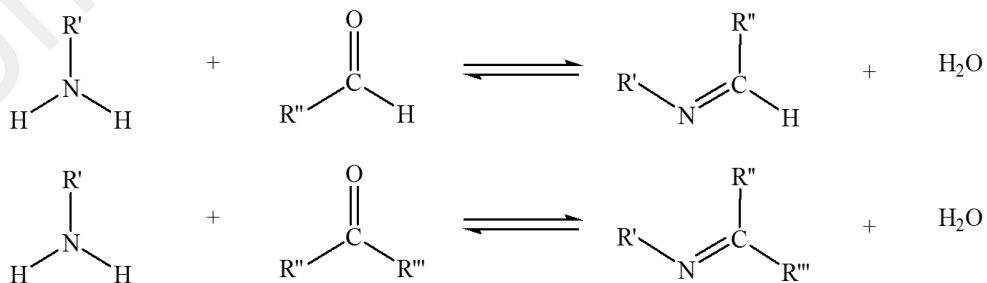


**Figure 2.1** General structure of a Schiff base ( $\text{R}_1$  = hydrogen, alkyl or aryl,  $\text{R}_2$ ,  $\text{R}_3$  = alkyl or aryl)

These compounds are usually synthesised by the condensation reaction of a primary amine with a carbonyl group (aldehydes or ketones) (**Scheme 2.1**). The reaction is reversible and generally takes place under acid or base catalysis, or upon heating.



**Scheme 2.1.** General equation for the synthesis of a Schiff base

A few examples of Schiff bases are shown in **Figure 2.2**.

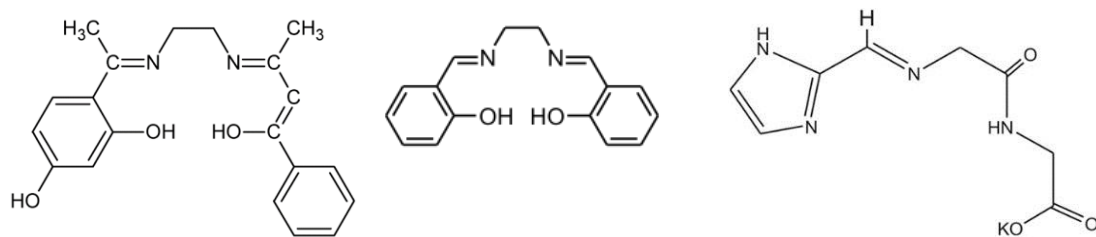


**Figure 2.2.** Examples of Schiff bases

Schiff bases play important roles in agriculture, pharmaceutical and industrial chemistry. Examples are as catalysts, pigments and dyes, intermediates in organic synthesis, polymer stabilizer, antiviral, enzymatic agents and in various biological systems [21-24].

The structure of Schiff bases, if single crystals, can be characterised directly using X-ray crystallography. Examples are vanillin-Schiff base (**Figure 2.3(a)**) [25], 2,2'-[decane-1,10-diylbis(nitrilomethylidyne)]diphenol (**Figure 2.3(b)**) [26], and 2,2'-[nonane-1,9-diylbis(nitrilomethylidyne)]diphenol (**Figure 2.3 (c)**) [27]. The structure of non-crystalline Schiff bases may be ascertained by combined instrumental analyses, namely elemental analyses, and NMR and IR spectroscopies.

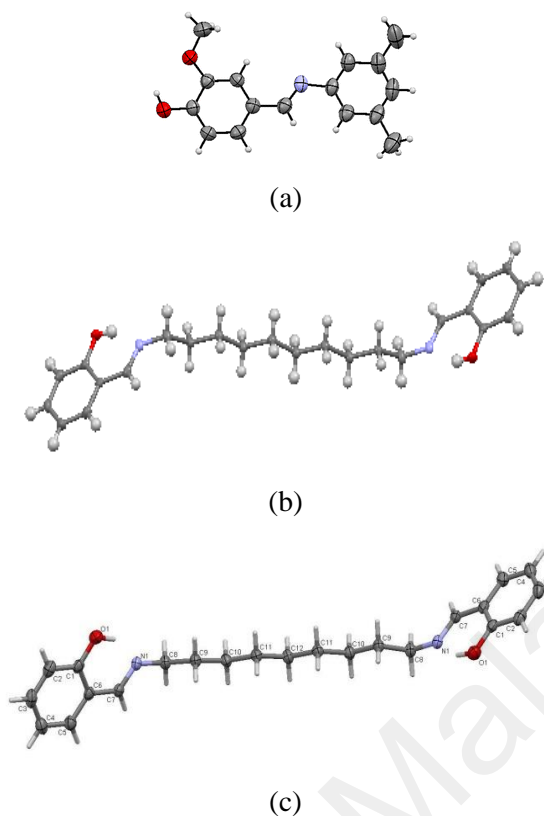


**Figure 2.3** Molecular structures of crystalline Schiff bases

Elemental analyses are used for identification and quantification of elements, elemental compounds and molecular species in terms of the weight percent of each element (C, H and N) in the compounds. It can also be used to determine the sample purity as it give very accurate results. This technique can be applied to both solid and liquid samples. For example, Khalaji *et. al* [28] reported that the calculated percentage composition of C, H and N for 2-[(4-methoxy-2-nitrophenyl)iminomethyl]phenol were 61.76% C, 4.44% H and 10.29% N, while the analytical results were 61.70% C, 4.51% H and 10.38% N.

$^1\text{H}$ -Nuclear magnetic resonance spectroscopy ( $^1\text{H}$ -NMR) is used for determining the content and purity of a sample as well as its molecular structure. For example, the spectrum can either be used to match against spectral libraries or to infer the basic structure directly. For example, Raman *et al.* [29] reported that a Schiff base derived from

benzyl-2,4-dinitrophenylhydrazone with aniline exhibited a multiplet signal at 7.3-7.8 ppm for aromatic H, and at 10.1 ppm for N-H.

Fourier transform infrared spectroscopy (FTIR) is a technique to identify the presence of certain functional groups in a molecule, and to confirm the identity of a pure compound and detect the presence of specific impurities. For Schiff bases, the most important functional group is C=N (imine) stretch, which appear as a strong peak at around  $1600\text{ cm}^{-1}$ . For example, a Schiff base derived from 8-acetyl-7-hydroxycoumarin and *p*-phenylenediamine showed characteristic bands for C=N, C=O and C-O vibrations at  $1590\text{ cm}^{-1}$ ,  $1710\text{ cm}^{-1}$  and  $1221\text{ cm}^{-1}$ , respectively [12].

### **2.3 Metal(II) complexes of Schiff bases: syntheses, chemical formulas and structures**

Schiff bases that coordinate to metal ions have been playing an important role in the development of coordination chemistry and have been studied extensively [7,8]. These compounds were also important in the development of inorganic biochemistry as they were reported to possess remarkable antibacterial, antifungal, anticancer and antimalarial activities [30-32]. In addition, they also have wide applications in food industry, dye industry, analytical chemistry, catalysis, magnetism and medical imaging [7,17,33].

#### **2.3.1 Copper(II) complexes of Schiff bases**

Complexes of Schiff bases with Cu(II) have been extensively studied [34,35]. They were synthesised either by reaction of Cu(II) acetate monohydrate [36,37] or Cu(II) salt (sulphate, chloride, nitrate) [38,39] with Schiff bases. The structure of a complex formed between Cu(II) and a Schiff base can be characterised directly using X-ray crystallography (for a crystal) or elemental analyses, IR and UV spectroscopies (for a non-crystalline complex).

For example, Sasaki *et al.* [40] reported the synthesis of [Cu(salabza)], where  $\text{H}_2\text{salabza} = N,N'$ -bis(salicylidene)-2-aminobenzylamine, by dissolving copper(II)

acetate monohydrate in a minimum volume of water and adding the solution to a solution of H<sub>2</sub>salabza in warm methanol. The complex was isolated as dark green crystals (**Figure 2.4**), and its crystal structure showed Cu(II) coordinated to phenolate oxygen and imine nitrogen, resulting in a distorted tetrahedral geometry at the copper(II) centre.

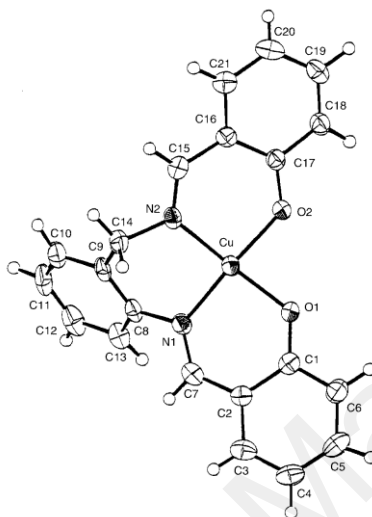


**Figure 2.4** Molecular structure of [Cu(salabza)] [40]

Another example is [Cu(Sal-6)]<sub>2</sub>, where Sal-6 = *N,N'*-bis(4-hydroxysalicylidene)-1-6-diaminooctane [41]. It was synthesised by adding a methanolic solution of copper(II) acetate over a period of 3-4 hours to a methanolic solution of the ligand using cannula. Then, the volume was reduced using a rotary evaporator. Pea-green crystals were obtained and the crystal structure (**Figure 2.5**) showed dimers with one end of two primary ligands bonded to each copper(II) centre, which have a tetrahedral environments and exhibited a *trans*-N<sub>2</sub>O<sub>2</sub> donor set.

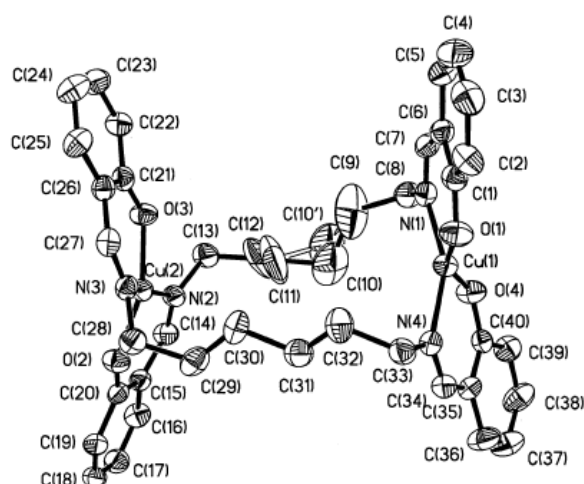


**Figure 2.5** Crystal structure of  $[\text{Cu}(\text{Sal-6})]_2$  [41]

For non-crystalline complex, the same analytical technique as for Schiff bases can be used. For example, the calculated values for  $[\text{CuL}_6]$ , where  $\text{L}_6 = N,N$ -bis(3,5-di(*tert*-butyl)salicylidene)-1,6-diaminohexane) (**Figure 2.6(a)**) [4] were 70.84% C, 8.92% H, and 4.59% N, while the results from the CHN elemental analyses were 71.78% C, 9.59% H, and 4.38% N.

For FTIR spectroscopy, the C=N group appears at around  $1550$  to  $1650\text{ cm}^{-1}$  in the Schiff bases, but shifts to lower energy by  $6$ - $11\text{ cm}^{-1}$  in complexes indicating coordination through to azomethine nitrogen [42,43]. For example, in 2003, Sandra and co-workers [44] reported an FTIR spectrum of  $[\text{Cu}(\text{L})\text{Cl}]\cdot\text{Cl}$  ( $\text{L} =$  salicylaldehyde  $\beta$ -hydrazone of isitin) (**Figure 2.6(b)**). It showed peaks for  $\nu(\text{C}=\text{N})$  at  $1560\text{ cm}^{-1}$ , Cu-N at  $461\text{ cm}^{-1}$  and Cu-O at  $498\text{ cm}^{-1}$ . Another example is  $[\text{Cu}(\text{SAH})(\text{H}_2\text{O})]$ , where SAH = bis(salicylaldiminato)hydrazone (**Figure 2.6(c)**), which showed peaks for  $\nu(\text{C}=\text{N})$ , Cu-N and Cu-O bands at  $1649\text{ cm}^{-1}$ ,  $450\text{ cm}^{-1}$  and  $514\text{ cm}^{-1}$ , respectively [45].

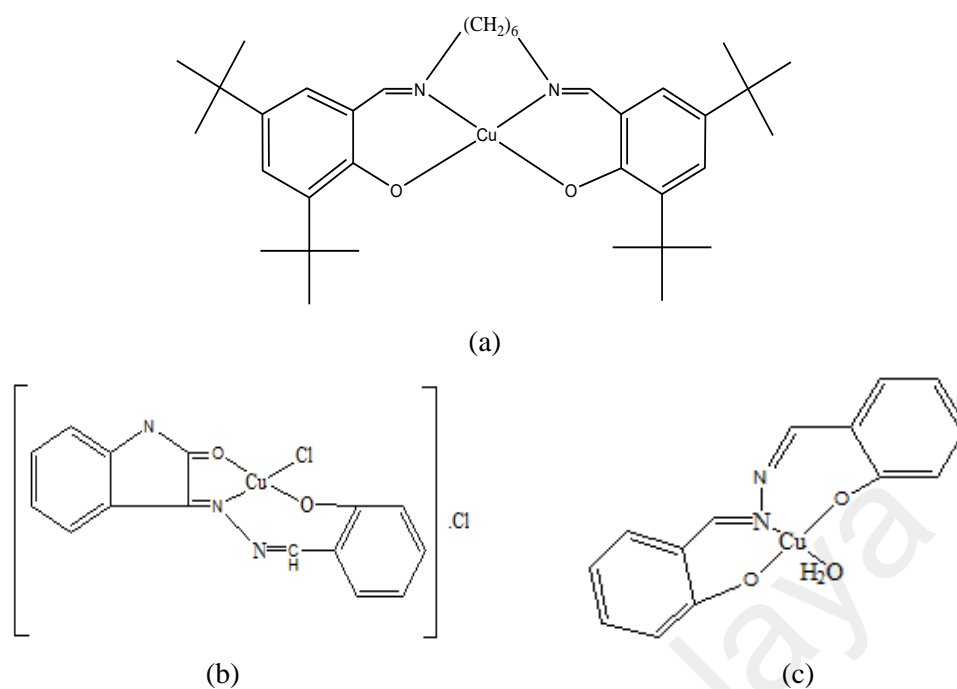


**Figure 2.6** Examples of Cu(II) complexes (a)  $[\text{CuL}_6]$ ; (b)  $[\text{Cu}(\text{L})\text{Cl}]\cdot\text{Cl}$ ; (c)  $[\text{Cu}(\text{SAH})(\text{H}_2\text{O})]$

Molecular absorption spectroscopy in the UV-visible spectral regions is widely used for qualitative and quantitative analyses of a large number of inorganic species. For complexes, UV-visible spectroscopy is useful to determine the geometry of the metal centre from the number and value(s) of  $\lambda_{\text{max}}$  (wavelength at maximum absorbance) of  $d-d$  absorption band(s) [46,47]. For Cu(II) complexes, there should be one  $d-d$  band and its  $\lambda_{\text{max}}$  value should be about 600 nm for square planar, 700 nm for square pyramidal, and 800 nm for octahedral geometry at the metal(II) centre. The molar absorptivity ( $\epsilon$ ) value for the  $d-d$  band is relatively low, roughly below  $1000 \text{ M}^{-1} \text{ cm}^{-1}$ , as the transition is forbidden. The  $\epsilon$  value can be calculated using the Beer-Lambert law ( $A = \epsilon bc$ ), where  $A$  is the absorbance,  $b$  is the path length, and  $c$  is the concentration. As an example, Aazam *et al.* [12] in 2005 reported the UV-vis spectrum of  $[\text{Cu}(\text{HL})(\text{OAc})_2]$ , where HL = 8-(1-(4-aminophenylamino)ethylidene)-2H-chromene-2,7(8H)-dione (**Figure 2.6(c)**), which showed a  $d-d$  band at 685 nm. The authors suggested a square planar geometry at the Cu(II) centre.

### 2.3.2 Nickel(II) complexes of Schiff bases

Most nickel(II) complexes are either octahedral, tetrahedral or square planar. Octahedral and tetrahedral complexes have two unpaired electrons, while square planar complexes have no unpaired electron. Complexes of Ni(II) with strong field ligands tend to be square planar, while those with weak field ligands tend to be tetrahedral.

As an example, Mukherjee *et al.* [7] reported the synthesis of  $[\text{Ni}(\text{HSalpn})(\text{NCS})(\text{H}_2\text{O})]\cdot\text{H}_2\text{O}$ , where  $\text{Salpn} = 2,2'$ -[propane-1,3-diylbis(nitrilomethylidene)]diphenol, by adding a solution of  $\text{Ni}(\text{SCN})_2\cdot 4\text{H}_2\text{O}$  in methanol-water (9:1 v/v) mixture to a solution of  $\text{H}_2\text{Salpn}$  in methanol with constant stirring for an hour at room temperature and then filtered. The complex was green crystals. The results from elemental analyses were 49.52% C, 4.36% H, and 9.57% N (calculated: 49.80% C, 4.88% H, and 9.68% N). Its FTIR spectrum shows peaks for  $\nu(\text{C}=\text{N})$  at  $1634\text{ cm}^{-1}$ ,  $\nu(\text{SCN})$  at  $2094\text{ cm}^{-1}$  and  $\nu(\text{H}_2\text{O})$  at  $3328\text{ cm}^{-1}$ . Its crystal structure (**Figure 2.7**) shows that Ni(II) was coordinated through O and N of the ligand in a distorted octahedral environment. Both axial positions were occupied by N atom of thiocyanate group and O atom of water molecule. The complex also contains non-coordinated water molecules and formed a strong hydrogen bond with the coordinated water molecules and a weaker H-bond with N atom of coordinated isothiocyanate.

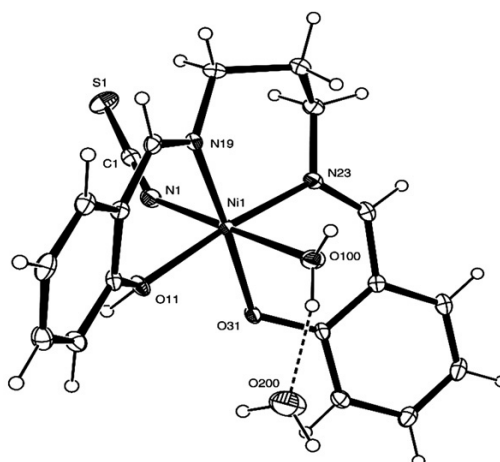


**Figure 2.7** Crystal structure of  $[\text{Ni}(\text{HSalpn})(\text{NCS})(\text{H}_2\text{O})]\cdot\text{H}_2\text{O}$  [7]

Ni(II) complexes with different geometries show differences in their UV-vis spectra. For octahedral complexes, the *d-d* bands are weak and the spectra usually show three absorptions at around 1428–770, 909–500 and 525–370 nm. These bands are assigned to  ${}^3A_{2g} \rightarrow {}^3T_{2g}$ ,  ${}^3A_{2g} \rightarrow {}^3T_{1g}$ , and  ${}^3A_{2g} \rightarrow {}^3T_{1g}(P)$  transitions, respectively. For tetrahedral complexes, the spectra are similar but the bands are at lower wavenumbers, usually at around 1420 to 1000 nm due to  ${}^3T_1 \rightarrow {}^3A_2$ , 935 to 760 nm due to  ${}^3T_1 \rightarrow {}^1E$ , 870 and 580 nm due to  ${}^3T_1 \rightarrow {}^3T_1(P)$  [48]. For square planar complexes, the *d-d* bands are found between 450 and 600 nm. For example, Yousef *et al.* [49] reported in 2013 that the UV-vis spectrum of  $[\text{Ni}(\text{HPTP})\text{Cl}]\cdot\text{H}_2\text{O}$ , where HPTP = (Z)-2-(4-(pyridine-2-yl)thiosemicarbazido)propanoate) (**Figure 2.8 (a)**), showed a broad band at 672 nm assigned to  ${}^1A_{1g} \rightarrow {}^1A_{2g}$  and at 396 nm assigned to spin-forbidden transition, suggesting a square planar geometry. Other examples are  $[\text{Ni}(\text{L})_2(\text{H}_2\text{O})_2]$  (L = 2-Benzoyl-3-hydroxy-1-naphthylamino-3-phenyl-2-propen-1-on) (**Figure 2.8(b)**), which showed three bands at 1002 nm, 595 nm, and 380 nm, suggesting an octahedral geometry [50], and  $[\text{Ni}(\text{L})_2]$  (L = 3-Methoxysalicyliden-*p*-aminoacetophenoneoxime) (**Figure 2.8(c)**), which showed a band at 632 nm, suggesting a tetrahedral geometry [42].

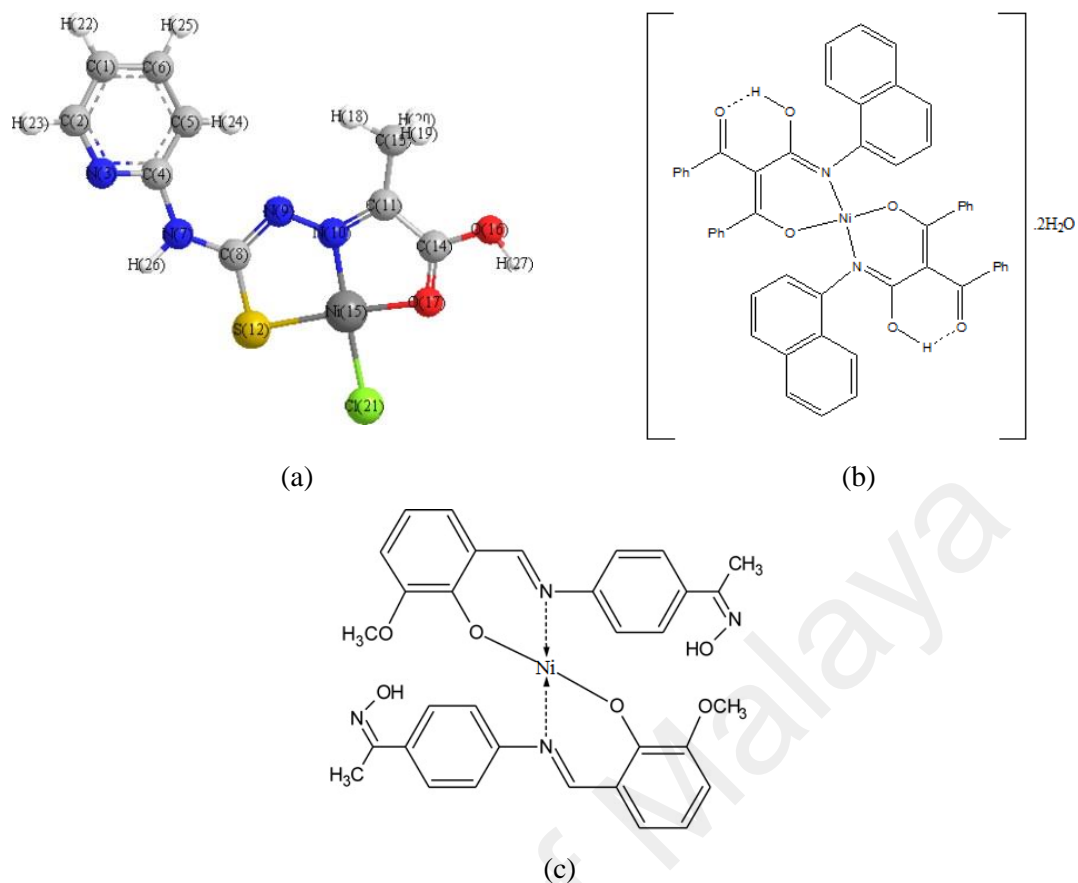


**Figure 2.8** Examples of Ni(II) complexes (a)  $[\text{Ni}(\text{HPTP})\text{Cl}]\cdot\text{H}_2\text{O}$ ; (b)  $[\text{Ni}(\text{L})_2(\text{H}_2\text{O})_2]\cdot 2\text{H}_2\text{O}$ ; (c)  $[\text{Ni}(\text{L})_2]$

### 2.3.3 Cobalt(II) complexes of Schiff bases

Most Co(II) complexes are octahedral, and depending on the ligands, may be high spin (HS) or low spin (LS). There are also tetrahedral complexes, while square planar complexes are quite rare. Another fact is Co(II) tends to be oxidised to cobalt(III) when coordinated with moderate to strong field ligands.

In 2013, Barnerjee *et al.* [51] reported a dinuclear complex,  $[\text{Co}_2(\text{L})(\text{H}_2\text{O})_2(\text{CH}_3\text{CO}_2)_2](\text{CH}_3\text{CO}_2)_2$ , (L was derived from *N*-(2-aminoethyl)piperazine and 2,6-diformyl-4-methylphenol) (**Figure 2.9**). This complex was prepared by adding *N*-(2-aminoethyl)piperazine to a heated methanolic solution of 2,6-diformyl-4-methylphenol, and the mixture refluxed for an hour, followed by adding a methanolic solution of  $\text{Co}(\text{CH}_3\text{COO})_2\cdot 2\text{H}_2\text{O}$ . The dark red solution formed crystals after it was kept in a  $\text{CaCl}_2$  desiccator for a few days. The calculated composition percentages of C, H and

N were 41.04% C, 6.89% N and 9.90% N, while the results obtained from the elemental analyses were 41.01% C, 6.85% H and 9.88% N. Its crystal structure (**Figure 2.9**) shows Co(II) ions in a distorted octahedral geometry, and two acetate ligands bridging the Co(II) ions in a *syn-syn* coordination mode.

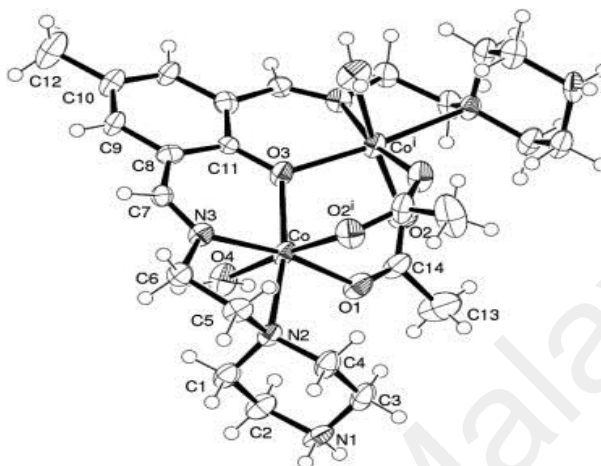


**Figure 2.9** Crystal structure of  $[\text{Co}_2(\text{L})\text{H}_2\text{O})_2(\text{CH}_3\text{CO}_2)_2](\text{CH}_3\text{CO}_2)_2$  [51]

Generally, the colour of octahedral Co(II) complexes is pink, tetrahedral is green, and square planar is brown [48,52]. For HS Co(II) octahedral complexes, there are two principle regions of the UV-vis absorption spectra: a band near 1250–1000 nm assigned to the  ${}^4\text{T}_{1g} \rightarrow {}^4\text{T}_{2g}$  transition, and another band near 500 nm with a higher intensity assigned to  ${}^4\text{T}_{1g} \rightarrow {}^4\text{T}_{1g}(\text{P})$  transition. For LS Co(II) octahedral complexes, the spectra show two bands near 1175 nm and in the range from 3300 – 1600 nm, both with similar intensity. On the other hand, the spectra for Co(II) tetrahedral complexes show two bands at 3330–1000 nm and 770–550 nm, assigned to  ${}^4\text{A}_2 \rightarrow {}^4\text{T}_1(\text{F})$  and  ${}^4\text{A}_2 \rightarrow {}^4\text{T}_1(\text{P})$  transitions, respectively. As an example, Raman *et al.* [29] reported that the spectrum of an octahedral HS  $[\text{Co}(\text{L})_2(\text{H}_2\text{O})_2]$  ( $\text{H}_2\text{L}$  was the Schiff base formed from benzyl-2,4-dinitophenylhydrazone and aniline) (**Figure 2.10(a)**) showed two spin-allowed transition at 560 and 460 nm, assigned to  ${}^4\text{T}_{1g}(\text{F}) \rightarrow {}^4\text{A}_{2g}(\text{F})$  and  ${}^4\text{T}_{1g}(\text{F}) \rightarrow {}^4\text{A}_{2g}(\text{P})$  transitions, respectively. Another example is  $[\text{Co}(\text{L})\text{Cl}]\text{Cl}$ , where L = salicylaldehyde  $\beta$ -hydrazone

of isitin (**Figure 2.10(b)**), reported by Konstantinovic *et al.* [44]. Its UV-vis spectrum showed three bands at 610, 628 and 645 nm, suggesting a tetrahedral geometry.

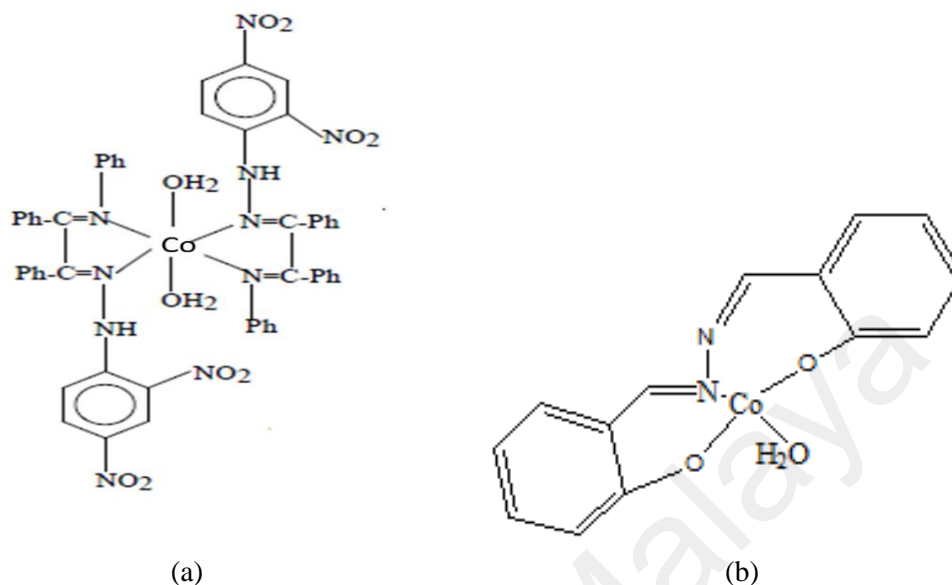


**Figure 2.10** Examples of Co(II) complexes: (a)  $[\text{Co}(\text{L})_2(\text{H}_2\text{O})_2]$ ; and (b)  $[\text{Co}(\text{L})\text{Cl}]\text{Cl}$

### 2.3.4 Iron complexes of Schiff bases

As for cobalt(II) complexes, iron(II) also formed octahedral (HS and LS), tetrahedral and square planar complexes. In addition, Fe(II) is easily oxidised to Fe(III) in the presence of oxygen and in alkaline condition.

As an example, Zeyrek *et al.* [53] reported their study for  $[\text{Fe}(\text{HL})](\text{ClO}_4)$ , where  $\text{HL}^{2-}$  was the anion derived from the Schiff base  $\text{H}_3\text{L}$  formed from triethylenetetramine and 5-chlorosalicylaldehyde (**Figure 2.11**). The complex was prepared by adding a solution of  $\text{Fe}(\text{ClO}_4)_2 \cdot 6\text{H}_2\text{O}$  in methanol to a solution of  $\text{H}_3\text{L}$  and stirring for 10 minutes. The complex was obtained as dark violet crystals after the solution was left to stand at room temperature for five days. The calculated composition percentages of C, H and N were 41.66% C, 3.84% H and 9.72% N, while the results obtained from the elemental analyses were 41.97% C, 3.10% H and 10.16% N. Its FTIR spectrum showed a strong band at  $1627\text{ cm}^{-1}$  assigned to  $\nu(\text{C}=\text{N})$ , suggesting that the imine nitrogen atoms are coordinated to the iron(III) ion. Its crystal structure (**Figure 2.11**) showed the metal atom

in a distorted octahedral geometry, with two terminal phenolic O and amine N atom *cis*, and the imine N atoms *trans*, to each other. The Fe-N (imine) bond distance (1.935(5) Å and 1.941(5) Å) were significantly shorter than Fe-N (amine) bond distance (1.999(4) Å and 2.008 Å), which suggests a LS spin Fe(III) complex (the Fe-L bond length for HS complexes is in the range of 2.00 to 2.10 Å, while for LS is in the range 1.93-1.96 Å [54]).

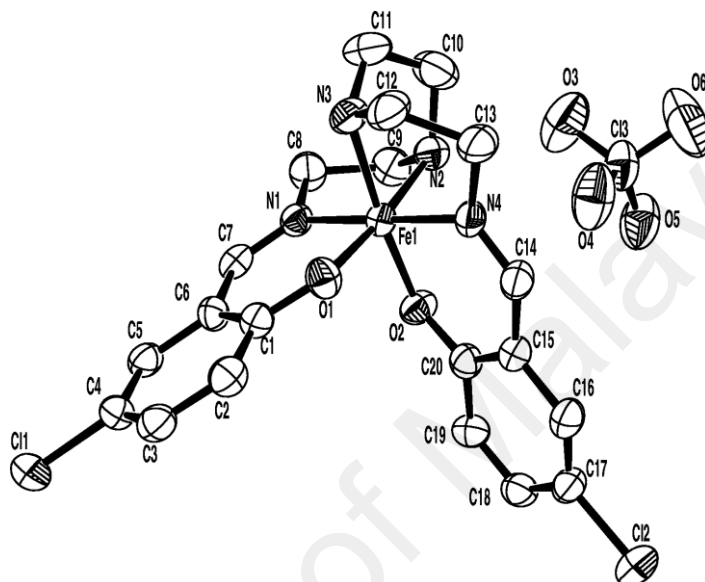


**Figure 2.11** Crystal structure of [Fe(HL)](ClO<sub>4</sub>) [53]

Abdullah *et al.* [55] reported a Fe(II) complex with the chemical formula [Fe<sub>2</sub>(OOC(CH<sub>2</sub>)<sub>14</sub>CH<sub>3</sub>)<sub>2</sub>(L3)(H<sub>2</sub>O)<sub>4</sub>]·2½H<sub>2</sub>O, where L<sup>3-</sup> was the anion of a Schiff base (H<sub>2</sub>L3) derived from 2-hydroxybenzaldehyde and 1,8-diaminooctane (**Figure 2.12**). This complex was obtained by refluxing [Fe(OOC(CH<sub>2</sub>)<sub>14</sub>CH<sub>3</sub>)<sub>2</sub>(EtOH)] with H<sub>2</sub>L3 in ethanol for 3 hours and the brown powder formed was filtered and dried at room temperature.

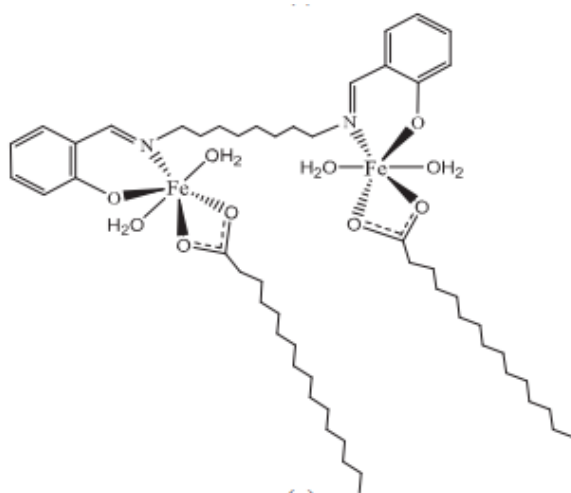


**Figure 2.12** Proposed structure of  $[\text{Fe}_2(\text{OOC}(\text{CH}_2)_{14}\text{CH}_3)_2(\text{L}_3)(\text{H}_2\text{O})_4] \cdot 2\frac{1}{2}\text{H}_2\text{O}$  [55]

The proposed structure of this complex was deduced based on combined instrumental results. The calculated composition percentages of C, H and N were 59.4% C, 9.3% H and 2.6% N, while the results obtained from the elemental analyses were 59.1% C, 8.8% H and 2.9% N. Its FTIR spectrum showed peaks (in  $\text{cm}^{-1}$ ) at 3396, 2917, 2849, 1612, 1574, 1446, 592 and 461, assigned to  $\nu(\text{H}_2\text{O})$ ,  $\nu(\text{asymCH}_2)$ ,  $\nu_{\text{sym}}(\text{CH}_2)$ ,  $\nu(\text{C}=\text{N})$ ,  $\nu(\text{asymCOO})$ ,  $\nu(\text{symCOO})$ ,  $\nu(\text{Fe}-\text{N})$  and  $\nu(\text{Fe}-\text{O})$ , respectively. The  $\Delta\text{COO}$  ( $\Delta\text{COO} = \nu_{\text{asymCOO}} - \nu_{\text{symCOO}}$ ) value was  $128 \text{ cm}^{-1}$ , suggesting a chelating binding mode of  $\text{CH}_3(\text{CH}_2)_{14}\text{COO}^-$  ligand at both Fe(II) centres. Its UV-vis spectrum showed two overlapping bands at 468 nm ( $\epsilon_{\text{max}} = 114.3 \text{ M}^{-1} \text{ cm}^{-1}$ ) and 510 nm ( $\epsilon_{\text{max}} = 63.5 \text{ M}^{-1} \text{ cm}^{-1}$ ), suggesting LS octahedral Fe(II) centres.

### 2.3.5 Manganese(II) complexes of Schiff bases

Many manganese complexes with ligands from Schiff bases have been reported in recent years. The most stable oxidation state for manganese in these complexes is +2. Mn(II) ion has  $d^5$  electronic configuration, and various geometries are expected, but most Mn(II) complexes are octahedral. In 2007, Pouralimardan *et al.* [56] reported a hydrazone Schiff base-manganese(II) complex with the chemical formula  $[\text{MnCl}_2(\text{H}_2\text{O})(\text{L}^5)]$ , where  $\text{L}^5$  was derived from pyridine-2-carbaldehyde and benzohydrazide (**Figure 2.13**). This complex

was synthesised by adding  $\text{MnCl}_2 \cdot 4\text{H}_2\text{O}$  into a solution of pyridine-2-carbaldehyde and stirring the mixture at room temperature for 30 min. Then, an ethanolic solution of benzohydrazide was added, and the reaction mixture was refluxed for 3 hours. The complex was obtained as yellow crystals. The calculated composition percentages of C, H and N were 43.30% C, 2.43% H and 11.78% N, while the results obtained from the elemental analyses were 42.30% C, 3.01% H and 11.39% N. Its FTIR spectrum displayed peaks at  $3124\text{ cm}^{-1}$  and  $1627\text{ cm}^{-1}$ , assigned to  $\nu(\text{N-H})$  and  $\nu(\text{C=N})$ , respectively. Its crystal structure (**Figure 2.13**) showed a distorted pseudo-octahedral manganese(II) atom coordinated to N,N,O donors of the ligand, and two *cis*-coordinated Cl and  $\text{H}_2\text{O}$  at axial positions.

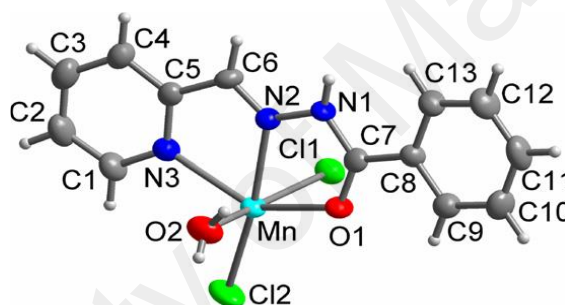


**Figure 2.13** Crystal structure of  $[\text{MnCl}_2(\text{H}_2\text{O})(\text{L}^5)]$  [56]

Another example was an octahedral Mn(II) complex with chemical formula  $[\text{Mn}(\text{L})(\text{H}_2\text{O})_2]$  (L= acetoacetanilido-*o*-phenylenediamine) (**Figure 2.14**) reported by Raman *et al.* [57]. This complex was prepared by refluxing an ethanolic solution of  $\text{H}_2\text{L}$  with  $\text{MnCl}_2$  for 6 hours, and then the volume was reduced to one third and cooled at  $0^\circ\text{C}$ . The calculated composition percentages of C, H and N were 60.6% C, 5.4% H and 10.9% N, while the results obtained from the elemental analyses were 60.2% C, 5.2% H and 10.7% N. Its IR spectrum showed a peak for  $\nu(\text{C=N})$  at around  $1600\text{--}1580\text{ nm}$ , indicating the coordination of azomethine nitrogen and Mn(II) ion. Its UV-vis spectrum did not show *d-d* transition band due to spin and Laporte forbidden transitions. Generally, the spin-forbidden bands for octahedral Mn(II) are found at about 538, 437, 397, 358 and 336

nm, assigned to  ${}^6A_{1g} \rightarrow {}^4T_{1g}(G)$ ,  ${}^6A_{1g} \rightarrow {}^4T_{2g}(G)$ ,  ${}^6A_{1g} \rightarrow {}^4E(G)$ ,  ${}^6A_{1g} \rightarrow {}^4A_{1g}(G)$ ,  ${}^6A_{1g} \rightarrow {}^4T_{2g}(G)$ , and  ${}^6A_{1g} \rightarrow {}^4E(D)$  transitions, respectively. For tetrahedral Mn(II) complexes, the bands are found between 525-400 nm ( ${}^4D$ ), 400 and 340 nm ( ${}^4P$  and  ${}^4D$ ) and 285 and 260 nm ( ${}^4F$ ). However in most cases, no bands were observed in the visible region as each orbital is singly occupied and the transition is spin forbidden [48].

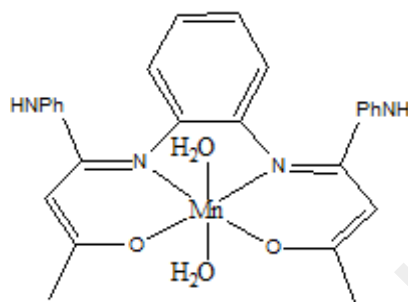


**Figure 2.14** Proposed structure of  $[Mn(L)(H_2O)_2]$  [57]

#### 2.4 Cyclam and its metal carboxylate complexes

Many macrocyclic ligands have been reported and synthesized because of their importance in coordination chemistry [58]. Coordination compounds containing macrocyclic ligands have been intensively studied due to their wide applications in biological and sensor fields [59-65]. An example is cyclam (1,4,8,11-tetraazacyclotetradecane; **Figure 2.15**). In coordination with metal complexes, cyclam binds strongly to many transition metal cations and compared to its open-chain analogue, the ligand often enhances thermodynamics and kinetic stabilities with respect to metal dissociation [66-69].

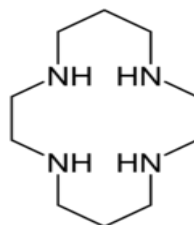


**Figure 2.15** Structure of cyclam

For example, Tajidi *et al.* [70] synthesised  $[\text{Cu}(\text{cyclam})(\text{H}_2\text{O})_2](\text{CH}_3(\text{CH}_2)_{10}\text{CO}_2)_2 \cdot 2\text{H}_2\text{O}$  by adding an ethanolic solution of cyclam to a warm ethanolic solution of dimeric copper(II) dodecanoate ( $[\text{Cu}_2(\text{CH}_3(\text{CH}_2)_{10}\text{CO}_2)_4]$ ), and heating gently for 2 h. The complex was obtained as purple plates. Its crystal structure (**Figure 2.16**) showed that the copper(II) ion in  $[\text{Cu}(\text{cyclam})(\text{H}_2\text{O})_2]^{2+}$  was located at the inversion center and coordinated to cyclam through the four aza-N atoms at the basal plane and two water molecules coordinated at axial positions of a distorted octahedron. Another two uncoordinated water molecules linked the complex cation with the dodecanoate counter ions through H-bonding. This complex exhibited metallomesogenic properties, and hence a potential functional material in the field of molecular electronic, photonic and spintronics.

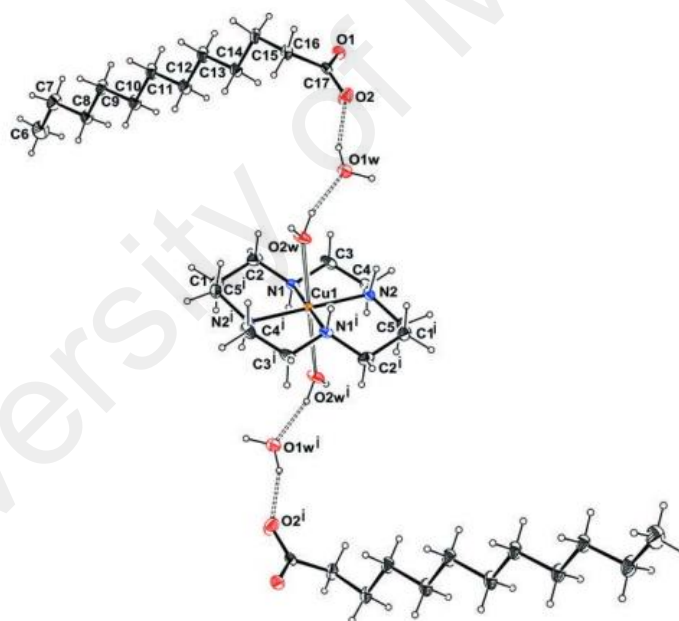


**Figure 2.16** Molecular structure of  $[\text{Cu}(\text{cyclam})(\text{H}_2\text{O})_2][\text{CH}_3(\text{CH}_2)_{10}\text{CO}_2]_2 \cdot 2\text{H}_2\text{O}$  [70]

Another example is  $[\text{Cu}(\text{cyclam})(\text{H}_2\text{O})_2](\text{C}_6\text{H}_5\text{COO})_2 \cdot 2\text{H}_2\text{O}$ , reported by Lindoy *et al.* [71]. The complex was synthesized from the reaction of bis(benzoato)copper(II) with cyclam in methanol. The complex was isolated as bluish-purple crystals. Its crystal structure (**Figure 2.17**) was similar to  $[\text{Cu}(\text{cyclam})(\text{H}_2\text{O})_2](\text{CH}_3(\text{CH}_2)_{10}\text{CO}_2)_2 \cdot 2\text{H}_2\text{O}$  [70].

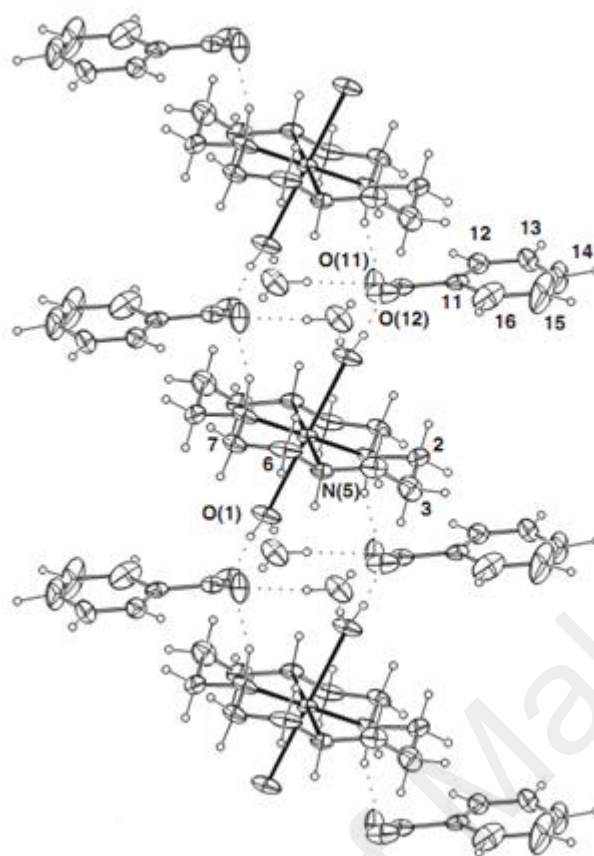


**Figure 2.17** Crystal structure of  $[\text{Cu}(\text{cyclam})(\text{H}_2\text{O})_2] \cdot (\text{C}_6\text{H}_5\text{COO})_2 \cdot (\text{H}_2\text{O})_2$  [71]

In the same paper, Lindoy *et al.* also reported  $[\text{Ni}(\text{cyclam})(\text{C}_6\text{H}_5\text{COO})_2]$ , which has a different structure from the corresponding Cu(II) complex. Its crystal structure (**Figure 2.18**) showed nickel(II) atom on an inversion centre with *trans*-unidentate O-benzoate ligands coordinated to the nickel(II) atom and the uncoordinated O H-bonded to two of the cyclam amine hydrogen, forming an octahedral geometry. Its UV-vis spectrum shows absorption bands at 522, 635, 721, 873 and a shoulder at 975 nm, suggesting the coordination of the complex was tetragonally distorted octahedral in solution.

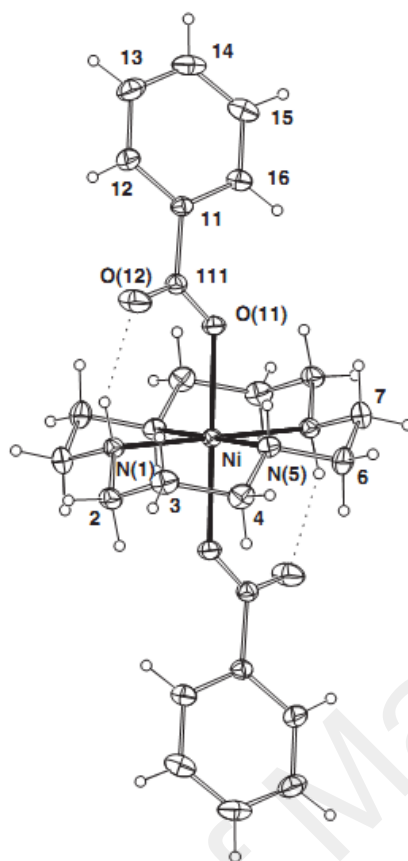


**Figure 2.18** Crystal structure of  $[\text{Ni}(\text{cyclam})(\text{C}_6\text{H}_5\text{COO})_2]$  [71]

## 2.5 Band gap

The band theory is the result of the application of molecular orbital theory to metals. The total number of molecular orbitals produced always equals to the number of atomic orbitals that overlap to produce them. These bonding and antibonding orbitals are so closely spaced in terms of energy that they are called a "band." The formation of a band is shown in **Figure 2.19**.

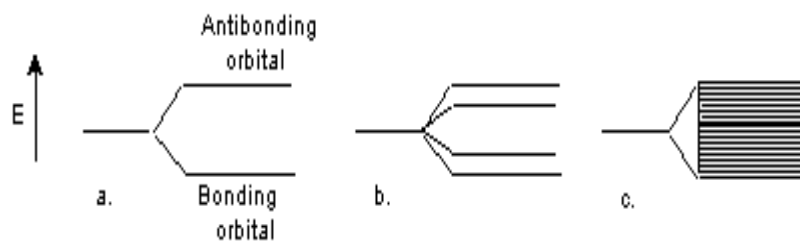


**Figure 2.19** The formation of a band

The band containing the valence shell electrons is called the valence band and any band that is either vacant or partially filled is called a conduction band. The energy difference between the top of the valence band to the bottom of the conduction is called band gap.

Based on band gap values (**Figure 2.20**), materials are categorised as conductors, insulators and semiconductors. Conductors do not have band gaps ( $E_g \sim 0$ ). All metals are conductors. These materials conduct electricity because electrons are able move freely and easily from the valence to the conduction bands. Insulators have large band gaps (usually more than 3 eV), making it impossible for an electron to jump to the conduction band. Most non-metals and organic compounds are insulators. These materials do not conduct electricity. Semiconductors have narrower band gaps ( $E_g \sim 1-3$  eV) than insulators. In these materials, electrons are able to jump from a valence band to a conduction band by acquiring a specific minimum amount of energy. Under certain conditions, they behaved as metals or insulators or have properties of both. They can conduct electricity if sufficient energy is provided (in the form of light or heat) to overcome the gap.

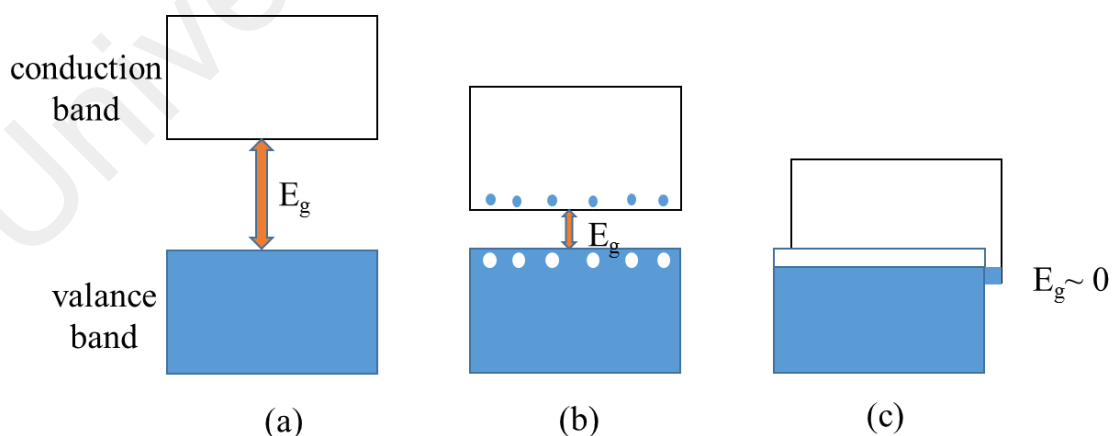


**Figure 2.20** Comparison of the electronic band structures of (a) insulators; (b) semiconductors; and (c) conductors

Youjun *et al.* [72] reported that the absorption property, especially the absorption in visible region, are very important for the photovoltaic (PV) materials. Semiconductors with low band gap ( $E_g < 1.8$  eV) are of interest because their absorption spectra cover from the visible to the near-infrared region [73] which have the greatest potential to form an efficient solar cell. Band gaps are important in semiconductors, nanomaterials and solar materials. The band gap can be determined from optical spectroscopy (absorption and emission) and cyclic voltammetry.

### 2.5.1 Absorption spectroscopy

Optical absorption spectroscopy is based on the principle of electronic transition in atoms or molecules upon absorbing suitable energy from an incident light that allows electrons to excite from a lower energy state (ground state) to higher excited energy state (excited state). Interaction with infrared light causes molecules to undergo vibrational transitions, and the shorter wavelength with higher energy radiations in the UV (200-400 nm) and visible (400-700 nm) range of the electromagnetic spectrum causes many atoms/molecules to undergo electronic transitions. Four types of electronic transition are possible:  $n \rightarrow \sigma^*$ ,  $n \rightarrow \pi^*$ ,  $\sigma \rightarrow \sigma^*$ , and  $\pi \rightarrow \pi^*$  (Figure 2.21).

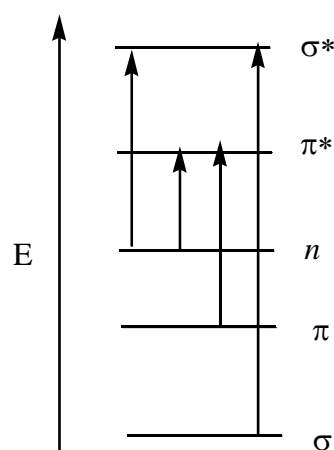


**Figure 2.21** Four types of electronic transition in molecules

For complexes, there are two types of electronic absorption transition;  $d-d$  transition and charge transfer transition. The  $d-d$  electronic transition deals with the

electronic transitions within the  $d$ -orbitals from lower energy to higher energy. Ligand-to-metal charge transfer (LMCT) may occur from the filled ligand molecular orbitals to an empty or partially filled metal  $d$ -orbitals (reduction of the metal), and metal-to-ligand charge transfer (MLCT) is the opposite [74].

Absorption spectroscopy is a simple technique to determine an optical band gap, based on the wavelength ( $\lambda$ ) of the onset of the absorption edge on the low energy side of a charge transfer band (CT). The formula is  $E_g = (hc/\lambda) \times 6.24 \times 10^{18}$  eV, where  $h$  is Planck constant ( $6.626 \times 10^{-34}$  J s) and  $c$  is the speed of light ( $3.0 \times 10^8$  m s $^{-1}$ ). For example, the absorption spectrum of TiO $_2$  is shown in **Figure 2.22**. From the spectrum, its optical band gap was 3.02 eV, defining it an insulator [75].

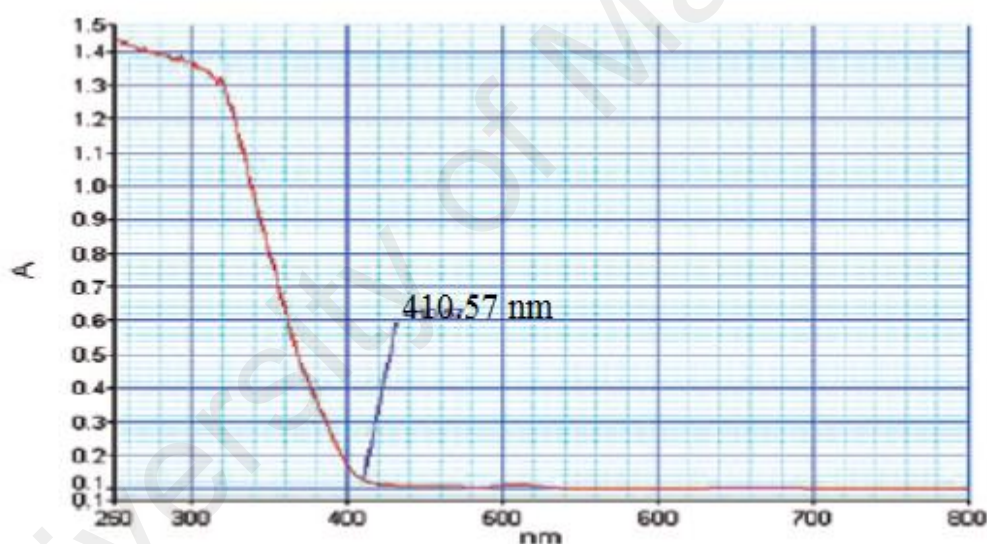


**Figure 2.22** UV-vis spectrum of TiO $_2$  [75]

Examples of band gap values for complexes were reported by Turan *et al.* [76] in 2014 for [Cu(L) $_2$ (OAc)](OAc).3.5H $_2$ O ( $E_g = 2.489$  eV) (**Figure 2.23(a)**) and [Cu(L) $_2$ (NO $_3$ ) $_2$ ].6H $_2$ O ( $E_g = 1.556$  eV) (**Figure 2.23(b)**), where L = 5,5-dimethyl-2-(2-(3-nitrophenyl)hydrazono)cyclohexane-1,3-dione). The lower band gaps ( $< 3.0$  eV) suggest that these complexes were semiconductors. These values were in the same range as highly efficient photovoltaic materials, such as CuO $_2$  (2.1 eV) and GaAs (1.43 eV), and hence

can be considered as potential materials for harvesting solar radiation in solar cells [77] and in electronic and optoelectronic devices [76].

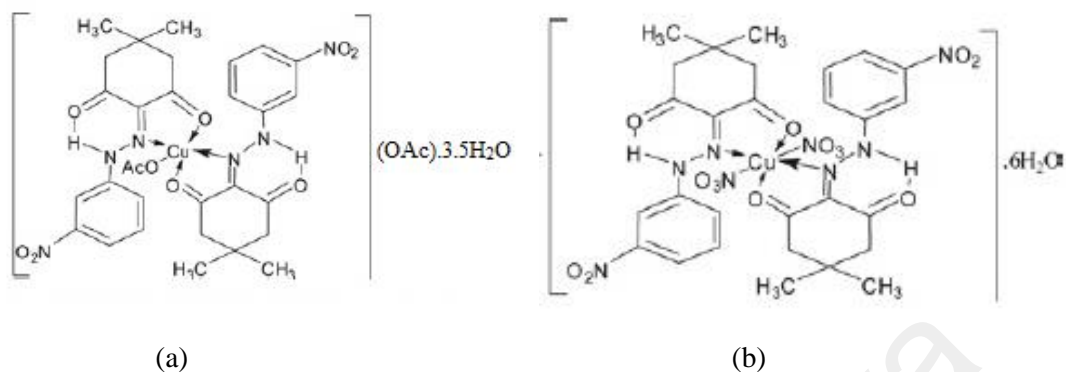


**Figure 2.23** Example of semiconductor materials

### 2.5.2 Emission spectroscopy

Emission spectroscopy measures the emission of radiation by material that has been excited. Emission is the process that creates a photon and takes the atom or molecule in an excited state back to the ground state. Fluorescence spectroscopy is one type of emission spectroscopy which is a fast, simple and inexpensive method. In fluorescence spectroscopy, a beam with a wavelength ranging between 180 – 800 nm passes through the solution in a cuvette and the light that is emitted from the sample is measured. Both an excitation and absorption spectra can be measured. To record an emission spectrum, the excitation wavelength is kept fixed, and to record excitation spectrum, the wavelength of the emission is kept fixed. When an atom or molecule absorb energy (photon), it is excited to a higher energy state. After a very short time (nanoseconds), the excited atom or molecule lose the energy and return to the ground state. The steps involved are: (a) internal conversion; and (b) competitive processes (emission, heat, energy transfer, and inter-system crossing), as shown in a Jablonski diagram (**Figure 2.24**) [78].

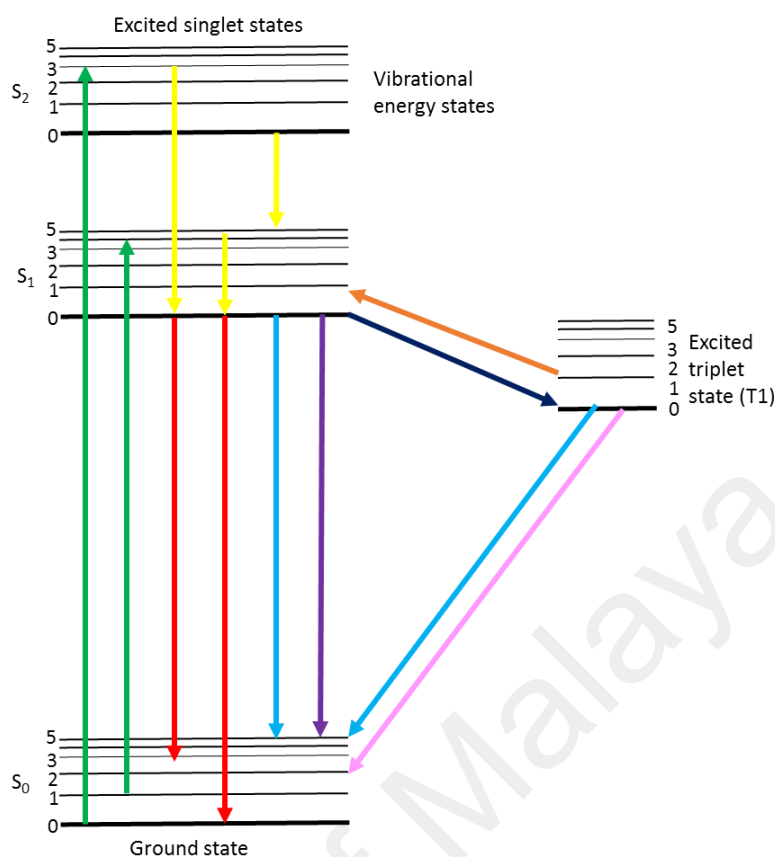


**Figure 2.24** Jablonski energy diagram [78] (green: excitation/absorption; yellow: internal conversion and vibrational conversion; red: fluorescence; dark blue: intersystem crossing; purple: quenching; blue: non-radiative relaxation; orange: delayed fluorescence; pink: phosphorescence)

When electrons go from the excited state to the ground state, there is a loss of vibrational energy. As a result, the emission spectrum is shifted to longer wavelengths than the excitation spectrum. The difference between the peak excitation and the peak emission wavelengths is known as Stokes shift (**Figure 2.25**). Each molecule has a distinct and individual Stokes shift. The greater the Stokes shift, the easier it is to separate excitation light from emission light. The Stokes shift is especially critical in multiplex fluorescence applications, because the emission wavelength of one atom may overlap, and therefore excite, another atom in the same sample. For example, Aazam [12] reported a metal-chelate Schiff base complexes with chemical formula  $[\text{MHL}_1(\text{OAc})_2(\text{H}_2\text{O})_2]$  (where  $\text{HL}_1 = 8\text{-}(1\text{-}(4\text{-aminophenylamino)ethylidene)-2\text{H-chromene-2,7(8H)-dione}$  and

M = Zn(II), Cd(II)). Its photoluminescence spectrum showed emission band at 446 nm and Stokes shift 51 nm for both complexes.

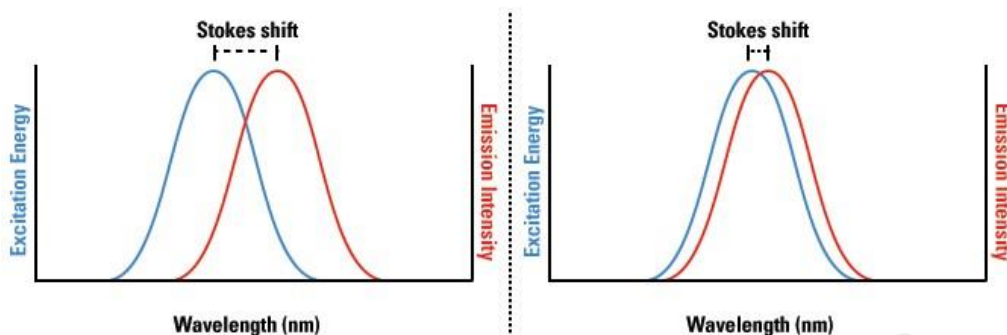


**Figure 2.25** The Stokes shift of the excitation and emission spectra of compounds

After excitation, molecules will remain in the excited state for a short time before returning to the ground state. This is called fluorescence lifetime ( $\tau$ ), which ranges from nanoseconds ( $10^{-9}$  s) to picoseconds ( $10^{-12}$  s). The fluorescence lifetime can be calculated from the data obtained from the emission spectrum. During the excited state lifetime, a molecules can undergo conformational changes as well as interact with other molecules and diffuse through the local environment. There are two techniques of lifetime measurement: the time domain and the frequency domain. In the time domain, a short pulse of light excites the sample, and the subsequent fluorescence emission is recorded as a function of time. This technique is based on fluorescence decay law, which is based on first-order kinetics. The decay law postulates that if a population of molecules is instantaneously excited when photons are absorbed, then the excited population (fluorescence intensity) as a function of time,  $I(t)$  gradually decays to the ground state.

Decay kinetics can be described by:

$$I(t) = \alpha e^{-t/\tau}$$

where  $\alpha$  is the intensity at time  $t = 0$ ,  $t$  is the time after the absorption, and  $\tau$  is the fluorescence lifetime. When  $I(t) = 0$ , the fraction of the fluorescence intensity has decreased

by a factor of  $1/e$ , or  $\sim 37\%$ . For example, **Table 2.1** show the  $\tau$  value for various fluorescein derivatives for commercial dyes, reported by Zhang and co-workers [79].

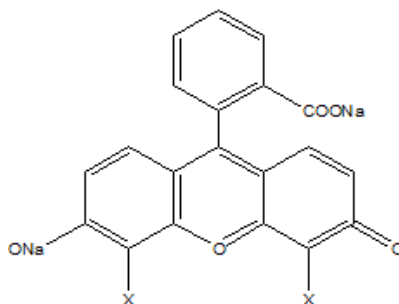


**Table 2.1** Fluorescence lifetime ( $\tau$ ) for various dyes

X	H	Cl	Br	I
$\tau$ (ns)	4.16	4.72	3.50	0.80

The onset of an emission spectrum may also use to calculate the optical band gap. Thirugnanasambandan *et al.* [80] reported Pb nanopowder as a new semiconductor. From its photoluminescence spectrum (**Figure 2.26**), the  $E_g$  values were 3.28 eV ( $\lambda_{em} = 380$  nm) and 1.64 eV ( $\lambda_{em} = 759$  nm), respectively.

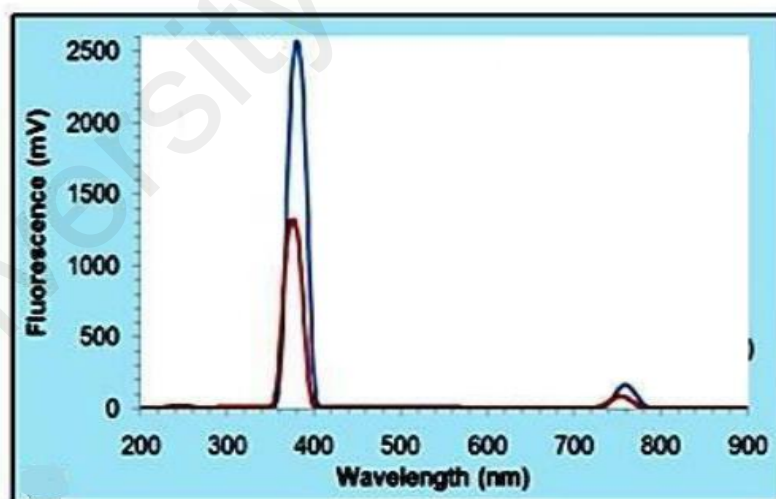


**Figure 2.26** Photoluminescence spectrum of Pb nanopowder (red: excitation, blue: emission)

### 2.5.3 Cyclic voltammetry

Cyclic voltammetry (CV) is most widely used for the preliminary determination of redox properties of a given species. The experiment is carried out under stationary condition

where the solution is kept unstirred. This is to make sure that the mass transport involves diffusion only. During the potential sweep, the potentiostat measures the current resulting from the applied potential. The resulting plot of current vs. potential is termed a cyclic voltammogram (CV). A typical CV profile exhibited by a species which undergoes a reversible electrochemical reaction is shown in **Figure 2.27**. An electrochemical process is reversible when the rate of the electron transfer is higher than the rate of mass transport.

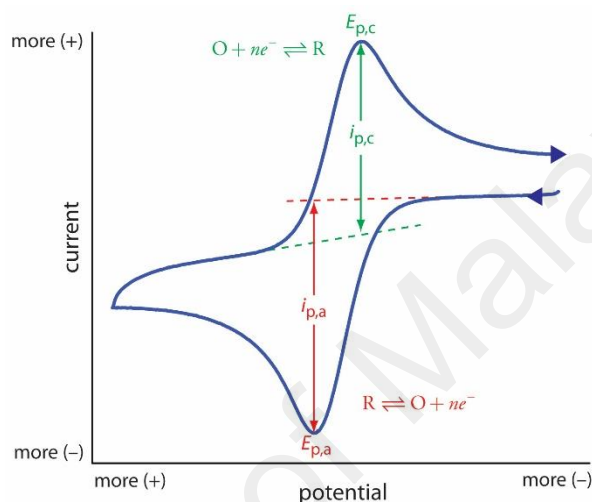


**Figure 2.27** Typical cyclic voltammogram for a reversible electrochemical process

In CV, it is assumed that only the oxidized form O is present initially. Thus, a negative-going potential scan is chosen for the first half cycle, starting from a value where no reduction occurs. As the applied potential approaches the characteristic  $E^\circ$  for the redox process, a cathodic current begins to increase, until a peak is reached. After traversing the potential region in which the reduction process takes place, the direction of the potential sweep is reversed. During the reverse scan, the reduced form R is reoxidized back to O and an anodic peak resulted. CV is characterized by several important parameters, the two peak current and two peak potentials. The well defines characteristic of reversible electrochemical reaction is: (a) the separation between the peak potentials ( $\Delta E_p$ ) is approximately  $59/n$  mV at  $25^\circ\text{C}$ , where  $n$  is the number of electrons transferred; and (b) the ratio of the reverse-to-forward peak currents is equal to one [81].

$$\Delta E_p = E_{pa} - E_{pc} = 59\text{mV}/n \quad (1)$$

$$i_{pr}/i_{pf} = 1 \quad (2)$$

As examples, [Fe<sup>III</sup>(salen)] (salen = *N,N'*-ethylenebis(salicylideneimine)) showed a one-electron oxidation process ( $E^{\circ'} = -0.28$  V), and [Fe<sup>II</sup>(saloph)] (saloph = *N,N'*-disalicylidene-*o*-phenylenediamine) showed a one-electron reduction process ( $E^{\circ'} = -0.33$ ). Both complexes underwent chemically and electrochemically reversible processes ( $i_{pr}/i_{pf} = 1$ ;  $\Delta E_p \sim 60$  mV). Therefore, it was inferred that they maintained their initial geometries [81].

An irreversible process is when the rate of electron transfer is lower than the rate of mass transport. Commonly, the separation between the forward peak and the reverse peak is so large that the latter peak is undetected. A quasireversible process occurs when the rate of electron transfer is in the same order of magnitude as that of mass transport. The separation ratio between the forward and reversed peaks is much greater than for a reversible process ( $\Delta E_p > 59$  mV). For example [Ni(3,5-Cl<sub>2</sub>saloph)], where 3,5-Cl<sub>2</sub>saloph is *N,N'*-bis(3,5-di-chlorosalicylidene)-benzene-1,2-diamine, showed characteristics of chemical reversibility ( $i_{pr}/i_{pf} = 1$ ) and electrochemical quasireversibility ( $\Delta E_p = 110$  mV) [81].

In addition, this technique also has been recognized as an easy and effective method to estimate the highest occupied molecular orbital (HOMO) and the lower unoccupied molecular orbital (LUMO) energy levels, and hence, the electrochemical band gap ( $E_g$ ), of a material. The oxidation process corresponds to removal of electron(s) from the HOMO energy level, while the reduction corresponds to addition of electron(s) to the LUMO energy level. Bredas *et al.* [82] reported that the onset potential of oxidation ( $E_{ox}$ ) and reduction ( $E_{red}$ ) of a material can be correlated to the ionization potential ( $I_p$ ) and electron affinity ( $E_a$ ) according to the empirical relationship that he proposed:

$$I_p(E_{HOMO}) = (E_{ox} + 4.4) \text{ eV}$$

$$E_a(E_{LUMO}) = (E_{red} + 4.4) \text{ eV}$$

$$E_g = I_p - E_a$$

The onset potential are estimated from the intersection of the two tangents drawn at the rising current and baseline charging current of the CV. For example, Abdullah *et al.* [83] reported a copper(II) mixed valence complex,  $[\text{Cu(II)Cu(II)(R)}_3(\text{RH})_2\text{L}_4].\text{CH}_3\text{COCH}_3$ , where  $\text{L} = \text{CH}_3\text{COCH}_2\text{C}(\text{OH})(\text{CH}_3)_2$  and  $\text{R} = \text{C}_6\text{H}_5\text{COO}$ , as a low band gap photovoltaic material. From the CV (**Figure 2.28**), they reported that the onset potential reduction process was  $-0.68 \text{ V}$ , and the onset potential oxidation process was  $+0.49 \text{ V}$ . From these values, the calculated HOMO and LUMO were  $4.9 \text{ V}$  and  $3.7 \text{ V}$ , respectively. Hence, the electrochemical band gap was  $1.2 \text{ eV}$ .

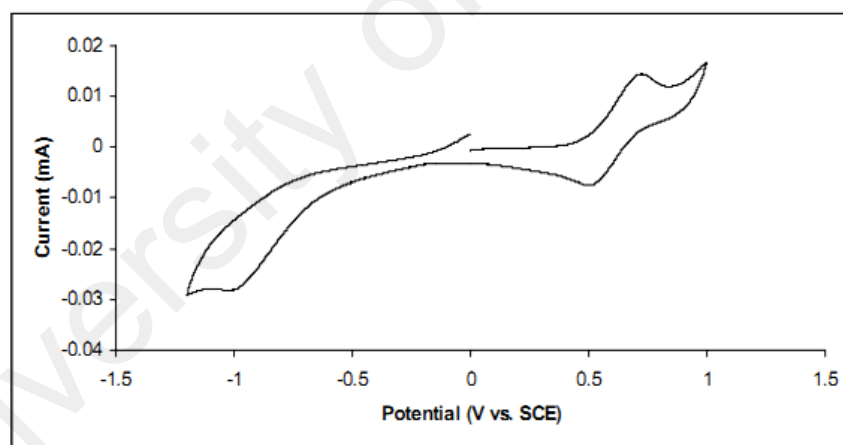


**Figure 2.28** CV of  $[\text{Cu(II)Cu(II)(R)}_3(\text{RH})_2\text{L}_4].\text{CH}_3\text{COCH}_3$  [83]

## 2.6 Magnetisms

A material may either be diamagnetic and paramagnetic. A diamagnetic material does not have unpaired electrons. Accordingly, the net value of the total spin quantum number is zero ( $S = 0$ ). It is repelled by magnetic field. In contrast, a paramagnetic material has one or more unpaired electrons (the overall quantum number will be greater than zero ( $S > 0$ )). It is attracted by magnetic field.

The classical theory of magnetism states that when a substance is placed within a magnetic field,  $H$ , the field within the substance,  $B$ , differs from  $H$  by the induced field (applied magnetic field),  $4\pi I$ , which is proportional to the intensity of magnetization,  $I$ .

$$B = H + 4\pi I$$

This equation may also be written as:

$$B/H = 1 + 4\pi I/H \text{ or } B/H = 1 + 4\pi\kappa$$

where  $B/H$  is magnetic permeability, and  $\kappa$  is the magnetic susceptibility per unit volume, ( $I/H$ ). Since the value of  $\kappa$  in a vacuum is zero,  $B = H$ . It is more convenient to measure mass (gram) susceptibility,  $\chi_g$ , which is related to the volume susceptibility through density ( $\rho$ ).

$$\chi_g = \kappa / \rho$$

The most common way of reporting a magnetic susceptibility value in the literature is by molar susceptibility, designated as  $\chi_M$ , which is a dimensionless quantity.

The relationship of molar susceptibility to mass susceptibility is:

$$\chi_M = \chi_g \text{ MW}$$

where  $\chi_g$  is mass susceptibility and MW is the molecular weight of the substance. The  $\chi_M$  value has to be corrected for diamagnetic contribution ( $\chi_{\text{dia}}$ ) from the ligands and metal ions (obtained from Pascal's constant) as follows:

$$\chi_M^{\text{corr}} = \chi_M - \chi_{\text{dia}}$$

where  $\chi_M^{\text{corr}}$  is corrected molar susceptibility. From the value of  $\chi_M^{\text{corr}}$ , the effective magnetic moment ( $\mu_{\text{eff}}$  in B.M.) can be calculated using the following equation:

$$\mu_{\text{eff}} = 2.84 (T\chi_M^{\text{corr}} - N\alpha)$$

where  $T$  is the absolute temperature, and  $N\alpha$  is the temperature-independent paramagnetism (TIP) for each metal ion. TIP is usually small and can be ignored. For example, the TIP value is  $60 \times 10^{-6} \text{ cm}^3 \text{ mol}^{-1}$  for Cu(II),  $100 \times 10^{-6} \text{ cm}^3 \text{ mol}^{-1}$  for Ni(II),

and  $200 \times 10^{-6} \text{ cm}^3 \text{ mol}^{-1}$  for Co(II). The experimental  $\mu_{\text{eff}}$  value is then compared with the theoretical value, calculated using the following equation:

$$\mu_{\text{eff}} = \sqrt{n(n+2)}$$

where  $n$  is number of unpaired electron(s).

Magnetic moment is often used in conjunction with electronic spectroscopy to obtain information of oxidation number of a metal ion and its geometry. A common method to determine the magnetic moment of a powder sample is known as the Guoy method.

Metal ion can be coordinated with ligands in different geometry, but the most common is octahedral, tetrahedral and square planar. According to the Crystal Field theory, the energy of the  $d$  orbitals in an octahedral complex are split into two sets:  $d_{x^2-y^2}$  and  $d_{z^2}$  ( $e_g$  subset) at higher energy, and  $d_{xy}$ ,  $d_{xz}$ ,  $d_{yz}$  orbitals ( $t_{2g}$  subset) at lower energy. (Figure 2.29). The electrons then filled these orbitals according to Aufbau principle, Pauli exclusion principle, and Hund's rule.

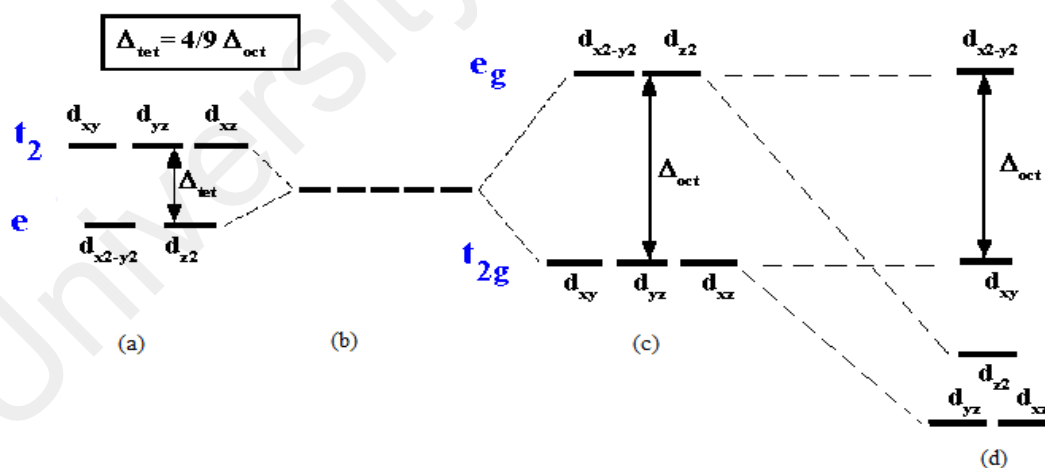


**Figure 2.29** Energy level of the  $d$  orbitals in: (a) tetrahedral; (b) free ion; (c) octahedral; and (d) square planar complexes

For octahedral complexes of metal ion with valence electronic configurations  $d^4$  to  $d^7$ , there are two possible arrangements depending on the ligand(s) (Figure 2.30). Weak field ligand(s) form high spin (HS) complexes (maximum number of unpaired

electrons), while strong field ligand(s) form low spin (LS) complexes (minimum number of unpaired electrons).

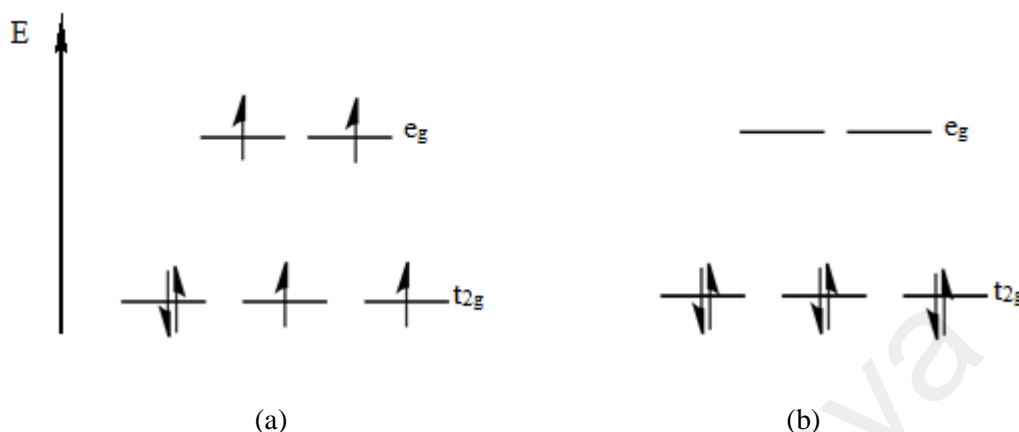


**Figure 2.30** *d*-orbital splitting for octahedral  $d^6$  (a) high spin; and (b) low spin

For tetrahedral complexes, the energy of the *d* orbitals also split into two sets, but in the opposite way (**Figure 2.29(a)**). This is because of lower electrostatic repulsion between the ligands and the electrons in the *d* orbitals of the metal ion since the ligands are not pointing directly at these orbitals. The difference between the two subsets of energies is much smaller than in octahedral complexes ( $\Delta_t = 4/9 \Delta_o$ ) since there are only four ligands in these complexes. Hence, all tetrahedral complexes have the maximum number of unpaired electrons.

Finally, square planar complexes are favoured by strong field ligands. The splitting of the *d* orbitals are larger (**Figure 2.29(d)**) than for octahedral complexes ( $\Delta \sim 1.3 \Delta_o$ ) because of the formation of stronger M-L bonds in the *x,y* plane. Hence, square planar complexes have minimum number of unpaired electrons.

Copper(II) ion has one unpaired electron (valence electronic configuration  $3d^9$ ). Hence, mononuclear copper(II) complexes are expected to have the spin-only  $\mu_{\text{eff}}$  value of 1.73 BM. For example, the  $\mu_{\text{eff}}$  value for  $[\text{Cu}(\text{L})\text{H}_2\text{O}]$ , where  $\text{H}_2\text{L}$  was bis(salicylaldiminato)hydrazone) (**Figure 2.31(a)**), was 1.84 BM. The authors suggested a square planar geometry at Cu(II) centre [45]. For binuclear complexes, the  $\mu_{\text{eff}}$  value is

actually lower than the spin-only value (2.44 B.M.). For example, the  $\mu_{\text{eff}}$  for  $[\text{Cu}_2(\text{CH}_3(\text{CH}_2)_{12}\text{COO})_4]$  (**Figure 2.31(b)**) was 1.45 B.M. at 20 °C [84]. This was ascribed to electronic communication between the two metal centres, through the bridging ligands (termed the superexchange mechanism).

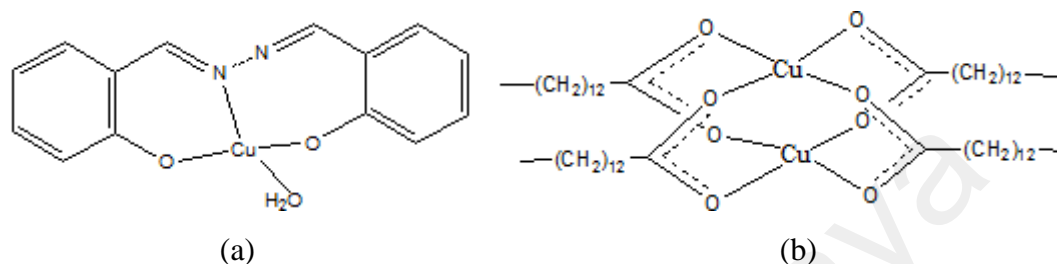


**Figure 2.31** Molecular structure of: (a)  $[\text{Cu}(\text{L})\text{H}_2\text{O}]$  [45]; and (b)  $[\text{Cu}_2(\text{CH}_3(\text{CH}_2)_{12}\text{COO})_4]$  [84]

Nickel(II) ion have two unpaired electrons (valence electronic configuration  $3d^8$ ). Hence, its octahedral complexes are expected to have the  $\mu_{\text{eff}}$  value of 2.83 BM. The reported values were in the range of 2.9 to 3.4 BM due to orbital contribution. Square planar complexes are diamagnetic ( $\mu_{\text{eff}} = 0$  BM), while the  $\mu_{\text{eff}}$  values for tetrahedral complexes were found to be in the range of 3.0 to 4.0 BM. However, complexes with larger tetrahedral distortion have lower magnetic moments. For example, Jha *et al.* [85] reported that the  $\mu_{\text{eff}}$  value for  $[\text{Ni}(\text{L})_2] \cdot 2\text{H}_2\text{O}$  (HL = 1-indenylacetohydroxamic acid) was 2.94 BM, and suggested an octahedral geometry at Ni(II) centre, while  $[\text{Ni}(\text{L})(\text{Py})(\text{HCOO})]$  (HL = *p*-methylphenylacetohydroxamic acid) was diamagnetic and suggested a square planar geometry.

Cobalt(II) ion has three unpaired electrons (valence electronic configuration  $3d^7$ ). The expected spin-only  $\mu_{\text{eff}}$  values for its octahedral complexes are either 3.87 BM for HS (3 unpaired electrons) or 1.73 BM for LS (1 unpaired electron). Typically, octahedral Co(II) complexes have the  $\mu_{\text{eff}}$  values between 4.7 to 5.2 BM for HS, and about 1.8 BM for LS. For tetrahedral complexes, the values are usually lower than 4.7 BM. For example, Canpolat *et al.* [42] reported the  $\mu_{\text{eff}}$  value for  $[\text{Co}(\text{L})_2]$ , where L is

*p*-aminoacetophenoneoxime-3-methoxysalicylaldiminato (**Figure 2.32**) as 4.23 BM, which is characteristic for a tetrahedral complex.

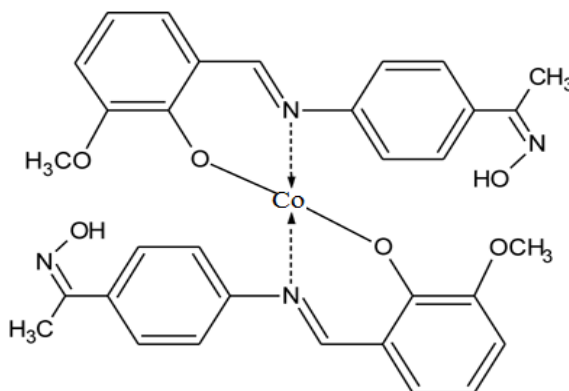
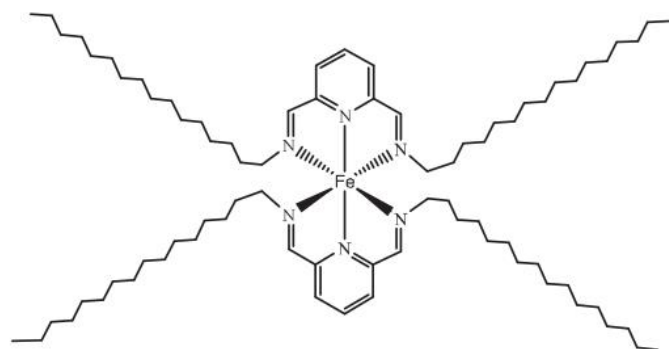
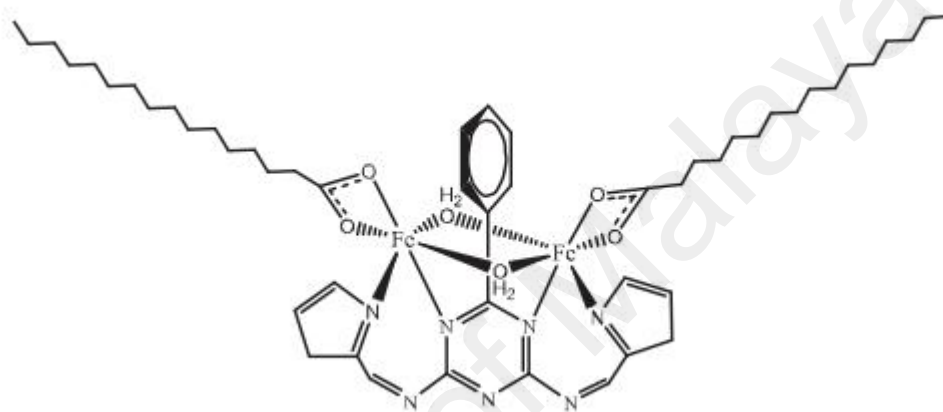


**Figure 2.32** Molecular structure of [Co(L)<sub>2</sub>] [42]

Iron(II) ion have four unpaired electrons (valence electronic configuration  $3d^6$ ). The expected spin-only  $\mu_{\text{eff}}$  values for its octahedral complexes are either 4.9 BM for HS (4 unpaired electrons) or 0 BM for LS (0 unpaired electron). For HS octahedral and for tetrahedral complexes, the observed  $\mu_{\text{eff}}$  values are around 5.1 to 5.7 BM and 5.3 to 5.5 BM, respectively. For example, Abdullah *et al.* [55] reported that [Fe(L)<sub>2</sub>](BF<sub>4</sub>), where H<sub>2</sub>L was a Schiff base formed from 2,6-pyridinedicarboxaldehyde and 1-aminohexadecane (**Figure 2.33(a)**), was diamagnetic at room temperature, indicating a LS complex. In the same paper, the authors also reported a HS octahedral, [Fe(OOC(CH<sub>2</sub>)<sub>14</sub>CH<sub>3</sub>)<sub>2</sub>(L)(H<sub>2</sub>O)<sub>2</sub>], where H<sub>2</sub>L is derived from reaction of pyrole-2-carboxaldehyde and 2,4-diamino-6-phenyl-1,3,5-triazine (**Figure 2.33(b)**), which has the  $\chi_{\text{m}}T$  value of 6.2 cm<sup>3</sup> K mol<sup>-1</sup> at 298 K (expected 6 cm<sup>3</sup> K mol<sup>-1</sup> for dimeric HS octahedral).



(a)



(b)

**Figure 2.33** Molecular structures of: (a)  $[\text{Fe}(\text{L})_2](\text{BF}_4)$ ; (b)  $[\text{Fe}(\text{OOC}(\text{CH}_2)_{14}\text{CH}_3)_2(\text{L})(\text{H}_2\text{O})_2]$  [55]

Manganese(II) ion have five unpaired electrons (valence electronic configuration  $3d^5$ ). The expected spin-only  $\mu_{\text{eff}}$  values for its octahedral complexes are either 5.9 BM for HS (5 unpaired electrons) or 1.73 BM for LS (1 unpaired electron). For HS octahedral complexes, the observed  $\mu_{\text{eff}}$  values were about 5.6 to 6.1 BM, which were also observed in tetrahedral complexes, while the values for LS octahedral complexes were about 1.8 to 2.1 BM. Thus, the  $\mu_{\text{eff}}$  values are not sufficient to distinguish the geometry of these complexes. For example, Salavati-Niasari and Amiri, [45] reported that the  $\mu_{\text{eff}}$  value for  $[\text{Mn}(\text{L})\text{H}_2\text{O}]$ , where  $\text{H}_2\text{L} = \text{bis}(\text{salicylaldiminato})\text{hydrazone}$ ) (**Figure 2.34(a)**), was 5.86 BM, and proposed a tetrahedral geometry for this complex. On the other hand, Yousef *et al.* reported the value of 6.01 BM for their yellow octahedral complex,

[Mn(HPTP)Cl(H<sub>2</sub>O)<sub>2</sub>] (HPTP = (Z)-2-(4-(pyridine-2-yl)thiosemicarbazido)propanoate)  
(Figure 2.34(b)) [49].

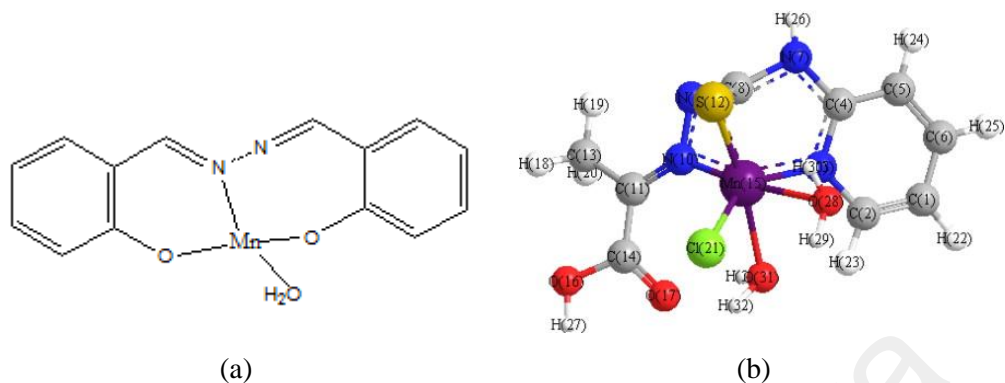


**Figure 2.34** Molecular structures of: (a) [Mn(L)H<sub>2</sub>O] [45]; and (b) [Mn(HPTP)Cl(H<sub>2</sub>O)<sub>2</sub>] [49]

## 2.7 Metallomesogens

The study of liquid crystals encompasses a multi-disciplinary field of research that includes the concepts and techniques from chemistry and physics, and in some cases, demands ideas from mathematics, biology and engineering. These materials generally have several common characteristics. Examples are rigidity of the long axis, and strong dipoles and/or easily polarizable substituents. The characteristic of liquid crystals that distinguishes them from liquids and solids is the tendency of their molecules (mesogens) to point along a common axis, called the director.

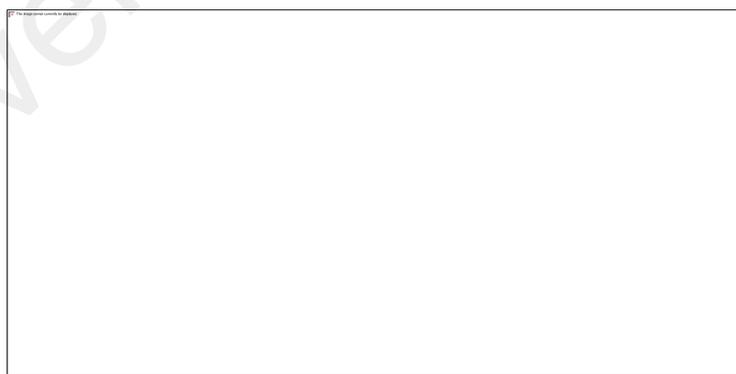
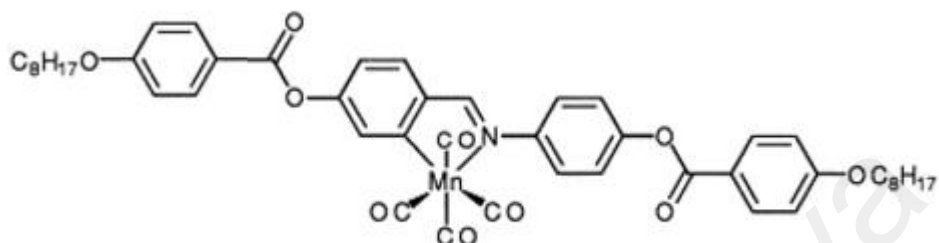


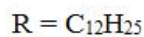
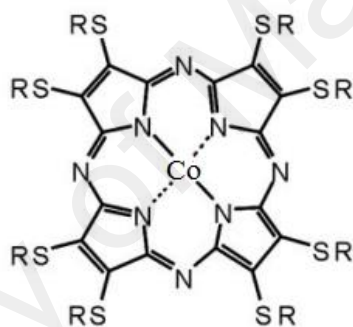
**Figure 2.35** The average alignment of the molecules for solid, liquid crystal and liquid.

Metallomesogens or metal-containing liquid crystals are a relatively well established field in science. Vorländer in 1923 was the first person to describe the first metallomesogens [86]. Thermotropic metallomesogens have been made incorporating

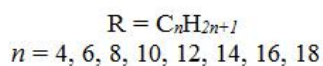
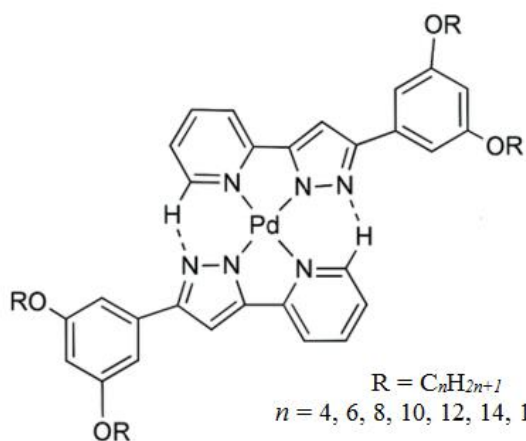
many metals from *s*, *p*, *d* and *f* blocks of the Periodic Table. Examples of all types of mesophases are known, such as rod-like (calamitic), disc-like (discotic) and polycatenar (many tailed), and many different varieties of ligands can be used, such as monodentate, bidentate and polydentate. Three examples of metallomesogens are shown in **Figure 2.36**.



(a)



(b)



(c)

**Figure 2.36:** Example of metallomesogen: (a) calamitic; (b) discotic; (c) polycatenar

Liquid crystals can show nematic, smectic or columnar mesophases according to their position order and orientational order (**Figure 2.37**). Some liquid crystals may only exhibit one type of mesophase, whilst others may exhibit different mesophases at different temperatures.

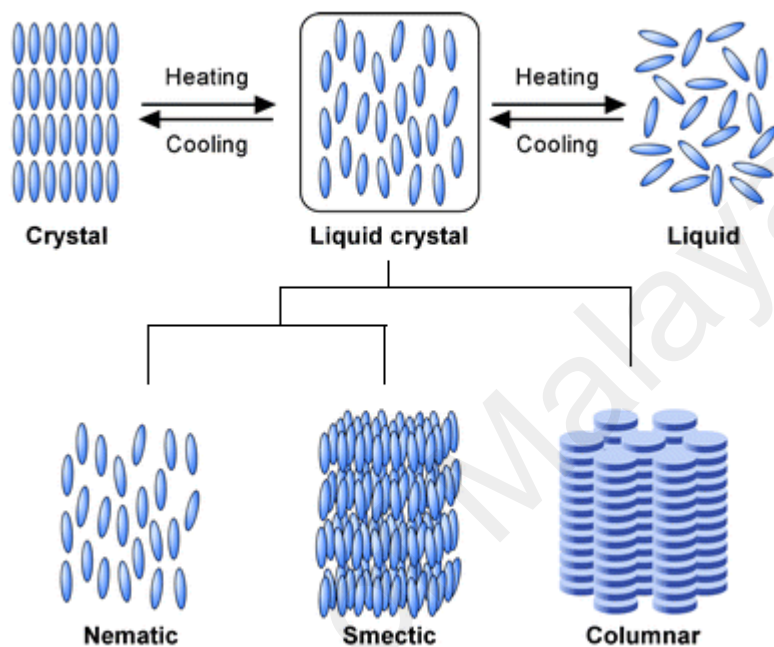


**Figure 2.37** Different phases of a liquid crystal

The nematic liquid crystal phase is characterized by molecules that have no positional order but tend to point in the same direction (along the director). It was noticed that the molecules point vertically but are arranged with no particular order (**Figure 2.38**).

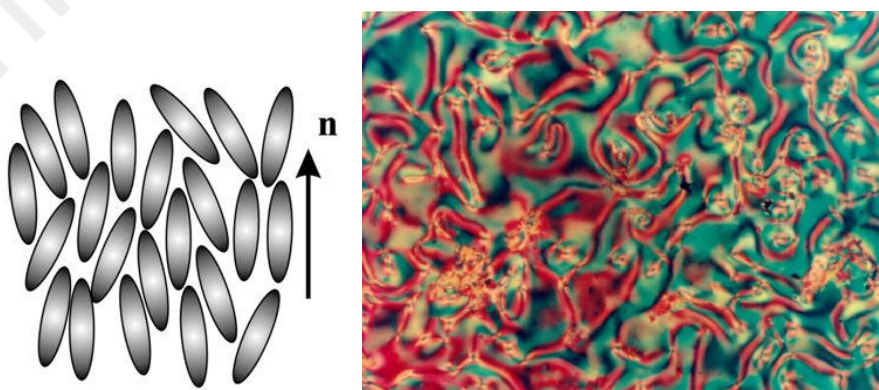
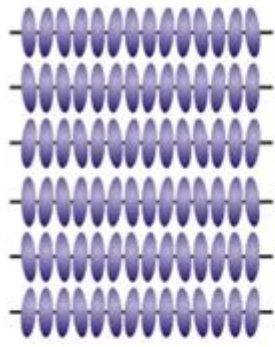


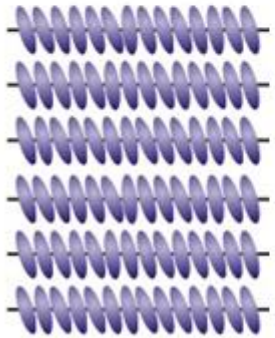
**Figure 2.38** The nematic phase

Liquid crystals are anisotropic materials, and the physical properties of the system vary with the average alignment with the director. If the alignment is large, the material is very anisotropic and if the alignment is small, the material is almost isotropic. Due to the microstructure of the nematic phase, many of the macroscopic properties are anisotropic. For example, nematics exhibit a birefringence due to polarised light and can undergo a reorientation (electro-optic switching) due to an anisotropy in the distribution of electrical charge across the molecule. Therefore, nematic liquid crystals possess a number of useful material properties such as a high birefringence, sensitivity to low frequency electric fields and structural flexibility.

The smectic phase is another distinct mesophase of liquid crystals. In smectic phase, the molecules maintain the general orientational order of nematics, but also tend to align themselves in layers or planes. The increased order means that the smectic state is more "solid-like" than the nematic. Many compounds are observed to form more than one type of smectic phase. The most commonly used smectics phase are smectic A (SmA) and smectic C (SmC) (**Figure 2.39**). In the smectic A mesophase, the director is perpendicular to the smectic plane, and there is no particular positional order in the layer while, in the smectic-C mesophase, molecules are arranged as in the smectic-A mesophase, but the director is at a constant tilt angle measured normally to the smectic plane.



Smectic A



Smectic C

**Figure 2.39** The smectic phases

Columnar liquid crystals are shaped like disks. This mesophase is grouped by their structural order and the ways of packing of the columns. The columns are packed together to form a two-dimensional crystalline array. The arrangement of the molecules within the columns and the arrangement of the columns themselves leads to new mesophases.

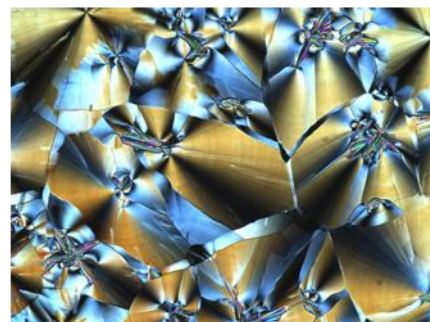


**Figure 2.40** Columnar liquid crystal

Optical polarizing microscopy (OPM) is a useful tool as it provides a lot information about the macroscopic structure of liquid crystal phases. The optical

properties of liquid crystal phases often directly reflect the symmetry of their structures. Anisotropy of the refractive index, or birefringence, is one of the characteristic physical properties of liquid crystals, and it allows for the visualization of the macroscopic molecular orientation. Although there are many experimental techniques available to investigate the structure and physical properties of liquid crystal phases, microscopic observations often give enough information to determine the structure even if a well-aligned domain is not obtained. The identification of a mesophase through optical polarizing microscopy usually involves the magnified view of a thin sample of mesomorphic material sandwiched between a glass microscope slide and a glass coverslip. In the case of an isotropic liquid, polarized light remains unaffected when the polarizer and analyser are in cross configuration, which give a black appearance. However, when an anisotropic, birefringent medium is present, polarized light is not extinguished and an optical texture appears that gives information relating to the arrangement of the molecules within the medium.

Differential scanning calorimetry (DSC) is a tool which complements optical methods in the study of liquid crystal phase transitions. The DSC can show the presence of phase transitions in a material by detecting the enthalpy change associated with each phase transition. The precise identity of the phase cannot be obtained but the enthalpy changes do indicate the types of phase involved. DSC has two furnaces, one to heat the sample and the other to heat the reference material. The two furnaces are separately heated but connected by two control loops to ensure that the temperature of both remains identical through a heating or cooling cycle and heating or cooling rate for each is constantly identical. If the phase transition occurs, energy must be supplied to the sample to prevent an imbalance in temperature between sample and reference. The energy required is measured and recorded by the instrument as a peak on a baseline. The sample

can be cooled using liquid nitrogen and a working temperature range of between -180 and 600 °C is possible.

For example, Bhattacharjee *et al.* [87] reported the thermal behaviour of Ni-16opd (**Figure 2.41**) by OPM and DSC. This complex showed enantiotropic mesomorphic behaviour and OPM showed that, upon cooling from isotropic phase, a spherulitic growth appeared which combine to a fan-like texture at 130°C (**Figure 2.42**) with large homeotropic regions, suggesting a columnar mesophase (Col). The mesophase was stable down to room temperature.

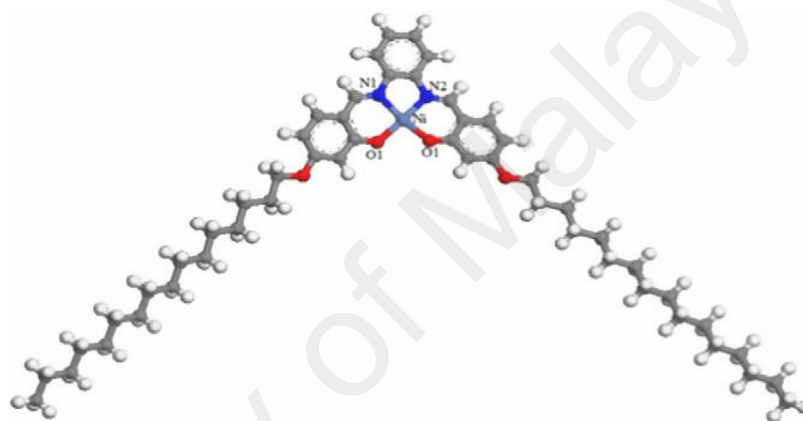


**Figure 2.41** X-ray structure of Ni-16opd [87]

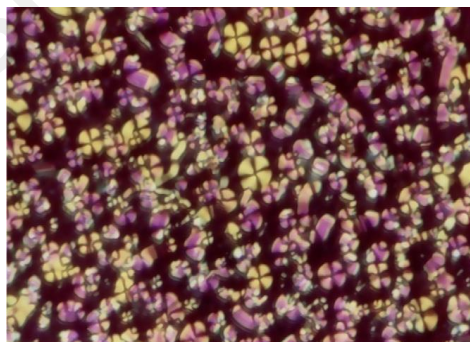


**Figure 2.42** Photomicrograph of Ni-16opd at 130 °C [87]

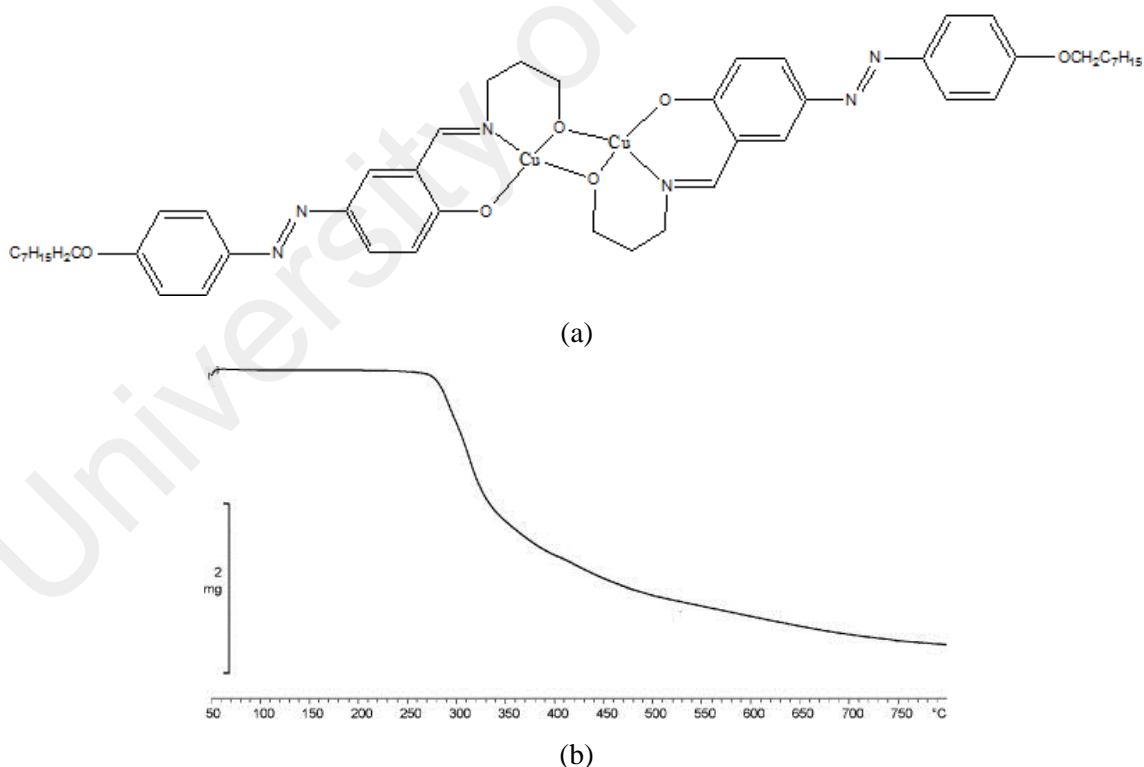
The DSC thermogram (**Table 2.2**) for the complex exhibited two transitions in heating cycle and two transitions in cooling cycle.

**Table 2.2** DSC data of complex Ni-16opd [87]

	T (°C)	Transition	$\Delta H$ (kJ mol <sup>-1</sup> )
<b>Heating</b>	108.2	Cr-Col <sub>r</sub>	2.9
	135.0	Col <sub>r</sub> -I	2.6
<b>Cooling</b>	133.9	I-Col <sub>r</sub>	2.5
	87.1	Col <sub>r</sub> -Cr	0.93

Cr = crystal, Col<sub>r</sub> = rectangular columnar, I = isotropic

For thermotropic liquid crystals, it is important to record their decomposition temperatures before studying their mesophases by POM and DSC. This may be done by thermogravimetric analysis (TGA). TGA measures weight changes in a material as a function of temperature (or time) under a controlled atmosphere. Its principle uses include measurement of thermal stability and composition of a material. For example, a dinuclear Cu(II) complex (**Figure 2.43**) started to decompose at around 280 °C, which was reported near its clearing temperature to the isotropic liquid [88].

**Figure 2.43** (a) molecular structure; and (b) TGA thermogram of Cu(II) complex [88]

## CHAPTER 3: EXPERIMENTAL

### 3.1 Introduction

The main objective of this research project was to synthesize and characterize homometallic and heterometallic complexes as molecular magnetic and/or low band gap metallomesogenic materials.

For the homometallic complexes, the ligands were anions of three Schiff bases ( $H_2L1$ ,  $H_2L2$  and  $H_2L3$ ) (**Figure 3.1**).

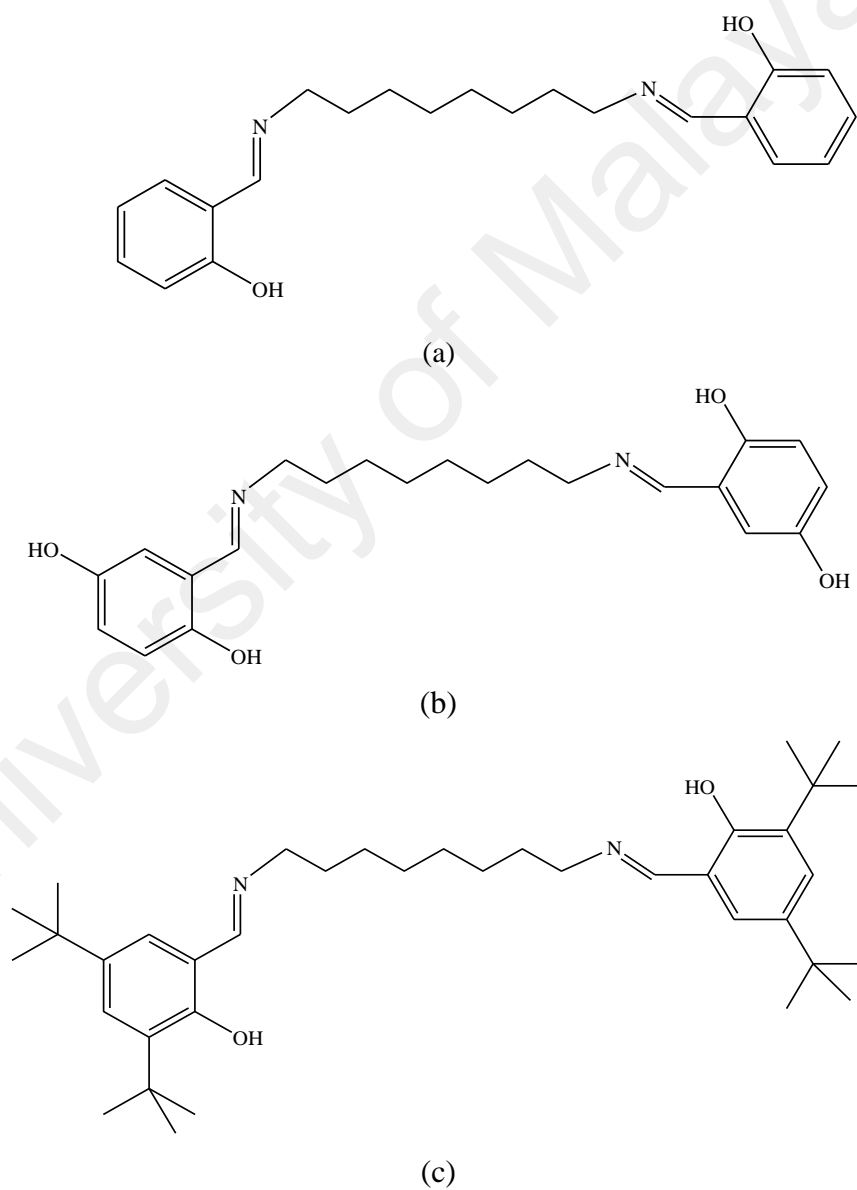


**Figure 3.1** Structural formulas of: (a)  $H_2L1$ ; (b)  $H_2L2$ ; and (c)  $H_2L3$

These Schiff bases were then reacted with  $[M(\text{CH}_3\text{COO})_2]$ , where  $M = \text{Cu(II)}$ ,  $\text{Ni(II)}$ ,  $\text{Co(II)}$ ,  $\text{Fe(II)}$  and  $\text{Mn(II)}$  to form a total of 15 complexes. In addition, four homometallic complexes were synthesized from the reaction of cyclam (**Figure 3.2**) with  $[M(\text{CH}_3(\text{CH}_2)_{14}\text{COO})_2]$ , where  $M = \text{Ni(II)}$ ,  $\text{Co(II)}$ ,  $\text{Fe(II)}$  and  $\text{Mn(II)}$ . For the heterometallic complexes, three complexes were synthesized from the reactions of  $\text{H}_2\text{L1}$ ,  $\text{H}_2\text{L2}$ , and  $\text{H}_2\text{L3}$  with a mixture of  $[\text{Cu}(\text{CH}_3\text{COO})_2]$  and  $[\text{Co}(\text{CH}_3\text{COO})_2]$ .

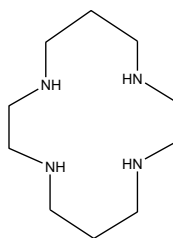


**Figure 3.2** Structural formula of cyclam (1,4,8,11-tetraazacyclotetradecane)

The numbers of complexes synthesized were 22, and they were analyzed by  $^1\text{H-NMR}$  (for ligands), X-ray crystallography (for crystals), elemental analyses, FTIR, UV-visible and fluorescence spectroscopies, cyclic voltammetry, room-temperature magnetic susceptibilities, thermogravimetry (TG), optical polarizing microscopy (OPM) and differential scanning calorimetry (DSC).

### 3.2 Chemicals

All chemicals (**Table 3.1**) and solvents used in this research were of analytical grade and used as received.

**Table 3.1** Chemicals used in this project

Name	Chemical formula	Molecular weight (g mol <sup>-1</sup> )
Copper(II) acetate monohydrate	[Cu(CH <sub>3</sub> COO) <sub>2</sub> ].H <sub>2</sub> O	199.65
Cobalt(II) acetate tetrahydrate	[Co(CH <sub>3</sub> COO) <sub>2</sub> ].4H <sub>2</sub> O	249.08
Cyclam	C <sub>10</sub> H <sub>24</sub> N <sub>4</sub>	200.32
Iron(II) acetate anhydrous	[Fe(CH <sub>3</sub> COO) <sub>2</sub> ]	173.93
1,8-diaminooctane	NH <sub>2</sub> (CH <sub>2</sub> ) <sub>8</sub> NH <sub>2</sub>	144.26
2,4-dihydroxybenzaldehyde	C <sub>6</sub> H <sub>3</sub> (OH) <sub>2</sub> CHO	138.12
3,5-ditertbutyl-2-hydroxybenzaldehyde	C <sub>6</sub> H <sub>3</sub> (C(CH <sub>3</sub> ) <sub>3</sub> ) <sub>2</sub> CHO	234.33
Manganese(II) acetate tetrahydrate	[Mn(CH <sub>3</sub> COO) <sub>2</sub> ].4H <sub>2</sub> O	245.09
Nickel(II) acetate tetrahydrate	[Ni(CH <sub>3</sub> COO) <sub>2</sub> ].4H <sub>2</sub> O	248.86

### 3.3 Synthesis of Metal(II) Complexes of H<sub>2</sub>L1

#### 3.3.1 Step-wise synthesis

##### (a) H<sub>2</sub>L1

A solution of 1,8-diaminooctane (1.4787 g; 1.03 mmol) in ethanol (100 mL) was added to a solution of 2-hydroxybenzaldehyde (2.00 g; 2.00 mmol) in ethanol (100 ml). A few drops of glacial acetic acid was added to the mixture as a catalyst. It was refluxed for 3 hours, and then left to stand at room temperature for 3 days. A yellow powder formed was filtered off, washed several times with cold ethanol, and dried in a warm oven. The yield was 3.1184 g (88.5%).

##### (b) Copper(II) complex

A solution of copper acetate monohydrate (0.8073 g, 4.04 mmol) in ethanol (50 mL) was added to a solution of H<sub>2</sub>L1 (0.7119 g, 2.02 mmol) in ethanol (100 ml). It was refluxed for 3 hours, and then left to stand at room temperature until the precipitate comes out. The

khaki-green powder formed was filtered off from the hot reaction and dried in an oven overnight. The yield was 0.6966 g (41.2%).

### **3.3.2 One-pot synthesis**

#### **(a) $[Cu(L1)]_2 \cdot H_2O$ (1)**

A mixture of 1,8-diaminooctane (0.3139 g; 2.18 mmol), 2-hydroxybenzaldehyde (0.50 g; 4.10 mmol) in ethanol (200 mL), and a few drop glacial acetic acid (catalyst) was refluxed for 1 hour. Copper(II) acetate monohydrate (0.8369 g; 4.20 mmol) was dissolved in a small amount of hot ethanol, and the solution was added portionwise and the hot reaction mixture, which was then refluxed for another 3 hours. The khaki-green powder formed was filtered off from the hot reaction and dried in an oven overnight. The yield was 0.8883 g (69,9%).

#### **(b) $[Ni_2(CH_3COO)_2(L1)] \cdot 3H_2O$ (2)**

The complex was similarly synthesized as for copper complex (**Section 3.3.2(a)**), using 1,8-diaminooctane (0.3142 g; 2.18 mmol), 2-hydroxybenzaldehyde (0.50 g; 4.10 mmol) and nickel(II) acetate tetrahydrate (1.0455 g; 4.20 mmol). The product was a green powder, and its yield was 0.7463 g (55.7%).

#### **(c) $[Co_2(CH_3COO)_2(L1)] \cdot 2H_2O$ (3)**

The complex was similarly synthesized as for copper complex (**Section 3.3.2(a)**), using 1,8-diaminooctane (0.3129 g; 2.17 mmol), 2-hydroxybenzaldehyde (0.5 mL; 4.10 mmol) and cobalt(II) acetate tetrahydrate (1.0533 g; 4.23 mmol). The product was a brown powder, and its yield was 0.7340 g (56.2%).

#### **(d) $[Fe(CH_3COO)(L1)]$ (4)**

The complex was similarly synthesized as for copper complex (**Section 3.3.2(a)**), using 1,8-diaminooctane (0.3208 g; 2.22 mmol), 2-hydroxybenzaldehyde (0.5 mL; 4.10 mmol)

and iron(II) acetate anhydrous (0.7401 g; 4.26 mmol). The product was a black powder and, its yield was 0.7679 g (79.0%).

**(e)  $[Mn_2(CH_3COO)_4(L1)].5H_2O$  (5)**

The complex was similarly synthesized as for copper complex (**Section 3.3.2(a)**), using 1,8-diaminooctane (0.3087 g; 2.14 mmol), 2-hydroxybenzaldehyde (0.5 mL; 4.10 mmol) and manganese(II) acetate tetrahydrate (1.1100 g; 4.53 mmol). The product was a black powder, and its yield was 1.2756 g (77.2%).

### **3.4 Synthesis of Metal(II) Complexes of H<sub>2</sub>L<sub>2</sub>**

#### **3.4.1 Step-wise synthesis**

**(a) H<sub>2</sub>L<sub>2</sub>**

The ligand H<sub>2</sub>L<sub>2</sub> was similarly synthesized as for ligand H<sub>2</sub>L<sub>1</sub> (**Section 3.3.1(a)**), using 1,8-diaminooctane (0.9274 g; 6.43 mmol) and 2,4-dihydroxybenzaldehyde (0.1748 g; 1.27 mmol). The product was an orange powder, and its yield was 2.2560 g (91.3%).

**(b) Copper(II) complex**

The complex was similarly synthesized as for copper complex (**Section 3.3.1(b)**), using H<sub>2</sub>L<sub>2</sub> (0.1018 g; 0.26 mmol), and copper(II) acetate monohydrate (0.1226 g; 0.53 mmol). The product was a brown powder, and its yield was 0.0711 g (49.6%).

#### **3.4.2 One-pot synthesis**

**(a)  $[Cu(CH_3COO)(HL_2)(H_2O)].H_2O$  (6)**

The complex was similarly synthesized as for copper complex (**Section 3.3.2(a)**), using 1,8-diaminooctane (1.4462 g; 10.02 mmol), 2,4-dihydroxybenzaldehyde (2.8070 g; 20.32 mmol) and copper(II) acetate monohydrate (4.0230 g; 20.15 mmol). The product was a brown powder, and its yield was 4.3595 g (80.4%).

**(b)  $[Ni_2(CH_3COO)_2(L2)].4H_2O$  (7)**

The complex was similarly synthesized as for copper complex (**Section 3.3.2(a)**), using 1,8-diaminooctane (1.4562 g; 10.09 mmol), 2,4-dihydroxybenzaldehyde (2.7840 g; 20.16 mmol) and nickel(II) acetate tetrahydrate (4.9828 g; 20.02 mmol). The product was a green powder, and its yield was 5.2317 g (75.8%).

**(c)  $[Co_2(CH_3COO)_2(L2)].H_2O$  (8)**

The complex was similarly synthesized as for copper complex (**Section 3.3.2(a)**), using 1,8-diaminooctane (1.4461 g; 10.02 mmol), 2,4-dihydroxybenzaldehyde (2.7685 g; 20.04 mmol) and cobalt(II) acetate tetrahydrate (5.0038 g; 20.09 mmol). The product was a black powder, and its yield was 3.3075 g (52.0%).

**(e)  $[Fe(CH_3COO)(HL2)].3H_2O$  (9)**

The complex was similarly synthesized as for copper complex (**Section 3.3.2(a)**), using 1,8-diaminooctane (1.4473 g; 10.03 mmol), 2,4-dihydroxybenzaldehyde (2.7620g; 20.00 mmol) and iron(II) acetate anhydrous (3.4795 g 20.01 mmol). The product was maroon powder, and its yield was 5.1054 g (92.4%).

**(d)  $[Mn(HL2)_2(H_2O)_2]$  (10)**

The complex was similarly synthesized as for copper complex (**Section 3.3.2(a)**), using 1,8-diaminooctane (1.4473 g; 10.03 mmol), 2,4-dihydroxybenzaldehyde (2.7710 g; 20.06 mmol) and manganese(II) acetate tetrahydrate (4.9252 g; 20.10 mmol). The product was a dark brown powder, and its yield was 3.0143 g (35.1%).

## 3.5 Synthesis of Metal(II) Complexes of H<sub>2</sub>L<sub>3</sub>

### 3.5.1 Step-wise synthesis

#### (a) H<sub>2</sub>L<sub>3</sub>

The ligand H<sub>2</sub>L<sub>3</sub> was similarly synthesized as for ligand H<sub>2</sub>L<sub>1</sub> (Section 3.3.1(a)), using 1,8-diaminooctane (0.7329 g; 5.08 mmol) and 3,5-ditertbutyl-2-hydroxybenzaldehyde (2.3727 g; 10.13 mmol). The product was orange crystals, and the yield was 2.6016 g (90.2%).

#### (b) Copper(II) complex

The complex was similarly synthesized as for copper complex (Section 3.3.1(b)), using H<sub>2</sub>L<sub>3</sub> (0.2658 g; 0.46 mmol), and copper(II) acetate monohydrate (0.1845 g; 0.92 mmol). The product was a brown powder, and its yield was 0.1141 g (44.7%).

### 3.5.2 One-pot synthesis

#### (a) [Cu(L<sub>3</sub>)] (11)

The complex was similarly synthesized as for copper complex (Section 3.3.2(a)), using 1,8-diaminooctane (0.1258 g; 0.85 mmol), 3,5-ditertbutyl-2-hydroxybenzaldehyde (0.4054 g; 1.70 mmol) and copper(II) acetate monohydrate (0.3465 g; 1.70 mmol). The product was a brown powder, and its yield was 0.4757 g (87.3%).

#### (b) [Ni(L<sub>3</sub>)] (12)

The complex was similarly synthesized as for copper complex (Section 3.3.2(a)), using 1,8-diaminooctane (0.4206 g; 2.90 mmol), 3,5-ditertbutyl-2-hydroxybenzaldehyde (0.9873 g; 4.20 mmol) and nickel(II) acetate tetrahydrate (1.0677 g; 4.20 mmol). The product was a dark green powder, and its yield was 0.6484 g (35.3%).

**(c)  $[Co_2(CH_3COO)_2(L3)].3H_2O$  (13)**

The complex was similarly synthesized as for copper complex (**Section 3.3.2(a)**), using 1,8-diaminooctane (0.3058 g; 2.12 mmol), 3,5-ditertbutyl-2-hydroxybenzaldehyde (0.9919 g 4.23 mmol,) and cobalt(II) acetate tetrahydrate (1.0539 g; 4.23 mmol). The product was a yellow powder, and its yield was 0.3047 g (16.8%)

**(d)  $[Fe(CH_3COO)(HL3)(H_2O)_2].3H_2O$  (14)**

The complex was similarly synthesized as for copper complex (**Section 3.3.2(a)**), using 1,8-diaminooctane (0.4268 g; 2.90 mmol), 3,5-ditertbutyl-2-hydroxybenzaldehyde (0.9955 g; 4.2 mmol) and iron(II) acetate anhydrous (0.7330 g; 4.2 mmol). The product was a dark purple powder, and its yield was 1.5262 g (67.4%).

**(e)  $[Mn(HL3)_2(H_2O)_2]$  (15)**

The complex was similarly synthesized as for copper complex (**Section 3.3.2(a)**), using 1,8-diaminooctane (0.4282 g; 2.9 mmol), 3,5-ditertbutyl-2-hydroxybenzaldehyde (0.9852 g; 4.20 mmol) and manganese(II) acetate tetrahydrate (1.1062 g; 4.20 mmol). The product was a black brown powder, and its yield was 1.0665 g (29.6%).

### **3.6 Metal(II)/(III)-Palmitate-Cyclam Complexes**

**(a)  $[Ni(CH_3(CH_2)_{14}COO)(cyclam)(H_2O)].(CH_3(CH_2)_{14}COO).4H_2O$  (16)**

Cyclam (0.2542 g; 1.27 mmol) was dissolved in ethanol (50 ml), and the colourless solution was added portionwise to a magnetically stirred hot suspension of  $[Ni(CH_3(CH_2)_{14}COO)_2(H_2O)_2]$  (0.7115 g; 1.18 mmol) in ethanol (100 ml). A clear brown solution formed was gently heat for an hour and then filtered hot. Brown crystals were formed on slow evaporation of the solution at room temperature. The yield was 0.8622 g (56.0%).

**(b) [Co(CH<sub>3</sub>(CH<sub>2</sub>)<sub>14</sub>COO)<sub>2</sub>(cyclam)].CH<sub>3</sub>(CH<sub>2</sub>)<sub>14</sub>COOH (17)**

The complex was similarly synthesized as for nickel complex (**Section 3.6(a)**), using [Co(CH<sub>3</sub>(CH<sub>2</sub>)<sub>14</sub>COO)<sub>2</sub>(H<sub>2</sub>O)<sub>2</sub>] (0.7366 g; 1.22 mmol) and cyclam (0.2547 g; 1.27 mmol). The product was dark purple crystals, and the yield was 0.8593 g (55.9%).

**(c) [Fe(CH<sub>3</sub>(CH<sub>2</sub>)<sub>14</sub>COO)(OH)(cyclam)].H<sub>2</sub>O.CH<sub>3</sub>CH<sub>2</sub>OH (18)**

The complex was similarly synthesized as for nickel complex (**Section 3.6(a)**), using [Fe(CH<sub>3</sub>(CH<sub>2</sub>)<sub>14</sub>COO)<sub>2</sub>(H<sub>2</sub>O)<sub>2</sub>] (0.7143 g; 1.19 mmol) and cyclam (0.2522 g; 1.26 mmol). The product was an orange powder, and its yield was 0.5274 g (52.4%).

**(d) [Mn(CH<sub>3</sub>(CH<sub>2</sub>)<sub>14</sub>COO)(OH)<sub>2</sub>(NH<sub>3</sub>)<sub>2</sub>(H<sub>2</sub>O)] (19)**

The complex was similarly synthesized as for nickel complex (**Section 3.6(a)**), using [Mn(CH<sub>3</sub>(CH<sub>2</sub>)<sub>14</sub>COO)<sub>2</sub>(H<sub>2</sub>O)<sub>2</sub>] (0.7083 g; 1.18 mmol) and cyclam (0.2510 g; 1.25 mmol). The product was a black powder, and its yield was 0.3916 g (83.7%).

### **3.7 Mixed-Metal Complexes**

**(a) [CuCo(CH<sub>3</sub>COO)<sub>2</sub>(HL1)<sub>2</sub>(H<sub>2</sub>O)] (20)**

The complex was similarly synthesized as for copper complex (**Section 3.3.2(a)**), using 1,8-diaminooctane (0.3177 g; 2.1 mmol) and 2-hydroxybenzaldehyde (0.5126 g; 4.2 mmol), copper(II) acetate monohydrate (0.4280 g; 2.1 mmol) and cobalt(II) acetate tetrahydrate (0.5277 g; 2.1 mmol). The product was a dark brown powder, and its yield was 0.7590 g (75.2%).

**(b) [CuCo(CH<sub>3</sub>COO)<sub>2</sub>(L2)].2H<sub>2</sub>O (21)**

The complex was similarly synthesized as for copper complex (**Section 3.3.2(a)**), using 1,8-diaminooctane (0.3146 g; 2.18 mmol) and 2,4-dihydroxybenzaldehyde (0.5844 g; 4.23 mmol), copper(II) acetate monohydrate (0.4215 g; 2.11 mmol) and cobalt(II) acetate

tetrahydrate (0.5291 g; 2.12 mmol). The product was a dark brown powder, and its yield was 1.0443 g (71.5%).

**(c) [CuCo(CH<sub>3</sub>COO)<sub>2</sub>(HL3)<sub>2</sub>] (22)**

The complex was similarly synthesized as for copper complex (**Section 3.3.2(a)**), using 1,8-diaminooctane (0.3100 g; 2.1 mmol) and 3,5-ditertbutyl-2-hydroxybenzaldehyde (1.0145 g; 4.2 mmol), copper(II) acetate monohydrate (0.4272 g; 2.1 mmol) and cobalt(II) acetate tetrahydrate (0.5317 g; 2.1 mmol). The product was a dark brown powder, and its yield was 1.1871 g (40.6%).

### **3.8 Instrumental Analyses**

#### **3.8.1 Nuclear magnetic resonance spectroscopy**

The nuclear magnetic resonance spectroscopy was recorded on a Jeol 400 MHz NMR spectrometer using CDCl<sub>3</sub> as solvent. The chemical shifts were references to that of the residual CDCl<sub>3</sub> in deuterated solvent.

#### **3.8.2 X-Ray Crystallography**

The data of X-Ray Crystallography was collected on a Bruker SMART APEX CCD diffractometer at about 100 K using graphite-monochromated Mo-K $\alpha$  radiation ( $\lambda = 0.71073 \text{ \AA}$ ). All structures were solved by direct method using SHELXS-97 program package.

#### **3.8.3 Elemental analyses**

The elemental analyses were recorded on a Perkim-Elmer CHNS/O analyser 2400 Series II. The sample (1-2 mg) in a tin capsule (5 x 8 mm) was folded into a tiny piece, inserted inside the analyser, and heated to a maximum temperature of 900 °C.

#### **3.8.4 FTIR- spectroscopy**

The FT-IR spectra were recorded on a Perkin-Elmer FT-IR Spectrum RX1 spectrometer. The sample was mixed with KBr in the mass ration of about 1:9 was ground using a clean dry mortar and pestle. The mixture was carefully packed to obtain a transparent thin pellet. The pellet was mounted on a holder and the spectrum was recorded from 4000-400  $\text{cm}^{-1}$ . The peaks were assigned by comparison with the corresponding wavenumber from the literature.

#### **3.8.5 Magnetic Susceptibility**

The magnetic moment was determined using a Sherwood Scientific magnetic susceptibility balance at room temperature. The sample was ground using a clean dry agate pestle and mortal. A small amount of the complex was packed into a short cylindrical tube to the mark, and its mass susceptibility was recorded. The molar magnetic susceptibility ( $\chi_M$ ) was then calculated using the equation:  $\chi_M = \chi_g \times M_r$ , where  $M_r$  was the formula mass of the complex.

#### **3.8.6 UV-visible spectroscopy**

The UV-vis spectra for both solid samples and solutions were recorded on a Shimadzu UV-NIR 3600 spectrophotometer. For solid sample, the sample was compressed and inserted into the cell holder. The spectrum obtained was calibrated against barium sulphate ( $\text{BaSO}_4$ ) as the background. For solution, a known mass of the sample was dissolved in a suitable solvent and the spectrum was recorded in 1-cm quartz cuvettes from 1000-200 nm. The molar absorptivity ( $\epsilon$ ) was calculated using the Beer-Lambert's Law,  $A = \epsilon cl$ .

### **3.8.7 Fluorescence spectroscopy**

Excitation and emission photoluminescence spectra were recorded on a PTI QuantaMaster™ 40 spectrofluorometer. The sample was held in a quartz fluorescence cuvette (l = 1 cm x 1 cm) and fluorescence was detected at 90° to the excitation beam with the corrected background. The emission spectrum was measured by exciting the sample at excitation wavelength for each complex and collecting the emitted fluorescence. Slit widths were adjusted for excitation emission. Fluorescence lifetime measurement was recorded on a TimeMaster (TM-200) LED-Based Strobe Lifetime spectrofluorometer obtained from Photon Technology International and using the stroboscopic technique. The observed fluorescence decay was analysed using Felix GX™ data acquisition and analysis software.

### **3.8.8 Cyclic voltammetry (CV)**

The CV were recorded on a Gamry Instrument Reference 600 potentiostat/galvanostat/ZRA. A three-electrode cell, consisting of a glassy carbon electrode as the working electrode, saturated calomel electrode (SCE) as reference electrode and platinum wire as the counter electrode, was used. The supporting electrolyte was tetrabutylammonium tetrafluoroborate (TBATFB). The sample solution was bubbled with N<sub>2</sub> gas prior to the measurement.

### **3.8.9 Thermogravimetric analysis (TGA)**

The TGA analyses were performed on a Pyris Diamond TG/DTA Perkin Elmer Thermogravimetric Analyzer TGA6 with scan rate of 20 °C min<sup>-1</sup> under N<sub>2</sub>. The powder (about 4-7 mg) was introduced into an alumina crucible, inserted into the sample holder, and heated from 50°C to 900 °C.

### ***3.8.10 Differential scanning calorimetry (DSC)***

The DSC thermographs were obtained on a Mettler Toledo DSC 822 model with a scan rate of  $5\text{ }^{\circ}\text{C min}^{-1}$ . The powder (about 0.6 mg to 0.8 mg) was introduced into an aluminium crucible and heated in the sample holder from  $25\text{ }^{\circ}\text{C}$  to  $250\text{ }^{\circ}\text{C}$  for the first heating cycle, followed by cooling from  $250\text{ }^{\circ}\text{C}$  to  $25\text{ }^{\circ}\text{C}$  for the cooling cycle, and finally back to  $250\text{ }^{\circ}\text{C}$  for the second heating cycle.

### ***3.8.11 Optical polarized microscopy (OPM)***

The optical microscopy was done on an Olympus polarizing microscope equipped with a Mettler Toledo FP90 central processor and FN82HT hot stage. The magnification was 50x. A small amount of the sample was placed into a clean glass slide, which was then placed on a hot stage. Heating and cooling rates can be adjusted between  $2\text{-}5\text{ }^{\circ}\text{C min}^{-1}$  depending on the suitability of the samples.

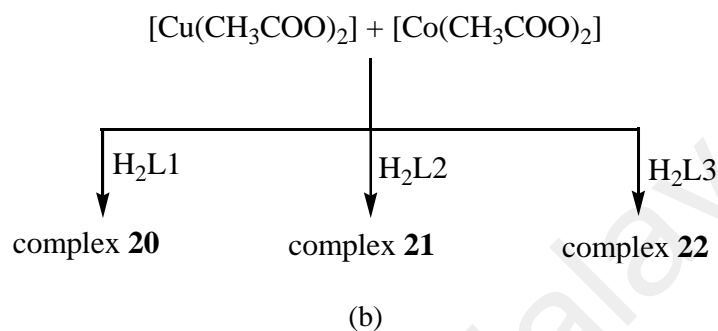
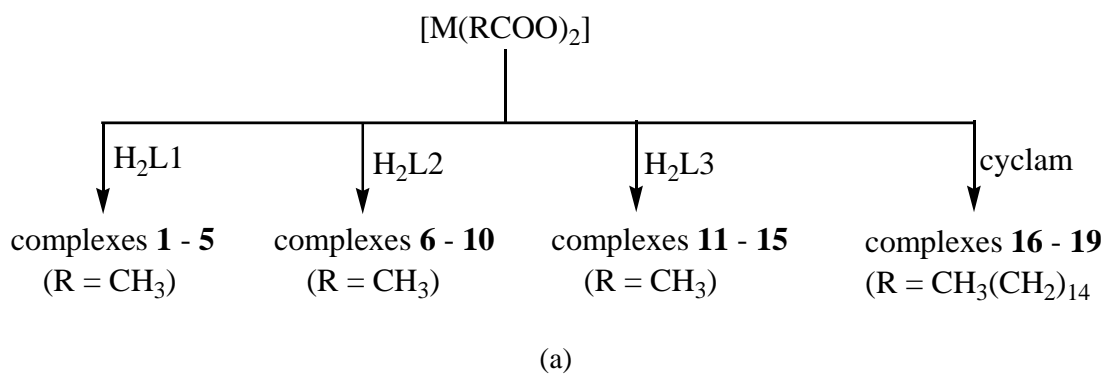
## CHAPTER 4: RESULTS AND DISCUSSION

### 4.1 Introduction

The main objective of this research project was to synthesize and characterize homometallic and heterometallic complexes as molecular magnetic and/or low band gap metallomesogenic materials.

For the homometallic complexes, the ligands were anions of three Schiff bases ( $H_2L1$ ,  $H_2L2$  and  $H_2L3$ ) formed from the condensation reactions of 1,8-diaminooctane with 2-hydroxybenzaldehyde, 2,4-dihydroxybenzaldehyde, and 3,5-di(*tert*-butyl)benzaldehyde, respectively. These Schiff bases were then reacted with  $[M(CH_3COO)_2]$ , where  $M = Cu(II)$ ,  $Ni(II)$ ,  $Co(II)$ ,  $Fe(II)$  and  $Mn(II)$  to form a total of 15 complexes. In addition, four homometallic complexes were synthesized from the reaction of cyclam with  $[M(CH_3(CH_2)_{14}COO)_2]$ , where  $M = Ni(II)$ ,  $Co(II)$ ,  $Fe(II)$  and  $Mn(II)$ . For the heterometallic complexes, three complexes were synthesized from the reactions of  $H_2L1$ ,  $H_2L2$ , and  $H_2L3$  with a mixture of  $[Cu(CH_3COO)_2]$  and  $[Co(CH_3COO)_2]$ . The total number of complexes were 22. These reactions are shown in **Scheme 4.1**.

The structural formulas of these ligands and complexes were deduced from the results of  $^1H$ -NMR (for ligands), X-ray crystallography (for crystals), elemental analyses, and FTIR and UV-visible spectroscopies (for complexes). The band gap energies of these complexes were calculated from UV-visible and fluorescence spectroscopies and from cyclic voltammetry. Then, their room-temperature magnetic susceptibilities were measured by the Gouy method, their thermal properties deduced from thermogravimetry (TG), and finally their mesomorphic properties by optical polarizing microscopy (OPM) and differential scanning calorimetry (DSC).



**Scheme 4.1.** (a) Homometallic complexes **1 – 19** (M = Cu(II), Ni(II), Co(II), Fe(II), Mn(II)); and (b) heterometallic complexes **20 – 22**

## 4.2 H<sub>2</sub>L1 and its Metal(II) Complexes

### 4.2.1 H<sub>2</sub>L1

H<sub>2</sub>L1 was obtained as a yellow powder from the reaction of H<sub>2</sub>N(CH<sub>2</sub>)<sub>8</sub>NH<sub>2</sub> with 2-HOC<sub>6</sub>H<sub>4</sub>CHO in ethanol. The yield was 88.5%, and it was soluble in chloroform but insoluble in other common organic solvents. Its structural formula (**Figure 4.1**) was ascertained from the combined results of elemental analyses, FTIR spectroscopy and <sup>1</sup>H-NMR spectroscopy.

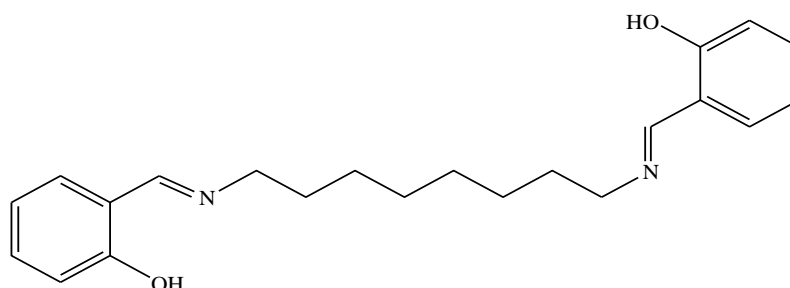


**Figure 4.1** Structural formula of H<sub>2</sub>L1

(a) *Structural deduction*

The results from the **elemental analyses** (74.95% C; 8.13% H; 8.26% N) were in good agreement with the chemical formula  $C_{22}H_{28}N_2O_2$  (formula weight, 352.47 g mol<sup>-1</sup>; 74.97% C, 8.01% H, 7.95% N).

Its **FTIR** spectrum (**Figure 4.2**) shows two peaks for  $CH_2$  ( $\nu_{asym}$ ) and  $CH_2$  ( $\nu_{sym}$ ) at 2919 cm<sup>-1</sup> and 2850 cm<sup>-1</sup>, respectively, a peak for the C=N (imine) bond at 1630 cm<sup>-1</sup>, a peak for aromatic C=C at 1608 cm<sup>-1</sup>, and a peak for aromatic ring at 1498 cm<sup>-1</sup>. However, the peak for the OH group was not observed. This is likely due to strong intramolecular hydrogen bond between OH $\cdots$ N=C, resulting in a broad band [89].

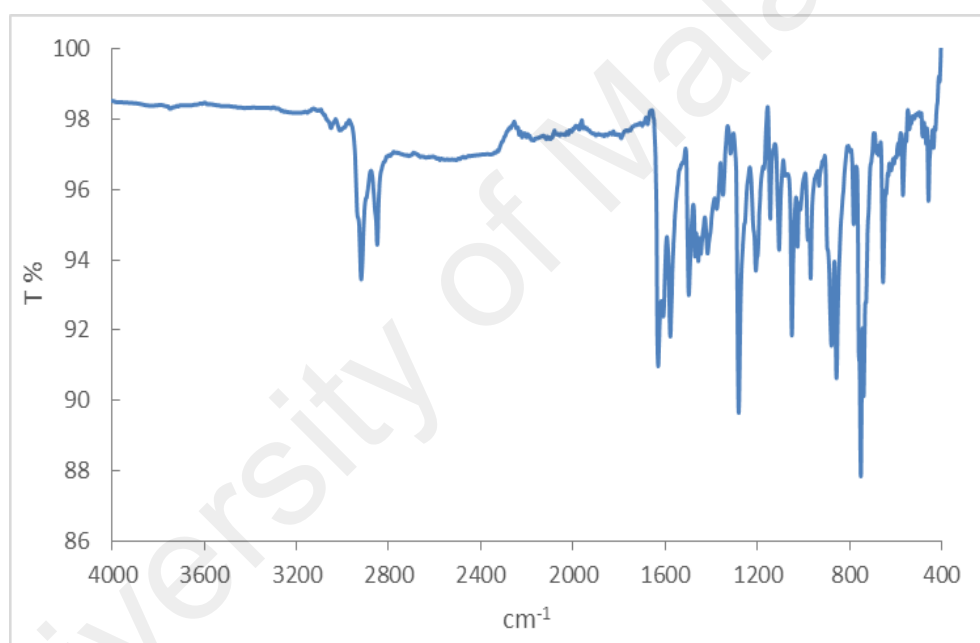


**Figure 4.2** The FTIR spectrum of H<sub>2</sub>L1

Its <sup>1</sup>H-NMR spectrum is shown in **Figure 4.3**, and the peak assignments are given in **Table 4.1**.

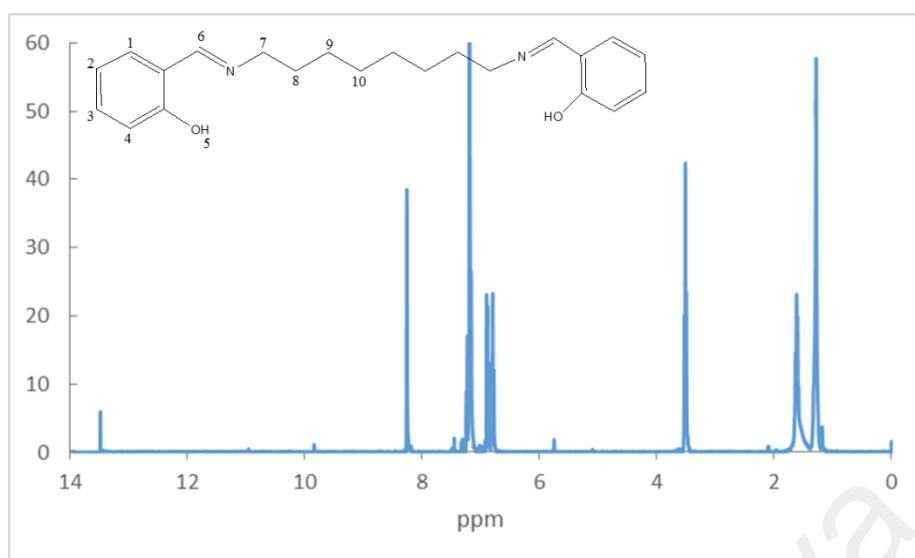


**Figure 4.3** The  $^1\text{H}$ -NMR spectrum of  $\text{H}_2\text{L1}$

**Table 4.1** The  $^1\text{H}$ -NMR data (in ppm) and peak assignment for  $\text{H}_2\text{L1}$

Chemical shift	Integral ratio	Multiplicity	Assignment
1.15-1.28	7.35	Multiplet	H-9, H-10
1.51-1.63	4.10	Multiplet	H-8
3.52	3.66	Triplet	H-7
6.76-6.89	3.49	mutiplet	H-3, H-4
7.15-7.25	3.93	mutiplet	H-1, H-2
8.24	1.77	singlet	H-6
13.60	1.00	singlet	H-5

*(b) Mesomorphic properties*

The phase transitions for  $\text{H}_2\text{L1}$  were studied by DSC, while its optical textures were captured by OPM on cooling from its isotropic liquid phase (*I*).

Its DSC scans (**Figure 4.4**) showed an endothermic peak at  $75.6\text{ }^\circ\text{C}$  ( $\Delta H = +48.1\text{ kJ mol}^{-1}$ ) for the crystal-to-mesophase transition on heating, and an exothermic peak at  $43.9\text{ }^\circ\text{C}$  ( $\Delta H = -40.4\text{ kJ mol}^{-1}$ ) for the mesophase-to-crystal transition on cooling. The results indicate that the ligand strongly supercooled. Its OPM showed a smectogenic optical texture at  $78.0\text{ }^\circ\text{C}$  (**Figure 4.5**), consistent with its calamitic (rod-like) molecular shape.

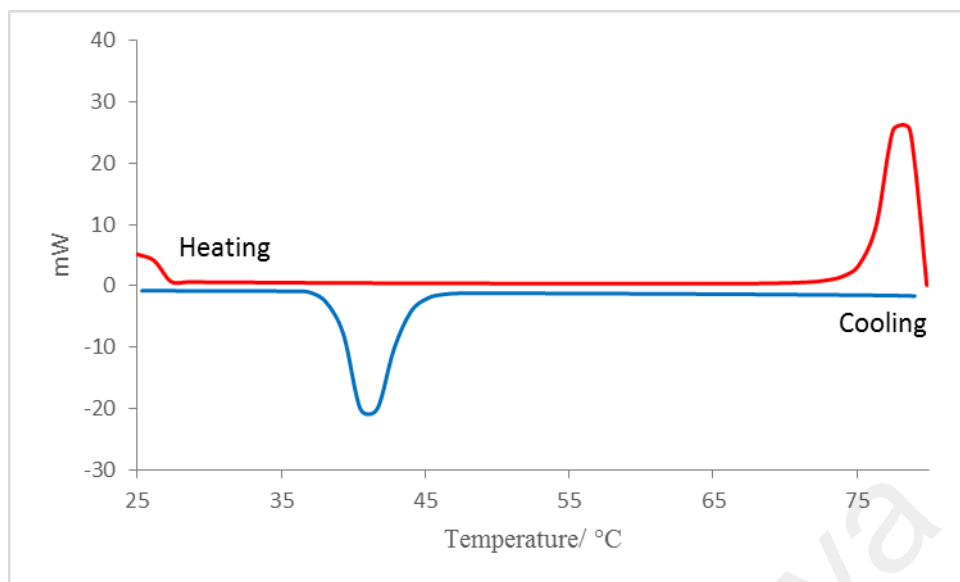


**Figure 4.4** DSC scans for H<sub>2</sub>L1

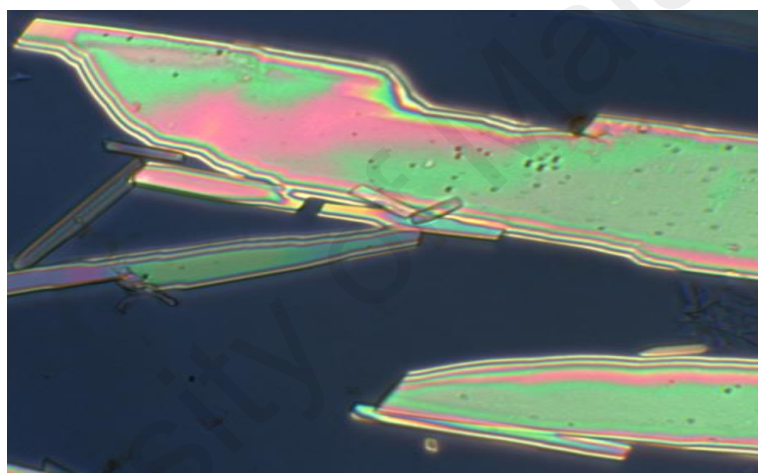
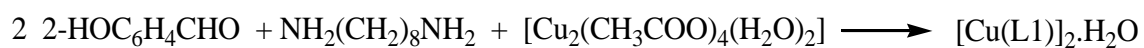


**Figure 4.5** A photomicrograph of H<sub>2</sub>L1 at 78 °C on cooling from I

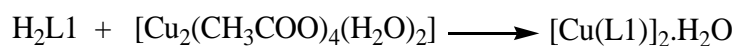
#### 4.2.2 [Cu(L1)]<sub>2</sub>.H<sub>2</sub>O

The Cu(II) complex of H<sub>2</sub>L1 (**Complex 1**) was synthesised by step-wise and one-pot reactions (**Scheme 4.2**).

*One-pot reaction:*



*Step-wise reaction:*



**Scheme 4.2** Synthetic steps for **Complex 1**

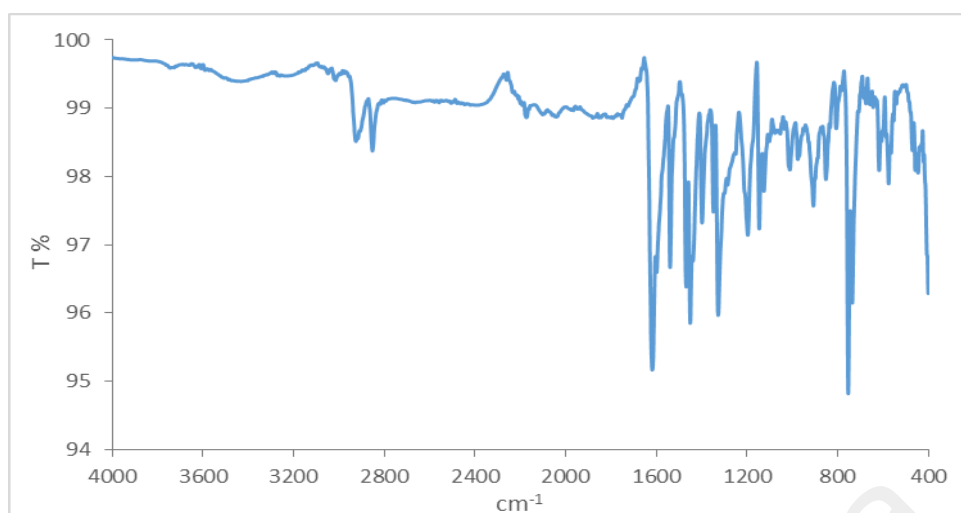
Both methods gave khaki green powders, and the yield was 41.2% (step-wise method) and 69.9% (one-pot method). The powders were soluble in chloroform, dimethylsulfoxide (DMSO) and tetrahydrofuran (THF), but insoluble in water and other common organic solvents. The CHN elemental analyses and FTIR spectra for both products are similar (**Figure 4.6**). From these, it may be concluded that the products obtained from both methods were the same. Thus, the following analyses are presented for the product obtained from the one-pot method only as it was a more facile method and gave a higher yield.

*(a) Structural deduction*

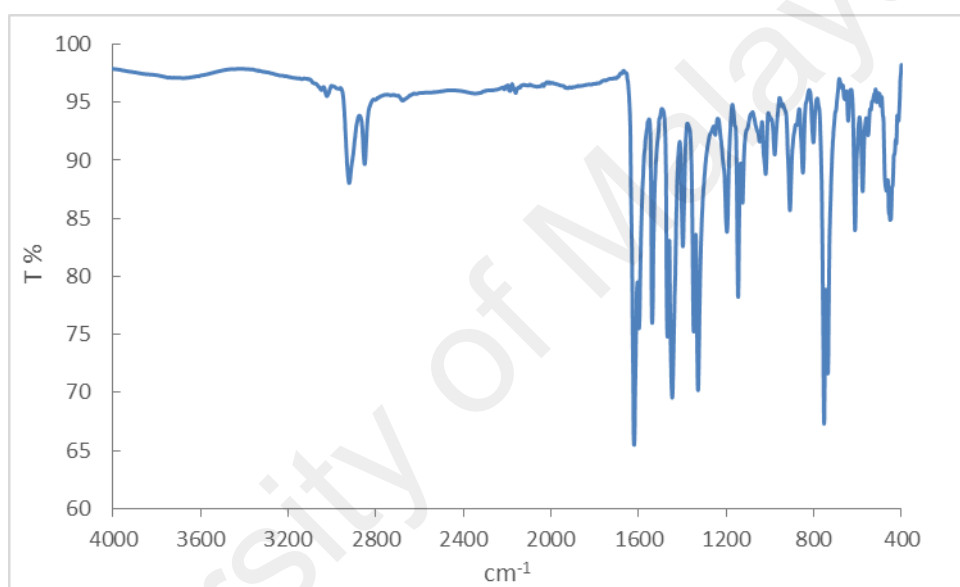
The structure of **Complex 1** was deduced from combined results of the elemental analyses, FTIR spectroscopy and UV-visible spectroscopy.

The results from the **elemental analyses** (62.48% C, 5.99% H, 6.78% N) were in good agreement with the chemical formula  $\text{Cu}_2\text{C}_{44}\text{H}_{54}\text{N}_4\text{O}_5$  (846.02 g mol<sup>-1</sup>; 62.47% C, 6.43% H, 6.62% N).

Its **FTIR** spectrum (**Figure 4.6**) shows two peaks for  $\text{CH}_2$  ( $\nu_{\text{asym}}$ ) and  $\text{CH}_2$  ( $\nu_{\text{sym}}$ ) at 2921 cm<sup>-1</sup> and 2851 cm<sup>-1</sup>, respectively, and a strong peak for the C=N at 1620 cm<sup>-1</sup>. The latter peak was shifted to a lower wavenumber compared to  $\text{H}_2\text{L1}$  (1630 cm<sup>-1</sup>) indicating coordination of the azomethine nitrogen to Cu(II) atom [90].



(a)



(b)

**Figure 4.6** FTIR spectra for **Complex 1** obtained from: (a) step-wise method, and (b) one-pot method

Its **UV-visible** spectrum was recorded in THF (**Figure 4.7**). The spectrum shows a broad *d-d* band at 679 nm ( $\epsilon_{\text{max}} = 75 \text{ M}^{-1} \text{ cm}^{-1}$ ) and a weak shoulder at 385 nm ( $\epsilon_{\text{max}} = 25 \text{ M}^{-1} \text{ cm}^{-1}$ ). These suggest a square pyramidal Cu(II) centre in the complex [91].

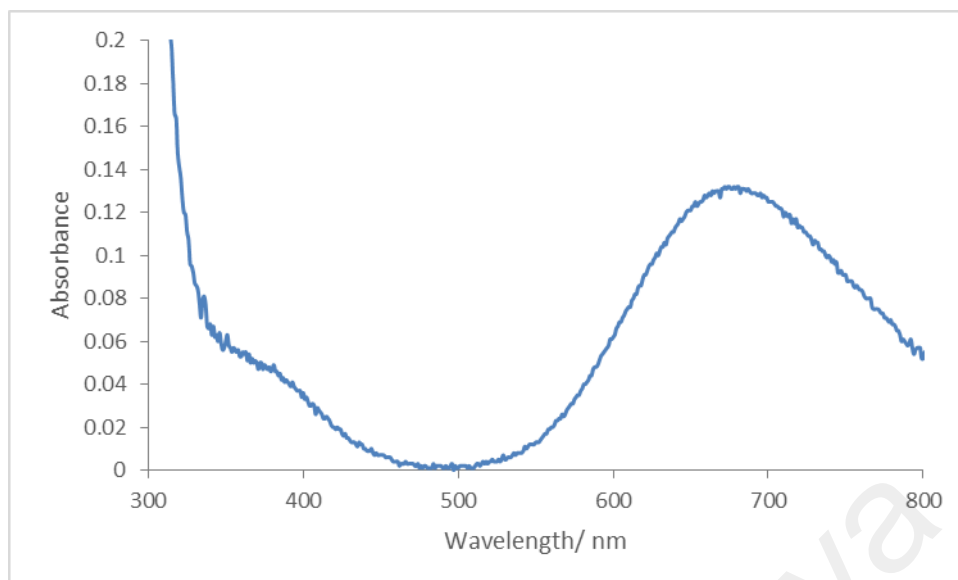


**Figure 4.7** UV-visible spectrum of **Complex 1** in THF

Combining the above results, the proposed structural formula for **Complex 1** is  $[\text{Cu}(\text{L}1)]_2 \cdot \text{H}_2\text{O}$  (**Figure 4.8**). The dimeric structure is similar with  $[\text{Cu}(\text{Sal-5})]_2$  reported by Nathan *et al.* [41], but differs from  $[\text{Cu}_2(\text{L})(\text{CH}_3\text{COO})_2] \cdot 2\text{H}_2\text{O}$  (L was dianionic Schiff base formed from  $\text{H}_2\text{N}(\text{CH}_2)_9\text{NH}_2$  and 2- $\text{HOC}_6\text{H}_4\text{CHO}$ ), reported by Abdullah *et al.* [27].

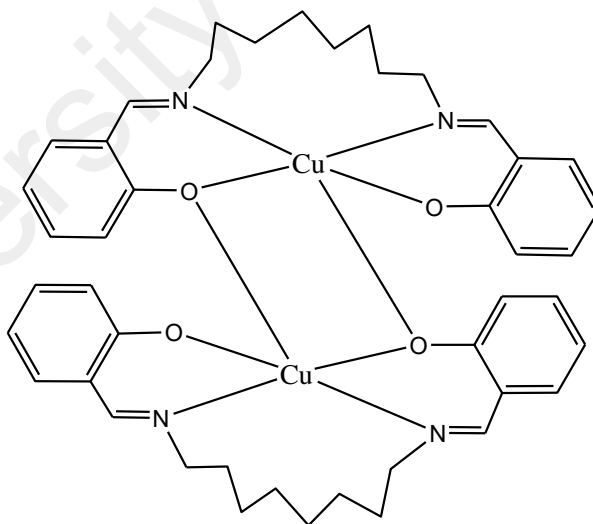


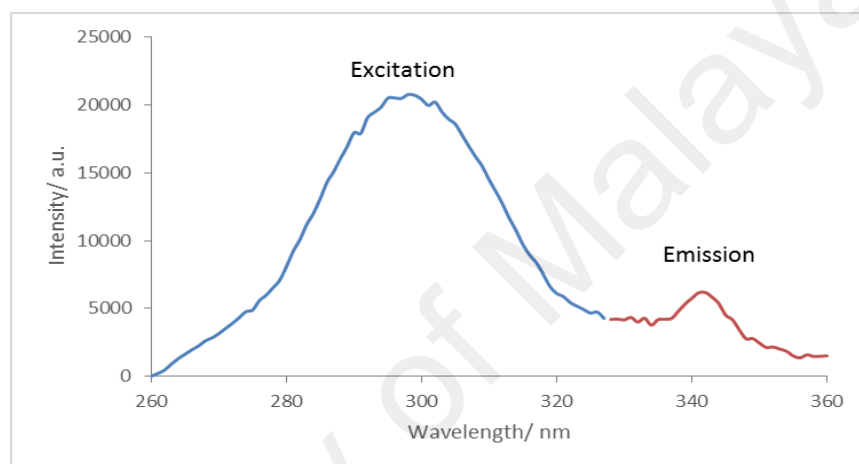
**Figure 4.8** Proposed structure for **Complex 1** (lattice  $\text{H}_2\text{O}$  is omitted)

(b) *Determination of bandgaps*

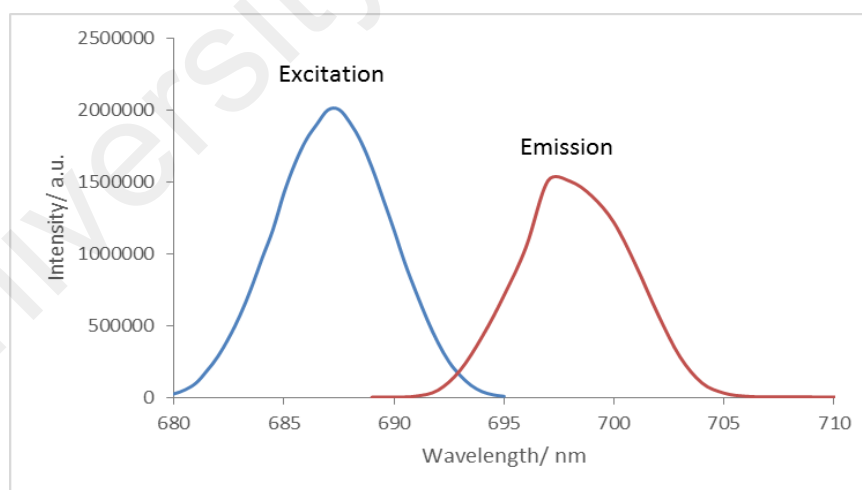
The **optical bandgap** ( $E_o$ ) may be calculated from both the absorption and fluorescence spectra, using the equation is  $E_o = hc/\lambda$ , where  $c$  = velocity of light ( $3.0 \times 10^8 \text{ m s}^{-1}$ ),  $h$  = Planck constant ( $6.626 \times 10^{-34} \text{ J s}^{-1}$ ), and  $\lambda$  (absorption edge of the CT band). The

calculated value in joule (J) was then converted to electron volt (eV). For complex **1**, the  $E_o$  value from its absorption spectrum (**Figure 4.7**) was 3.53 eV ( $\lambda = 351$  nm).

Its **fluorescence** spectra (**Figure 4.9**) were recorded in chloroform. Upon excitation at 298 nm (LMCT band), it shows an emission peak at 342 nm, while upon excitation at 688 nm (*d-d* band), it shows an emission peak at 697 nm. The Stokes shifts (the difference between the excitation and emission wavelengths) are 44 nm and 9 nm, respectively. Its  $E_o$  value were 3.82 eV ( $\lambda = 325$  nm) and 1.76 eV ( $\lambda = 704$  nm).



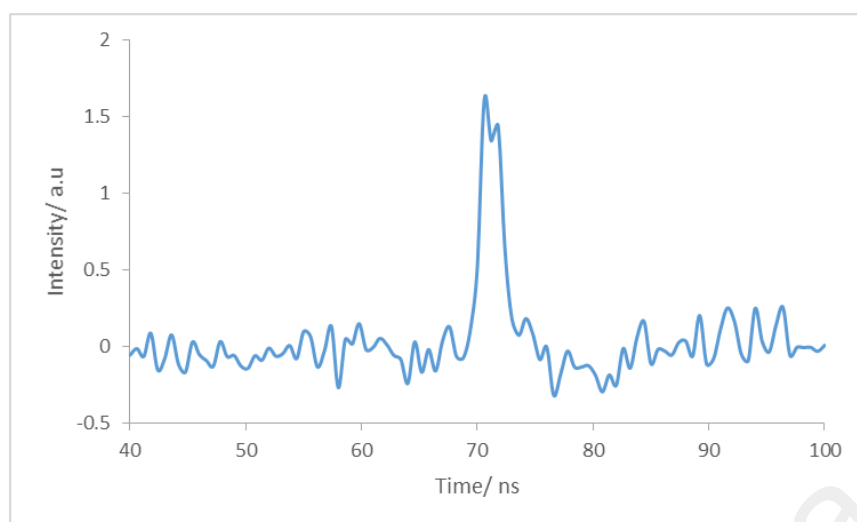
(a)



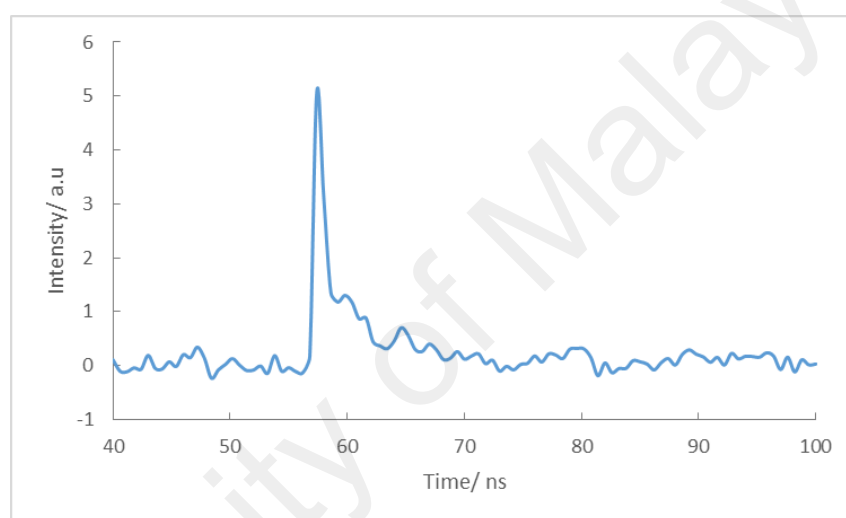
(b)

**Figure 4.9** Fluorescence spectra for **Complex 1** after excitation at: (a) 298 nm, and (b) 688 nm

The **fluorescence lifetime** ( $\tau$ ) of the excited complex was calculated from its decay curve (**Figure 4.10**). The value was 1.0 ns (for both  $\lambda_{emission} = 342$  nm and 697 nm).



(a)



(b)

**Figure 4.10** Fluorescence decay of **Complex 1** at  $\lambda_{emission}$  (a) 342 nm, and (b) 697 nm

**Electrochemical bandgaps ( $E_e$ )** may be calculated by cyclic voltammetry (CV).

For complex **1**, its **CV** was determined in DMSO at a scan rate of  $50 \text{ mV s}^{-1}$  in the potential range of  $-1.5 \text{ V}$  to  $+1.5 \text{ V}$ . The voltammogram (**Figure 4.11**) shows a weak cathodic peak at  $-0.98 \text{ V}$ , assigned to the reduction of  $[\text{Cu(II)}]$  to  $[\text{Cu(I)}]$ , but no corresponding anodic peak, indicating an irreversible redox process. This suggests that the structure of the reduced complex was not stable. Hence, its electrochemical band gap could not be calculated [92].

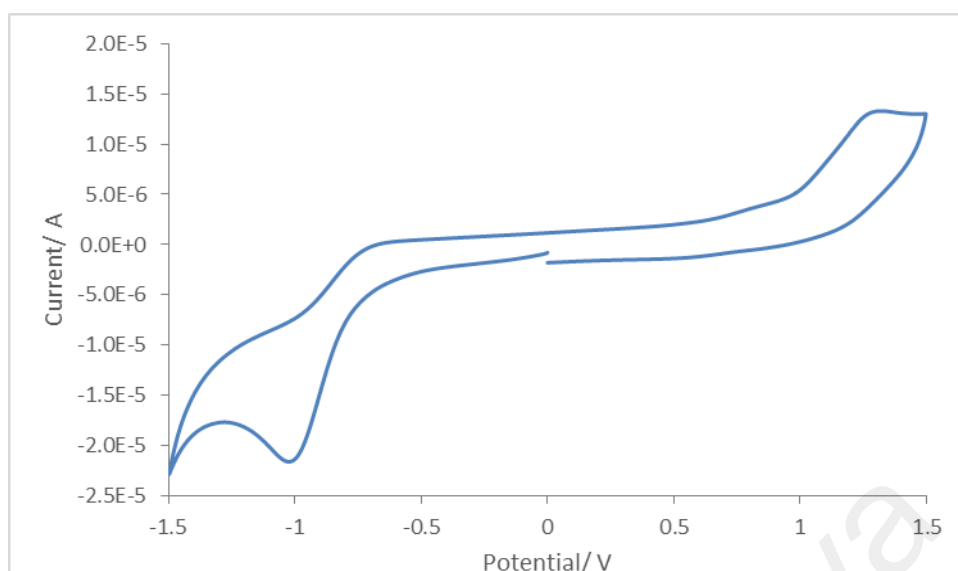


**Figure 4.11** Cyclic voltammogram for **Complex 1**

*(c) Magnetic properties*

Its **effective magnetic moment** ( $\mu_{\text{eff}}$ ) was 1.89 BM at 298 K. The value was calculated using the formula:  $\mu_{\text{eff}} = 2.83[T(\chi_{\text{m}}^{\text{corr}} - N\alpha)]^{1/2}$ , and the following data: FM = 422.14 g mol<sup>-1</sup> (monomer),  $\chi_{\text{g}} = 3.18 \times 10^{-6}$  cm<sup>3</sup> g<sup>-1</sup>,  $\chi_{\text{m}} = 1.34 \times 10^{-3}$  cm<sup>3</sup> mol<sup>-1</sup>,  $\chi_{\text{dia}} = -2.20 \times 10^{-4}$  cm<sup>3</sup> mol<sup>-1</sup>, and  $\chi_{\text{m}}^{\text{corr}} = 1.56 \times 10^{-3}$  cm<sup>3</sup> mol<sup>-1</sup>. The calculated value is higher than expected spin-only value of 1.73 BM for a mononuclear Cu(II) complex ( $S = 1/2$ ), indicating ferromagnetic interaction between Cu(II) centre [93].

*(d) Thermal properties*

Its **TGA trace (Figure 4.12)** shows an initial weight loss of 76.5% from about 268 °C to 900 °C, assigned to the decomposition of L1<sup>2-</sup> ion (calculated, 82.9%). Hence, **Complex 1** was thermally stable up to 268 °C. The experimental value was lower than the expected value as the trace did not plateau out at temperatures above 900 °C due to incomplete decomposition of the organic ligand. Also, it is inferred that the lattice H<sub>2</sub>O has evaporated before the thermal analysis was recorded since the trace does not show an initial loss below its decomposition temperature.

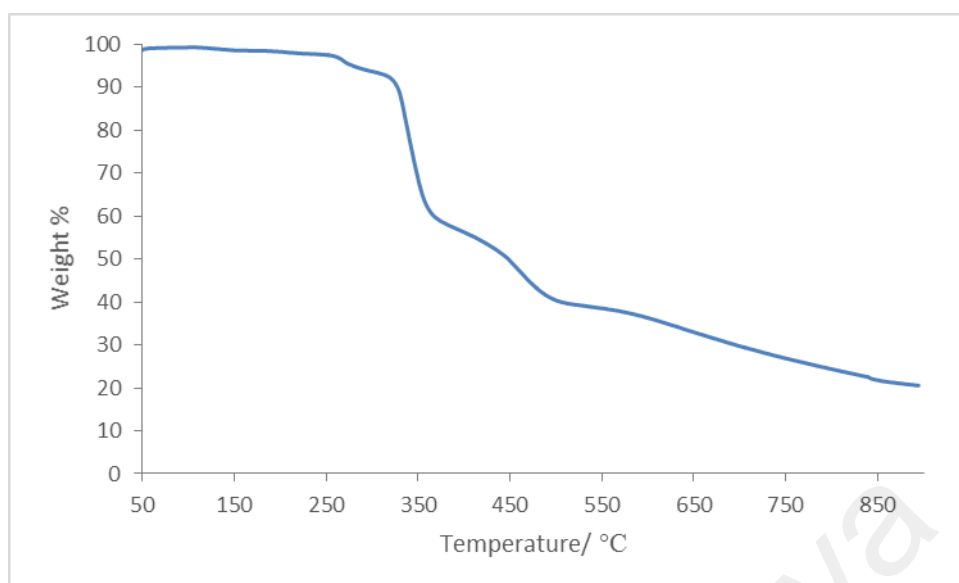


**Figure 4.12** TGA of **Complex 1**

*(e) Mesomorphic properties*

Its DSC spectrum (**Figure 4.13**) was recorded for a heating-cooling cycle from 25 °C to 210 °C. On heating, there were two endothermic peaks at 148.2 °C ( $\Delta H = +3.13 \text{ kJ mol}^{-1}$ ) and 184.4 °C ( $\Delta H = +16.6 \text{ kJ mol}^{-1}$ ), assigned as the evaporation of lattice water molecule and dissociation of the dimers, respectively. On cooling, there was a broad exothermic peak at 174.2 °C ( $\Delta H = -8.6 \text{ kJ mol}^{-1}$ ), assigned to the reformation of the dimers.

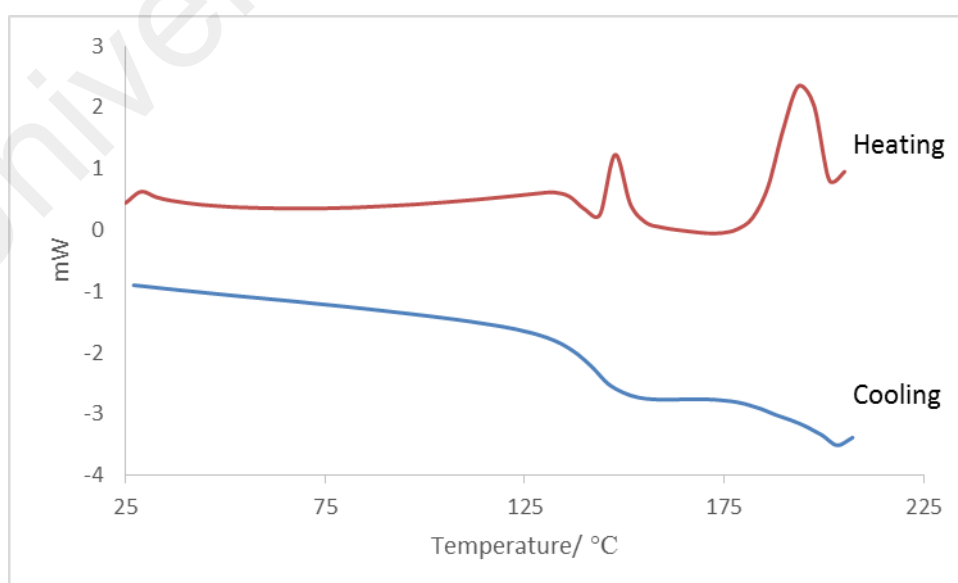


**Figure 4.13** DSC of **Complex 1**

Viewed under an **OPM**, **Complex 1** (**Figure 4.14**) was observed to clear at 200 °C. Upon cooling from the isotropic liquid, the complex exhibited birefringence at 154 °C, signifying an isotropic liquid-to-crystal transition. Hence, **Complex 1** was not mesomorphic.

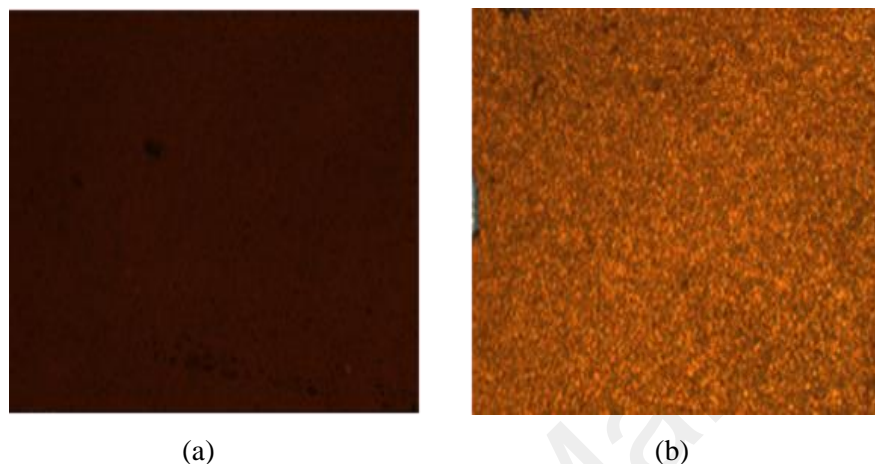


**Figure 4.14** Photomicrographs of **Complex 1** (a) on heating at 200 °C; and (b) on cooling at 154 °C

#### 4.2.3 $[Ni_2(CH_3COO)_2(L1)].3H_2O$

The Ni(II) complex of H<sub>2</sub>L1 was synthesised using the one-pot reaction only since this was an easier method and found to give a higher yield of the product (for **Complex 1**). In this method, 2-hydroxybenzaldehyde, 1,8-diaminooctane and  $[Ni(CH_3COO)_2].4H_2O$  were reacted in ethanol to form a green powder (**Complex 2**) in good yield (55.7%). It was soluble in chloroform and insoluble in water and other common organic solvents.

##### (a) Structural deduction

The structure of **Complex 2** was similarly deduced as for **Complex 1**. The results from the **elemental analyses** (48.67% C, 5.01% H, 4.29% N) were in good agreement with the chemical formula  $Ni_2C_{26}H_{38}N_2O_9$  (638.13 g mol<sup>-1</sup>; 48.8% C, 5.98% H, 4.38 % N).

Its **FTIR** spectrum (**Figure 4.15**) shows a broad peak at 3266 cm<sup>-1</sup> for H<sub>2</sub>O, two peaks for CH<sub>2</sub> ( $\nu_{asym}$ ) and CH<sub>2</sub> ( $\nu_{sym}$ ) at 2923 cm<sup>-1</sup> and 2854 cm<sup>-1</sup>, respectively, a strong peak for the C=N at 1627 cm<sup>-1</sup>, a strong peak at 1544 cm<sup>-1</sup> for  $\nu_{asym}COO$ , and a peak at

1446  $\text{cm}^{-1}$  for  $\nu_{\text{sym}}\text{COO}$ . From the latter peaks, the  $\Delta$  value was 98  $\text{cm}^{-1}$ , suggesting a chelating binding mode for  $\text{CH}_3\text{COO}^-$  ligand [94].

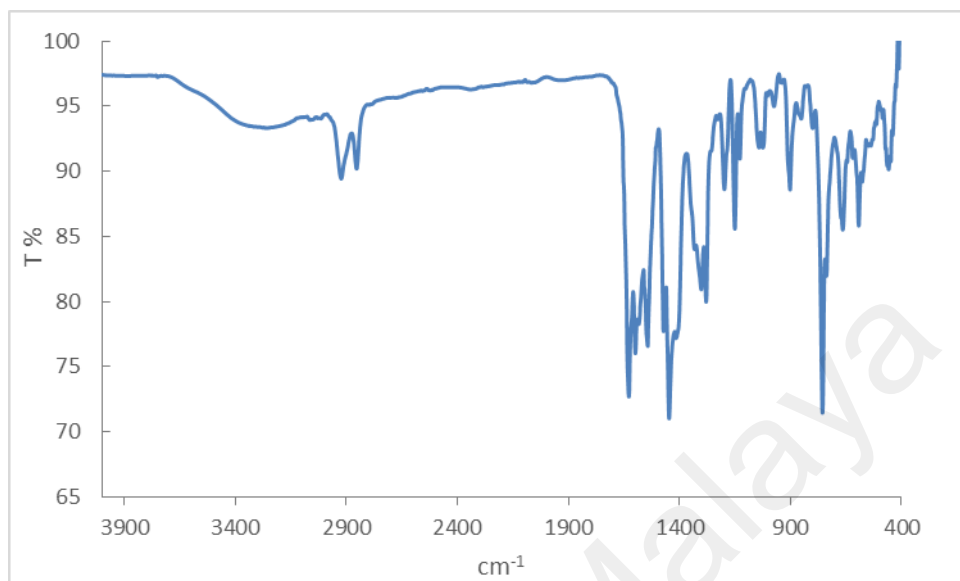


**Figure 4.15** FTIR spectrum for **Complex 2**

Its **UV-visible** spectrum, recorded in chloroform (**Figure 4.16**), shows a *d-d* band at 410 nm ( $\epsilon_{\text{max}} = 446 \text{ M}^{-1} \text{ cm}^{-1}$ ) and metal-to-ligand charge transfer (MLCT) band at 325 nm ( $\epsilon_{\text{max}} = 1305 \text{ M}^{-1} \text{ cm}^{-1}$ ). This suggests a tetrahedral geometry at both Ni(II) centres of this complex [29].

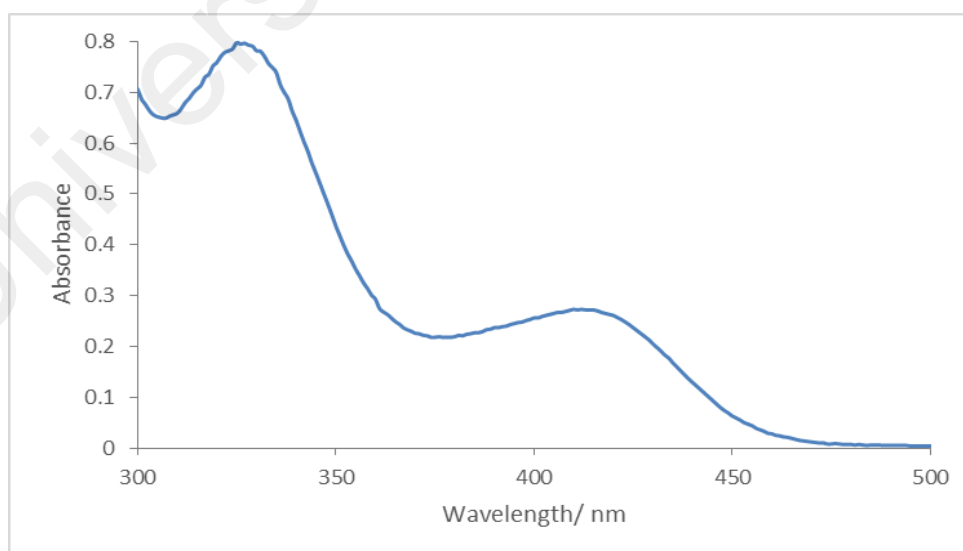


**Figure 4.16** UV-visible spectrum of **Complex 2**

Combining the above data, the proposed structural formula for **Complex 2** is  $[\text{Ni}_2(\text{CH}_3\text{COO})_2(\text{L1})].3\text{H}_2\text{O}$  (**Figure 4.17**). Hence, unlike the corresponding Cu(II) complex, it was a dinuclear complex with two  $\text{CH}_3\text{COO}^-$  and one  $\text{L1}^{2-}$  ions coordinated to Ni(II) ion.

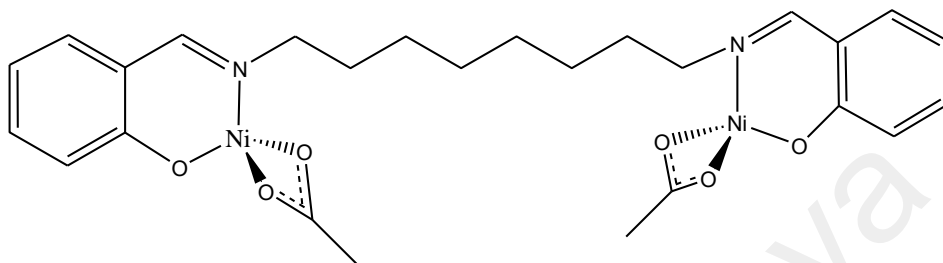
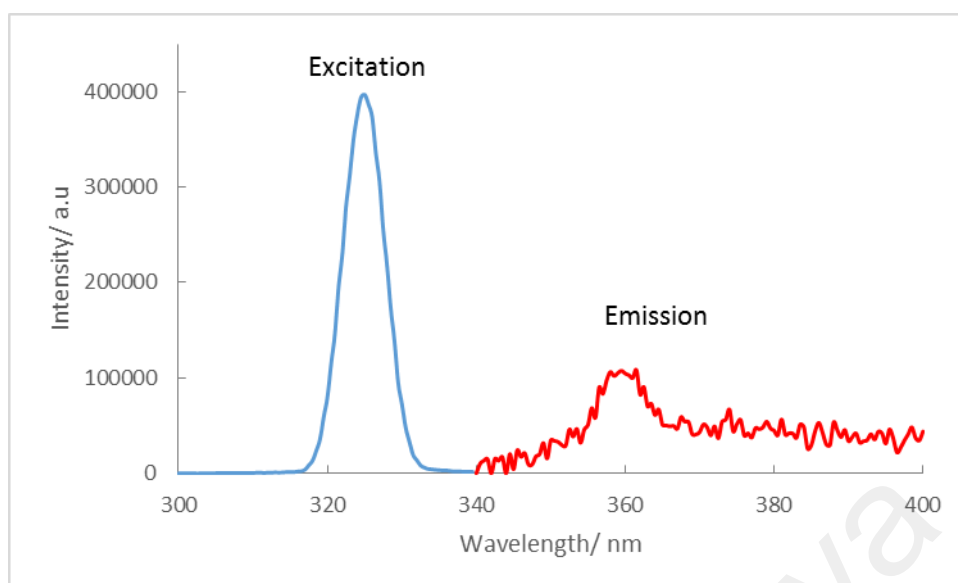


**Figure 4.17** Proposed structure for **Complex 2** (lattice  $\text{H}_2\text{O}$  is omitted)

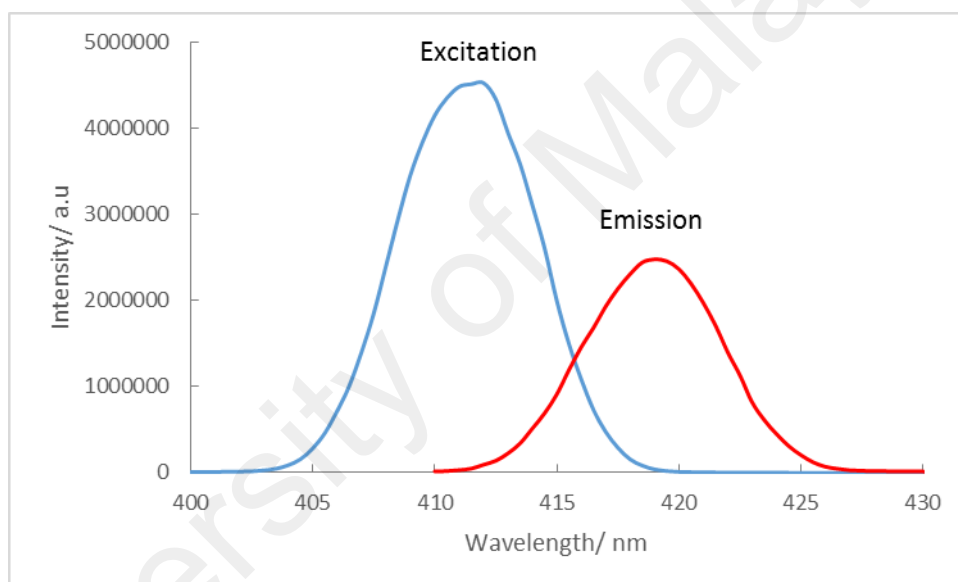
(b) *Determination of bandgaps*

Its  $E_o$  value, calculated as before from its UV-vis spectrum, was 3.30 eV ( $\lambda = 375$  nm).

Its **fluorescence** spectra (**Figure 4.18**) were recorded in chloroform. Upon excitation at 325 nm (MLCT band), it shows an emission peak at 360 nm, while upon excitation at 411 nm (*d-d* band), it shows an emission peak at 419 nm. Hence, the Stokes shifts were 35 nm and 8 nm, respectively. Additionally, its  $E_o$ , was 3.38 eV ( $\lambda = 367$  nm).



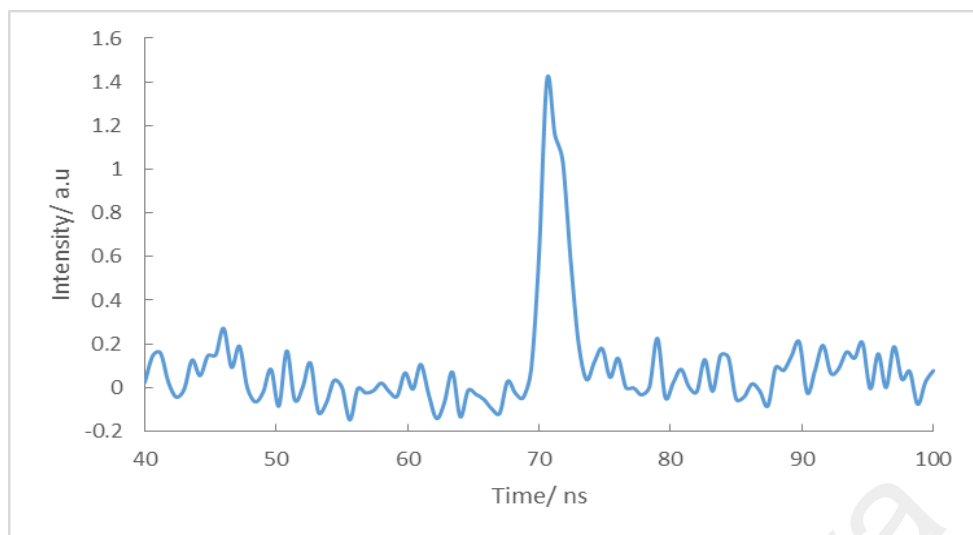
(a)



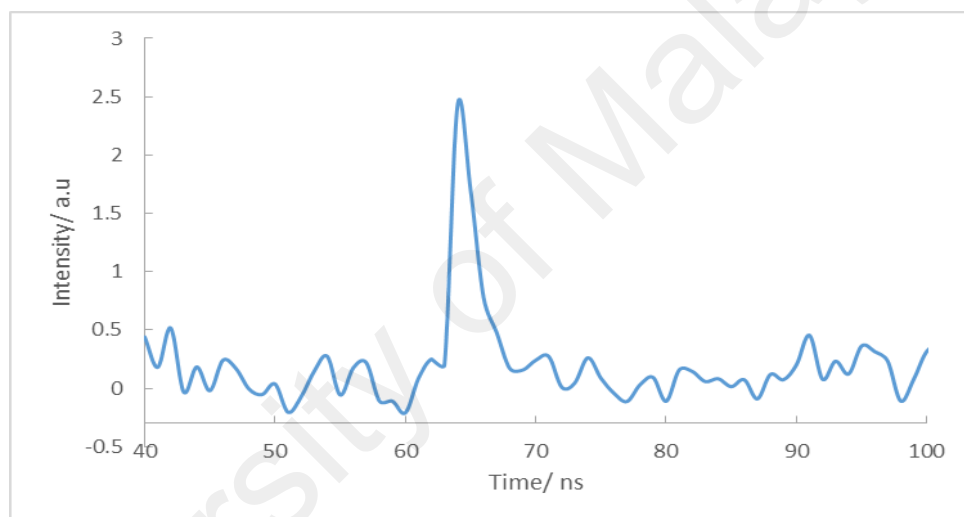
(b)

**Figure 4.18** Fluorescence spectra of **Complex 2** after excitation at: (a) 325 nm, and (b) 411 nm

Its  $\tau$  value, calculated from its decay curve (**Figure 4.19**) was 1.0 ns (for both  $\lambda_{emission} = 340$  nm and 697 nm).



(a)



(b)

**Figure 4.19** Fluorescence decay of **Complex 2** at  $\lambda_{emission}$  (a) 360 nm, and (b) 419 nm

Its **CV** scan was recorded anodically in chloroform at a scan rate of  $50 \text{ mV s}^{-1}$  in the potential range of +2.0 V to -2.0 V. The voltammogram (**Figure 4.20**) shows an anodic peak at +1.24 V assigned to the overlapping oxidation of Ni(II) to Ni(III) and oxidation of the ligand, and two cathodic peaks observed at +0.8 V and -1.7 V assigned to the reduction of Ni(III) to Ni(II) and the ligand, respectively.

The separation between the forward and the reverse peak ( $\Delta E_p$ ) was 440 mV and its  $I_{pc}/I_{pa}$  ratio is 0.18, indicating a quasireversible redox reaction

( $\Delta E_p > 59$  mV at 30 °C) and chemically unstable reduced complex ( $I_{pc}/I_{pa}$  ratio for chemically stable reduced complex is 1) [81].

The electrochemical band gap ( $E_e$ ) was calculated from its CV voltammogram using the relationship:  $E_e = |\text{HOMO} - \text{LUMO}|$ , where HOMO and LUMO is the highest occupied molecular orbital and the lowest unoccupied molecular orbital, respectively. The values are determined as follows: HOMO = onset oxidation peak voltage + 4.4 eV, and LUMO = onset reduction peak voltage + 4.4 eV. For **2**, the values for HOMO and LUMO were 5.30 V and 5.40 V, respectively. Hence, the  $E_e$  value was 0.1 eV.

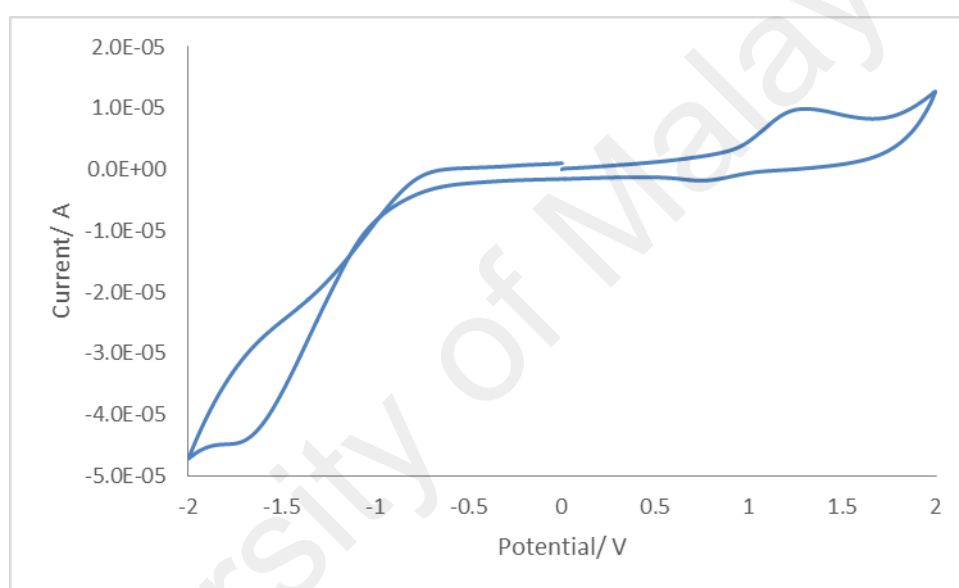


**Figure 4.20** Cyclic voltammogram for **Complex 2**

*(c) Magnetic properties*

Its  $\mu_{\text{eff}}$  value, calculated as previously done from the values of  $\text{FM} = 638.13 \text{ g mol}^{-1}$ ,  $\chi_g = 1.09 \times 10^{-5} \text{ cm}^3 \text{ g}^{-1}$ ,  $\chi_m = 6.98 \times 10^{-3} \text{ cm}^3 \text{ mol}^{-1}$ ,  $\chi_{\text{dia}} = -2.81 \times 10^{-4} \text{ cm}^3 \text{ mol}^{-1}$ , and  $\chi_m^{\text{corr}} = 7.26 \times 10^{-3} \text{ cm}^3 \text{ mol}^{-1}$ , was 4.13 BM at 298 K. The value is similar to that found for  $[\text{Ni}_2(\text{L})_2(\text{CH}_3\text{COO})_2] \cdot 4\text{H}_2\text{O}$ , where  $\text{L} = 3\text{-(4'-aminobiphenyl-4-ylimino)-butan-2-one oxime}$  ( $\mu_{\text{eff}} = 4.04$  BM at room temperature), which also has tetrahedral Ni(II) centres [95].

*(d) Thermal properties*

Its TGA trace (**Figure 4.21**) shows an initial weight loss of 8.0% from about 50 °C to 116 °C due to the evaporation of lattice H<sub>2</sub>O (calculated, 8.5%). The next weight loss of 71.8% from 307 °C to 683 °C is assigned to the decomposition of L1<sup>2-</sup> and CH<sub>3</sub>COO<sup>-</sup> ions (calculated, 73.1%). The amount of residue at temperatures above 683 °C was 20.2%, which is in a good agreement with the calculated value of 23.4%, assuming pure NiO [96]. Accordingly, the decomposition temperature for **Complex 2** was 307 °C.

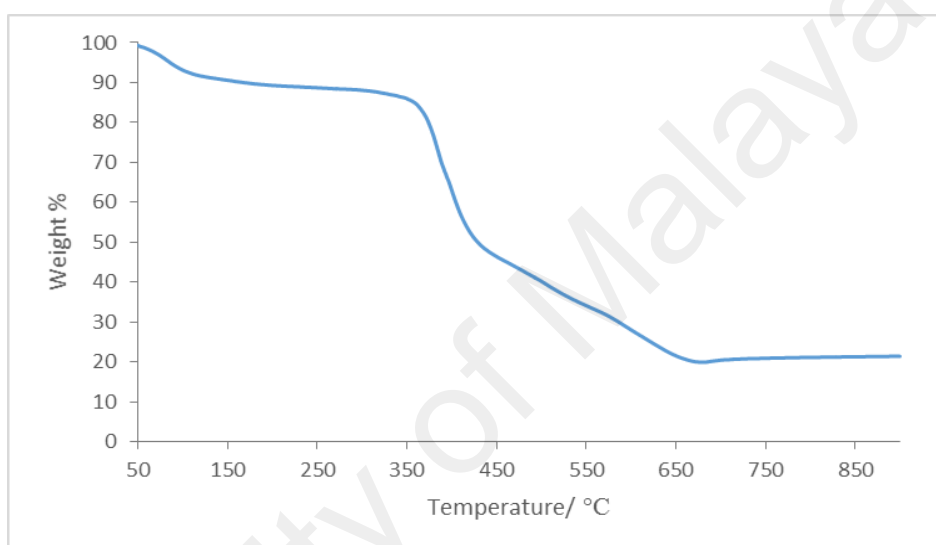


**Figure 4.21** TGA of **Complex 2**

*(e) Mesomorphic properties*

Its DSC spectrum (**Figure 4.22**) was recorded for a heating-cooling cycle from 25 °C to 225 °C. On heating, there was an endothermic peak at 138.1 °C ( $\Delta H = +107 \text{ kJ mol}^{-1}$ ), assigned as its melting temperature. However, there was no peak on cooling.

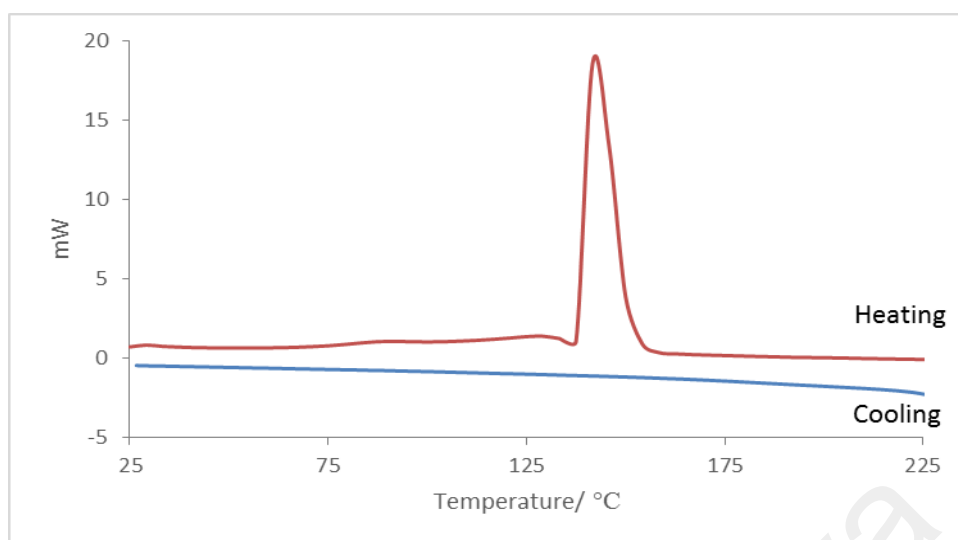


**Figure 4.22** DSC of **Complex 2**

Viewed under OPM, **Complex 2** (**Figure 4.23**) did not show any optical textures. It was further noted that the sample remained fluid on cooling from its isotropic temperature (227 °C) to room temperature. Combining both the DSC and OPM results, it is suggested that on heating at temperatures above 100 °C, the imine bonds of this complex were hydrolysed by the lattice H<sub>2</sub>O to form 1,8-diaminooctane and 2-HOC<sub>6</sub>H<sub>4</sub>CHO (a liquid at 30 °C) [26].

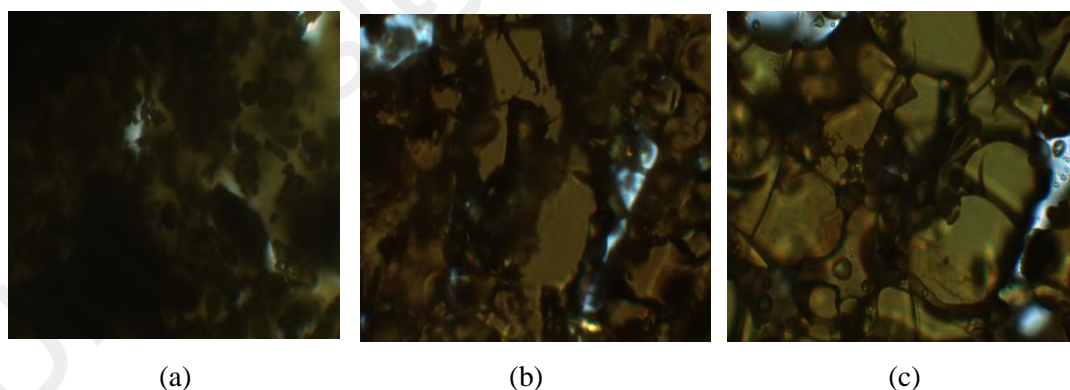


**Figure 4.23** Photomicrographs of **Complex 2** (a) on heating at 138 °C; (b) on heating at 227 °C; and (c) on cooling at 30 °C

#### 4.2.4 [Co<sub>2</sub>(CH<sub>3</sub>COO)<sub>2</sub>(L1)].2H<sub>2</sub>O

The Co(II) complex of H<sub>2</sub>L1 was also synthesised by the one-pot method, using 2-hydroxybenzaldehyde, 1,8-diaminooctane and [Co(CH<sub>3</sub>COO)<sub>2</sub>].4H<sub>2</sub>O in ethanol. The

product was a dark brown powder (**Complex 3**), and the yield was 56.2%. Its solubility was similar to **Complex 2**.

(a) *Structural deduction*

Based on the analytical data discussed below, it is proposed that its structural formula is similar to **Complex 2**.

The results from the **elemental analyses** (49.29 % C, 5.53 % H, 4.57 % N) were in good agreement with the chemical formula  $\text{Co}_2\text{C}_{26}\text{H}_{36}\text{N}_2\text{O}_8$  (622.44 g mol<sup>-1</sup>; 50.17 % C, 5.83 % H, 4.50 % N).

Its **FTIR** spectrum (**Figure 4.24**) shows peaks for the expected functional groups and bonds at similar wavenumbers (3246 cm<sup>-1</sup>, 2921 cm<sup>-1</sup>, 2853 cm<sup>-1</sup>, 1596 cm<sup>-1</sup>, 1536 cm<sup>-1</sup>, and 1442 cm<sup>-1</sup>) as the corresponding Cu(II) and Ni(II) complexes. The  $\Delta\nu(\text{COO})$  value is 94 cm<sup>-1</sup>, suggesting a chelating binding mode for  $\text{CH}_3\text{COO}^-$  ion.

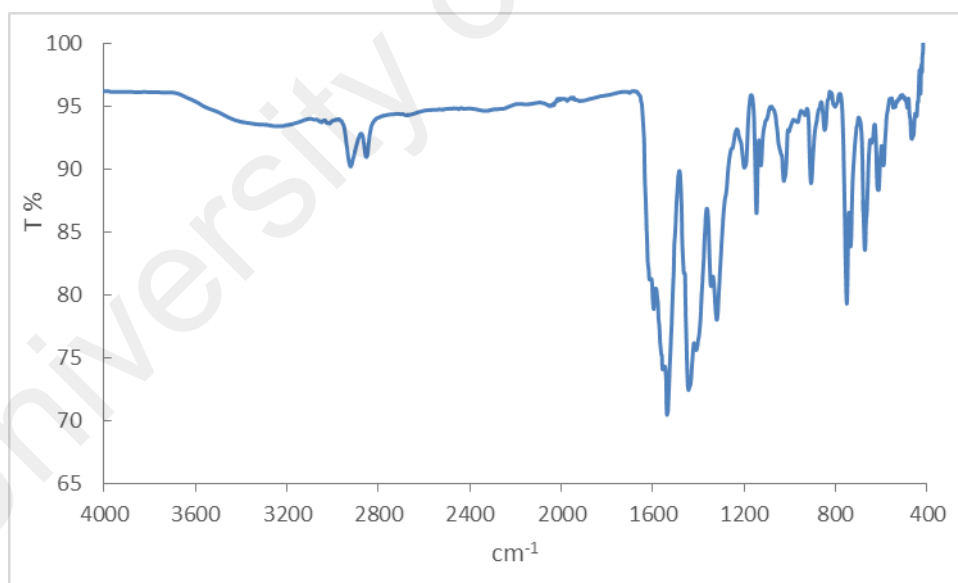


**Figure 4.24** FTIR spectrum for **Complex 3**

Its **UV-visible** spectrum was recorded in chloroform (**Figure 4.25**). The spectrum shows a *d-d* band at 608 nm ( $\epsilon_{\text{max}} = 153 \text{ M}^{-1} \text{ cm}^{-1}$ ) and MLCT band at 364 nm ( $\epsilon_{\text{max}} = 2509 \text{ M}^{-1} \text{ cm}^{-1}$ ). The position of the *d-d* peak was similar to tetrahedral Co(II)

complexes reported in the literature. An example is  $[\text{Co}(\text{L})_2]$ , where  $\text{L} = 3\text{-methoxysalicyliden-}p\text{-aminoacetophenoneoxime}$  ( $\lambda_{\text{max}} = 669 \text{ nm}$ ) [42].

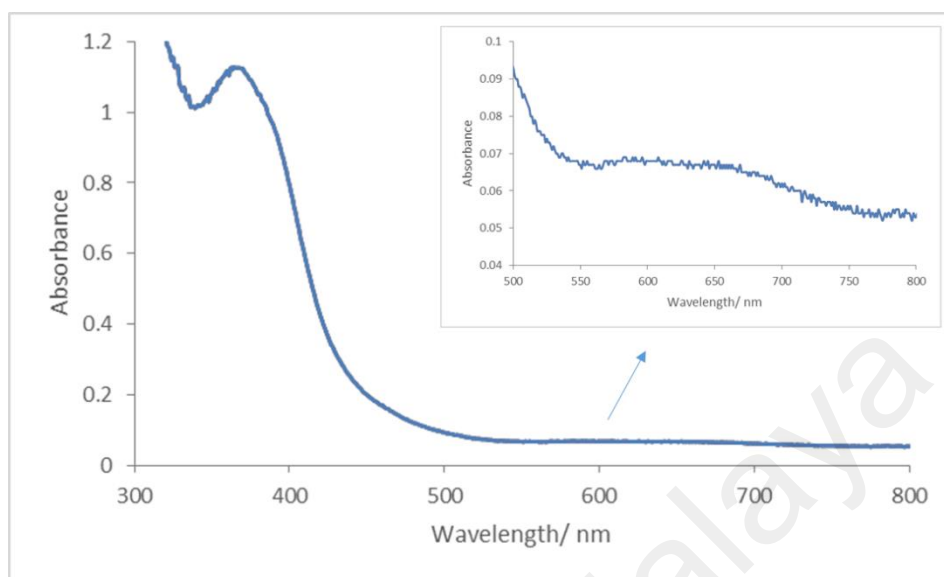
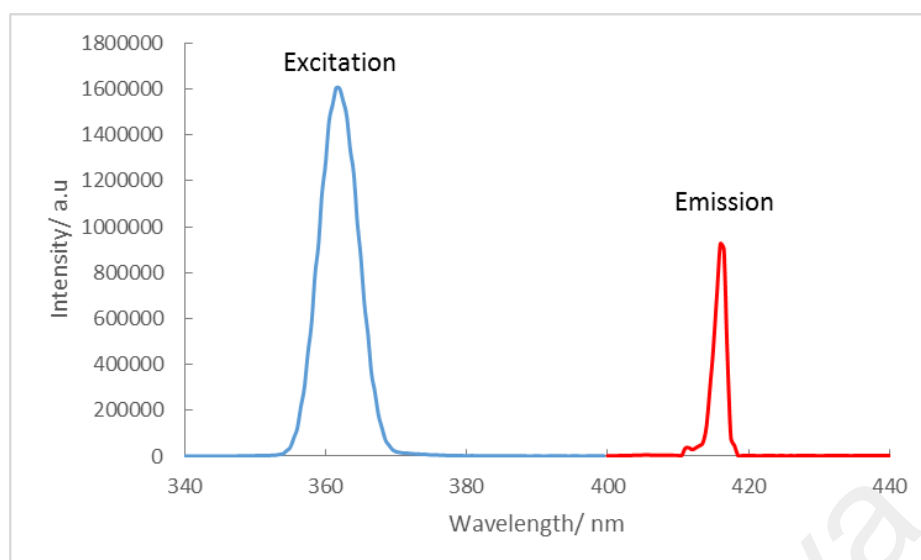


**Figure 4.25** UV-visible spectrum of **Complex 3**

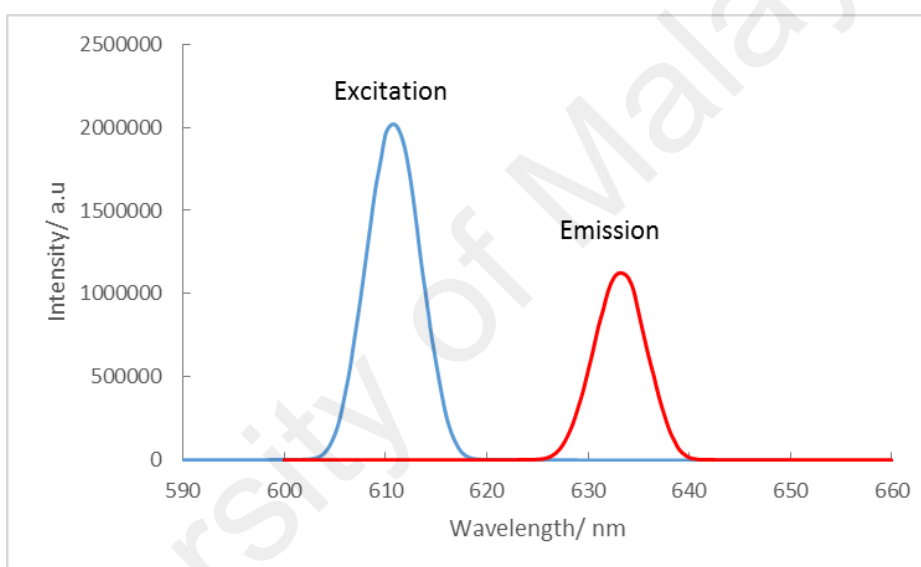
(b) *Determination of bandgaps*

Its  $E_o$  value, calculated as before from its UV-vis spectrum, was 2.82 eV ( $\lambda = 440 \text{ nm}$ ).

Its **fluorescence** spectra (**Figure 4.26**) were recorded in chloroform. Upon excitation at 362 nm (MLCT band), it shows an emission peak at 416 nm, while upon excitation at 611 nm ( $d-d$  band), it shows an emission peak at 633 nm. Accordingly, its Stokes shifts were 54 nm and 22 nm, respectively. Additionally, its  $E_o$ , was 2.96 eV ( $\lambda = 419 \text{ nm}$ ).



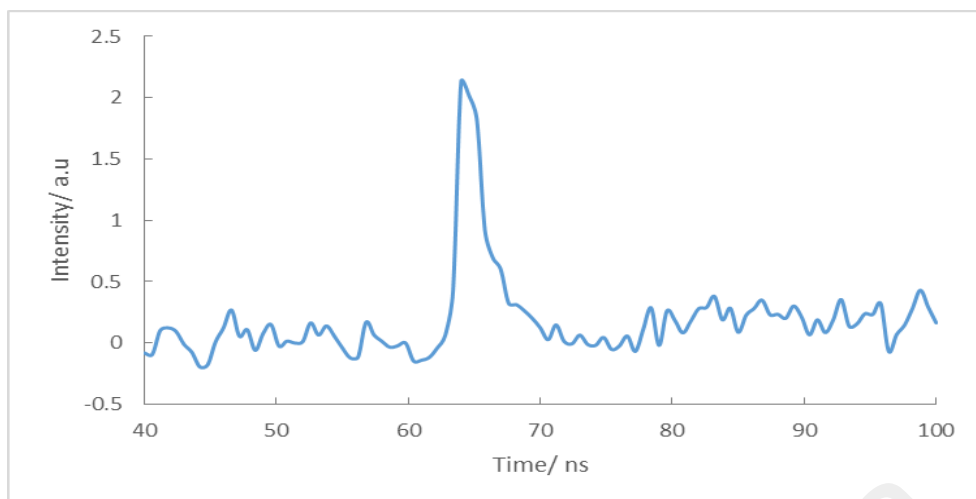
(a)



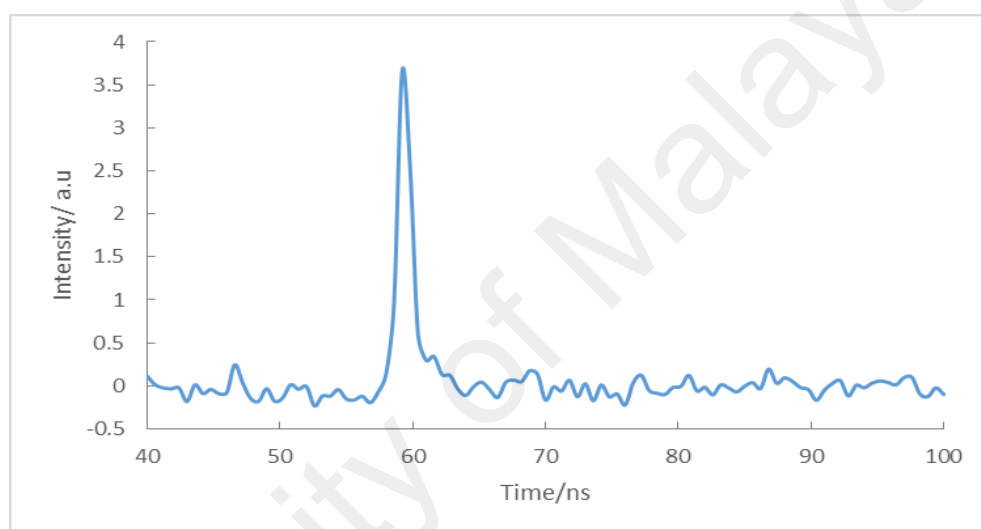
(b)

**Figure 4.26** Fluorescence spectra of **Complex 3** after excitation at: (a) 362 nm, and (b) 611 nm

Its  $\tau$  value, calculated from its decay curve (**Figure 4.27**) was 1.0 ns (for both  $\lambda_{emission} = 316$  nm and 633 nm).



(a)



(b)

**Figure 4.27** Fluorescence decay of **Complex 3** at  $\lambda_{emission}$ , (a) 416 nm, and (b) 633 nm

Its CV (**Figure 4.28**) was recorded anodically in chloroform at a scan rate  $50 \text{ mV s}^{-1}$  in the potential range of +2.0 V to -2.0 V. However, there were no redox peaks for Co(II). Hence, its electrochemical band gap cannot be calculated.

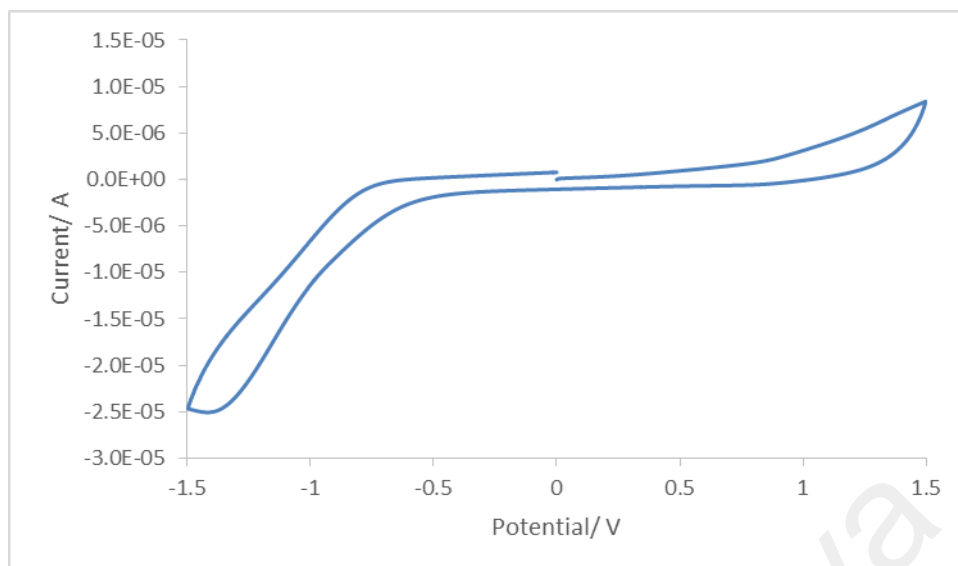


**Figure 4.28** Cyclic voltammogram for **Complex 3**

*(c) Magnetic properties*

Its  $\mu_{\text{eff}}$  value, similarly calculated as for the previously discussed complexes, from the values of  $\text{FM} = 622.44 \text{ g mol}^{-1}$ ,  $\chi_{\text{g}} = 2.51 \times 10^{-5} \text{ cm}^3 \text{ g}^{-1}$ ,  $\chi_{\text{m}} = 1.56 \times 10^{-2} \text{ cm}^3 \text{ mol}^{-1}$ ,  $\chi_{\text{dia}} = -2.68 \times 10^{-4} \text{ cm}^3 \text{ mol}^{-1}$ , and  $\chi_{\text{m}}^{\text{corr}} = 1.59 \times 10^{-2} \text{ cm}^3 \text{ mol}^{-1}$ , was 6.13 BM at 298 K. This value is comparable to  $[\text{Co}_2(\text{L})\text{Cl}_2(\text{H}_2\text{O})_2]$ , where  $\text{L} = 3\text{-hydroxy-N-phenyl-but-2-enamidine}$  ( $\mu_{\text{eff}} = 5.97 \text{ BM}$  at room temperature), which also have two tetrahedral  $\text{Co(II)}$  centres [95].

*(d) Thermal properties*

Its TGA trace (**Figure 4.29**) shows an initial weight loss of 4.8% from about 50 °C to 225 °C due to evaporation of lattice  $\text{H}_2\text{O}$  (calculated, 5.8%). The next weight loss of 72.0% from 247 °C to 623 °C is assigned to decomposition of  $\text{L}^{1-}$  and  $\text{CH}_3\text{COO}^-$  ions (calculated, 75.3%). The amount of residue at temperatures above 637 °C was 23.2%, which is in a good agreement with the calculated value of 24.1 %, assuming pure  $\text{CoO}$  [96,97]. Hence, **Complex 3** was thermally stable up to 247 °C.

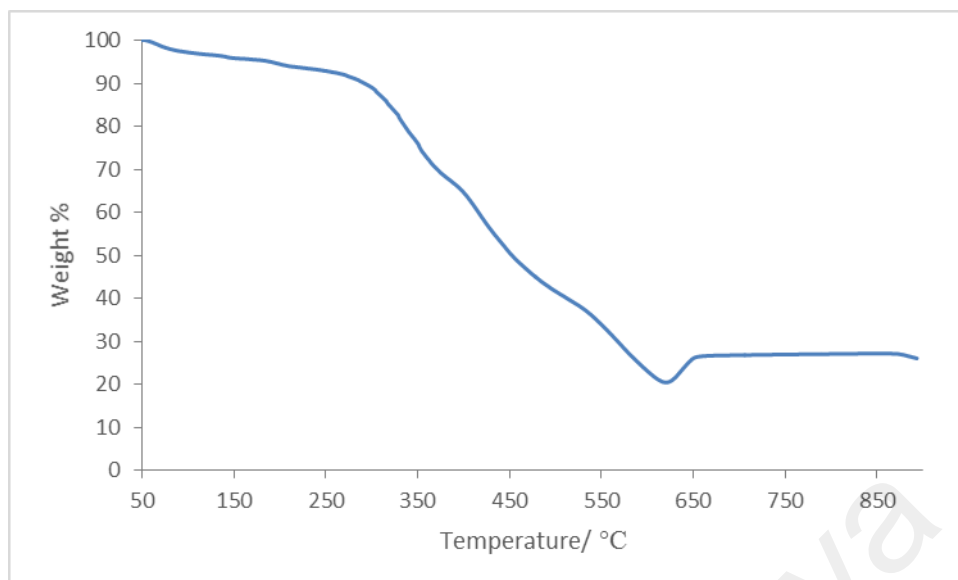


**Figure 4.29** TGA of **Complex 3**

*(e) Mesomorphic properties*

The DSC scan of **Complex 3** (**Figure 4.30**) was recorded for a heating-cooling cycle from 25 °C to 230 °C. On heating, there were endothermic peaks at 75.8 °C ( $\Delta H = +3.49 \text{ kJ mol}^{-1}$ ) assigned as the evaporation of lattice water molecules, 133.5 °C ( $\Delta H = +56.31 \text{ kJ mol}^{-1}$ ) assigned to its melting temperature, and 177.2 °C ( $\Delta H = +5.70 \text{ kJ mol}^{-1}$ ) and 198.3 °C ( $\Delta H = +4.45 \text{ kJ mol}^{-1}$ ) intuitively assigned to weak bond breaking processes. However, there were no peaks on cooling.

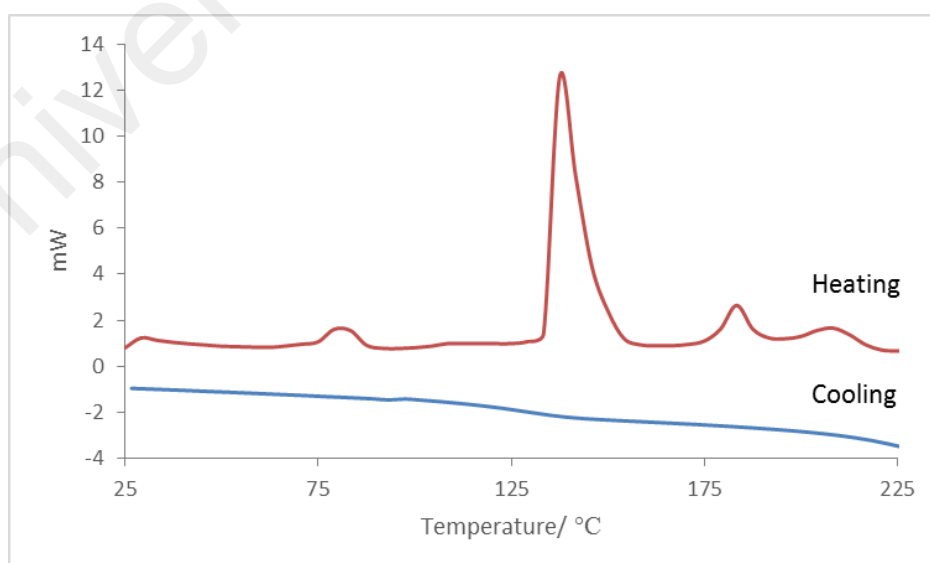


**Figure 4.30** DSC of **Complex 3**

Viewed under **OPM** (recorded for a heating-cooling cycle from 25 °C to 225 °C), **Complex 3** did not show any optical textures. The sample remained fluid on cooling from its isotropic liquid phase (222 °C) to room temperature (**Figure 4.31**). These observations were similar to **Complex 2**, and may be similarly explained. Hence, this complex did not exhibit mesomorphism.

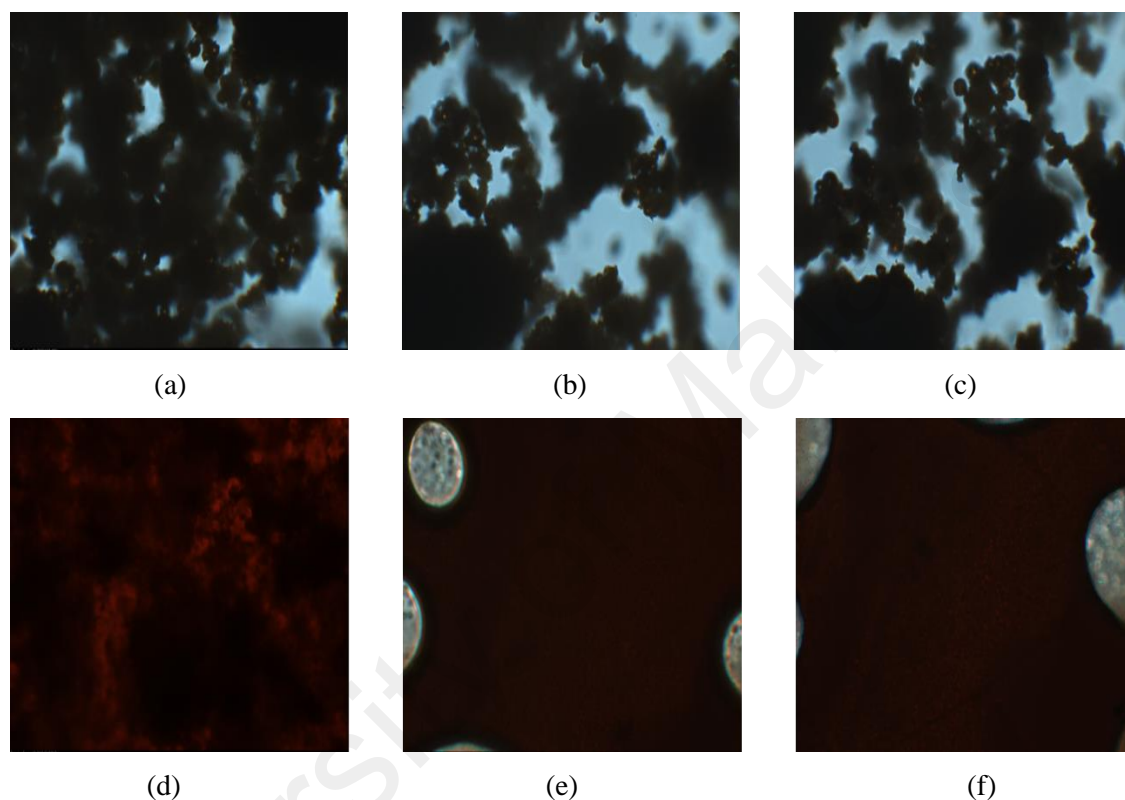


**Figure 4.31** Photomicrographs of **Complex 3**: (a) on heating at 75.8 °C; (b) on heating at 133.5 °C; (c) on heating at 177.2 °C; (d) on heating at 198.3 °C; (e) on heating at 225 °C; and (f) on cooling at 30 °C

#### 4.2.5 $[Fe(CH_3COO)(L1)]$

The Fe(II) complex of H<sub>2</sub>L1 was also synthesised by the one-pot method, from the reaction of 2-hydroxybenzaldehyde, 1,8-diaminooctane and  $[Fe(CH_3COO)_2]$  in ethanol. The product was a dark reddish-brown powder, and the yield was 79.0%. Its solubility was similar to **Complexes 2** and **3**.

(a) *Structural deduction*

Based on the same instrumental analyses, it is proposed that the structural formula of the complex was  $[\text{Fe}(\text{CH}_3\text{COO})(\text{L1})]$  (**Complex 4**). Hence, in contrast to the previously discussed complexes of  $\text{H}_2\text{L1}$ , **Complex 4** was mononuclear.

The results from the **elemental analyses** (60.95% C, 6.28% H, 5.56% N) were in good agreement with the chemical formula  $\text{FeC}_{24}\text{H}_{29}\text{N}_2\text{O}_4$  ( $465.34 \text{ g mol}^{-1}$ ; 61.95% C, 6.28% H, 6.02% N).

Its **FTIR** spectrum (**Figure 4.32**) shows peaks for the expected functional groups and bonds at similar wavenumbers ( $3360 \text{ cm}^{-1}$ ,  $2922 \text{ cm}^{-1}$ ,  $2853 \text{ cm}^{-1}$ ,  $1614 \text{ cm}^{-1}$ ,  $1542 \text{ cm}^{-1}$ , and  $1445 \text{ cm}^{-1}$ ) as the corresponding metal(II) complexes. From the latter peaks, the  $\Delta\nu$  value was  $94 \text{ cm}^{-1}$ , suggesting a chelating binding mode for  $\text{CH}_3\text{COO}^-$  ligand.

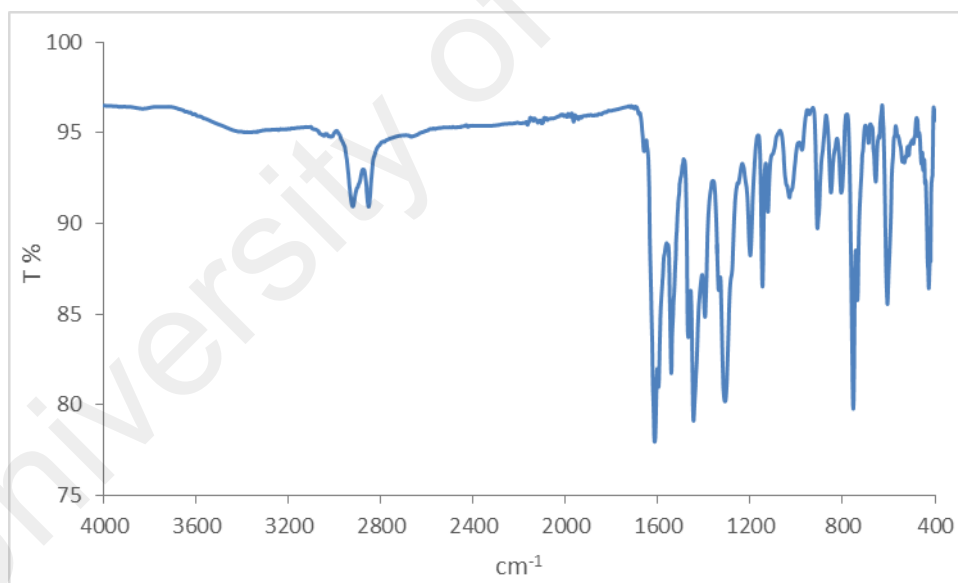


**Figure 4.32** FTIR spectrum for **Complex 4**

Its **UV-visible** spectrum was recorded in chloroform (**Figure 4.33**). The spectrum shows a broad *d-d* band at 500 nm ( $\epsilon_{\text{max}} = 117 \text{ M}^{-1} \text{ cm}^{-1}$ ), a shoulder at 409 nm ( $\epsilon_{\text{max}} = 296 \text{ M}^{-1} \text{ cm}^{-1}$ ) and a MLCT band at 322 nm ( $\epsilon_{\text{max}} = 2033 \text{ M}^{-1} \text{ cm}^{-1}$ ). This value is agree with the reported octahedral Fe(II) high spin complexes.

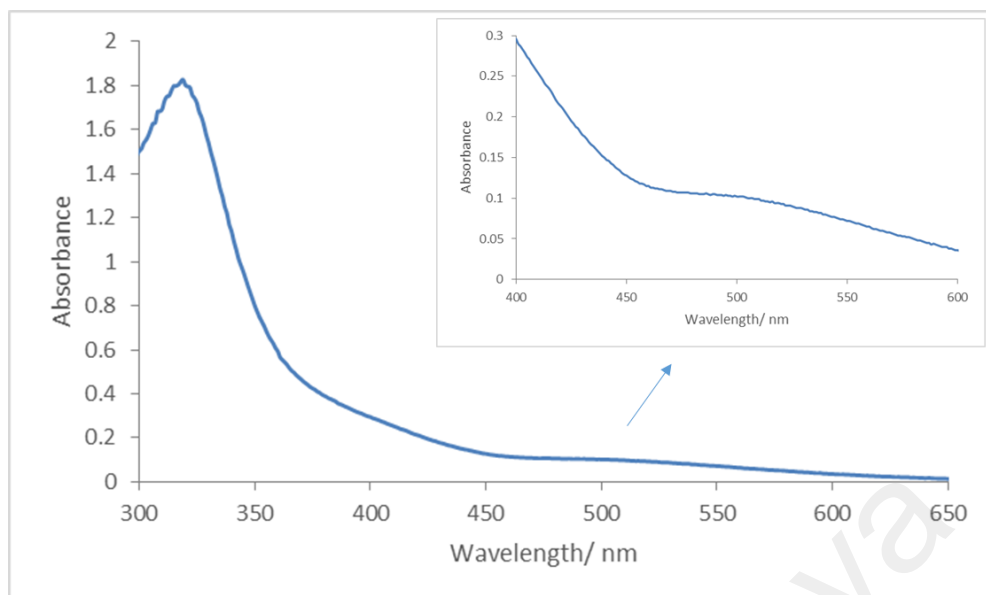


**Figure 4.33** UV-visible spectrum of **Complex 4**

Combining the results of elemental analyses and FTIR and UV-visible spectroscopies, the proposed structural formula of **Complex 4** ( $[\text{Fe}(\text{CH}_3\text{COO})(\text{HL1})]$ ) is shown in **Figure 4.34**. Unlike the Fe(II) complex reported by Abdullah *et. al* [55], it was dinuclear. The shorter alkyl chain of the carboxylate tend to form more planar structure.

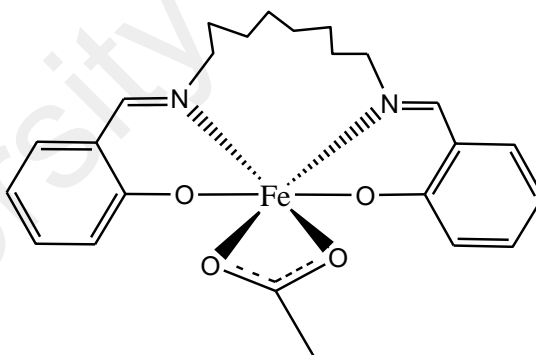
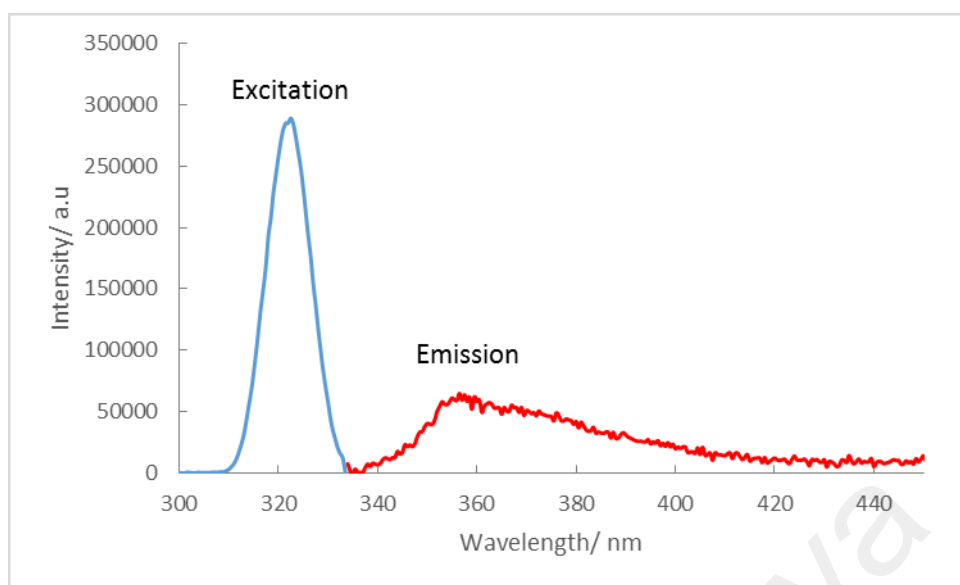


**Figure 4.34** Proposed structure for **Complex 4**

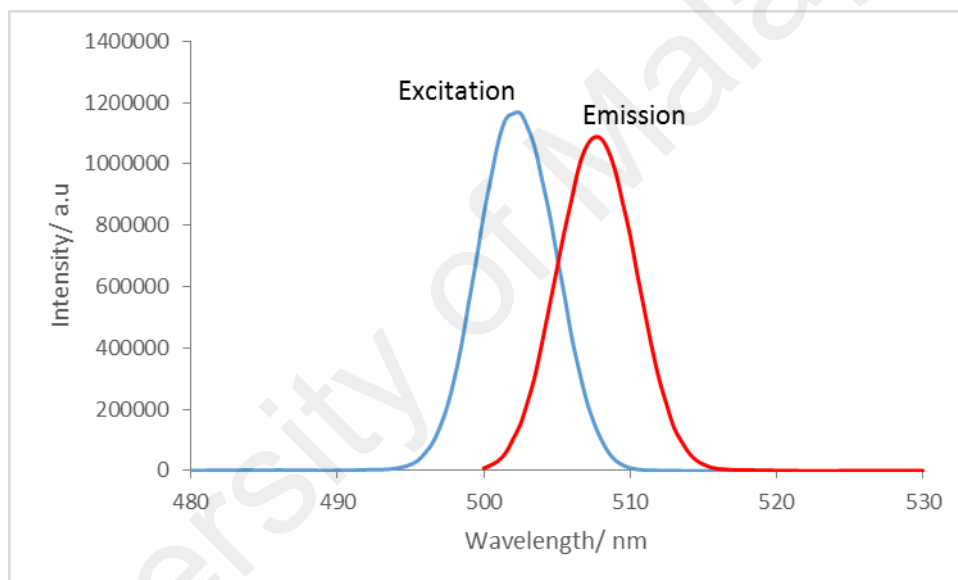
*(b) Determination of bandgaps*

Its  $E_o$  value, calculated as before from its UV-vis spectrum, was 3.30 eV ( $\lambda = 440$  nm).

Its **fluorescence** spectra (**Figure 4.35**) were recorded in chloroform. Upon excitation at 322 nm (MLCT band), it shows an emission peak at 355 nm, while upon excitation at 502 nm (*d-d* band), it shows an emission peak at 508 nm. Hence, its Stokes shifts were 33 nm and 6 nm, respectively. Its  $E_o$  was 3.02 eV ( $\lambda = 411$  nm).



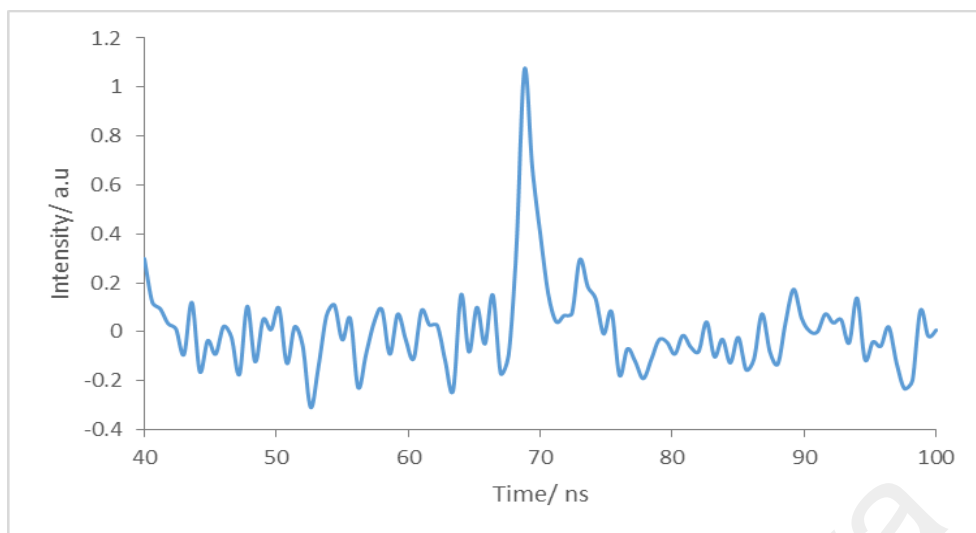
(a)



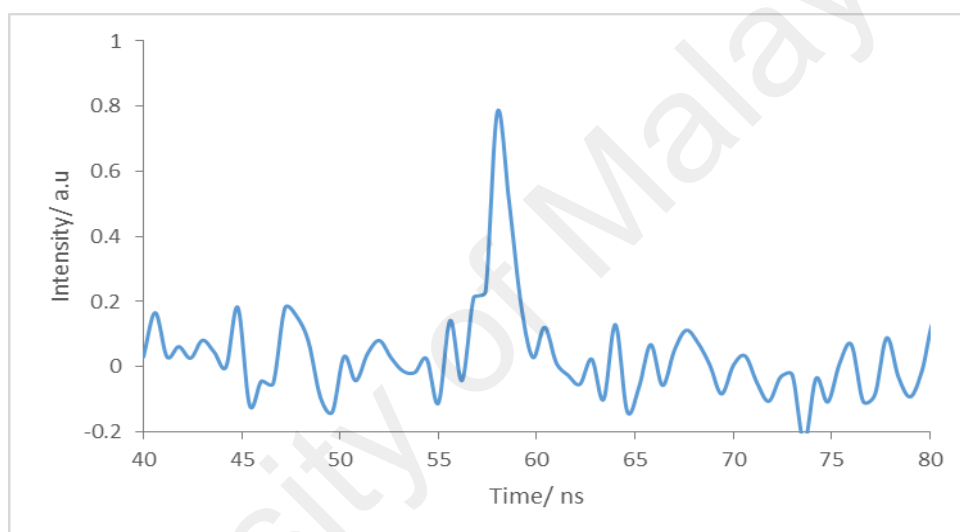
(b)

**Figure 4.35** Emission spectra of **Complex 4** after excitation at: (a) 322 nm, and (b) 502 nm

Its  $\tau$  value, calculated from its decay curve (**Figure 4.36**), was 1.0 ns ( $\lambda_{\text{emission}} = 355$  nm) and 0.7 ns ( $\lambda_{\text{emission}} = 508$  nm).



(a)



(b)

**Figure 4.36** Fluorescence decay of **Complex 4** at  $\lambda_{emission}$ , (a) 355 nm, and (b) 508 nm

Its CV scan (**Figure 4.37**) was recorded anodically in chloroform at a scan rate of  $50 \text{ mV s}^{-1}$  in the potential range of +2.0 V to -2.0 V. However, there were no redox peaks for Fe(II). Hence, its electrochemical band gap cannot be calculated. From this, it may be suggested that the complex has an insulating effect because its structure is more planar and stable, protecting the central Cu from being easily reduced and oxidised (higher potentials). Similar deduction was made for  $[\text{Cu}_2(\text{RCOO})_4(\text{RCOOH})_2]$  (R = 2-hexyldecanoate) [92].

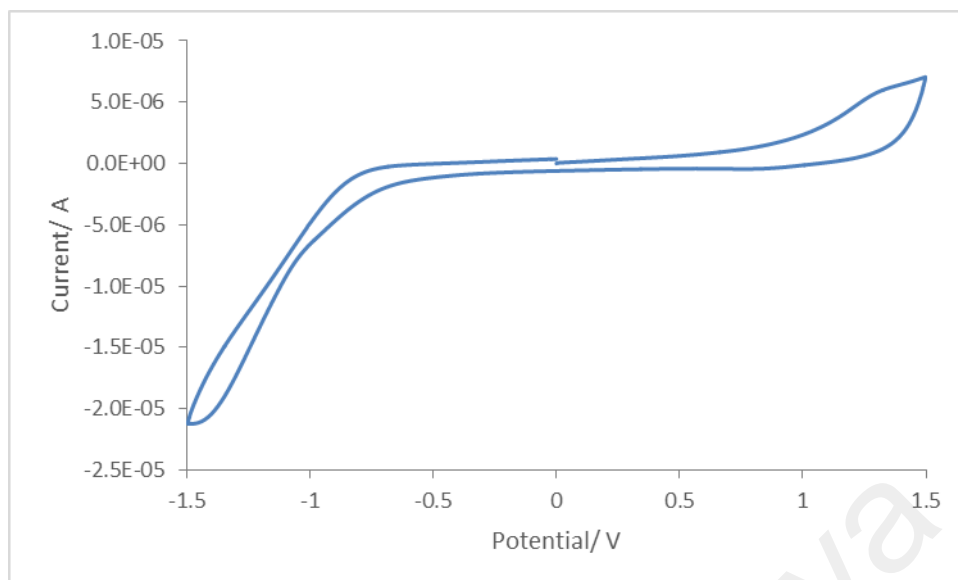


**Figure 4.37** Cyclic voltammogram for **Complex 4**

*(c) Magnetic properties*

Its  $\chi_m T$  value, calculated as previously done from the values of  $FM = 465.34 \text{ g mol}^{-1}$ ,  $\chi_g = 2.12 \times 10^{-5} \text{ cm}^3 \text{ g}^{-1}$ ,  $\chi_m = 9.86 \times 10^{-3} \text{ cm}^3 \text{ mol}^{-1}$ ,  $\chi_{\text{dia}} = -2.17 \times 10^{-4} \text{ cm}^3 \text{ mol}^{-1}$ , and  $\chi_m^{\text{corr}} = 1.01 \times 10^{-2} \text{ cm}^3 \text{ mol}^{-1}$ , was  $3.00 \text{ cm}^3 \text{ K mol}^{-1}$ . This value agreed with theoretical value  $3.00 \text{ cm}^3 \text{ K mol}^{-1}$  for a high spin (HS) Fe(II) complex ( $S = 2$ ) [98].

*(d) Thermal properties*

Its TGA trace (**Figure 4.38**) shows an initial weight loss of 83.3% from about  $134 \text{ }^\circ\text{C}$  to  $760 \text{ }^\circ\text{C}$  due to decomposition of  $\text{L1}^-$  and  $\text{CH}_3\text{COO}^-$  ligands (calculated, 88.0%). The amount of residue at temperature  $760 \text{ }^\circ\text{C}$  was 16.7%, which is in a good agreement with the calculated value of 15.3% (assuming pure FeO) [99]. Hence,  $T_{\text{dec}}$  for **Complex 4** was  $134 \text{ }^\circ\text{C}$ .

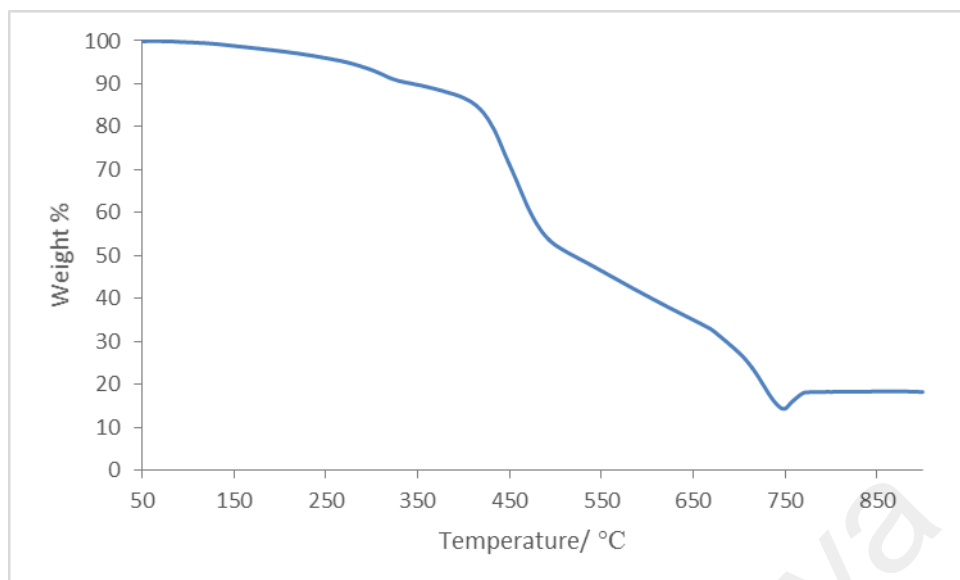


**Figure 4.38** TGA of **Complex 4**

*(e) Mesomorphic properties*

The DSC scan of **Complex 4** (**Figure 4.39**) was recorded for a heating-cooling cycle from 25 °C to 115 °C. On heating, there was an endothermic peak at 72.5 °C ( $\Delta H = +4.46 \text{ kJ mol}^{-1}$ ) and assigned as crystal to crystal transition. However, there were no peaks on cooling.

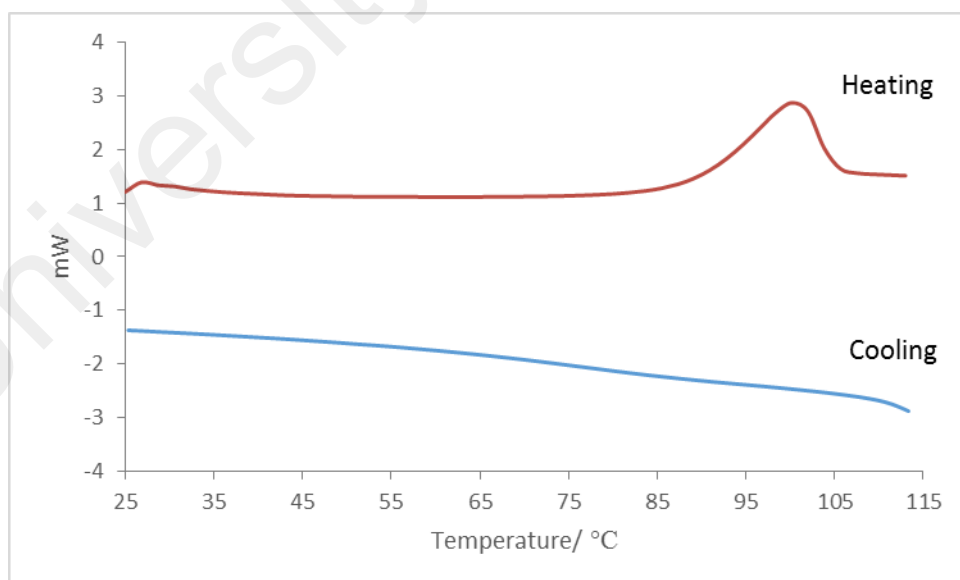


**Figure 4.39** DSC of **Complex 4**

Viewed under **OPM**, which was recorded for a heating-cooling cycle from 25 °C to 115 °C, the complex did not show any optical textures. Hence, this complex did not exhibit mesomorphism.

#### 4.2.6 $[Mn_2(CH_3COO)_4(L1)].5H_2O$

The Mn(II) complex of H<sub>2</sub>L1 was also synthesised by the one-pot method, from the reaction of 2-hydroxybenzaldehyde, 1,8-diaminooctane and  $[Mn(CH_3COO)_2].4H_2O$  in ethanol. The product was a dark purple powder (**Complex 5**), and the yield was 77.2%. Its solubility was similar to **Complexes 2 - 4**.

##### (a) Structural deduction

Based on the instrumental data discussed below, the proposed structural formula for **Complex 5** is  $[Mn_2(CH_3COO)_4(L1)].5H_2O$  (a dinuclear complex).

The results from the **elemental analyses** (45.78% C, 5.92% H, 2.99% N) were in good agreement with the chemical formula  $Mn_2C_{30}H_{48}N_2O_{15}$  (786.58 g mol<sup>-1</sup>; 45.81% C, 6.15% H, 3.56% N).

Its **FTIR** spectrum (**Figure 4.40**) shows peaks for the expected functional groups and bonds at similar wavenumbers (3230 cm<sup>-1</sup>, 2927 cm<sup>-1</sup>, 2854 cm<sup>-1</sup>, 1615 cm<sup>-1</sup>, 1548 cm<sup>-1</sup>, 1435 cm<sup>-1</sup> and 1391 cm<sup>-1</sup>) as the corresponding metal(II) complexes. From the latter peaks, the  $\Delta\nu(COO)$  values are 112 cm<sup>-1</sup> and 157 cm<sup>-1</sup>, suggesting chelating and bridging binding modes for CH<sub>3</sub>COO<sup>-</sup> ligands, respectively.

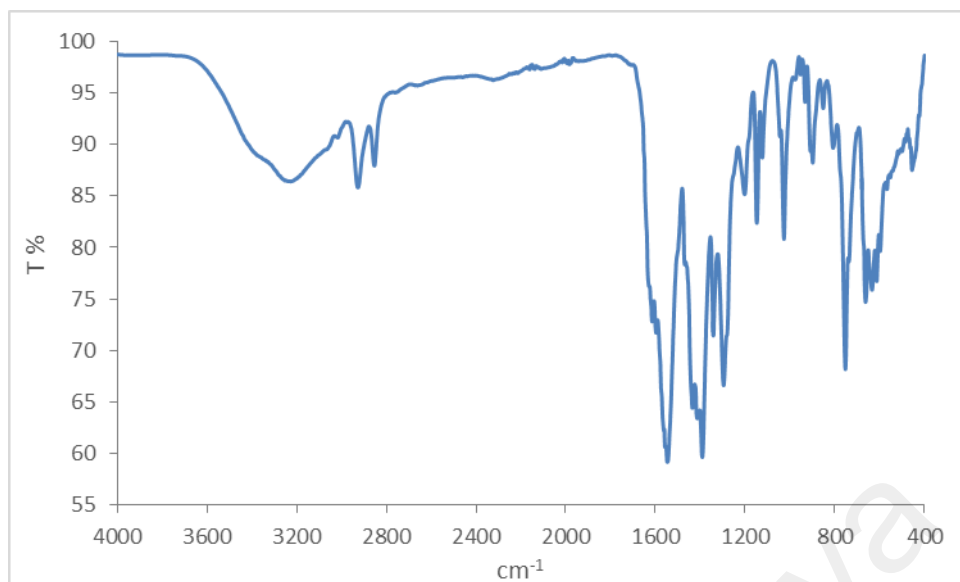


**Figure 4.40** FTIR spectrum for **Complex 5**

Its **UV-visible** spectrum was recorded in chloroform (**Figure 4.41**). The spectrum shows a *d-d* band at 685 nm ( $\epsilon_{\text{max}} = 235 \text{ M}^{-1} \text{ cm}^{-1}$ ) and MLCT band at 370 nm ( $\epsilon_{\text{max}} = 3422 \text{ M}^{-1} \text{ cm}^{-1}$ ). The *d-d* band suggests an octahedral geometry at each Mn(II) centres, as suggested for  $[\text{Mn}(\text{HPTP})\text{Cl}(\text{H}_2\text{O})_2]$  (HPTP = (Z)-2-(4-(pyridine-2-yl)thiosemicarbazido)propanoate), which also has an octahedral Mn(II) centre [49].

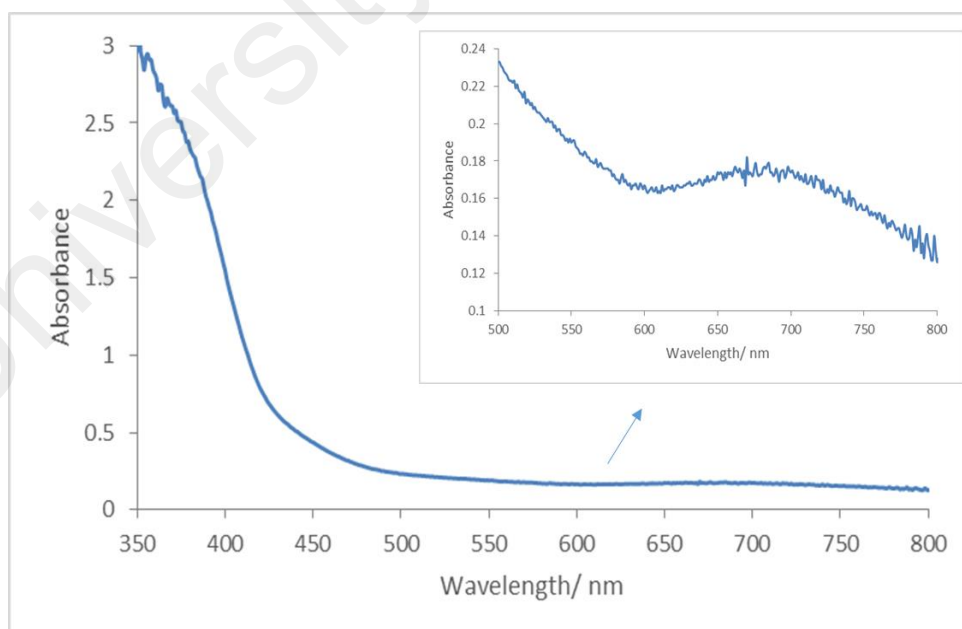


**Figure 4.41** UV-visible spectrum of **Complex 5**

Combining the results of elemental analyses and FTIR and UV-visible spectroscopies, the proposed structural formula of **Complex 5** ( $[\text{Mn}_2(\text{CH}_3\text{COO})_4(\text{L1})].5\text{H}_2\text{O}$ ) is shown in **Figure 4.42**

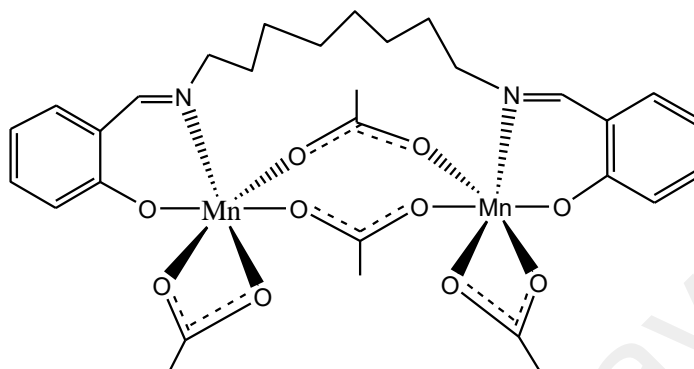
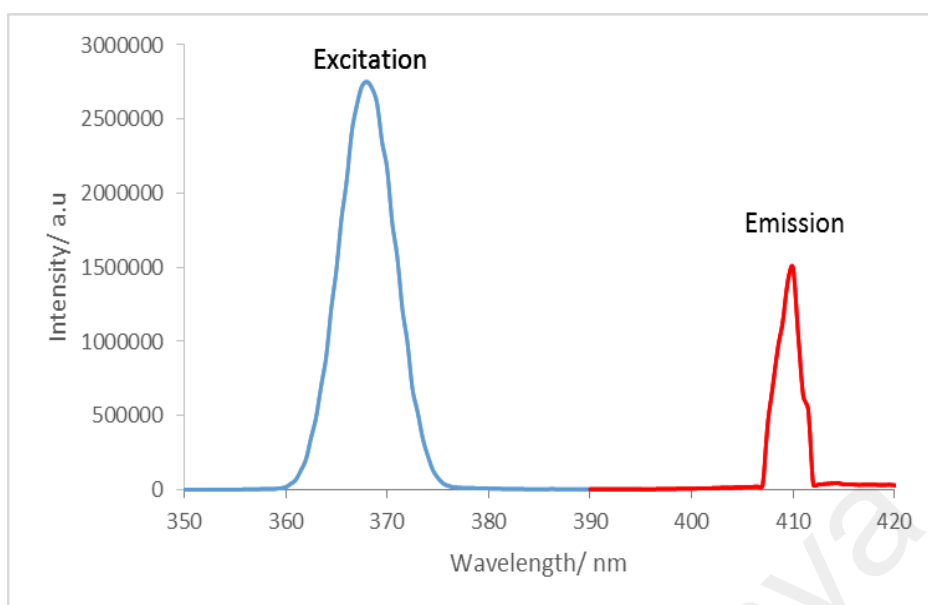


**Figure 4.42** Proposed structure for **Complex 5** (lattice  $\text{H}_2\text{O}$  molecules are not shown)

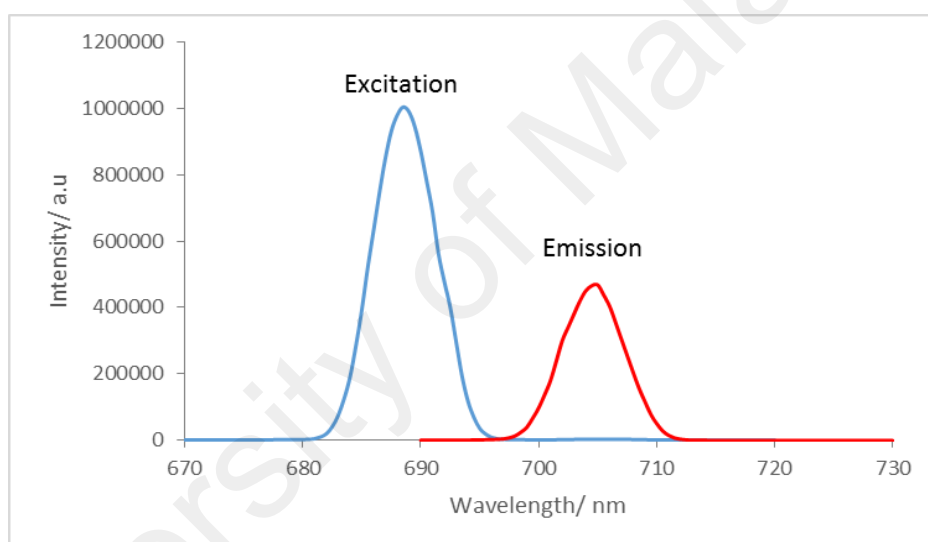
(b) *Determination of bandgaps*

Its  $E_o$  value, calculated as before from its UV-vis spectrum, was 2.81 eV ( $\lambda = 442$  nm).

Its **fluorescence** spectra (**Figure 4.43**) were recorded in chloroform. Upon excitation at 368 nm (MLCT band), it shows an emission peak at 410 nm, while upon excitation at 689 nm (*d-d* band), it shows an emission peak at 705 nm. Hence, its Stokes shift were 42 nm and 16 nm, respectively. Additionally, its  $E_o$  was 3.01 eV ( $\lambda = 412$  nm).



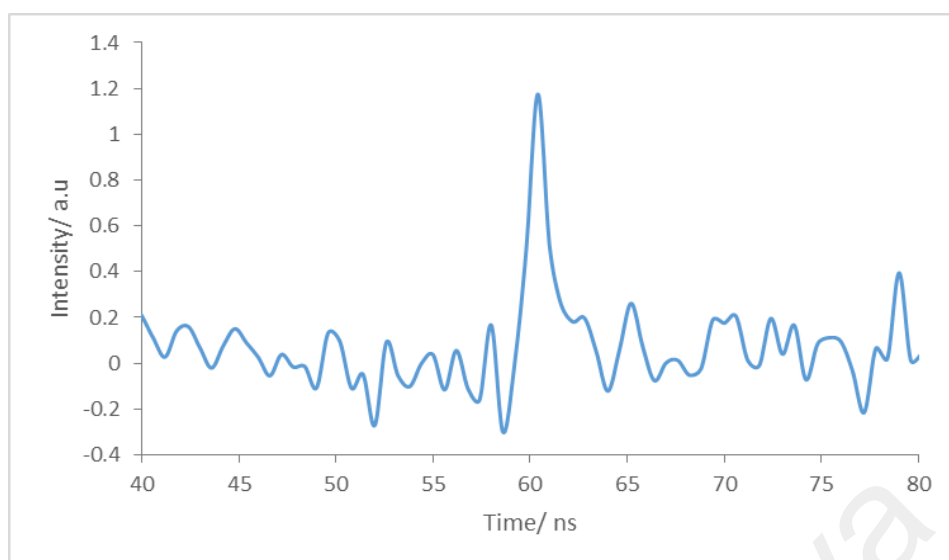
(a)



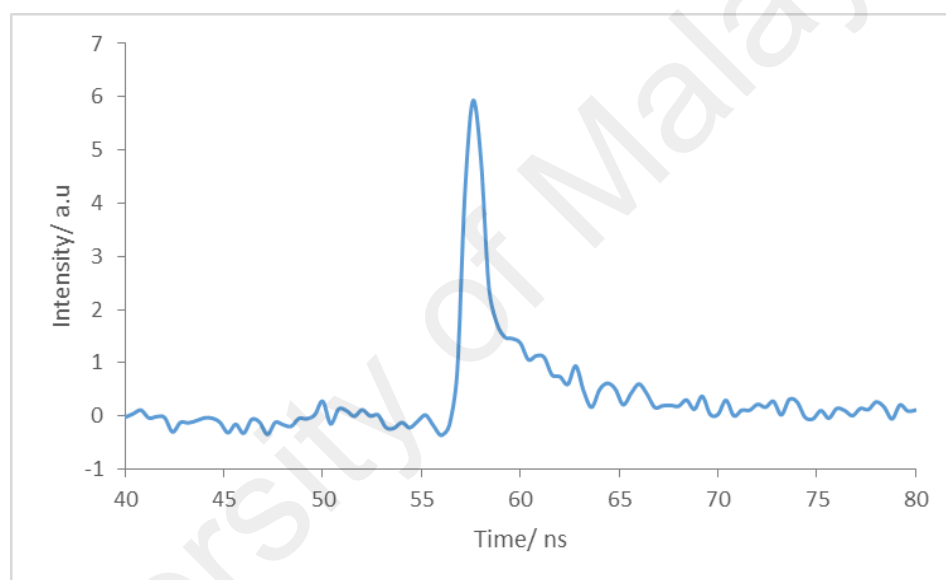
(b)

**Figure 4.43** Fluorescence spectra of **Complex 5** after excitation at: (a) 368 nm; and (b) 689 nm

Its  $\tau$  value, calculated from its decay curve (**Figure 4.44**) was 2.4 ns ( $\lambda_{\text{emission}} = 410$  nm) and 0.8 ns ( $\lambda_{\text{emission}} = 705$  nm).



(a)



(b)

**Figure 4.44** Fluorescence decay of **Complex 5** at  $\lambda_{emission}$ , (a) 410 nm, (b) 705 nm

Its CV was recorded anodically in chloroform at a scan rate  $50 \text{ mV s}^{-1}$  in the potential range of +2.0 V to -2.0 V. The voltammogram (**Figure 4.45**) shows an anodic peak at +1.42 V assigned to the oxidation of the ligand, and the corresponding cathodic peak at -1.42 V assigned to the reduction of the ligand. There was also an anodic peak at +0.6 V assigned to the oxidation of Mn(II) to Mn(III), but there were no corresponding reduction peak, indicating the irreversibility of metal-based redox process. Hence, its electrochemical band gap cannot be calculated.

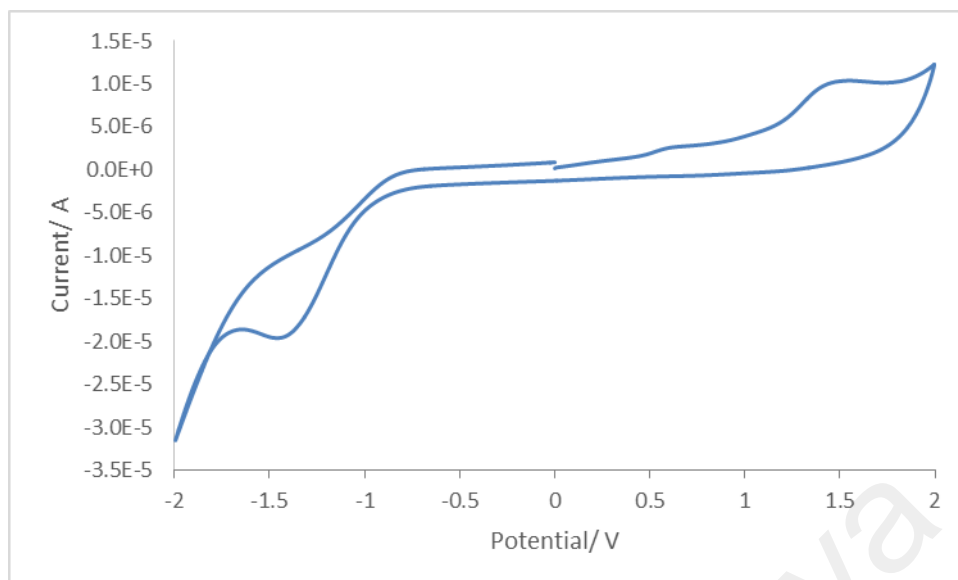


**Figure 4.45** Cyclic voltammogram for **Complex 5**

*(c) Magnetic properties*

Its  $\chi_m T$  value, calculated as previously done from the values of  $FM = 786.58 \text{ g mol}^{-1}$ ,  $\chi_g = 1.19 \times 10^{-5} \text{ cm}^3 \text{ g}^{-1}$ ,  $\chi_m = 9.36 \times 10^{-3} \text{ cm}^3 \text{ mol}^{-1}$ ,  $\chi_{\text{dia}} = -3.34 \times 10^{-4} \text{ cm}^3 \text{ mol}^{-1}$ , and  $\chi_m^{\text{corr}} = 9.69 \times 10^{-3} \text{ cm}^3 \text{ mol}^{-1}$ , was  $2.89 \text{ cm}^3 \text{ K mol}^{-1}$ . The theoretical value for a high spin (HS) Mn(II) complex ( $S = 5/2$ ) is  $4.377 \text{ cm}^3 \text{ K mol}^{-1}$ , and for a low spin (LS) Mn(II) complex ( $S = 1/2$ ) is  $0.375 \text{ cm}^3 \text{ K mol}^{-1}$  [98]. From this, it may be inferred that this complex was made up of 27% HS and 73% LS Mn(II) at room temperature (298 K).

*(d) Thermal properties*

Its TGA trace (**Figure 4.46**) shows an initial weight loss of 10.9% from about  $50 \text{ }^\circ\text{C}$  to  $150 \text{ }^\circ\text{C}$  due to loss of lattice water molecules (calculated, 11.5%). The next weight loss of 67.4% from  $231 \text{ }^\circ\text{C}$  to  $717 \text{ }^\circ\text{C}$  was due to decomposition of  $L1^{2-}$  and  $\text{CH}_3\text{COO}^-$  ligands (calculated, 74.6%). The amount of residue at temperatures above  $717 \text{ }^\circ\text{C}$  was 21.7%, which is in agreement with the calculated value of 20.1% (assuming pure  $\text{Mn}_2\text{O}_3$ ) [100]. Hence, **Complex 5** was thermally stable up to  $231 \text{ }^\circ\text{C}$ .

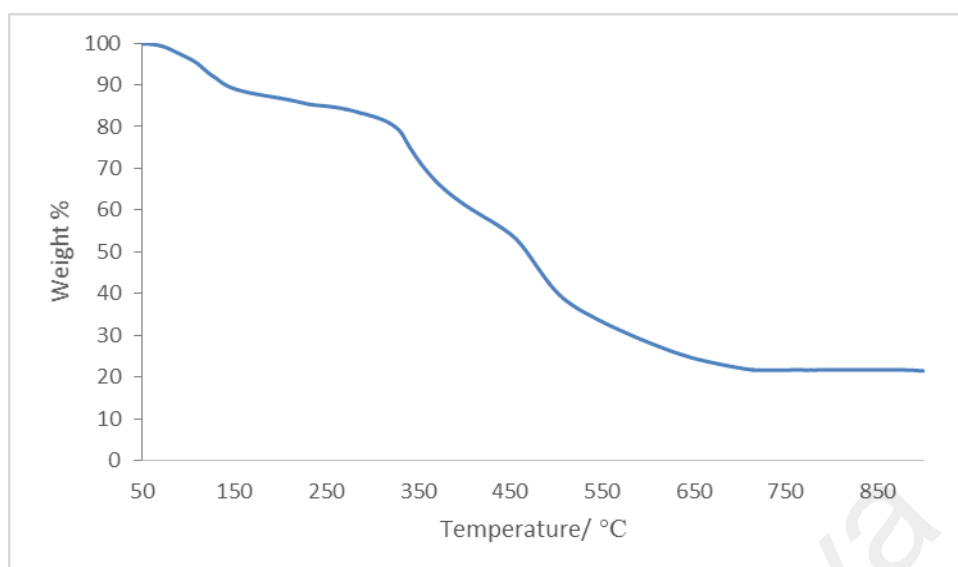


**Figure 4.46** TGA of **Complex 5**

*(e) Mesomorphic properties*

The DSC scan of **Complex 5** (**Figure 4.47**) was recorded for a heating-cooling cycle from 25 °C to 225 °C. On heating, there was an endothermic peak at 81.0 °C ( $\Delta H = 53.57 \text{ kJ mol}^{-1}$ ) assigned as the melting temperature of the dimers (Cr1). Another two endothermic peaks were observed at 108.0 °C ( $\Delta H = 9.9 \text{ kJ mol}^{-1}$ ) and 149.4 °C ( $\Delta H = 51.2 \text{ kJ mol}^{-1}$ ), assigned as the breaking of the dimers to monomers (Cr1-Cr2) and to monomers to mesophase transition (Cr2-M), respectively. On cooling, an exothermic peak was observed at 144.8 °C ( $\Delta H = - 3.5 \text{ kJ mol}^{-1}$ ) corresponding to M-Cr2 transition.

**Table 4.2** DSC data for **Complex 5**

Cycle	Temperature (°C)	$\Delta H$ (kJ mol <sup>-1</sup> )	Assignment
Heating	81.0	53.57	Melting of dimers (Cr1)
	108.0	9.9	Cr1- Cr2
	149.4	51.2	Cr2- M
Cooling	144.8	3.5	M-Cr2

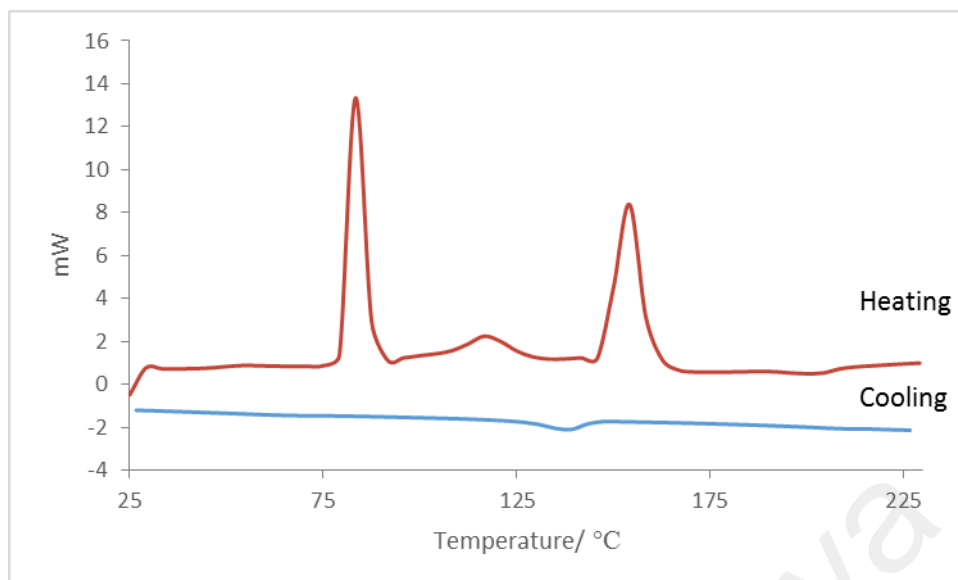
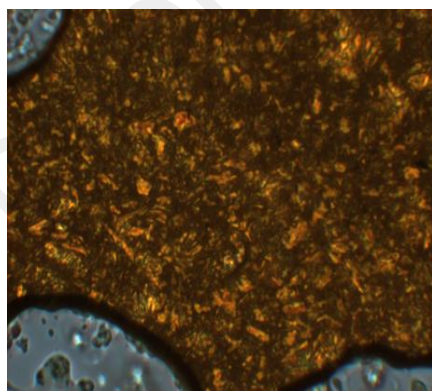
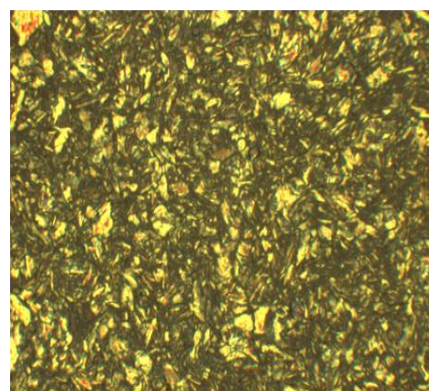


**Figure 4.47** DSC of **Complex 5**

Viewed under **OPM**, which was recorded for a heating-cooling cycle from 25 °C to 200 °C, **Complex 5** (**Figure 4.48**) was observed to be fluid at 200 °C and cleared at 230 °C (accompanied by decomposition). On cooling from this temperature, there were no optical texture and the sample remained fluid until room temperature. However, when a new sample was heated to 200 °C, and cooled from this temperature, it exhibited a strong birefringence at 129 °C, which did not change on further cooling to room temperature (30 °C). The results suggest that **Complex 5** exhibited mesomorphisms.



(a)



(b)

**Figure 4.48** Photomicrographs of **Complex 5** on: (a) heating at 200 °C; and (b) cooling at 129 °C

#### 4.2.7 Summary

The analytical results for **Complexes 1-5** are summarised in **Table 4.3**. **Complex 1** was dimeric, **4** was mononuclear, while **Complexes 2, 3** and **5** were dinuclear. All complexes were paramagnetic.

The optical bandgaps (from the CT absorption bands and emission bands) for all complexes were similar (2.81 eV – 3.61 eV), suggesting that the band gap were independent of the metal (II) centre and nuclearity of the complexes. Hence, these complexes were semiconductors, and their values were similar to reported photovoltaic materials, such as 6H-SiC (2.9 eV) [101] and [Cu(HPTP)](H<sub>2</sub>O)<sub>2</sub> (3.26 eV) [77]. Accordingly, these complexes were potential solar cell materials [49].

In contrast, **Complex 2** has electrochemical band gap 0.1 eV and for the other complexes, the electrochemical band gap cannot be calculated because the complexes were redox inactive. The significantly lower  $E_e$  value compared to  $E_o$  is expected as the electrochemical process involved an electron in the antibonding 3d orbital, while the optical process involved photonic excitation of an electron from ligand orbital(s) to metal.

Except for **Complex 5**, the lifetimes of all excited complexes were similar (0.7 ns to 1.3 ns). The lifetime for **Complex 5** was the longest at 2.4 ns. It is to be noted that these lifetimes were sufficiently long to allow for the electronic injection from absorbed dyes into nanocrystalline TiO<sub>2</sub>, reported to occur within several hundred femtoseconds [102]. The Stokes shift values for all complexes were in the range of 35-54 nm (CT transition) and 6-22 nm (*d-d* transition). The larger Stokes shift is more favourable and an important parameter in photovoltaic and solar cell.

These complexes were thermally stable ( $T_{dec} = 134\text{ }^{\circ}\text{C}$  to  $307\text{ }^{\circ}\text{C}$ ) and unlike the other complexes, the coordination mode of acetate anion in **Complex 5** were chelating and bridging between the Mn(II) centres. This will results a more planar structure and enhance the anisotropy molecular shape. Hence, only **Complex 5** was mesomorphic.

**Table 4.3** Analytical results for metal(II) complexes of *H<sub>2</sub>L1*

<b>Complex</b>		<b>1</b>	<b>2</b>	<b>3</b>	<b>4</b>	<b>5</b>
<b>Chemical Formula</b>		[Cu(L1)] <sub>2</sub> .H <sub>2</sub> O	[Ni <sub>2</sub> (CH <sub>3</sub> COO) <sub>2</sub> (L1)].3H <sub>2</sub> O	[Co <sub>2</sub> (CH <sub>3</sub> COO) <sub>2</sub> (L1)].2H <sub>2</sub> O	[Fe(CH <sub>3</sub> COO)(L1)]	[Mn <sub>2</sub> (CH <sub>3</sub> COO) <sub>4</sub> (L1)].5H <sub>2</sub> O
<b>CH<sub>3</sub>COO mode</b>		-	chelating			bridging
<b>Geometry</b>		square pyramidal	tetrahedral		octahedral	
<b>E<sub>o</sub></b> <b>(eV)</b>	<b>absorption</b>	3.53	3.30	2.82	3.30	2.81
	<b>emission</b>	3.82	3.38	2.96	3.02	3.01
<b>Stokes shift (nm)</b> <b>CT, <i>d-d</i></b>		44, 9	35, 8	54, 8	54, 22	42, 16
<b>τ (ns)</b>		1.0	1.0	1.0	1.0, 0.7	2.4, 0.8
<b>CV</b>		redox inactive	redox active	redox inactive		
<b>μ<sub>eff</sub> (BM)</b>		1.80	4.13	6.13	4.95	23 % HS, 77 % LS
<b>T<sub>dec</sub> (°C)</b>		268	307	247	134	224
<b>Mesomorphism</b>		Non-mesomorphic				Mesomorphic

### 4.3 H<sub>2</sub>L2 and its Metal(II) Complexes

#### 4.3.1 H<sub>2</sub>L2

H<sub>2</sub>L2 (**Figure 4.49**) was obtained as a yellow powder from the reaction of H<sub>2</sub>N(CH<sub>2</sub>)<sub>8</sub>NH<sub>2</sub> and 2,4-(HO)<sub>2</sub>C<sub>6</sub>H<sub>3</sub>CHO in ethanol. Its yield was 91.3%, and it was soluble in ethyl acetate but insoluble in other common organic solvents.

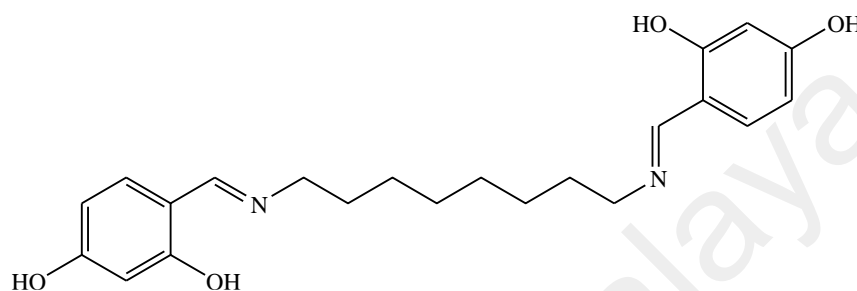


**Figure 4.49** Structural formula of H<sub>2</sub>L2

#### (a) Structural deduction

The results from the **elemental analyses** (67.93 % C, 7.32 % H, 7.14 % N) were in good agreement with the chemical formula C<sub>22</sub>H<sub>28</sub>N<sub>2</sub>O<sub>4</sub> (384.47 g mol<sup>-1</sup>; 68.73% C, 7.34% H, 7.29% N). Its **FTIR** spectrum (**Figure 4.50**) shows a broad peak for OH group at 3201 cm<sup>-1</sup>, two medium peaks for  $\nu_{\text{as}}\text{CH}_2$  and  $\nu_{\text{s}}\text{CH}_2$  at 2938 cm<sup>-1</sup> and 2852 cm<sup>-1</sup>, respectively, and a sharp peak for C=N at 1639 cm<sup>-1</sup>. Its **<sup>1</sup>H-NMR** spectrum is shown in **Figure 4.51**, and the peak assignments are given in **Table 4.4**.

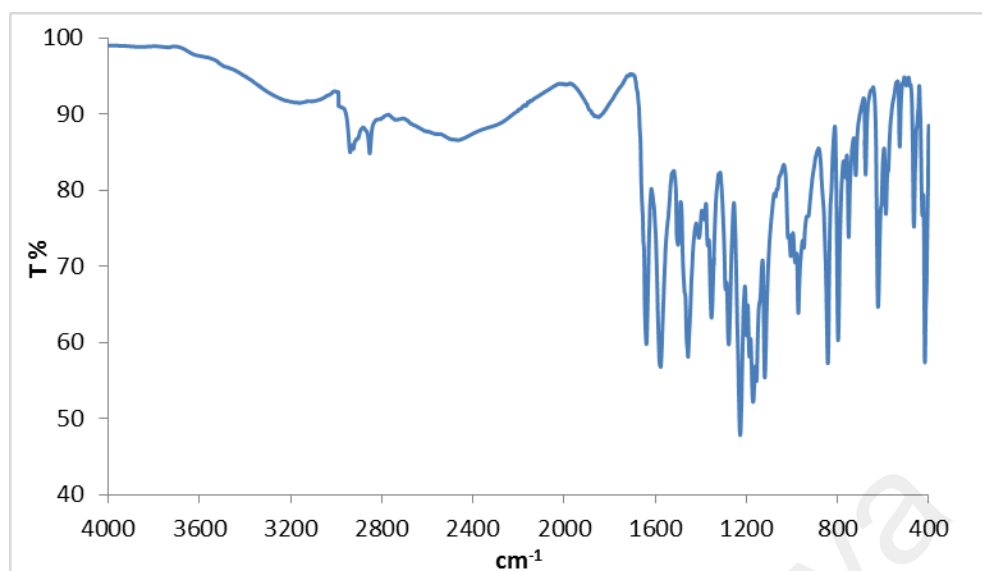


**Figure 4.50** The FTIR spectrum of H<sub>2</sub>L2

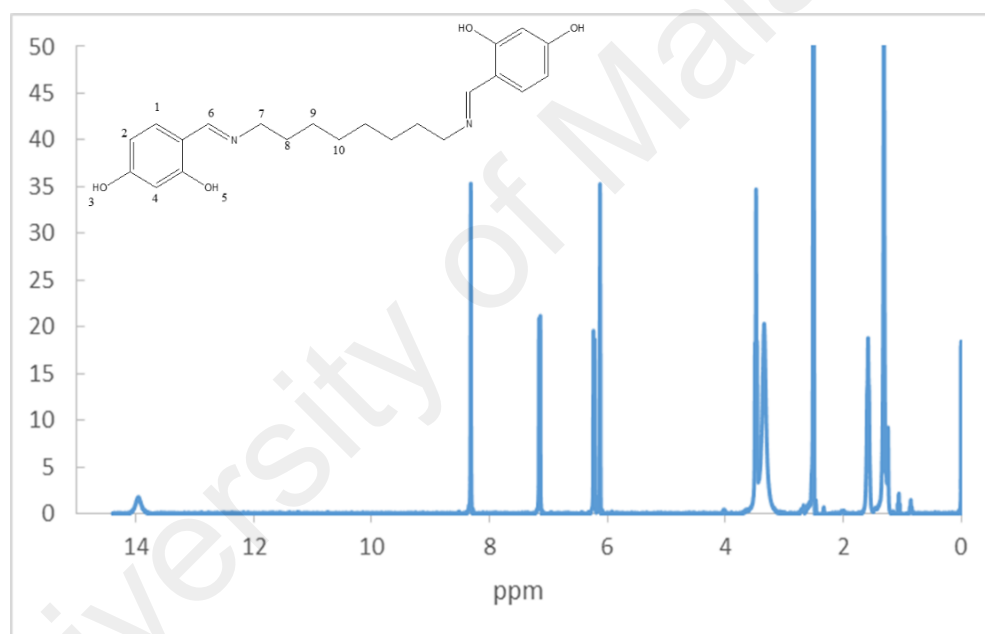


**Figure 4.51** The <sup>1</sup>H-NMR spectrum of H<sub>2</sub>L2

**Table 4.4** The <sup>1</sup>H-NMR data and peak assignment for H<sub>2</sub>L2

Chemical shift (ppm)	Integral ratio	Multiplicity	Assignment
1.04-1.31	5.74	multiplet	H-8, H-9, H-10
3.34-3.50	4.07	multiplet	H-4, H-7
6.12	0.97	singlet	H-3
6.21-6.24	0.92	doublet	H-1, H-2
7.16	1.03	singlet	H-6
8.32	1.00	singlet	H-5

(b) *Mesomorphic properties*

Its DSC spectrum (**Figure 4.52**) was recorded for a heating-cooling cycle from 25 °C to 220 °C. On heating, there was an endothermic peak at 200.4 °C ( $\Delta H = +47.6 \text{ kJ mol}^{-1}$ ) assigned for crystal-to-isotropic liquid transition. However on cooling, there were no peaks observed.

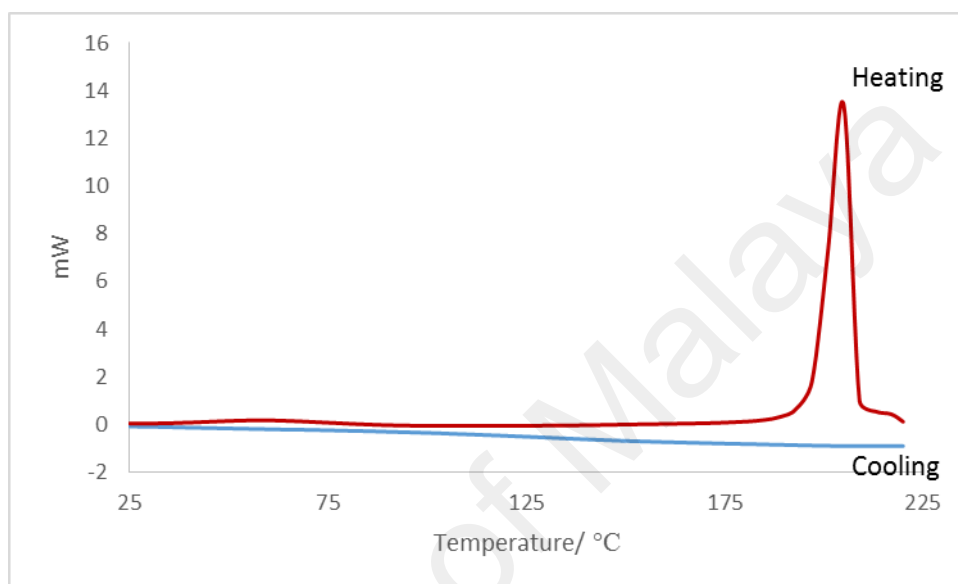


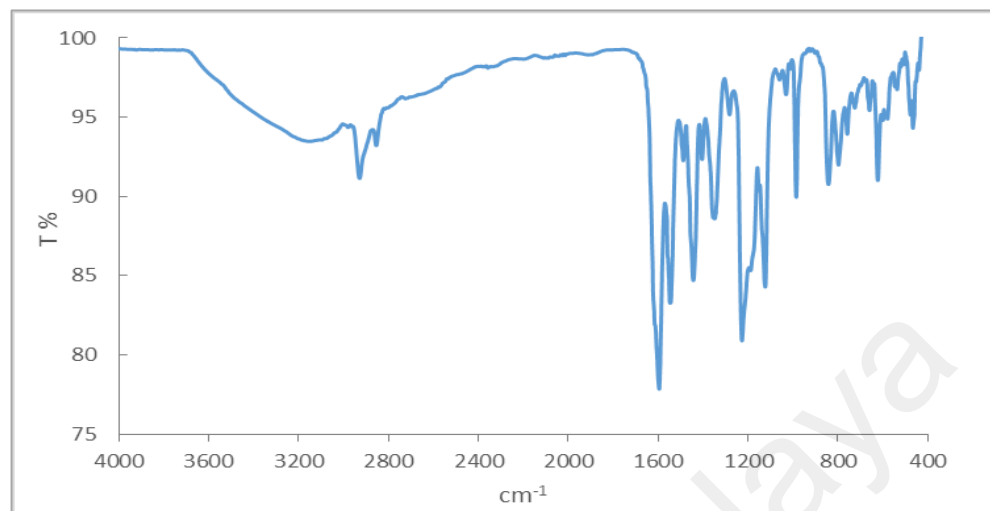
**Figure 4.52** DSC of H<sub>2</sub>L<sub>2</sub>

Viewed under **OPM**, which was recorded for a heating-cooling cycle from 25 °C to 220 °C, there were no optical textures observed. Hence, this ligand did not exhibit mesomorphism.

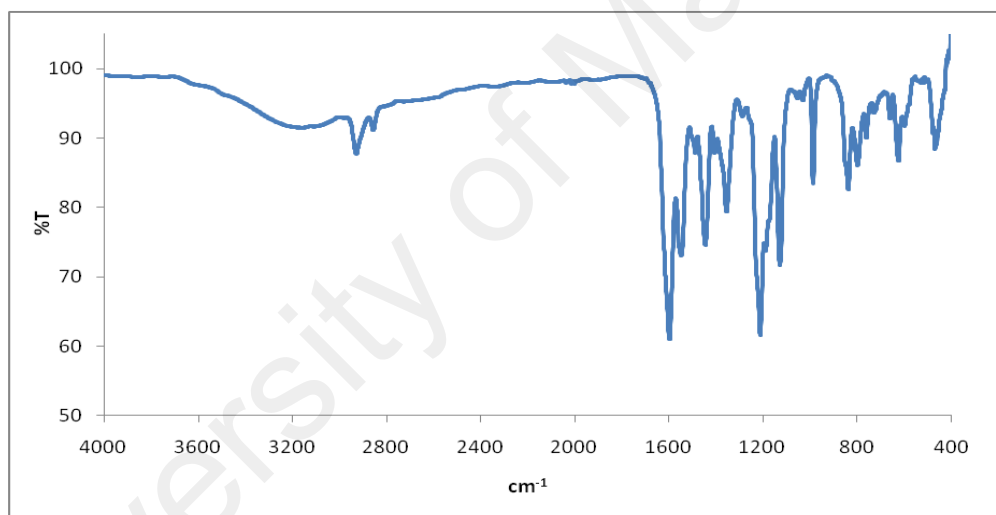
#### 4.3.2 $[\text{Cu}(\text{CH}_3\text{COO})(\text{HL}_2)(\text{H}_2\text{O})] \cdot \text{H}_2\text{O}$

The Cu(II) complex of H<sub>2</sub>L<sub>2</sub> was also synthesised by two methods involving step-wise and one-pot reactions. Both methods gave khaki green powders (**Complex 6**), and the yield was 49.6% (step-wise method) and 80.4% (one-pot method). Both powders were soluble in DMSO, dimethylformamide (DMF), and tetrahydrofuran (THF), but insoluble in water and other common organic solvents. The CHN elemental analyses and FTIR spectra of both powders are similar (**Figure 4.53**). From these, it may be concluded that the

products obtained from both methods are the same. Thus, the instrumental results are discussed for the product obtained from the one-pot method only.



(a)



(b)

**Figure 4.53** FTIR spectrum of **Complex 6**: (a) step-wise method, and (b) one-pot method.

*(a) Structural deduction*

Based on the instrumental data discussed below, the structural formula of **Complex 6** is  $[\text{Cu}(\text{CH}_3\text{COO})(\text{HL}_2)(\text{H}_2\text{O})] \cdot \text{H}_2\text{O}$ . Hence, unlike the **Complex 1**, it was mononuclear with one  $\text{CH}_3\text{COO}^-$  ion and one  $\text{HL}_2^-$  ion as ligands.

The results from the **elemental analyses** (52.49% C, 5.78% H, 5.25% N) were in good agreement with the chemical formula  $\text{CuC}_{24}\text{H}_{34}\text{N}_2\text{O}_8$  (542.08 g mol<sup>-1</sup>; 53.18% C, 6.32% H, 5.17% N).

Its FTIR spectrum (Figure 4.53) shows peaks as similarly found and assigned for previously discussed complexes at  $3159\text{ cm}^{-1}$ ,  $2927\text{ cm}^{-1}$ ,  $2855\text{ cm}^{-1}$ ,  $1593\text{ cm}^{-1}$ ,  $1547\text{ cm}^{-1}$  and  $1444\text{ cm}^{-1}$ , respectively. From the latter two peaks, the  $\Delta$  value was  $103\text{ cm}^{-1}$ , suggesting a chelating binding mode for  $\text{CH}_3\text{COO}^-$  ligand. Also found are peaks for coordinated  $\text{H}_2\text{O}$  at  $836\text{ cm}^{-1}$  [12], Cu-N at  $517\text{ cm}^{-1}$ , and Cu-O at  $467\text{ cm}^{-1}$  [103].

Its UV-visible spectrum (Figure 4.54), recorded in DMSO, shows a *d-d* band at  $632\text{ nm}$  ( $\epsilon_{\text{max}} = 142\text{ M}^{-1}\text{ cm}^{-1}$ ) and a LMCT band at  $440\text{ nm}$  ( $\epsilon_{\text{max}} = 1398\text{ M}^{-1}\text{ cm}^{-1}$ ). The position of the *d-d* band suggests a square pyramidal geometry at Cu(II) centre.

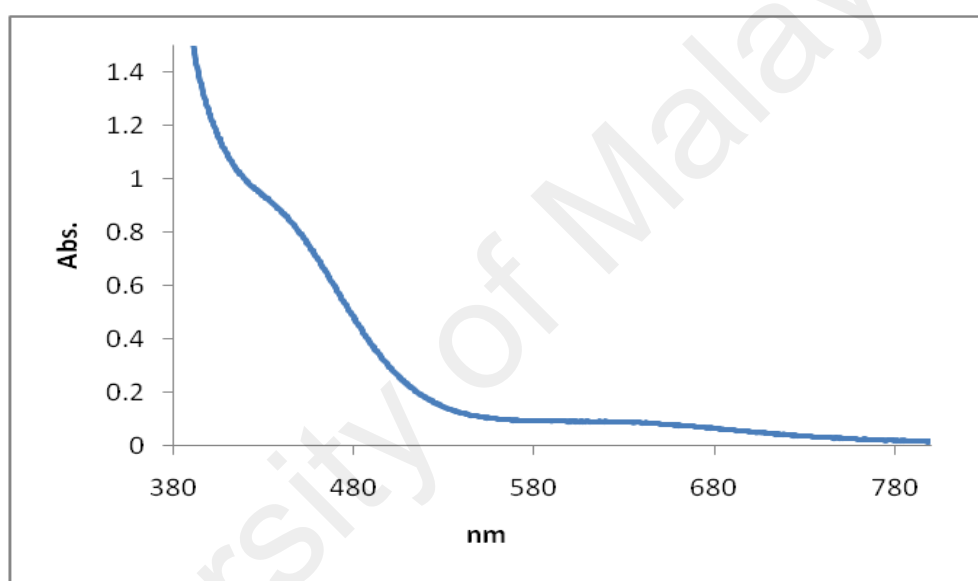


Figure 4.54 UV-visible spectrum of Complex 6

Combining the results of elemental analyses, and FTIR and UV-vis spectroscopies, the proposed structural formula for Complex 6 ( $[\text{Cu}(\text{CH}_3\text{COO})(\text{HL}_2)(\text{H}_2\text{O})]\cdot\text{H}_2\text{O}$ ) is shown in Figure 4.55.

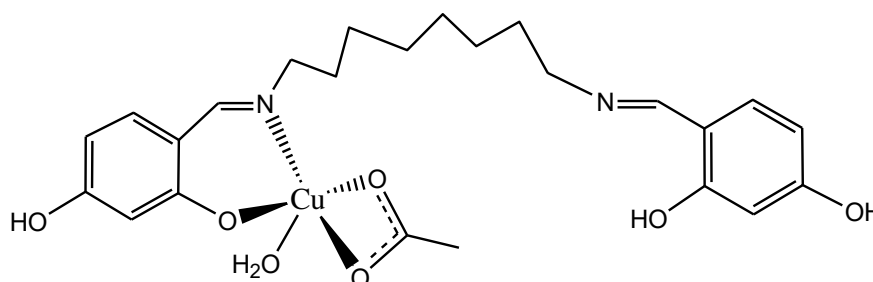
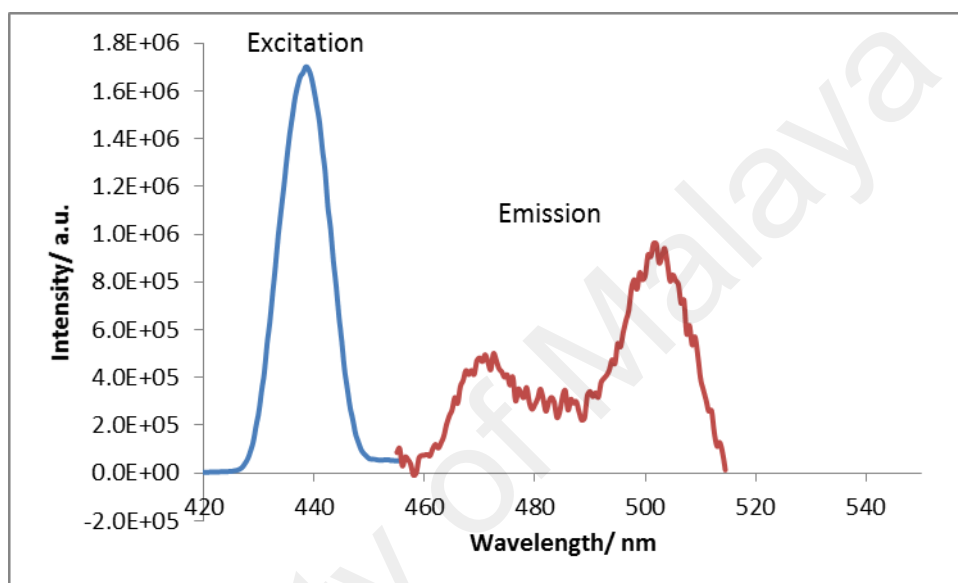


Figure 4.55 Proposed structure for Complex 6. Lattice  $\text{H}_2\text{O}$  is not shown

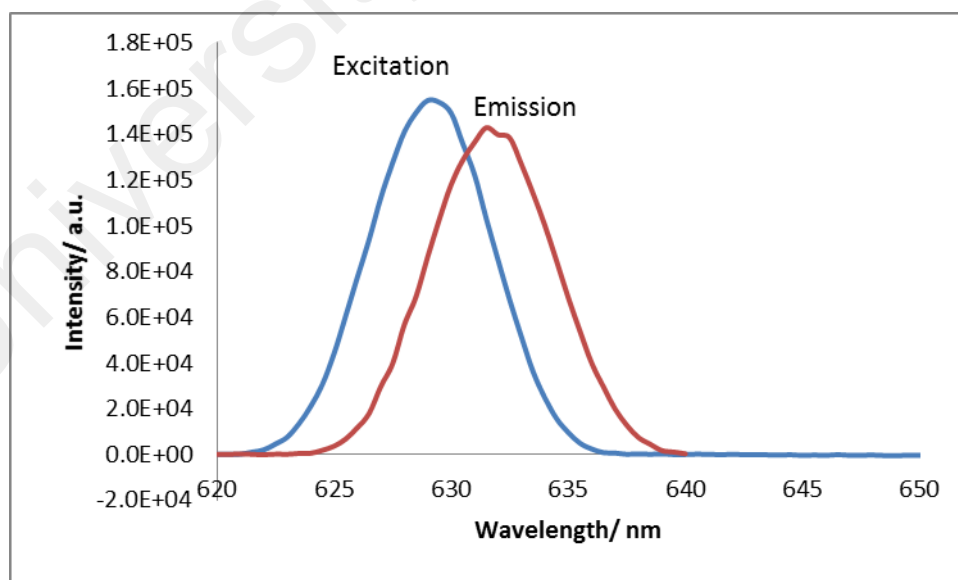
(b) Determination of bandgaps

Its  $E_o$  value, calculated as before from its UV-vis spectrum, was 2.29 eV ( $\lambda = 542$  nm).

Its **fluorescence** spectra (**Figure 4.56**) were recorded in DMSO. Upon excitation at 438 nm (LMCT band), it shows two emission peaks at 472 nm and 501 nm, and upon excitation at 629 nm (*d-d* band), it shows an emission peak at 632 nm. The Stokes shifts were 34 nm, 63 nm and 3 nm, respectively, and its  $E_o$  was 2.41 eV ( $\lambda = 515$  nm).



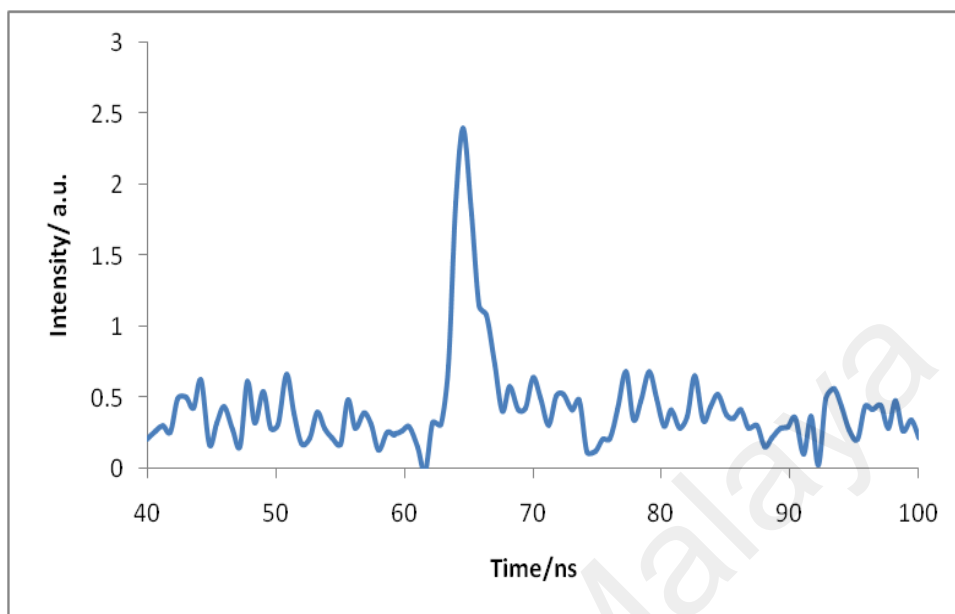
(a)



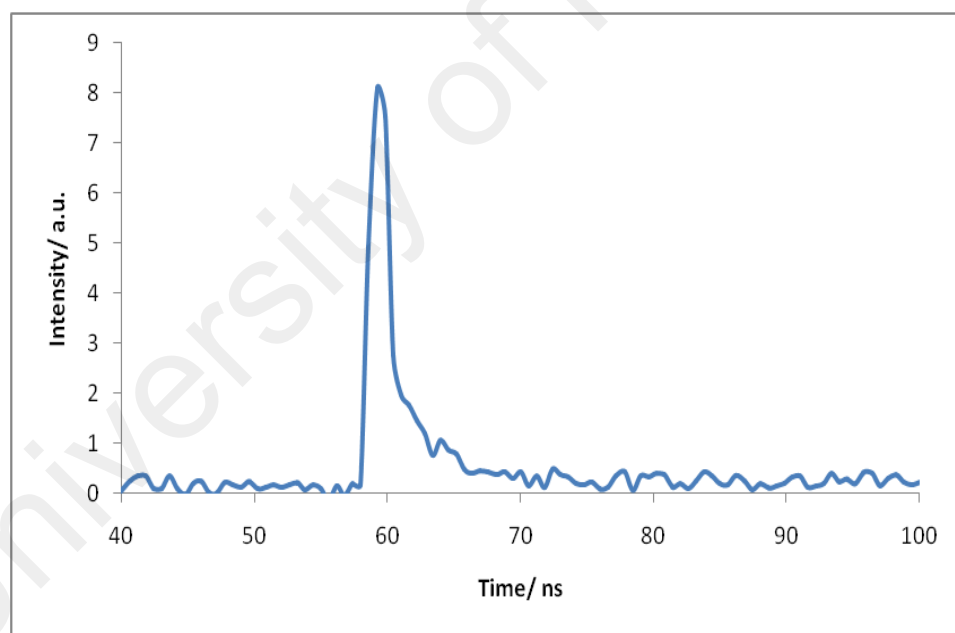
(b)

**Figure 4.56** Emission spectra of **Complex 6** after excitation at: (a)  $\lambda = 438$  nm, and (b)  $\lambda = 629$  nm.

Its  $\tau$  value, calculated from its decay curve (**Figure 4.57**) was 2.0 ns ( $\lambda_{\text{emission}} = 501$  nm and 632 nm).



(a)



(b)

**Figure 4.57** Fluorescence decay of **Complex 6** at (a)  $\lambda_{\text{emission}} = 501$  nm, and (b)  $\lambda_{\text{emission}} = 632$  nm.

Its **CV** was recorded cathodically in DMSO at a scan rate of  $50 \text{ mV s}^{-1}$  in the potential range of +1.0 V to -1.0 V. The voltammogram (**Figure 4.58**) shows a cathodic peak at -0.78 V, assigned to the reduction of [Cu(II)] to [Cu(I)], and the

corresponding anodic peak at +0.45 V, assigned to the oxidation of [Cu(I)] to [Cu(II)]. The  $\Delta E_p$  was 1230 mV, indicating a quasireversible redox reaction ( $\Delta E_p > 59$  mV at 30 °C), and its  $I_{pa}/I_{pc}$  ratio was 0.8, indicating the reduced complex was chemically unstable. The HOMO and LUMO of the complex was 0.11 V and -0.60 V, respectively. Hence, its  $E_e$  value was 0.71 eV.

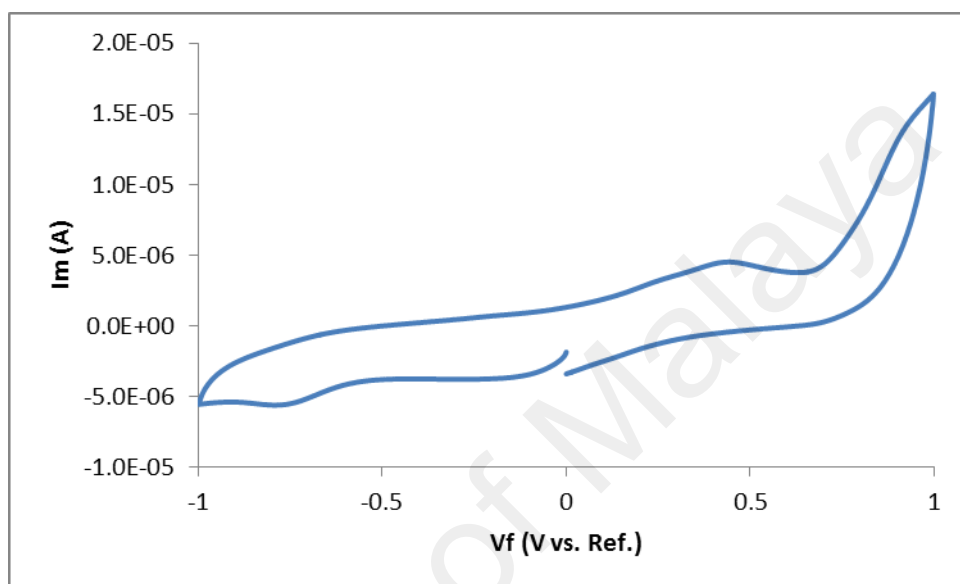


**Figure 4.58** Cyclic voltammogram for **Complex 6**

*(c) Magnetic properties*

Its  $\mu_{\text{eff}}$  value, calculated as previously done using the following data:  $M = 542.08$  g mol<sup>-1</sup>,  $\chi_g = 2.5 \times 10^{-6}$  cm<sup>3</sup> g<sup>-1</sup>,  $\chi_m = 1.34 \times 10^{-3}$  cm<sup>3</sup> mol<sup>-1</sup>,  $\chi_{\text{dia}} = -2.00 \times 10^{-4}$  cm<sup>3</sup> mol<sup>-1</sup> and  $\chi_m^{\text{corr}} = 1.54 \times 10^{-3}$  cm<sup>3</sup> mol<sup>-1</sup>, was 1.88 BM at 298 K. This value is the same as **Complex 1** (1.89 B.M) and may be similarly explained.

*(d) Thermal properties*

Its TGA trace (**Figure 4.59**) shows an initial weight loss of 3.6% from about 51 °C to 145 °C due to the evaporation of lattice H<sub>2</sub>O (calculated, 3.3%). The next weight loss of 4.4% (219 °C to 303 °C) and 10.3% (302 °C to 458 °C) were assigned to the evaporation of coordinated water molecule (calculated, 3.3%) and the decomposition of CH<sub>3</sub>COO<sup>-</sup> ion (calculated, 10.9%), respectively. This was followed by a gradual weight loss of 38.3% at

458 °C up to 900 °C (the maximum temperature of the instrument), assigned to the decomposition of HL2<sup>-</sup>, suggesting incomplete decomposition of the organic ligand. Hence, **Complex 6** was thermally stable up to 219 °C.

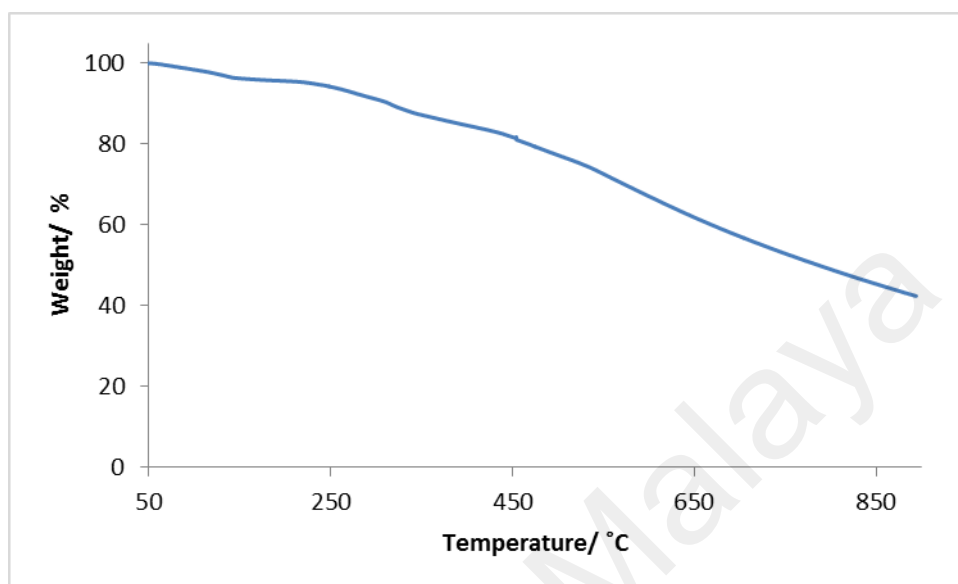


**Figure 4.59** TGA of **Complex 6**

(e) *Mesomorphic properties*

Its DSC spectrum (**Figure 4.60**) was recorded for a heating-cooling cycle from 25 °C to 190 °C. There was an endothermic peak at 163.1 °C ( $\Delta H = +15.5 \text{ kJ mol}^{-1}$ ) assigned to the breaking of H-bonds. However, there were no peaks on cooling.

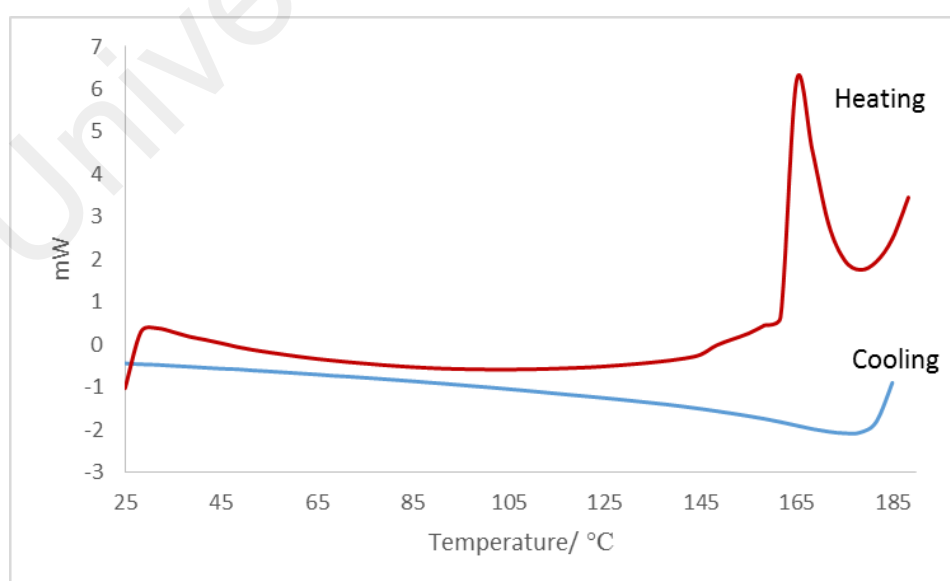


**Figure 4.60** DSC of **Complex 6**

Viewed under **OPM**, which was recorded for heating-cooling cycle from 25 °C to 190 °C, the complex did not show any optical textures. Hence, this complex did not exhibit mesomorphism.

#### 4.3.3 $[Ni_2(CH_3COO)_2(L2)].4H_2O$

The Ni(II) complex of H<sub>2</sub>L<sub>2</sub> was also synthesised by the one-pot method involving 2,4-dihydroxybenzaldehyde, 1,8-diaminooctane and  $[Ni(CH_3COO)_2].4H_2O$  in ethanol. The product was a green powder, and the yield was 75.8%. It was insoluble in most organic solvents.

##### (a) Structural deduction

Based on the same instrumental analyses, it is proposed that the structural formula of the green powder was  $[Ni_2(CH_3COO)_2(L2)].4H_2O$  (**Complex 7**). Hence, unlike the corresponding Cu(II) (**Complex 6**), it was dinuclear and has two acetate ions and one L<sup>2-</sup> ion coordinated to Ni(II) ion.

The results from the **elemental analyses** (45.32% C, 5.97% H, 3.61% N) were in good agreement with the proposed chemical formula Ni<sub>2</sub>C<sub>26</sub>H<sub>40</sub>N<sub>2</sub>O<sub>12</sub> (689.99 g mol<sup>-1</sup>; 45.26% C, 5.84% H, 4.06% N).

Its **FTIR** spectrum (**Figure 4.61**) shows peaks for the expected functional groups and bonds at similar wavenumbers (3128 cm<sup>-1</sup>, 2923 cm<sup>-1</sup>, 2854 cm<sup>-1</sup>, 1575 cm<sup>-1</sup>, 1541 cm<sup>-1</sup> and 1441 cm<sup>-1</sup>) as the corresponding Cu(II) complex. From the latter peaks, the  $\Delta \nu_{COO}$  value was 100 cm<sup>-1</sup>, suggesting chelating binding mode for CH<sub>3</sub>COO<sup>-</sup> ligand.

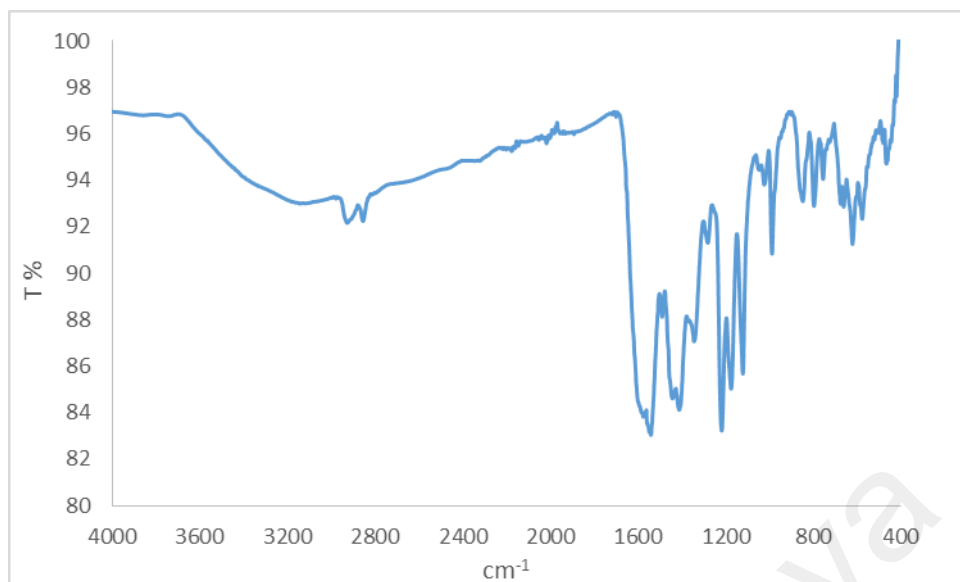


**Figure 4.61** FTIR spectrum for **Complex 7**

Its **UV-visible** spectrum (**Figure 4.62**), recorded in the solid state, shows *d-d* bands at 1123 nm and 651 nm, suggesting that the geometry of Ni(II) in the complex was tetrahedral [104].

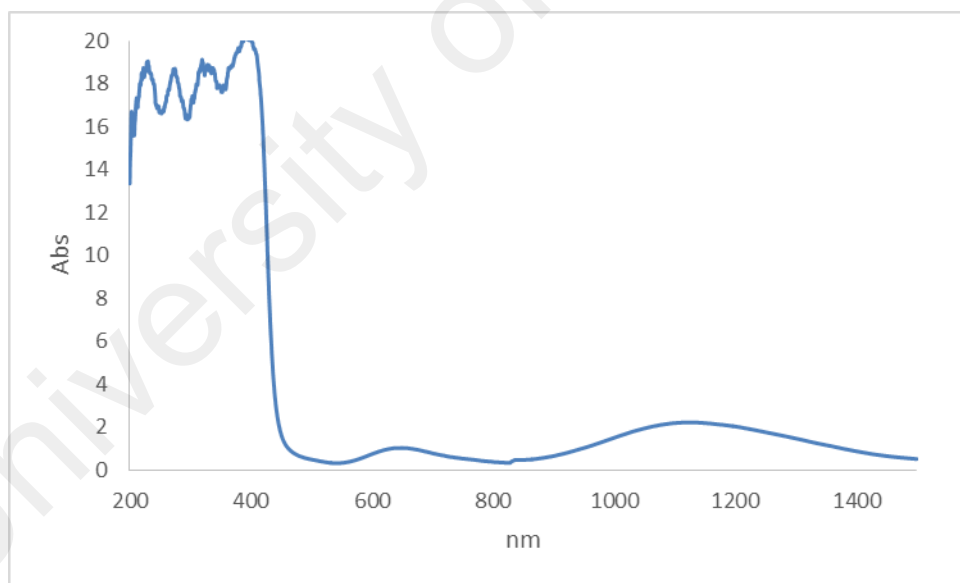


**Figure 4.62** UV-visible spectrum of **Complex 7**

Combining the results of elemental analyses, and FTIR and UV-vis spectroscopies, the proposed structural formula for **Complex 7** is shown in **Figure 4.63**.

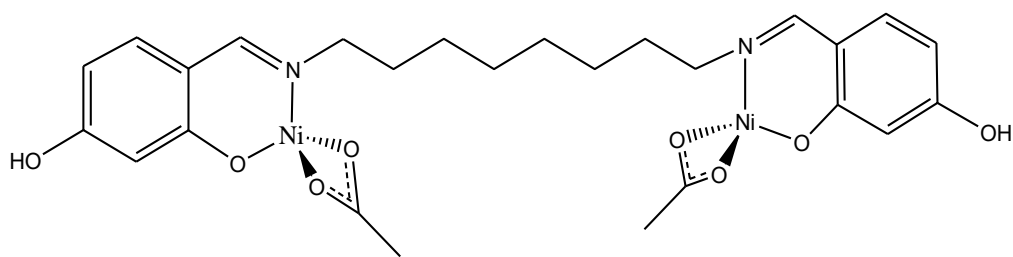


**Figure 4.63** Proposed structure for **Complex 7** (lattice H<sub>2</sub>O molecules are omitted)

*(b) Determination of bandgaps*

Its  $E_o$  value, calculated as before from its UV-vis spectrum, was 2.75 eV ( $\lambda = 451$  nm).

Fluorescence spectroscopy and cyclic voltammetry could not be performed for the complex as it was insoluble in most common solvents.

*(c) Magnetic properties*

Its  $\mu_{\text{eff}}$  value, calculated as previously done using the following data:

FM = 689.99 g mol<sup>-1</sup>,  $\chi_g = 9.90 \times 10^{-6}$  cm<sup>3</sup> g<sup>-1</sup>,  $\chi_m = 6.83 \times 10^{-3}$  cm<sup>3</sup> mol<sup>-1</sup>,  $\chi_{\text{dia}} = -2.66 \times 10^{-4}$  cm<sup>3</sup> mol<sup>-1</sup> and  $\chi_m^{\text{corr}} = 7.10 \times 10^{-3}$  cm<sup>3</sup> mol<sup>-1</sup>, was 4.15 BM at 298 K.

This value lies in the range reported for a dinuclear complex with tetrahedral Ni(II) ions [85].

*(d) Thermal properties*

Its TGA trace (**Figure 4.64**) shows an initial weight loss of 8.1% from about 50 °C to 131 °C due to evaporation of lattice H<sub>2</sub>O (calculated, 10.4%). The lower than calculated value suggests loss of lattice H<sub>2</sub>O molecules during storage. The next weight loss of 75.8% from 234 °C to 758 °C was assigned to decomposition of L2<sup>2-</sup> and CH<sub>3</sub>COO<sup>-</sup> ions (calculated, 72.5%). The amount of residue at temperatures above 637 °C was 16.1%, which is in a good agreement with the calculated value of 21.6 %, assuming pure NiO [105]. Hence, **Complex 7** was thermally stable up to 234 °C.

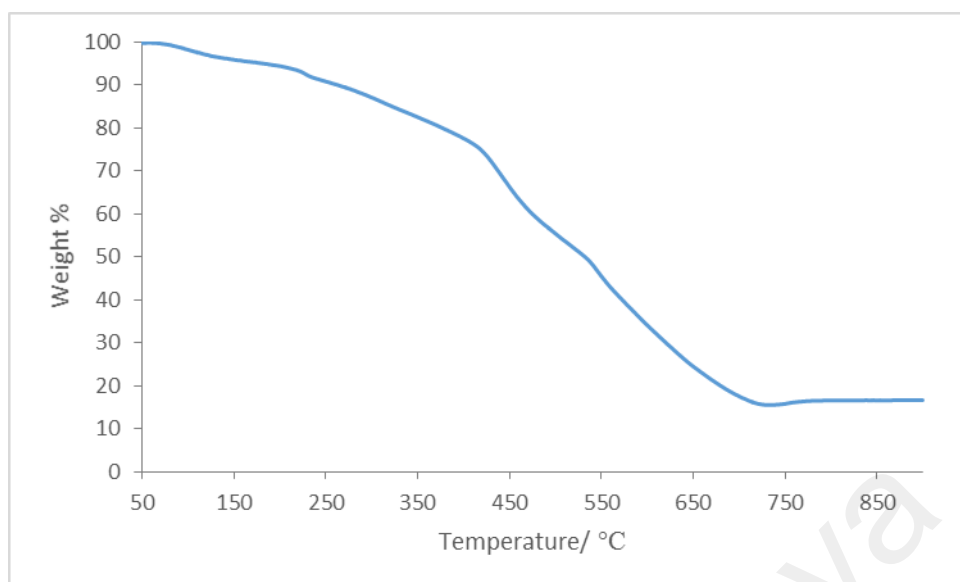


**Figure 4.64** TGA of **Complex 7**

*(e) Mesomorphic properties*

Its **DSC** spectrum (**Figure 4.65**) was recorded for a heating-cooling cycle from 25 °C to 200 °C. On heating, there were two overlapping endothermic peaks at 152.9 °C ( $\Delta H = +13.4 \text{ kJ mol}^{-1}$ ) and 183.4 °C ( $\Delta H = +9.4 \text{ kJ mol}^{-1}$ ), assigned as the hydrolysis of C=N and the breaking of H-bonds, respectively. On cooling, there were no peaks.

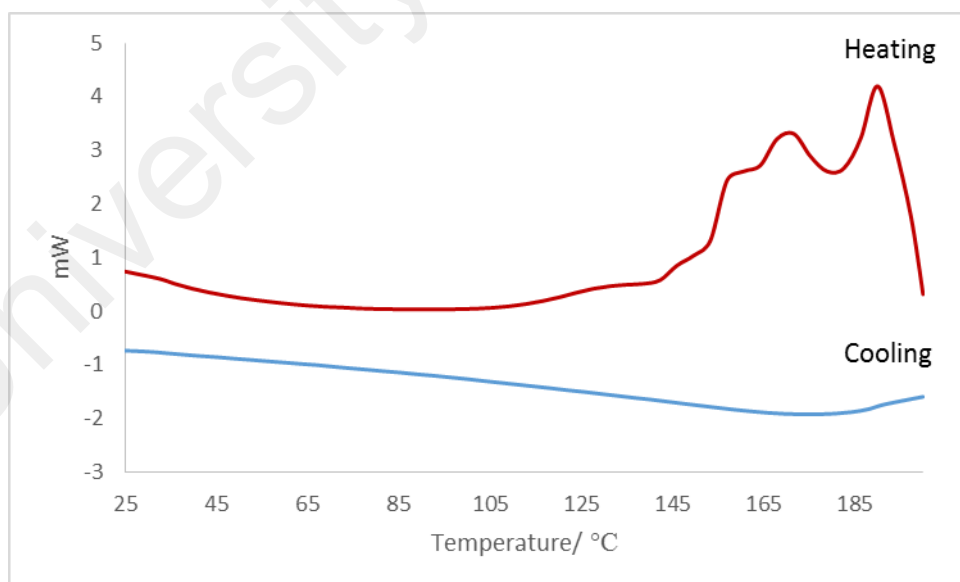


**Figure 4.65** DSC of **Complex 7**

Viewed under **OPM**, it was recorded for heating-cooling cycle from 25 °C to 200 °C. The complex was did not show any phase transitions. Hence, this complex did not exhibit mesomorphism.

#### 4.3.4 $[Co_2(CH_3COO)_2(L2)].H_2O$

The Co(II) complex of H<sub>2</sub>L<sub>2</sub> was also synthesized by the one-pot method, involving 2,4-dihydroxybenzaldehyde, 1,8-diaminooctane and  $[Co(CH_3COO)_2].4H_2O$  in ethanol. The product was a black powder (**Complex 8**), and the yield was 52.0%. It was insoluble in most common organic solvents.

##### (a) Structural deduction

Based on the same instrumental analyses, it is proposed that the structural formula of **Complex 8** is  $[Co_2(CH_3COO)_2(L2)].H_2O$ , which is similar to **Complex 7** ( $[Ni_2(CH_3COO)_2(L2)].4H_2O$ ).

The results from the **elemental analyses** (50.07% C, 5.84% H, 4.55% N) were in good agreement with the proposed chemical formula  $Co_2C_{26}H_{34}N_2O_9$  (636.42 g mol<sup>-1</sup>; 49.07% C, 5.38% H, 4.40 % N).

Its **FTIR** spectrum (**Figure 4.66**) shows peaks for the expected functional groups and bonds at similar wavenumbers (3223 cm<sup>-1</sup>, 2922 cm<sup>-1</sup>, 2852 cm<sup>-1</sup>, 1600 cm<sup>-1</sup>, 1539 cm<sup>-1</sup>, and 1436 cm<sup>-1</sup>) as the corresponding complexes. From the latter peaks, the  $\Delta \nu_{COO}$  value was 103 cm<sup>-1</sup>, suggesting chelating binding mode for CH<sub>3</sub>COO<sup>-</sup> ion.

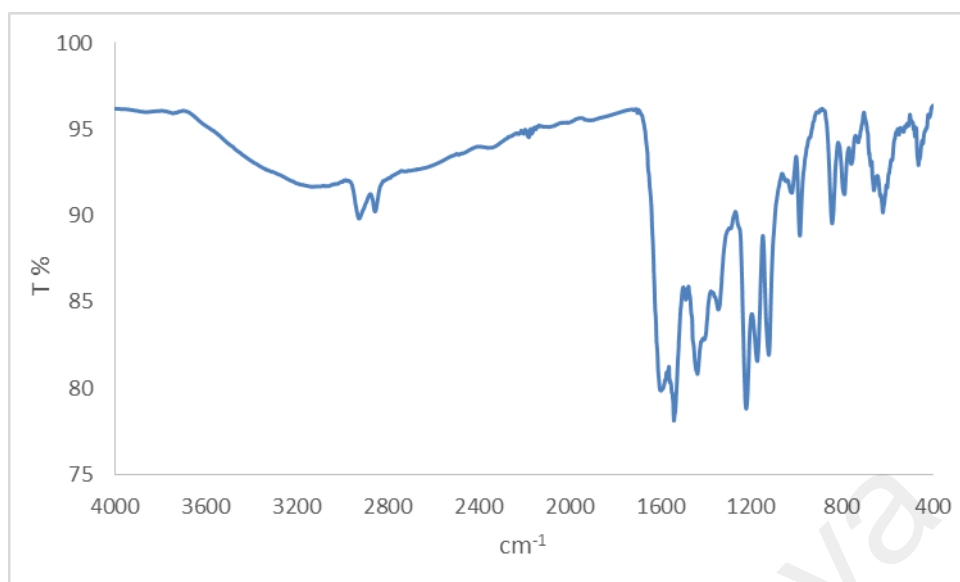


**Figure 4.66** FTIR spectrum for **Complex 8**

Its UV-visible spectrum (**Figure 4.67**), recorded in the solid state, show *d-d* bands at 1177 nm, 950 nm and 587 nm, suggesting that the geometry of Co(II) in the complex was tetrahedral [106].

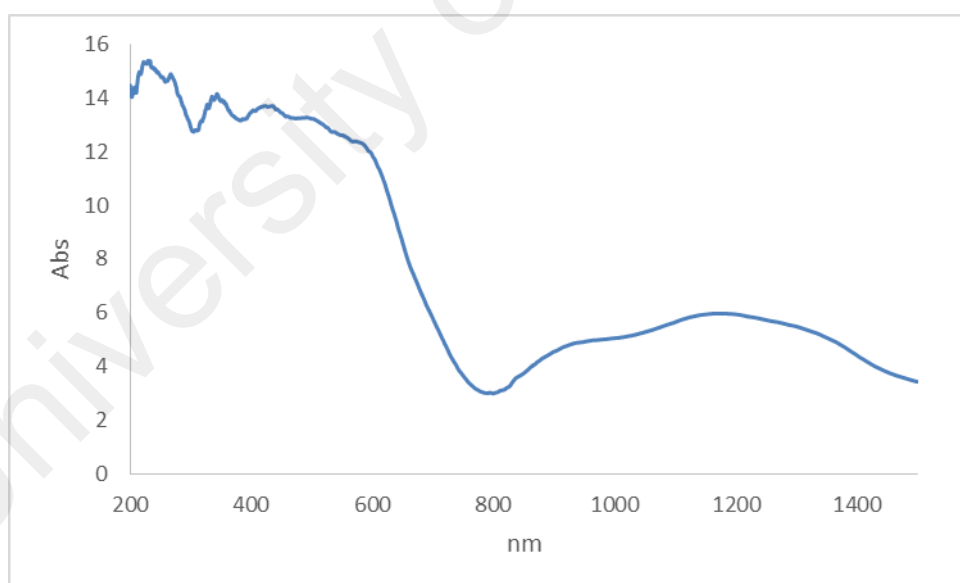


**Figure 4.67** UV-visible spectrum of **Complex 8**

(b) *Determination of bandgaps*

Its  $E_o$  value, calculated as before from its UV-vis spectrum, was 2.78 eV ( $\lambda = 445$  nm).

Fluorescence spectroscopy and cyclic voltammetry could not be performed for the complex as it was insoluble in most common solvents.

*(c) Magnetic properties*

Its  $\mu_{eff}$  value, calculated using the following data: FM = 636.42 g mol<sup>-1</sup>,  $\chi_g = 1.79 \times 10^{-5}$  cm<sup>3</sup> g<sup>-1</sup>,  $\chi_m = 1.14 \times 10^{-2}$  cm<sup>3</sup> mol<sup>-1</sup>,  $\chi_{dia} = -2.27 \times 10^{-4}$  cm<sup>3</sup> mol<sup>-1</sup>, and  $\chi_m^{corr} = 1.16 \times 10^{-2}$  cm<sup>3</sup> mol<sup>-1</sup>, was 5.24 B.M at 298 K. This value is comparable with the reported tetrahedral dinuclear Co(II) complexes [95,107].

*(d) Thermal properties*

Its TGA trace (**Figure 4.68**) shows an initial weight loss of 2.9% from about 50 °C to 123 °C due to evaporation of lattice H<sub>2</sub>O (calculated, 2.8%). The next weight loss of 77.3% from 197 °C to 795 °C is assigned to decomposition of L<sub>2</sub><sup>2-</sup> and CH<sub>3</sub>COO<sup>-</sup> ligands (calculated, 78.6%). The amount of residue at temperatures above 795 °C was 19.8%, which is in a good agreement with the calculated value of 23.5%, assuming pure CoO [96,100]. **Complex 8** was thermally stable up to 197 °C.

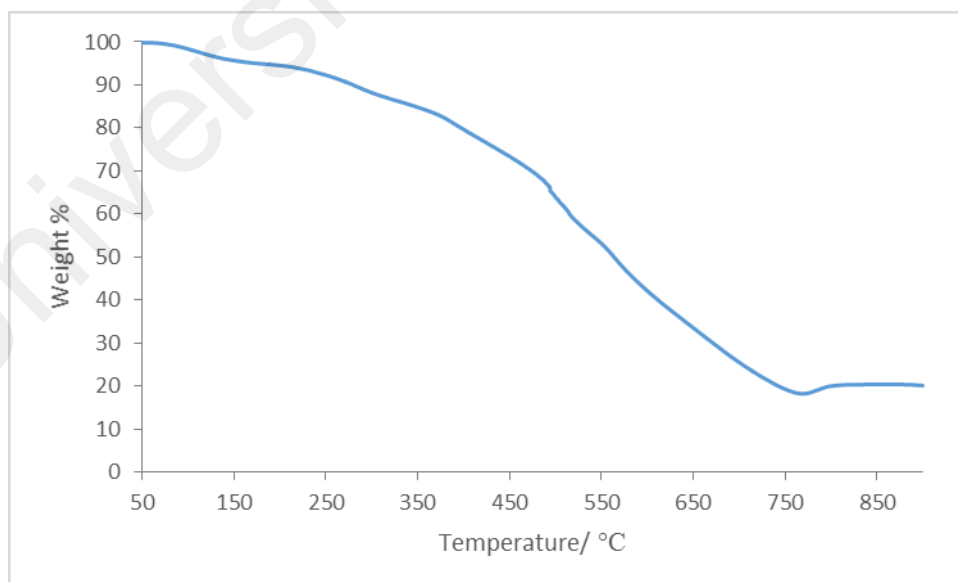


**Figure 4.68** TGA of **Complex 8**

(e) *Mesomorphic properties*

Its DSC spectrum (**Figure 4.69**) was recorded for heating-cooling cycle from 25 °C to 160 °C decomposed. On heating, there were two endothermic peaks at 109.4 °C ( $\Delta H = +2.7 \text{ kJ mol}^{-1}$ ) and 137.6 °C ( $\Delta H = +14.6 \text{ kJ mol}^{-1}$ ), assigned as hydrolysis of C=N and the breaking of H-bonds, respectively. On cooling, no peaks were observed.

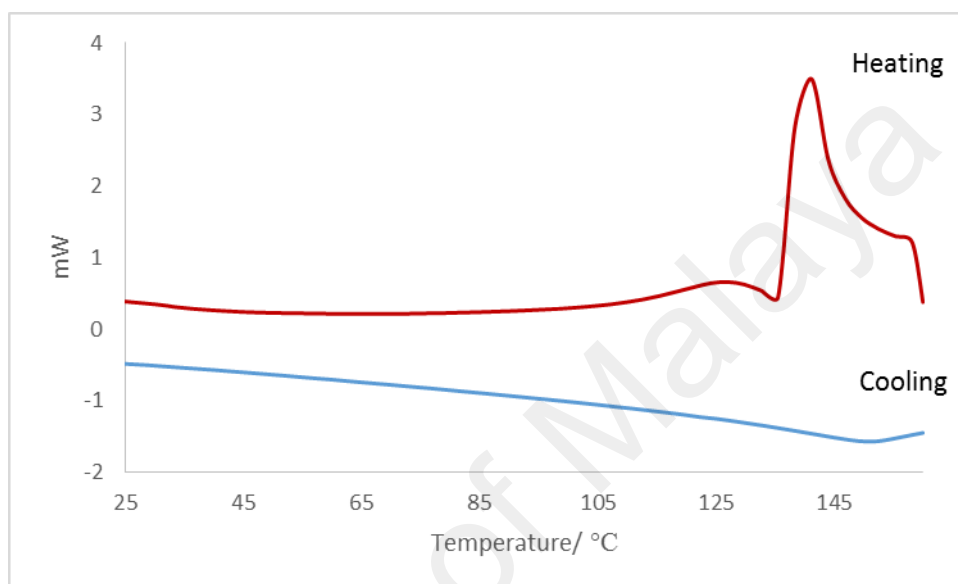


**Figure 4.69** DSC of **Complex 8**

Viewed under **OPM**, it was recorded for heating-cooling cycle from 25 °C to 160 °C. The complex did not show any phase transitions. Hence, this complex did not exhibit mesomorphism.

#### 4.3.5 $[\text{Fe}(\text{CH}_3\text{COO})(\text{HL}_2)].3\text{H}_2\text{O}$

The Fe(II) complex of H<sub>2</sub>L<sub>2</sub> was also synthesised by the one-pot method, involving 2,4-dihydroxybenzaldehyde, 1,8-diaminooctane and  $[\text{Fe}(\text{CH}_3\text{COO})_2]$  in ethanol. The product was a dark brown reddish powder, and the yield was 92.4%. It was insoluble in most common solvents.

(a) Structural deduction

Based on the same instrumental analyses, it is proposed that the structural formula of the complex was  $[\text{Fe}(\text{CH}_3\text{COO})(\text{HL}_2)] \cdot 3\text{H}_2\text{O}$  (**Complex 9**). Hence, its structural formula was similar to **Complex 4** ( $[\text{Fe}(\text{CH}_3\text{COO})(\text{HL}_1)]$ ).

The results from the **elemental analyses** (52.94% C, 6.45% H, 4.25% N) were in good agreement with the proposed chemical formula  $\text{FeC}_{24}\text{H}_{36}\text{N}_2\text{O}_9$  (552.40 g mol<sup>-1</sup>; 52.18% C, 6.57% H, 5.07% N).

Its **FTIR** spectrum (**Figure 4.70**) shows peaks for the expected functional groups and bonds at similar wavenumbers (3420 cm<sup>-1</sup>, 2928 cm<sup>-1</sup>, 2856 cm<sup>-1</sup>, 1611 cm<sup>-1</sup>, 1582 cm<sup>-1</sup>, and 1442 cm<sup>-1</sup>) as the corresponding complexes. From the latter peaks, the  $\Delta(\text{COO})$  value is 140 cm<sup>-1</sup>, suggesting chelating binding mode for  $\text{CH}_3\text{COO}^-$  ion.

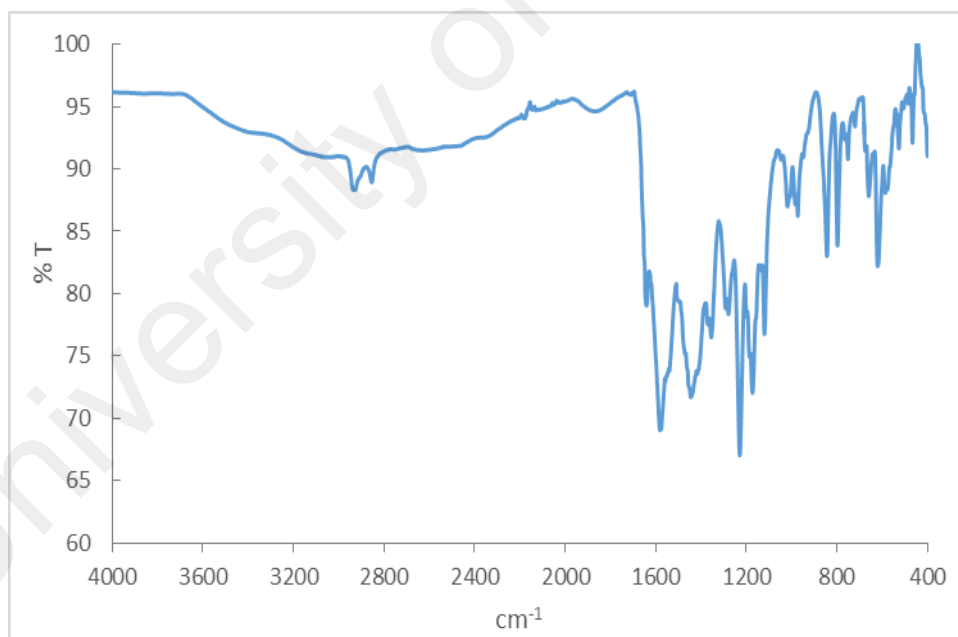


**Figure 4.70** FTIR spectrum for **Complex 9**

Its **UV-visible** spectrum (**Figure 4.71**), recorded in the solid state, shows *d-d* bands at 1013 nm, 477 nm and 356 nm, suggesting tetrahedral geometry at Fe(II) centre.

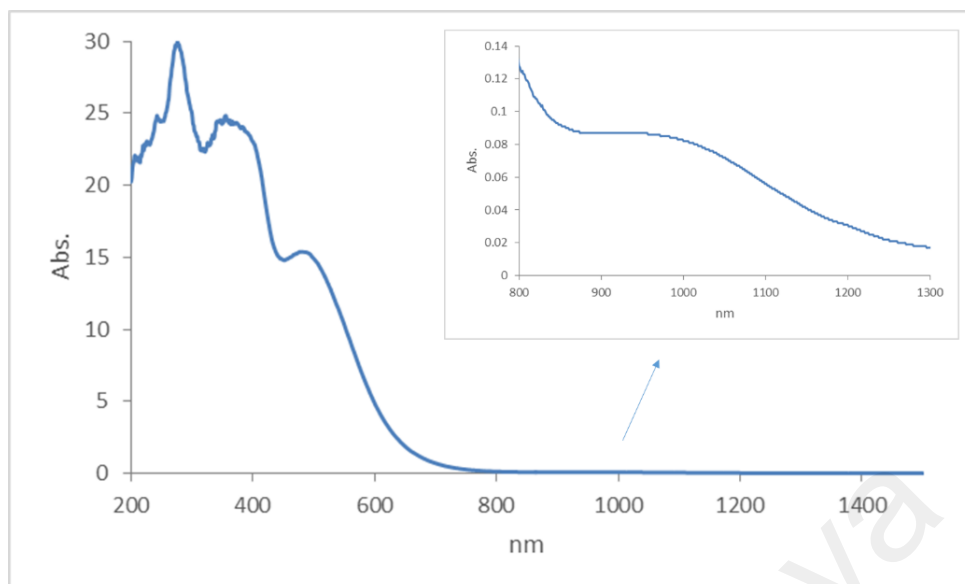


**Figure 4.71** UV-visible spectrum of **Complex 9**

Combining the results of elemental analyses and FTIR and UV-visible spectroscopies, the proposed structural formula of **Complex 9** is  $[\text{Fe}(\text{CH}_3\text{COO})(\text{HL}_2)] \cdot 3\text{H}_2\text{O}$  (**Figure 4.72**).

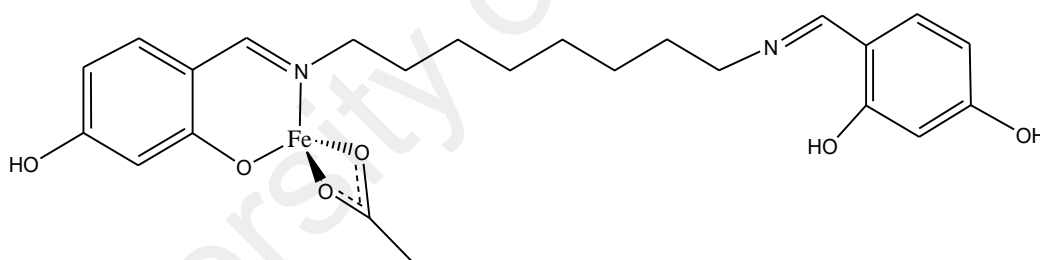


**Figure 4.72** Proposed structure for **Complex 9** (lattice  $\text{H}_2\text{O}$  is omitted)

*(b) Determination of bandgaps*

Its  $E_g$  value, calculated as before from its UV-vis spectrum, was 3.10 eV ( $\lambda = 400$  nm).

Fluorescence spectroscopy and cyclic voltammetry could not be performed as the complex was insoluble in most common solvents.

*(c) Magnetic properties*

Its  $\mu_{\text{eff}}$  value, calculated as previously done using the following data:

$$\text{FM} = 552.40 \text{ g mol}^{-1}, \chi_g = 1.81 \times 10^{-5} \text{ cm}^3 \text{ g}^{-1}, \chi_m = 9.88 \times 10^{-3} \text{ cm}^3 \text{ mol}^{-1},$$

$\chi_{\text{dia}} = -2.21 \times 10^{-4} \text{ cm}^3 \text{ mol}^{-1}$  and  $\chi_{\text{m}}^{\text{corr}} = 1.02 \times 10^{-2} \text{ cm}^3 \text{ mol}^{-1}$  was 4.93 BM at 298 K. The value is consistent with the proposed tetrahedral geometry at the Fe(II) center [108].

*(d) Thermal properties*

Its TGA trace **Figure 4.73**) shows an initial weight loss of 2.0% from about 50 °C to 108 °C due to evaporation of H<sub>2</sub>O (calculated 9.8%, suggesting some of the lattice H<sub>2</sub>O molecules were lost during storage). The next weight loss of 84.5% from 170 °C to 842 °C was assigned to decomposition of HL<sub>2</sub><sup>-</sup> and CH<sub>3</sub>COO<sup>-</sup> ions (calculated, 79.9%). The amount of residue at temperature 842 °C was 13.5%, which is in a good agreement with the calculated 13.0% (assuming pure FeO) [99]. Hence, **Complex 9** was thermally stable up to 170 °C.

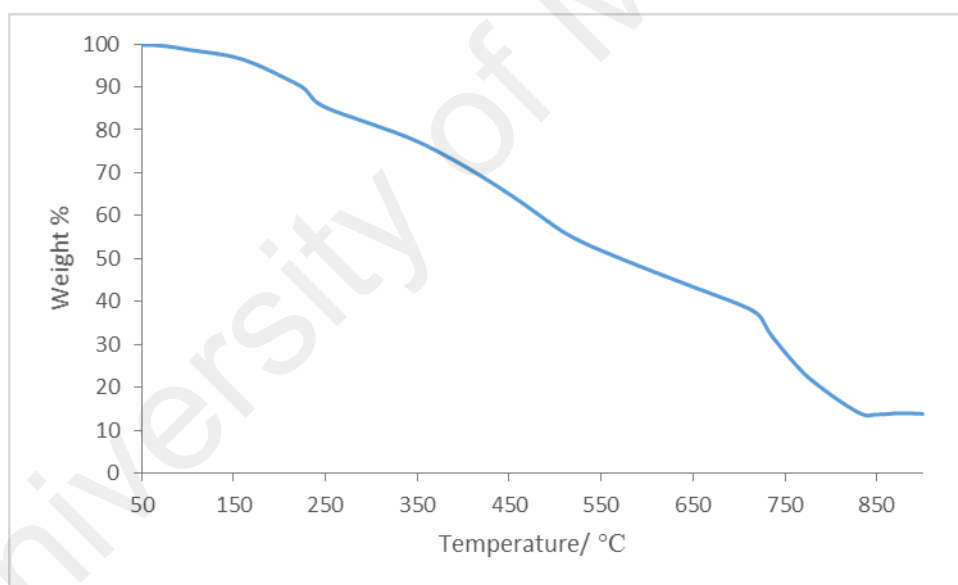


**Figure 4.73** TGA of **Complex 9**

*(e) Mesomorphic properties*

Its DSC spectrum (**Figure 4.74**) was recorded for a heating-cooling cycle from 25 °C to 150 °C. On heating, there was an endothermic peak at 131.1 °C ( $\Delta H = +9.3 \text{ kJ mol}^{-1}$ ) assigned as the breaking of H-bonds. On cooling, there were no peaks observed.

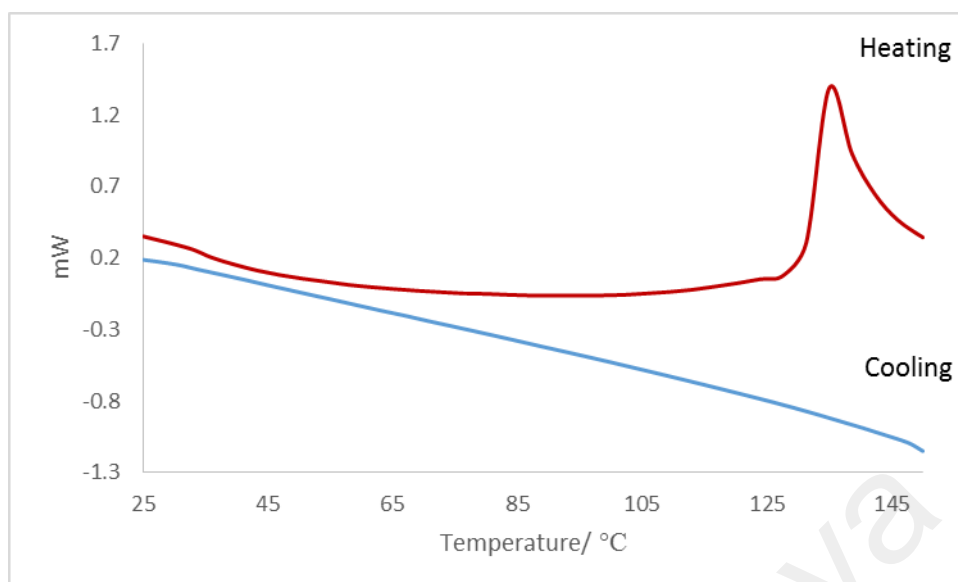


**Figure 4.74** DSC of **Complex 9**

Viewed under **OPM**, which was recorded for heating-cooling cycle from 25 °C to 150 °C, the complex did not show any optical textures. Hence, **Complex 9** did not exhibit mesomorphism.

#### 4.3.6 [Mn(HL2)<sub>2</sub>(H<sub>2</sub>O)<sub>2</sub>]

The Mn(II) complex of H<sub>2</sub>L2 was also synthesized by the one-pot method, involving 2,4-dihydroxybenzaldehyde, 1,8-diaminooctane and [Mn(CH<sub>3</sub>COO)<sub>2</sub>].4H<sub>2</sub>O in ethanol. The product was a dark brown powder (**Complex 10**), and the yield was 35.1%. It was insoluble in most common solvents.

##### (a) Structural deduction

Based on the instrumental data discussed below, the structural formula of **Complex 10** is [Mn(HL2)<sub>2</sub>(H<sub>2</sub>O)<sub>2</sub>].

The results from the **elemental analyses** (61.61% C, 6.90% H, 5.71% N) were in good agreement with the proposed chemical formula MnC<sub>44</sub>H<sub>58</sub>N<sub>4</sub>O<sub>10</sub> (857.89 g mol<sup>-1</sup>; 61.6% C, 6.81% H, 6.53% N).

Its **FTIR** spectrum (**Figure 4.75**) shows peaks for the expected functional groups and bonds at similar wavenumbers ( $3376\text{ cm}^{-1}$ ,  $2926\text{ cm}^{-1}$ ,  $2853\text{ cm}^{-1}$  and  $1639\text{ cm}^{-1}$ ) as the corresponding metal complexes. The peaks for  $\text{CH}_3\text{COO}^-$  ligand were not found.

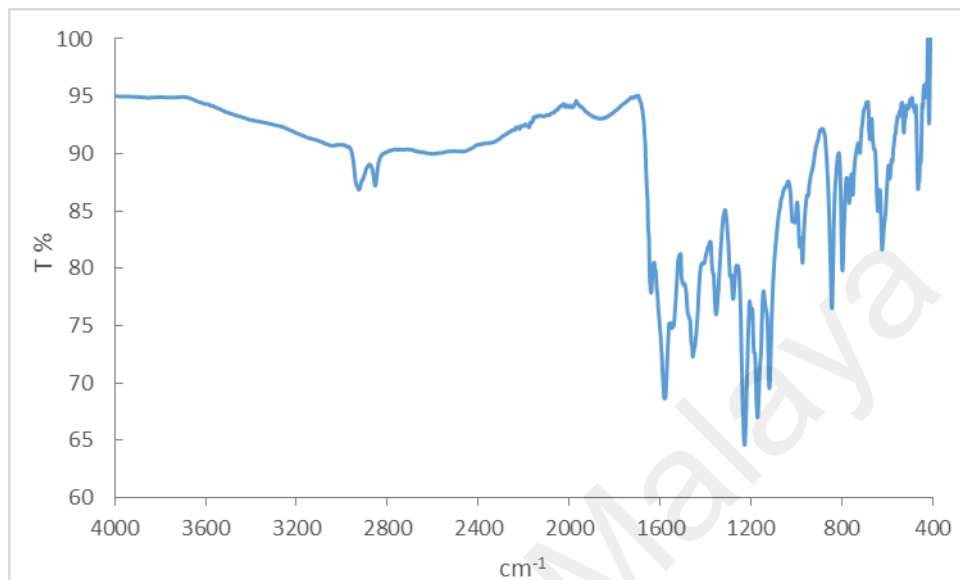


**Figure 4.75** FTIR spectrum for **Complex 10**

Its **UV-visible** spectrum (**Figure 4.76**), recorded in the solid state, show *d-d* bands at 677 nm, 478 nm and 400 nm, suggesting that the geometry of Mn(II) in the complex was octahedral [109].

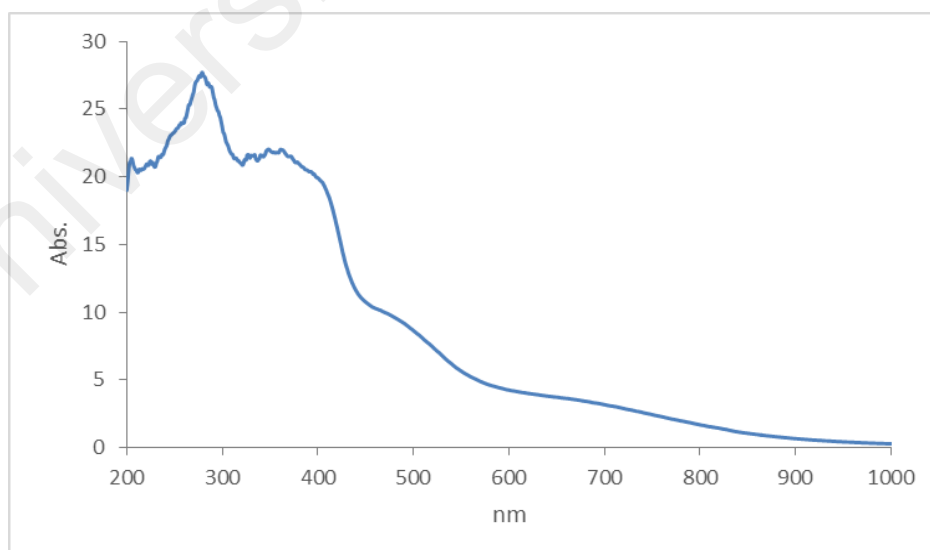


**Figure 4.76** UV-visible spectrum of **Complex 10**

Combining the results of elemental analyses and FTIR and UV-visible spectroscopies, the proposed structural formula of **Complex 10** is shown in **Figure 4.77**.

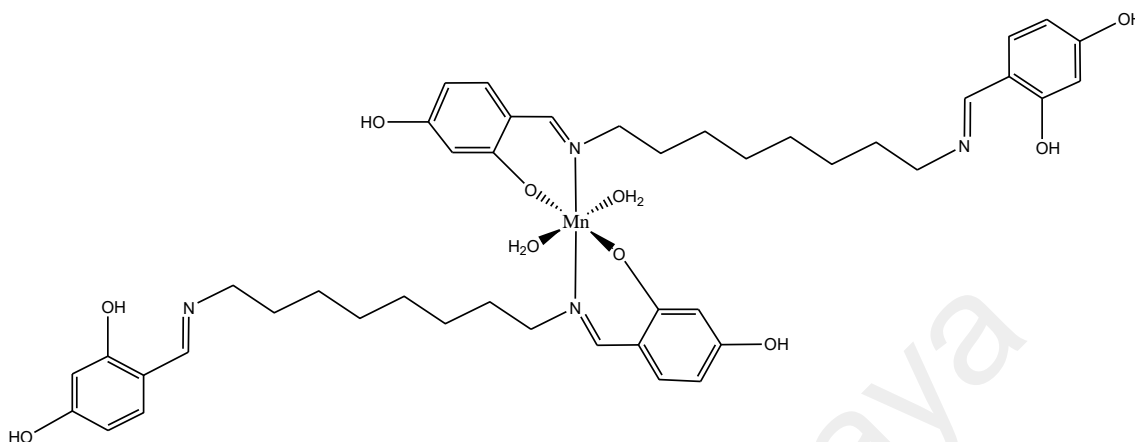


**Figure 4.77** Proposed structure for **Complex 10**

*(b) Determination of bandgaps*

Its  $E_o$  value, calculated as before from its UV-vis spectrum, was 3.10 eV ( $\lambda = 400$  nm).

Fluorescence spectroscopy and cyclic voltammetry could not be performed for the complex as it was insoluble in most common solvents.

*(c) Magnetic properties*

Its  $\chi_m^{corr}T$  value was calculated as previously done using the following data:

FM = 857.89 g mol<sup>-1</sup>,  $\chi_g = 0.955 \times 10^{-5}$  cm<sup>3</sup> g<sup>-1</sup>,  $\chi_m = 8.19 \times 10^{-3}$  cm<sup>3</sup> mol<sup>-1</sup>,  $\chi_{dia} = -3.09 \times 10^{-4}$  cm<sup>3</sup> mol<sup>-1</sup>, and  $\chi_m^{corr} = 8.50 \times 10^{-3}$  cm<sup>3</sup> mol<sup>-1</sup>, was 2.53 cm<sup>3</sup> K mol<sup>-1</sup>.

From this, it may be inferred that this complex was made up of 54% HS and 46% LS Mn(II) at room temperature.

*(d) Thermal properties*

Its TGA trace (**Figure 4.78**) shows an initial weight loss of 3.6% from about 112 °C to 230 °C due to loss of coordinated water molecules (calculated, 4.2%). The next rapid weight loss of 88.5% from about 230 °C to 900 °C due to decomposition of two HL2<sup>-</sup> ion (calculated, 89.4%). Hence, the complex was thermally stable up to 230 °C.

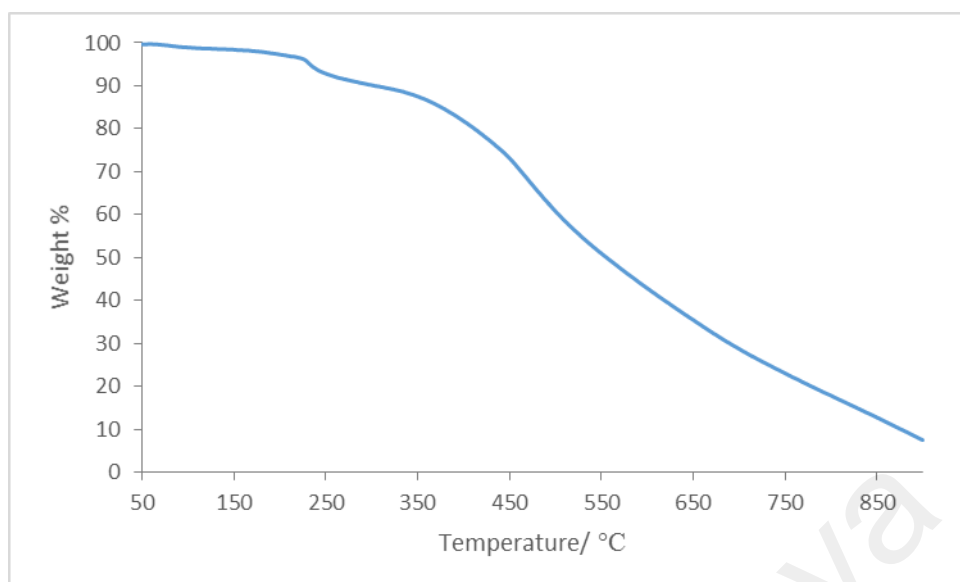


**Figure 4.78** TGA of Complex 10

*(e) Mesomorphic properties*

Its DSC spectrum (**Figure 4.79**) was recorded for heating-cooling cycle from 25 °C to 210 °C. On heating, there were two endothermic peaks at 145.1 °C ( $\Delta H = +12.2 \text{ kJ mol}^{-1}$ ), and 195.1 °C ( $\Delta H = +42.1 \text{ kJ mol}^{-1}$ ), assigned [as the hydrolysis of C=N bond and the breaking of H-bond, respectively]. On cooling, there were no peaks.

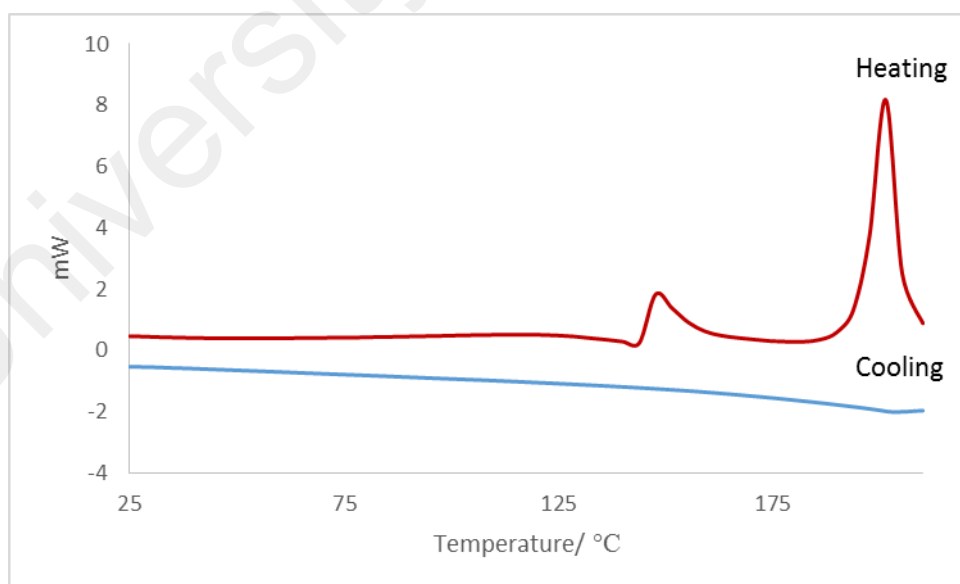


**Figure 4.79** DSC of Complex 10

Viewed under **OPM**, which was recorded for heating-cooling cycle from 25 °C to 210 °C, the complex did not show any optical textures. Hence, **Complex 10** did not exhibit mesomorphism.

#### **4.3.7 Summary**

The analytical results for **Complexes 6-10** are summarised in **Table 4.5**. **Complexes 6, 9 and 10** were mononuclear, while **Complexes 7 and 8** were dinuclear. All complexes were paramagnetic.

The optical bandgaps from the CT absorption bands for all complexes were similar (2.29 eV– 3.10 eV), while for an emission bands and electrochemical bandgap only can be calculated for **Complex 6** (2.41 eV and 0.71 eV, respectively). Hence, these complexes were semiconductors and potentials as photovoltaic and solar cells materials.

Except for **Complex 6**, the lifetimes and the Stokes shift value of other complexes cannot be calculated. The lifetime and Stokes shift values for **Complex 6** was 1.9 ns and, 34 and 63 nm, respectively for CT band and 2.0 eV and 3 nm, respectively for *d-d* band.

All complexes were thermally stable. Their decomposition temperatures range from 197 °C to 234 °C. Finally, all complexes were not mesomorphic.

**Table 4.5** Analytical results for metal(II) complexes of  $H_2L2$

Complex		6	7	8	9	10
Chemical Formula		[Cu(R')(HL2)(H <sub>2</sub> O)].H <sub>2</sub> O	[Ni <sub>2</sub> (R') <sub>2</sub> (L2)].4H <sub>2</sub> O	[Co <sub>2</sub> (R') <sub>2</sub> (L2)].H <sub>2</sub> O	[Fe(R')(HL2)].3H <sub>2</sub> O	[Mn(HL2) <sub>2</sub> (H <sub>2</sub> O) <sub>2</sub> ]
CH <sub>3</sub> COO mode		chelating				-
Geometry		square pyramidal	tetrahedral			octahedral
E <sub>o</sub> (eV)	absorption	2.29	2.75	2.78	3.10	3.10
	emission	2.41	-	-	-	-
	electrochemical	0.71	-	-	-	-
Stokes Shift (nm)		34, 63,3	-	-	-	-
CT, <i>d-d</i>						
τ (ns)		2.0	-	-	-	-
CV		redox active	-	-	-	-
μ <sub>eff</sub> (B.M.)		1.88	4.15	5.24	4.93	54 % HS, 46 % LS
T <sub>dec</sub> (°C)		219	234	197	170	230
Mesomorphism		Non-mesomorphic				

R' = CH<sub>3</sub>COO

## 4.4 H<sub>2</sub>L3 and its Metal(II) Complexes

### 4.4.1 H<sub>2</sub>L3

H<sub>2</sub>L3 was obtained as orange crystals from the reaction of H<sub>2</sub>N(CH<sub>2</sub>)<sub>8</sub>NH<sub>2</sub> with 3,5-di(*tert*-butyl)-2-hydroxybenzaldehyde in ethanol. Its yield was 90.2% and it was soluble in chloroform but insoluble in other common organic solvents.

#### (a) Structural deduction

The structural formula of H<sub>2</sub>L3 was ascertained by elemental analyses and IR spectroscopy, and confirmed by X-ray crystallography.

The results from the **elemental analyses** (79.6% C, 11.1% H, 4.9% N) were in good agreement with the chemical formula C<sub>38</sub>H<sub>60</sub>N<sub>2</sub>O<sub>2</sub> (576.90 g mol<sup>-1</sup>; 79.1% C, 10.5% H, 4.9% N). Its **FTIR** spectrum (**Figure 4.80**) shows two medium peaks for CH<sub>2</sub> (v<sub>as</sub>) and CH<sub>2</sub> (v<sub>s</sub>) at 2959 cm<sup>-1</sup> and 2860 cm<sup>-1</sup>, respectively, and a strong peak for C=N at 1634 cm<sup>-1</sup>.

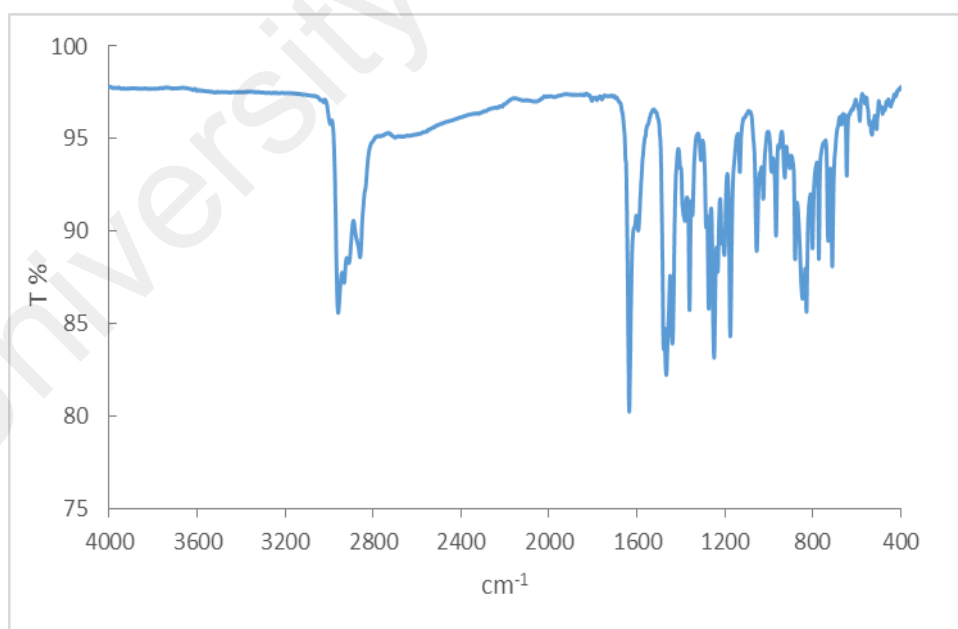


**Figure 4.80** The FTIR spectrum of H<sub>2</sub>L3

The molecular structure and the packing diagram for H<sub>2</sub>L3 are shown in **Figure 4.81** and **Figure 4.82**, respectively. The crystallographic and structure refinement data is

given in **Table 4.6** and selected bond lengths and angles are given in **Table 4.7**. The molecule crystallised in the triclinic *P-1* space group. The two aromatic rings of each molecule were almost coplanar to each other, while the two OH groups pointed in the opposite direction. There were strong intramolecular N-H-O hydrogen bonding interactions, and the molecules packed so as to optimise the van der Waals interaction between the *tert*-butyl groups at the aromatic rings of neighbouring molecules.

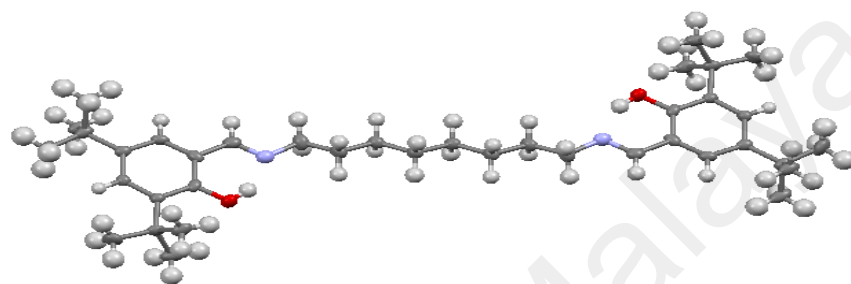


**Figure 4.81** An ORTEP presentation of H<sub>2</sub>L3

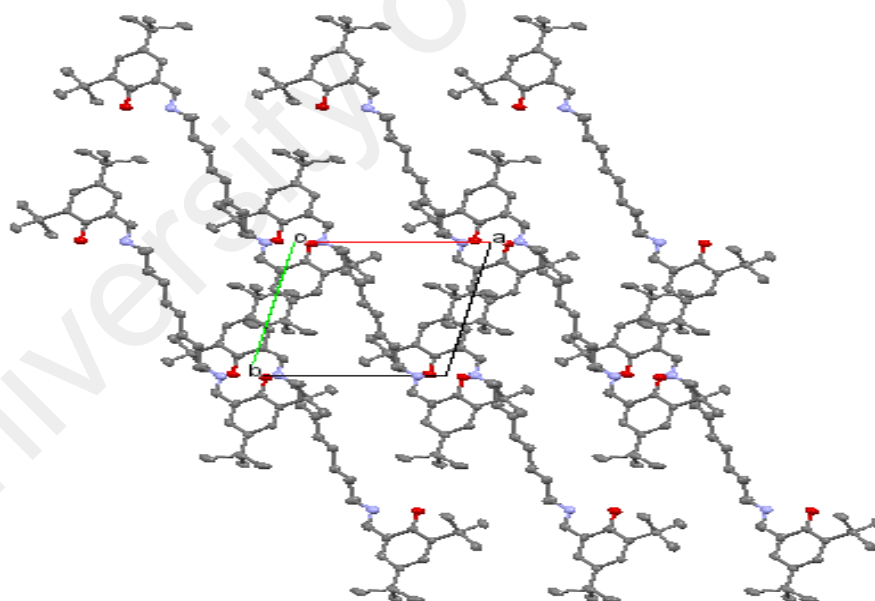


**Figure 4.82.** The packing diagram viewed along the *c*-axis (H atoms are omitted for clarity).

**Table 4.6** Crystal data and structure refinement for H<sub>2</sub>L3

Chemical formula	C <sub>38</sub> H <sub>60</sub> N <sub>2</sub> O <sub>2</sub>
Formula weight (g mol <sup>-1</sup> )	576.88
Temperature (K)	293(2)
Wavelength(Å)	0.71073
Crystal system, space group	Triclinic, <i>P</i> -1
Unit cell dimension	$a$ (Å) = 8.4479(5) $\alpha$ (°) = 93.434(5) $b$ (Å) = 9.7130(7) $\beta$ (°) = 97.544(5) $c$ (Å) = 11.1572(7) $\gamma$ (°) = 100.786(5)
Volume (Å <sup>3</sup> )	888.18(10)
Z, Calculated density (g cm <sup>-3</sup> )	1, 1.079
Absorption coefficient (mm <sup>-1</sup> )	0.065
$F(000)$	318
Theta range for data collection (°)	2.870 - 25.990
Index ranges	$-10 \leq h \leq 9$ , $-11 \leq k \leq 11$ , $-13 \leq l \leq 10$
Reflections collected	7840
Independent reflections	3496 (0.0325)
Data/restraints/parameters	3496/0/197
Goodness-of-fit on $F^2$	1.031
Final $R$ indices	R1 = 0.0863
$[I \geq 2.0\sigma(I)]$	wR2 = 0.2238
$R$ indices (all data)	R1 = 0.1102, wR2 = 0.2464
$\Delta\rho_{\max}$ , $\Delta\rho_{\min}$ (e Å <sup>-3</sup> )	1.460, -0.375

**Table 4.7** Selected bond lengths (Å) and angles (°) for H<sub>2</sub>L3

Bond length			
O(1)-C(1)	1.336(3)	N(1)-C(7)	1.254(4)
O(1)-H(1A)	0.8200	N(1)-C(8)	1.481(4)
Angle			
C(1)-O(1)-H(1A)	109.5	N(1)-C(7)-H(7A)	119.3
C(7)-N(1)-C(8)	117.6(3)	N(1)-C(8)-C(9)	110.4(3)
O(1)-C(1)-C(6)	122.1(3)	N(1)-C(8)-H(8A)	109.6
O(1)-C(1)-C(2)	117.8(2)	N(1)-C(8)-H(8B)	109.6
N(1)-C(7)-C(2)	121.4(3)		

**Table 4.8** Hydrogen bonds for H<sub>2</sub>L3 (Å and °).

D-H...A	D-H	H...A	D...A	<(DHA)
O(1)-H(1A)...N(1)	0.82	1.84	2.5752(14)	148.0
C(9)-H(9B)...O(1)#2	0.97	2.55	3.3492(15)	139.3

(b) *Mesomorphic properties*

Its DSC spectrum (**Figure 4.83**) was recorded for a heating-cooling cycle from 25 °C to 100 °C. On heating, there was an endothermic peak at 89.7 °C ( $\Delta H = +61.3 \text{ kJ mol}^{-1}$ ) assigned for crystal-to-isotropic liquid transition. On cooling, there were no peaks.

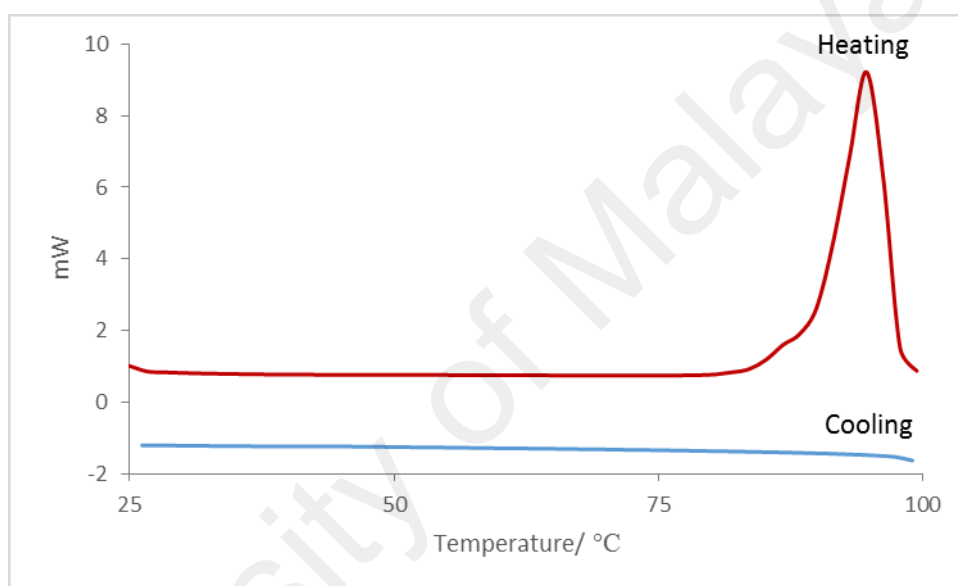


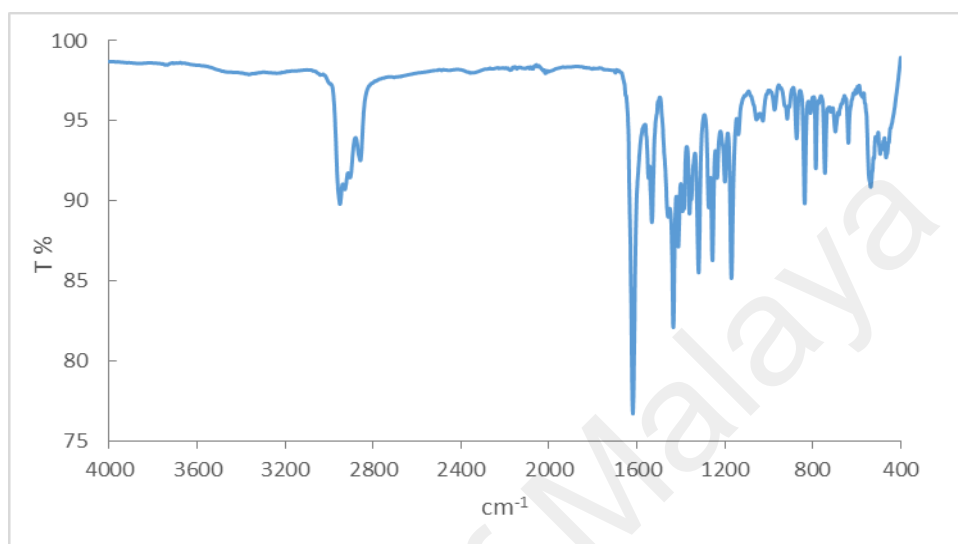
**Figure 4.83** DSC of H<sub>2</sub>L3

Viewed under **OPM**, on cooling-heating cycle from 25 °C to 100 °C, the ligand did not show any optical textures. This is likely a consequent of the unfavorable packing pattern dictated by the two *tert*-butyl groups at the aromatic ring, as indicated from its molecular structure.

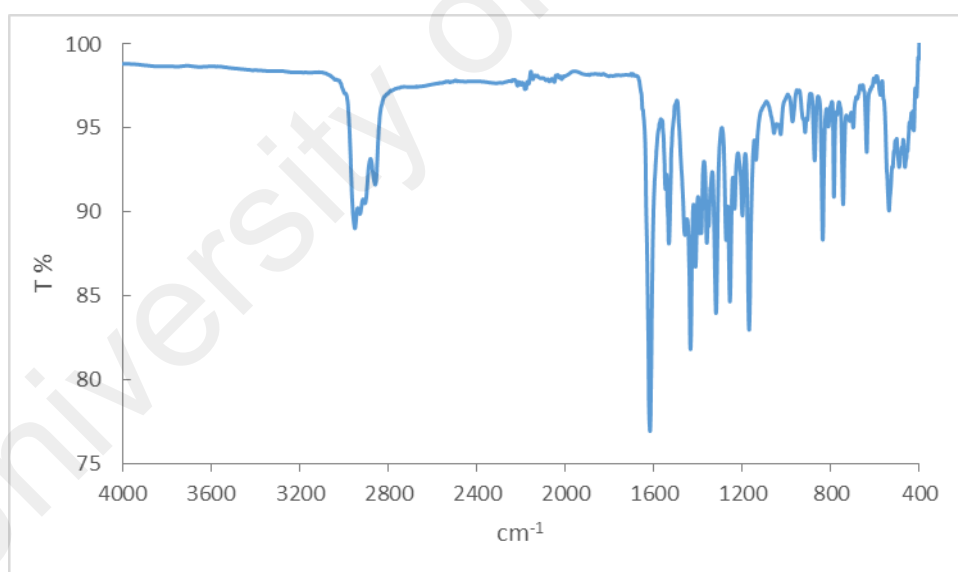
#### 4.4.2 [Cu(L3)]

As for previously discussed complexes, the Cu(II) complex of H<sub>2</sub>L3 was synthesised by two methods: step-wise and one-pot reactions. Both methods gave khaki green powders (**Complex 11**), and the yield was 44.7% (step-wise method) and 87.3% (one-pot method). Both powders were soluble in chloroform but insoluble in water and other common

organic solvents. The CHN elemental analyses and FTIR spectra of both products are similar (**Figure 4.84**). From these, it may be concluded that the products obtained from both methods were similar. Thus the following data are shown for the product obtained from the one-pot reaction only.



(a)



(b)

**Figure 4.84** FTIR spectrum of **Complex 11**: (a) step-wise reaction, and (b) one-pot reaction

*(a) Structural deduction*

Based on the instrumental data discussed below, the structural formula of **Complex 11** is [Cu(L3)]. The proposed structure is similar with [Cu(L)] as reported by Kasumov *et al.*,

where L was *N,N*-bis(3,5-di-(*tert*-butyl)salicylidene)-1,*x*-diaminoalkane (*x* = 2, 3, 4, 5 and 6) [4].

The results from the **elemental analyses** (70.54% C, 9.69% H, 4.40% N) were in good agreement with the chemical formula  $\text{CuC}_{38}\text{H}_{58}\text{N}_2\text{O}_2$  (638.43 g mol<sup>-1</sup>; 71.49% C, 9.16% H, 4.39% N).

Its **FTIR** spectrum (**Figure 4.84**) shows a broad peaks similarly found for **Complex 1** at 2951 cm<sup>-1</sup>, 2929 cm<sup>-1</sup>, 2859 cm<sup>-1</sup>, and 1618 cm<sup>-1</sup>.

Its **UV-visible** spectrum (**Figure 4.85**), recorded in chloroform, shows a broad *d-d* band at 667 nm ( $\epsilon_{\text{max}} = 432 \text{ M}^{-1} \text{ cm}^{-1}$ ). This suggests a square pyramidal geometry at Cu(II) centre of this complex in solution.

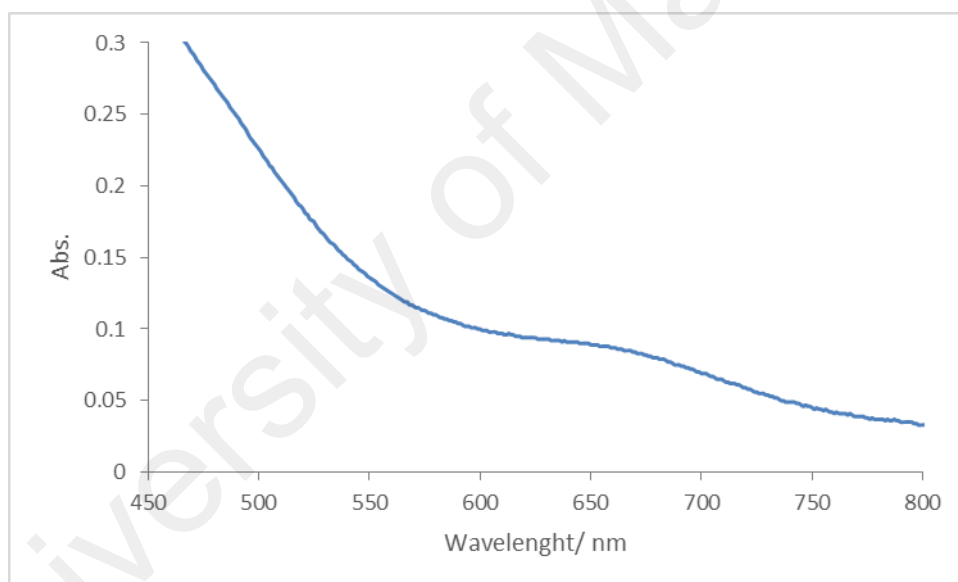


**Figure 4.85** UV-visible spectrum of **Complex 11**

Combining the results of elemental analyses and FTIR and UV-vis spectroscopies, the proposed structural formula for the complex is shown in **Figure 4.86**.

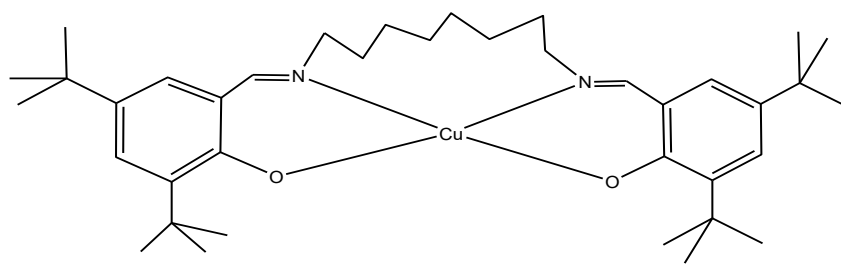


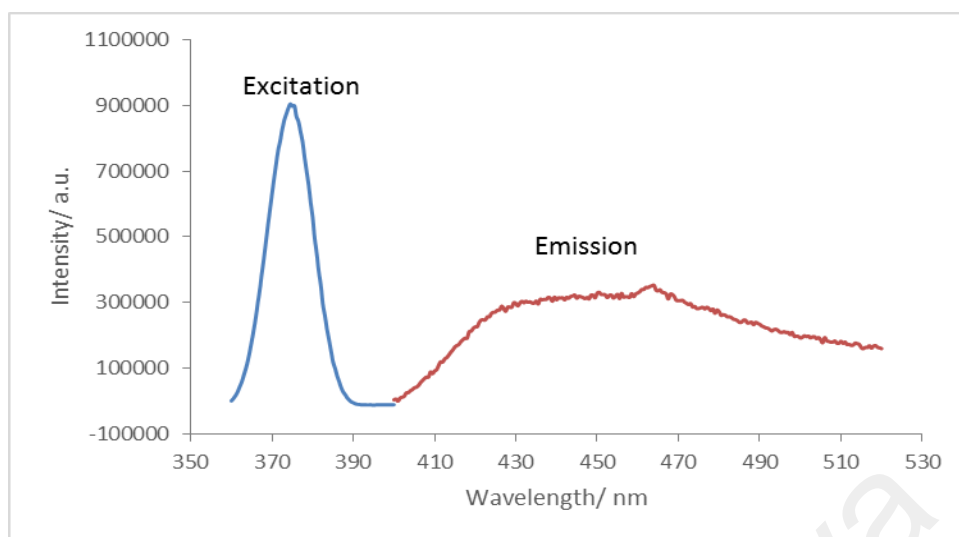
**Figure 4.86** Proposed structure for **Complex 11**

*(b) Determination of bandgaps*

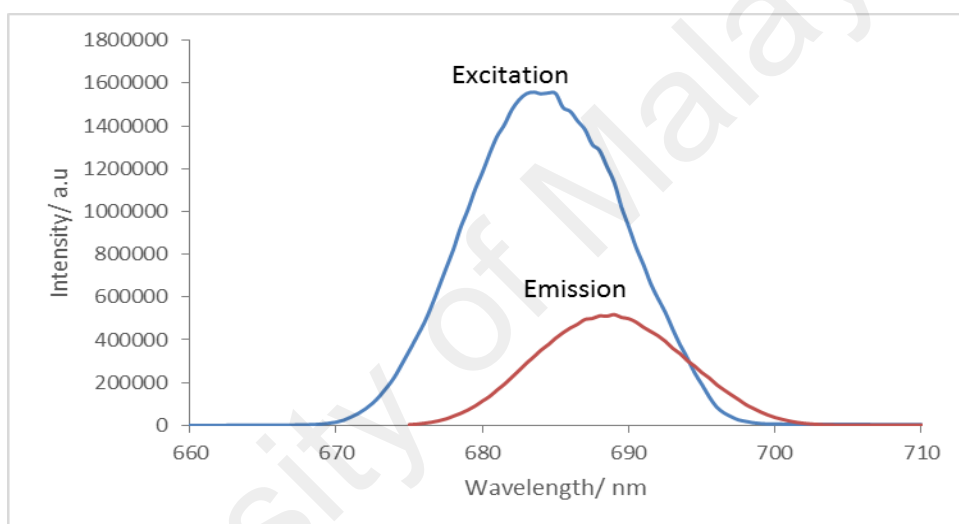
Its  $E_o$  value, calculated as before from the UV-vis spectrum, was 2.29 eV ( $\lambda = 542$  nm).

Its **fluorescence** spectra (**Figure 4.87**) were recorded in chloroform. Upon excitation at 374 nm (LMCT band), there was an emission peak at 450 nm, while upon excitation at 683 nm (*d-d* band), there was an emission peak at 689 nm. The Stokes shifts were 90 nm and 6 nm. Additionally, its  $E_o$ , was 2.39 eV ( $\lambda = 520$  nm).

Its  $\tau$  value, calculated from its decay curve (**Figure 4.88**) was 1.3 ns ( $\lambda_{emission} = 464$  nm) and 1.0 ns ( $\lambda_{emission} = 689$  nm).

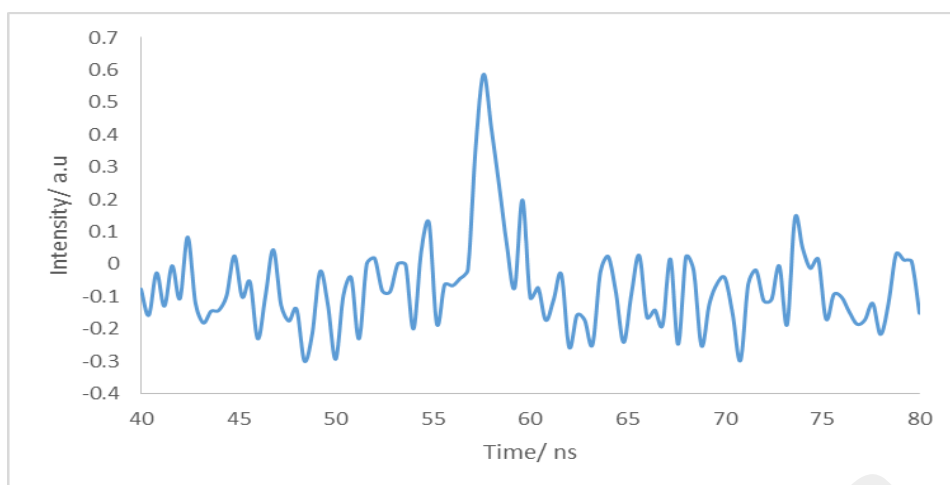


(a)

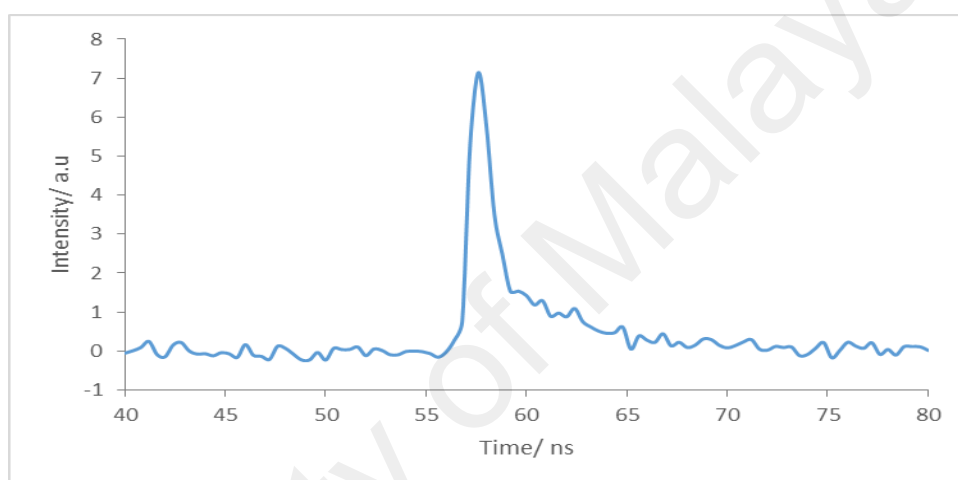


(b)

**Figure 4.87** Fluorescence spectra of **Complex 11** after excitation at: (a) 374 nm, and (b) 683 nm



(a)



(b)

**Figure 4.88** Fluorescence decay of **Complex 11** after excitation at: (a) 465 nm, and (b) 689 nm

Its **CV** was recorded cathodically in chloroform at a scan rate of  $50 \text{ mV s}^{-1}$  in the potential range of +1.5 V to -1.5 V. The voltammogram (**Figure 4.89**) shows a reduction peak at -0.97 V assigned to the reduction of [Cu(II)] to [Cu(I)], and no corresponding oxidation peak, indicating irreversible process. It may be inferred from this that the structure of the reduced complex was not stable in this solution. Hence its electrochemical band gap cannot be calculated.

Also observed were two anodic peaks at +1.02 V and + 0.80 V, and the corresponding cathodic peaks at +1.10 and 1.37 V, assigned to the oxidation and reduction of the ligand, respectively.

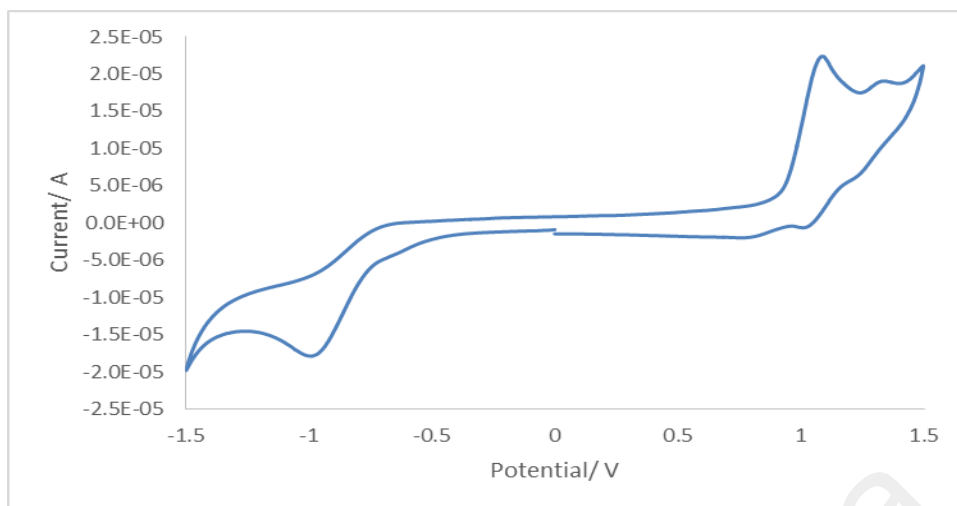


**Figure 4.89** Cyclic voltammogram for **Complex 11**

*(c) Magnetic properties*

Its  $\mu_{\text{eff}}$  value, calculated as before from the values of  $FM = 638.43 \text{ g mol}^{-1}$ ,  $\chi_{\text{g}} = 1.56 \times 10^{-6} \text{ cm}^{-3} \text{ g}^{-1}$ ,  $\chi_{\text{m}} = 9.96 \times 10^{-4} \text{ cm}^{-3} \text{ mol}^{-1}$ ,  $\chi_{\text{dia}} = -3.94 \times 10^{-4} \text{ cm}^{-3} \text{ mol}^{-1}$  and  $\chi_{\text{m}}^{\text{corr}} = 1.39 \times 10^{-3} \text{ cm}^{-3} \text{ mol}^{-1}$ , was 1.80 B.M. The value was in agreement with the spin only value of 1.73 B.M for a mononuclear copper(II) complex (one unpaired electron).

*(d) Thermal properties*

The TGA trace (**Figure 4.90**) shows an initial weight loss of 87.0% from about 280 °C to 680 °C, assigned to decomposition of  $L3^{2-}$  ligand (expected 88.8%). The amount of residue at temperatures above 680 °C was 13.0%, which is in a good agreement with the expected value of 12.4%, assuming pure CuO [96,110]. Hence, **Complex 11** was thermally stable up to 280 °C.

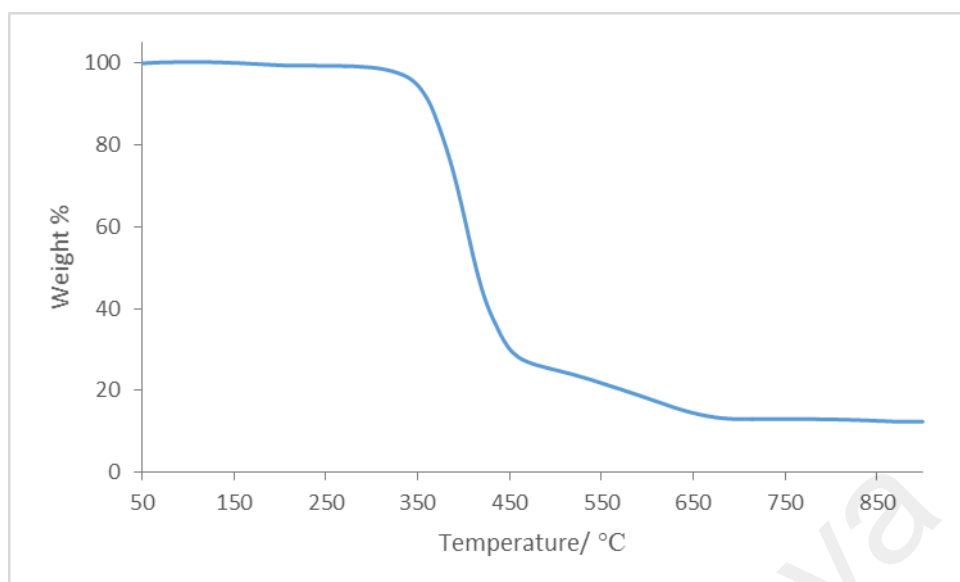


**Figure 4.90** TGA of **Complex 11**

*(e) Mesomorphic properties*

Its **DSC** spectrum (**Figure 4.91**) was recorded for a heating-cooling cycle from 25 °C to 250 °C. On heating, there was an endothermic peak at 144.8 °C ( $\Delta H = +8.21 \text{ kJ mol}^{-1}$ ) assigned as the breaking of H-bond. On cooling, there were no peaks.

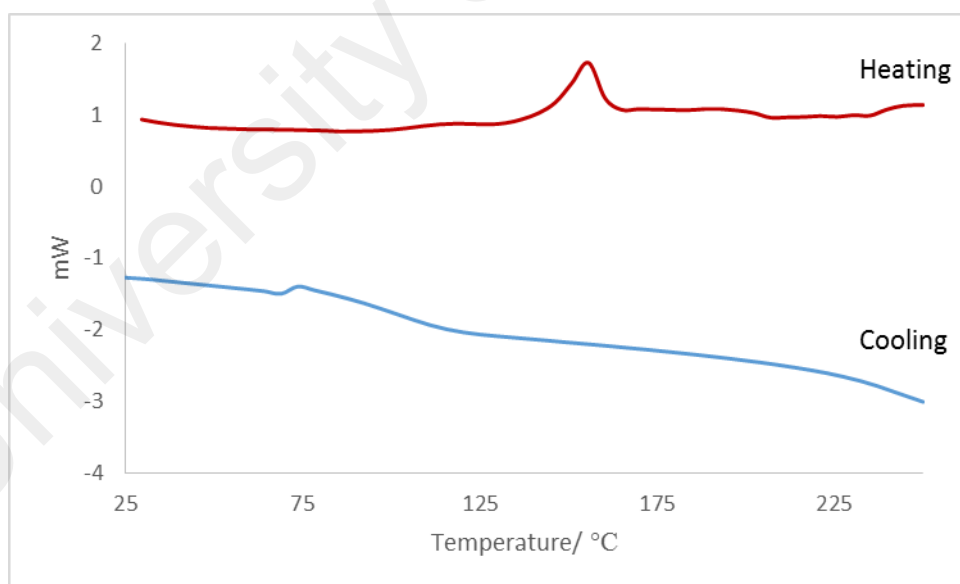


**Figure 4.91** DSC of **Complex 11**

Viewed under **OPM**, which was recorded for heating-cooling cycle from 25 °C to 250 °C, the complex did not show any optical textures. Hence, **Complex 11** did not exhibit mesomorphism.

#### 4.4.3 [Ni(L3)]

The Ni(II) complex of H<sub>2</sub>L3 was also synthesised by the one-pot method, involving H<sub>2</sub>N(CH<sub>2</sub>)<sub>8</sub>NH<sub>2</sub>, 3,5-di(*tert*-butyl)-2-hydroxybenzaldehyde and [Ni(CH<sub>3</sub>COO)]<sub>2</sub>·4H<sub>2</sub>O in ethanol. The product was a green powder (**Complex 12**), and the yield was 35.3%. It was soluble in chloroform but insoluble in water and other common organic solvents.

##### (a) Structural deduction

Based on the same instrumental analyses as discussed previously, it is proposed that the structural formula of **Complex 12** is [Ni(L3)], which is similar with **Complex 11** [Cu(L3)].

The results from the **elemental analyses** (72.40% C, 9.84% H, 4.15% N) were in good agreement with the chemical formula NiC<sub>38</sub>H<sub>58</sub>N<sub>2</sub>O<sub>2</sub> (633.57 g mol<sup>-1</sup>; 72.04% C, 9.23% H, 4.42% N).

Its **FTIR** spectrum (**Figure 4.92**) shows peaks for the expected functional groups and bonds at similar wavenumbers (2951 cm<sup>-1</sup>, 2858 cm<sup>-1</sup>, and 1624 cm<sup>-1</sup>) as the corresponding Cu(II) complex.

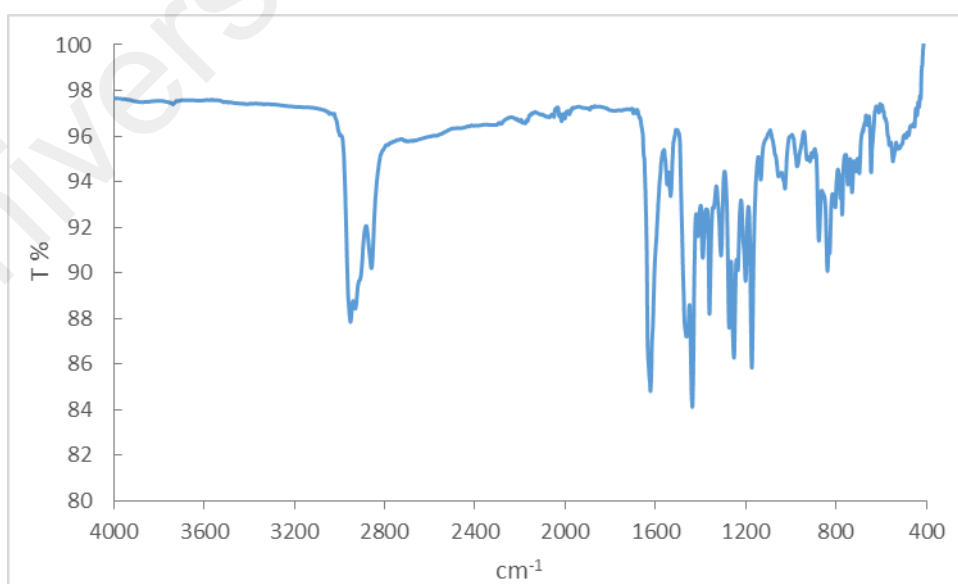


**Figure 4.92** FTIR spectrum for **Complex 12**

Its **UV-visible** spectrum, recorded in chloroform (**Figure 4.93**), shows a *d-d* band at 654 nm ( $\epsilon_{\max} = 446 \text{ M}^{-1} \text{ cm}^{-1}$ ) and an MLCT band at 405 nm ( $\epsilon_{\max} = 2333 \text{ M}^{-1} \text{ cm}^{-1}$ ). This suggests a distorted tetrahedral geometry at Ni(II) centres [104].

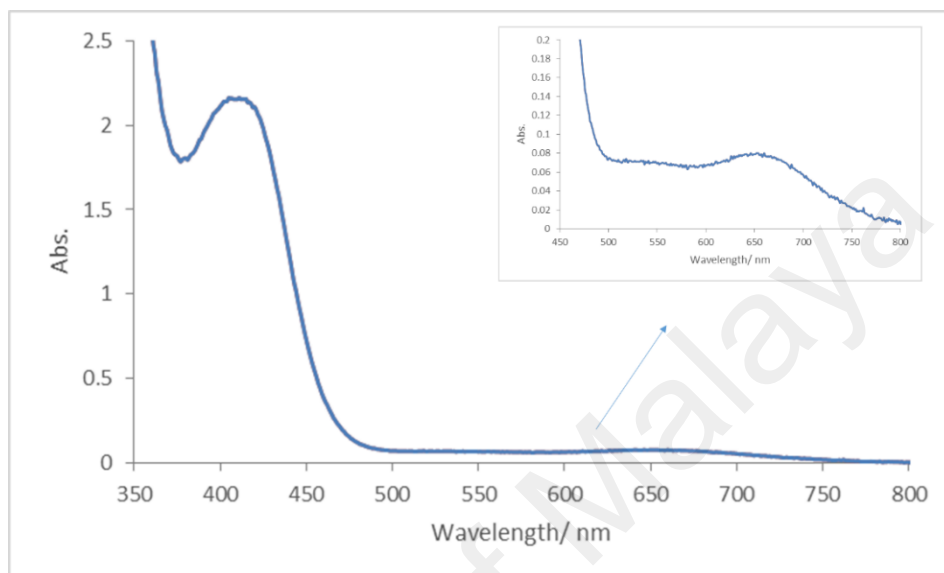


**Figure 4.93** UV-visible spectrum of **Complex 12**

Combining the results of elemental analyses and FTIR and UV-vis spectroscopies, the proposed structural formula for the complex is shown in **Figure 4.94**.

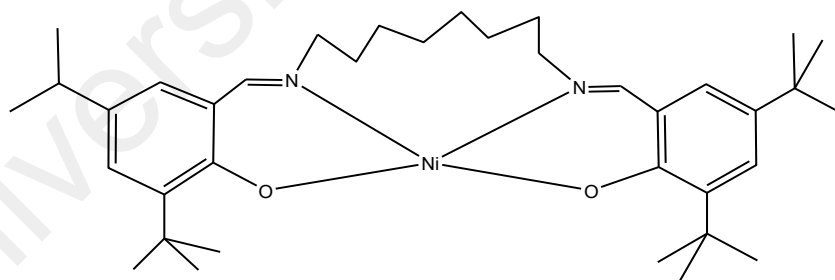


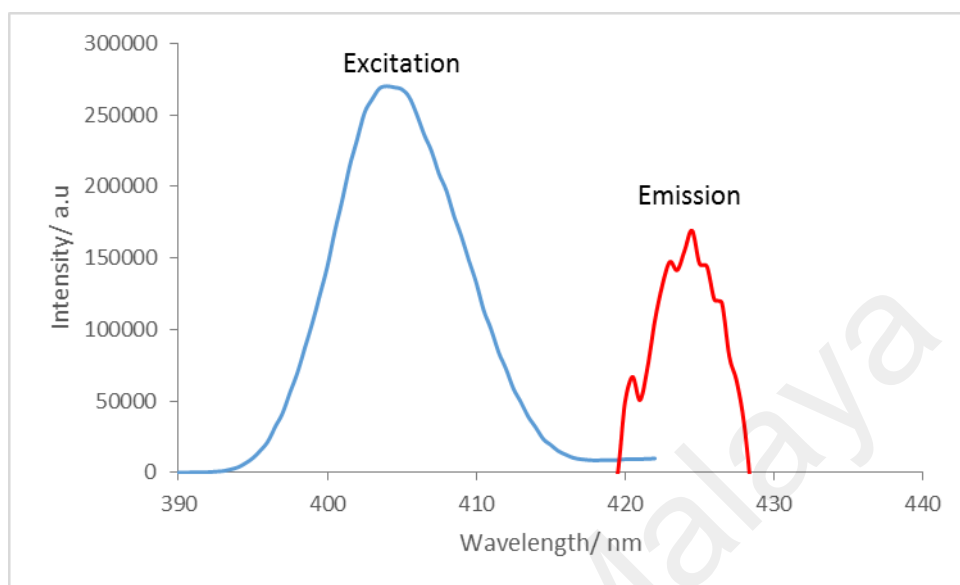
**Figure 4.94** Proposed structure of **Complex 12**

*(b) Determination of bandgaps*

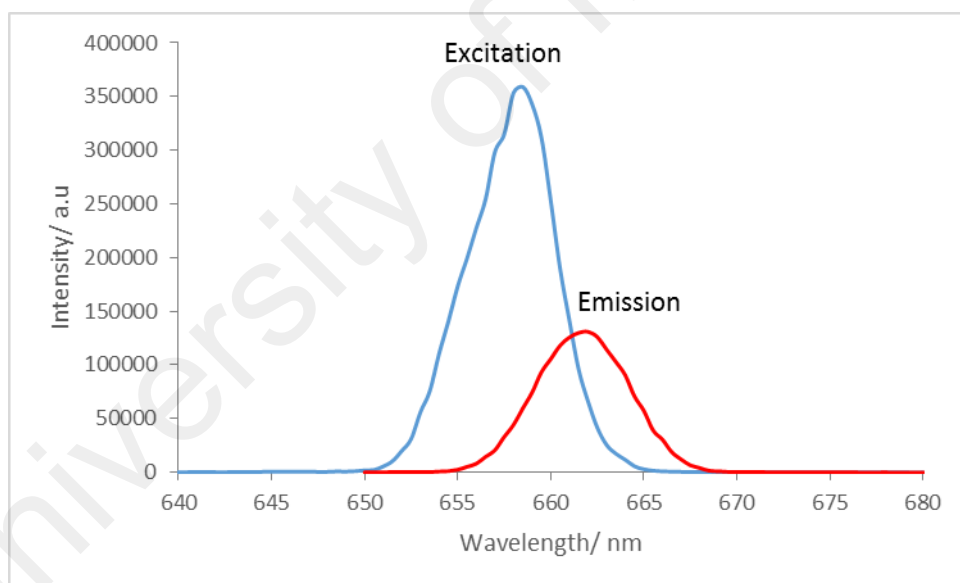
Its  $E_o$  value, calculated as before from its UV-vis spectrum, was 2.67 eV ( $\lambda = 465 \text{ nm}$ ).

Its **fluorescence** spectra (**Figure 4.95**) were recorded in chloroform. Upon excitation at 404 nm (MLCT band), it shows an emission peak at 425 nm, while upon excitation at 659 nm (*d-d* band), it shows an emission peak at 662 nm. Hence, the Stokes

shifts were 21 nm and 3 nm, respectively. Additionally, its  $E_o$  value was 2.89 eV ( $\lambda = 429$  nm).



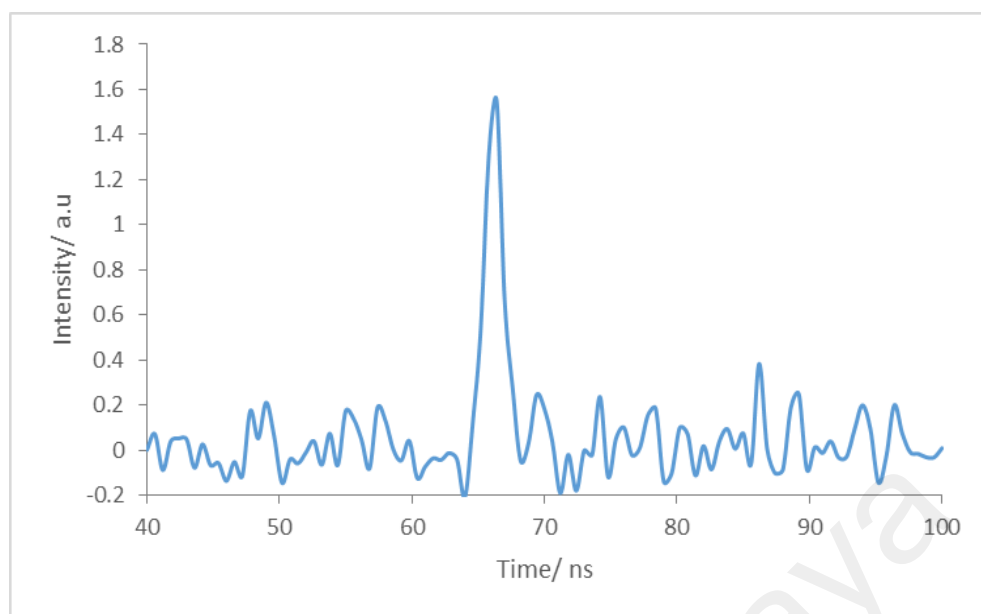
(a)



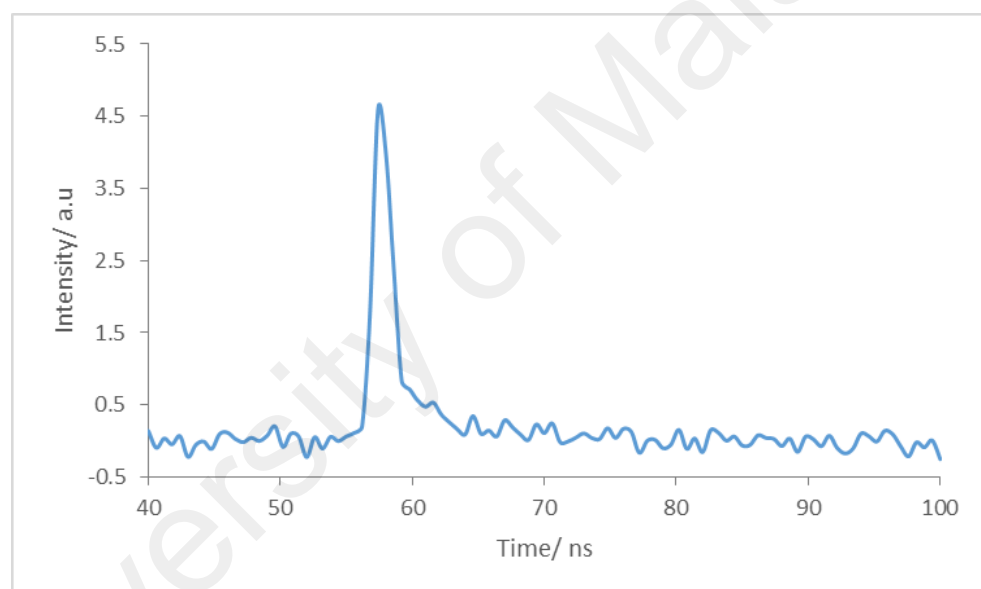
(b)

**Figure 4.95** Fluorescence spectra of **Complex 12** after excitation at: (a) 404 nm, and (b) 659 nm

Its  $\tau$  value, calculated from its decay curve (**Figure 4.96**) was 1.0 ns ( $\lambda_{emission} = 425$  nm and 662 nm).



(a)



(b)

**Figure 4.96** Fluorescence decay of **Complex 12** at  $\lambda_{emission}$ : (a) 425 nm, and (b) 662 nm

Its CV was recorded anodically in chloroform at a scan rate  $50 \text{ mV s}^{-1}$  in the potential range of +1.0 V to -1.0 V. The voltammogram (**Figure 4.97**) shows an anodic peak at +0.51 V assigned to the oxidation of [Ni(II)] to [Ni(III)] and no corresponding reduction peak. Hence its electrochemical band gap cannot be calculated.

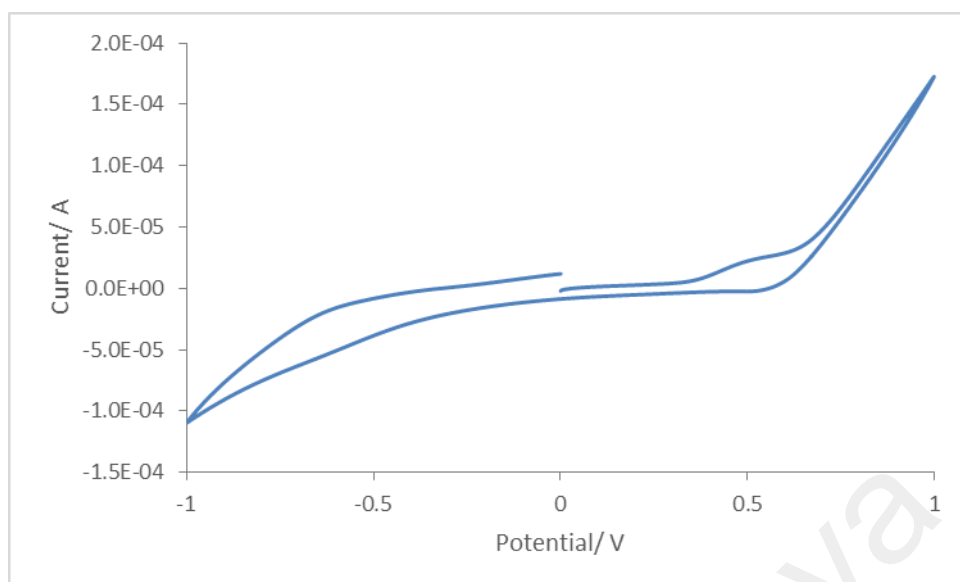


**Figure 4.97** Cyclic voltammogram for **Complex 12**

*(c) Magnetic properties*

Its  $\mu_{\text{eff}}$  value, calculated as before from  $\text{FM} = 633.57 \text{ g mol}^{-1}$ ,  $\chi_{\text{g}} = 0.636 \times 10^{-5} \text{ cm}^3 \text{ g}^{-1}$ ,  $\chi_{\text{m}} = 4.03 \times 10^{-3} \text{ cm}^3 \text{ mol}^{-1}$ ,  $\chi_{\text{dia}} = -3.94 \times 10^{-4} \text{ cm}^3 \text{ mol}^{-1}$  and  $\chi_{\text{m}}^{\text{corr}} = 4.42 \times 10^{-3} \text{ cm}^3 \text{ mol}^{-1}$ , was 3.21 B.M at 298 K. This value is in the normal range (2.9–3.9 B.M.) for tetrahedral nickel(II) complex [111].

*(d) Thermal properties*

Its TGA trace (**Figure 4.98**) shows an initial weight loss of 96.3% from about 283 °C to 591 °C, assigned to decomposition of  $\text{L3}^{2-}$  ion (expected 90.7%). Hence, **Complex 12** was thermally stable up to 283 °C.

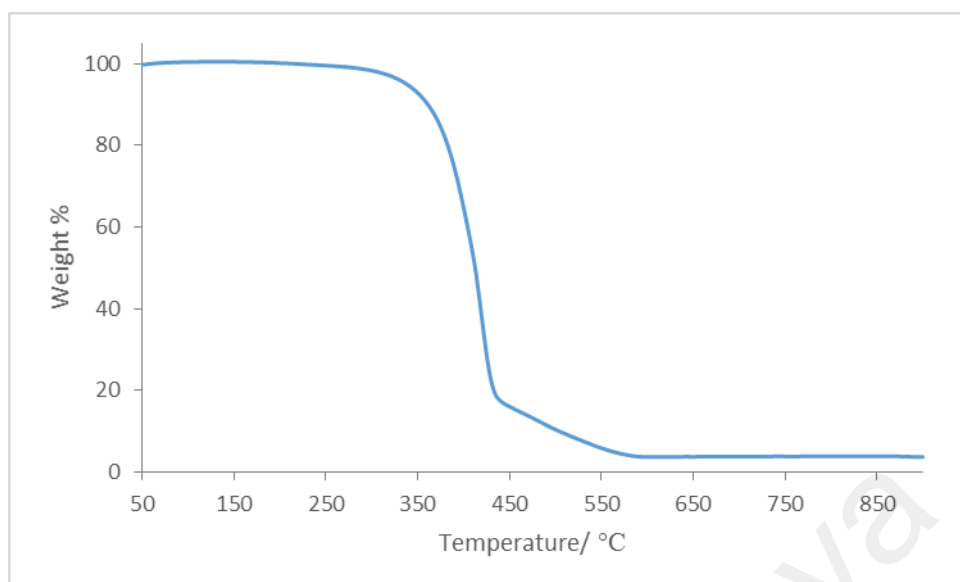


**Figure 4.98** TGA of Complex 12

*(e) Mesomorphic properties*

Its DSC spectrum (**Figure 4.99**) was recorded for heating-cooling cycle from 25 °C to 250 °C. On heating, there were three endothermic peaks at 36.2 °C ( $\Delta H = +0.39 \text{ kJ mol}^{-1}$ ), 51.9 °C ( $\Delta H = +0.41 \text{ kJ mol}^{-1}$ ) and 68.7 °C ( $\Delta H = +1.73 \text{ kJ mol}^{-1}$ ), assigned as the breaking of weak bonds. On cooling, there were no peaks.

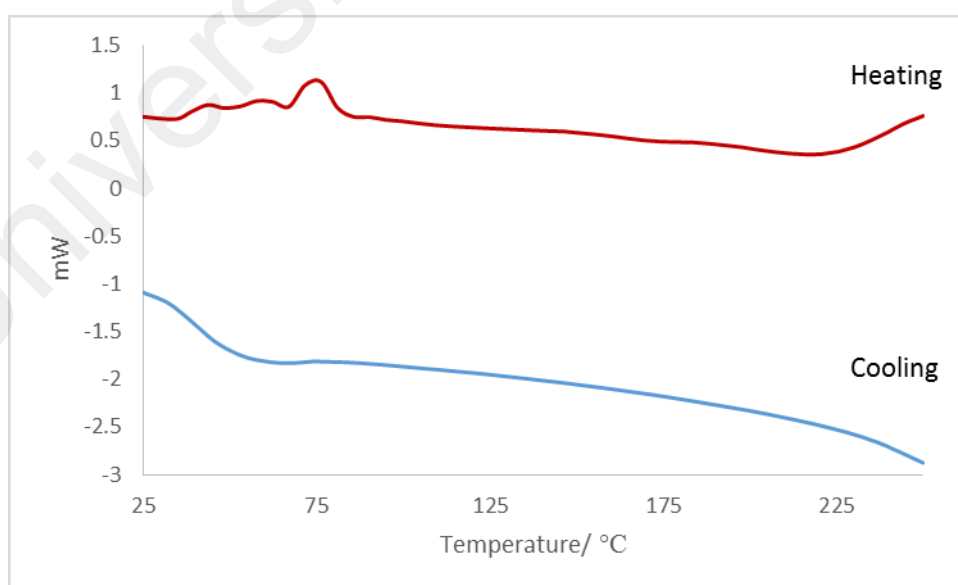


**Figure 4.99** DSC of Complex 12

Viewed under **OPM**, which was recorded for heating-cooling cycle from 25 °C to 250 °C, the complex did not show any optical textures. Hence, **Complex 12** did not exhibit mesomorphism.

#### 4.4.4 $[Co_2(CH_3COO)_2(L3)].3H_2O$

The Co(II) complex of H<sub>2</sub>L3 was also synthesised by the one-pot method involving the reaction of H<sub>2</sub>N(CH<sub>2</sub>)<sub>8</sub>NH<sub>2</sub>, 3,5-di(*tert*-butyl)-2-hydroxybenzaldehyde and [Co(CH<sub>3</sub>COO)<sub>2</sub>].4H<sub>2</sub>O in ethanol. The product was an orange powder (**Complex 13**), and the yield was 16.8%. It was soluble in chloroform and insoluble in other organic solvents.

##### a) Structural deduction

Based on the same instrumental analyses, it was proposed that the structural formula of **Complex 13** is  $[Co_2(CH_3COO)_2(L3)].3H_2O$ .

The results from the **elemental analyses** (58.46% C, 8.12% H, 2.67% N) were in good agreement with the chemical formula Co<sub>2</sub>C<sub>26</sub>H<sub>34</sub>N<sub>2</sub>O<sub>9</sub> (864.88 g mol<sup>-1</sup>; 58.3% C, 8.16% H, 3.24 % N).

Its **FTIR** spectrum (**Figure 4.100**) shows peaks for the expected functional groups and bonds at similar wavenumbers as the corresponding Cu(II) and Ni(II) complexes (3423 cm<sup>-1</sup>, 2948 cm<sup>-1</sup>, 2859 cm<sup>-1</sup>, and 1598 cm<sup>-1</sup>), in addition to two peaks at 1530 cm<sup>-1</sup> (νCOO<sub>asym</sub>) and 1429 cm<sup>-1</sup> (νCOO<sub>sym</sub>). Accordingly, the Δ νCOO value was 101 cm<sup>-1</sup>, suggesting chelating binding mode for CH<sub>3</sub>COO<sup>-</sup> ligand.

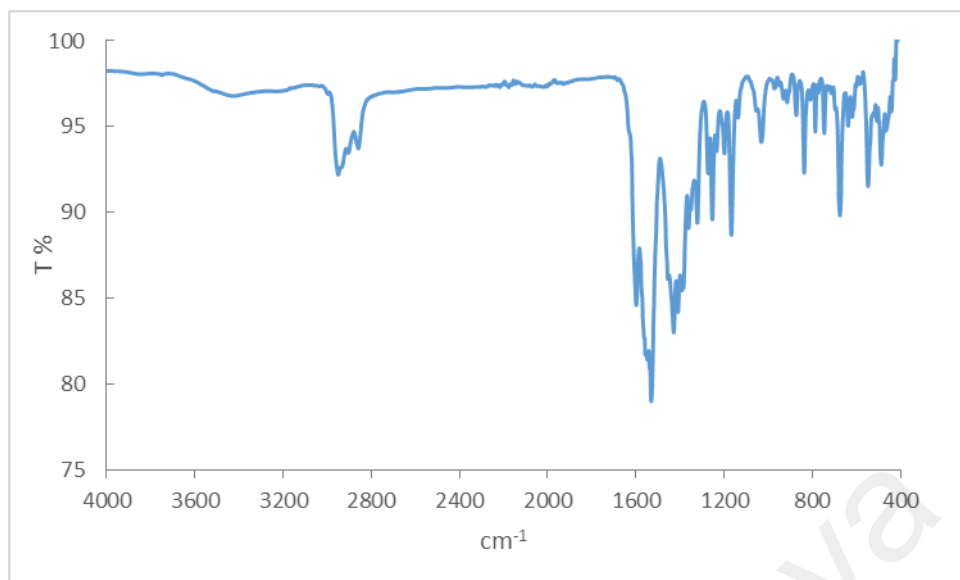


**Figure 4.100** FTIR spectrum for **Complex 13**

Its **UV-visible** spectrum was recorded in chloroform (**Figure 4.101**). The spectrum shows two *d-d* bands at 570 nm ( $\epsilon_{\text{max}} = 109 \text{ M}^{-1} \text{ cm}^{-1}$ ) and 468 nm ( $\epsilon_{\text{max}} = 449 \text{ M}^{-1} \text{ cm}^{-1}$ ) which appeared as a shoulder on a strong MLCT band at 376 nm ( $\epsilon_{\text{max}} = 5047 \text{ M}^{-1} \text{ cm}^{-1}$ ). This suggests a distorted tetrahedral geometry at Co(II) centres.

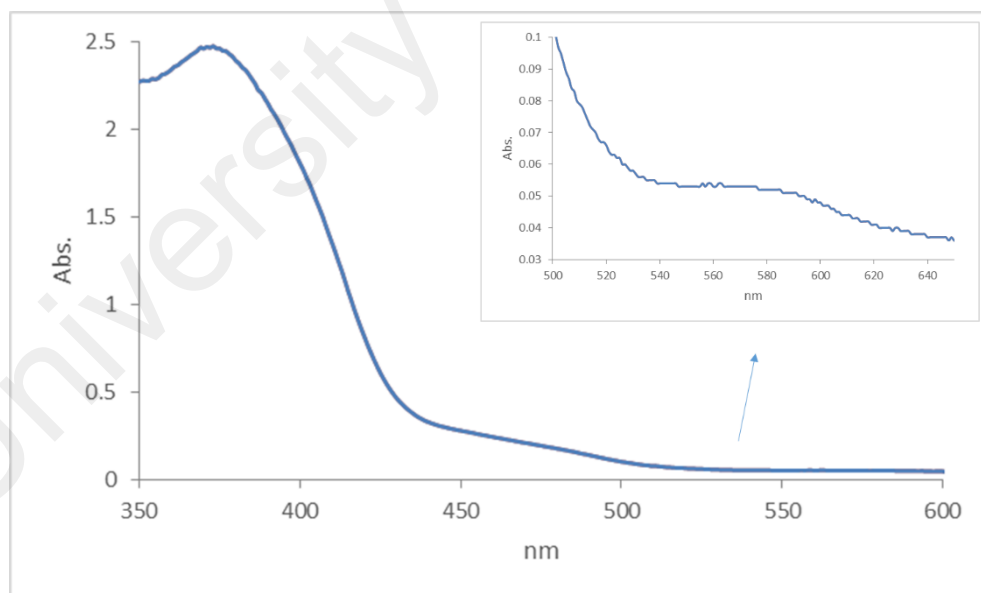


**Figure 4.101** UV-visible spectrum of **Complex 13**

Combining the results of elemental analyses and FTIR and UV-vis spectroscopies, the proposed structural formula for the complex is shown in **Figure 4.102**.

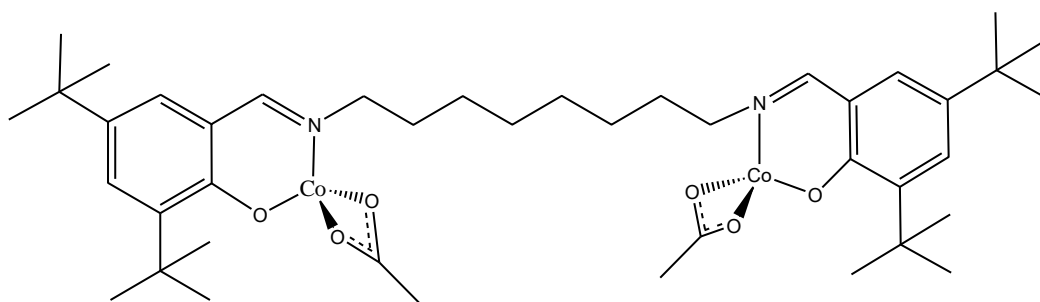


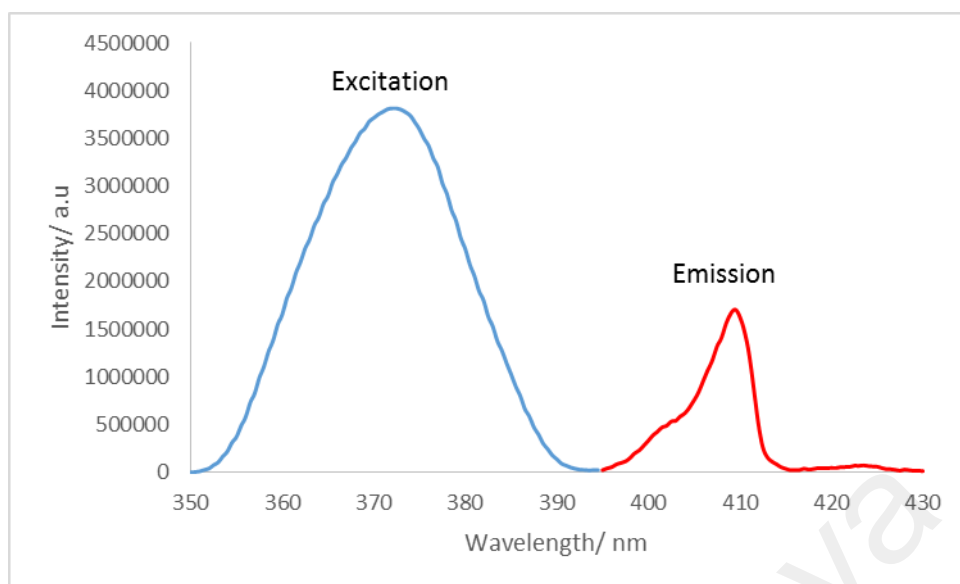
**Figure 4.102** Proposed structure for **Complex 13** (lattice water molecules are omitted)

(b) *Determination of bandgaps*

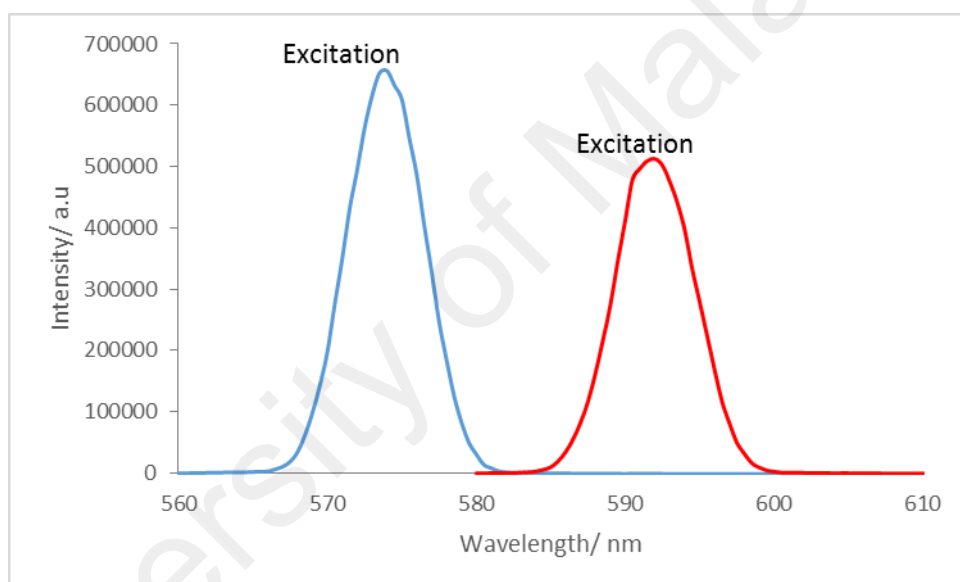
Its  $E_o$  value, calculated as before from its UV-vis spectrum, was 2.85 eV ( $\lambda = 435$  nm).

Its **fluorescence** spectra (**Figure 4.103**) were recorded in chloroform. Upon excitation at 372 nm (MLCT band), it shows an emission peak at 410 nm, while upon excitation at 574 nm (*d-d* band), it shows an emission peak at 592 nm. Hence, its Stokes shifts were 37 nm and 18 nm, respectively. Additionally, its  $E_o$ , was 3.00 eV ( $\lambda = 414$  nm).

Its  $\tau$  value, calculated from its decay curve (**Figure 4.104**) were 3.9 ns ( $\lambda_{emission} = 410$  nm) and 3.2 ns ( $\lambda_{emission} = 592$  nm).

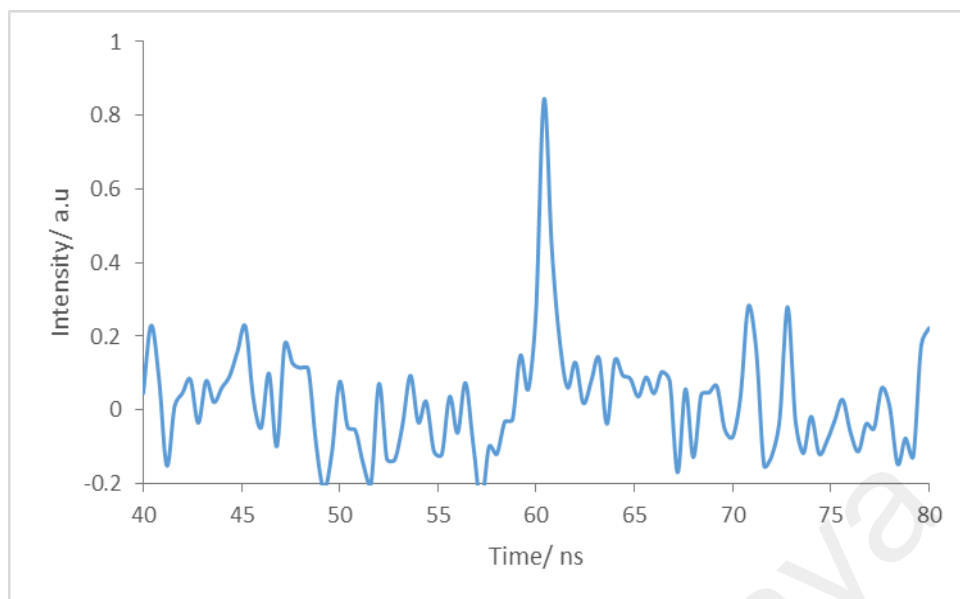


(a)

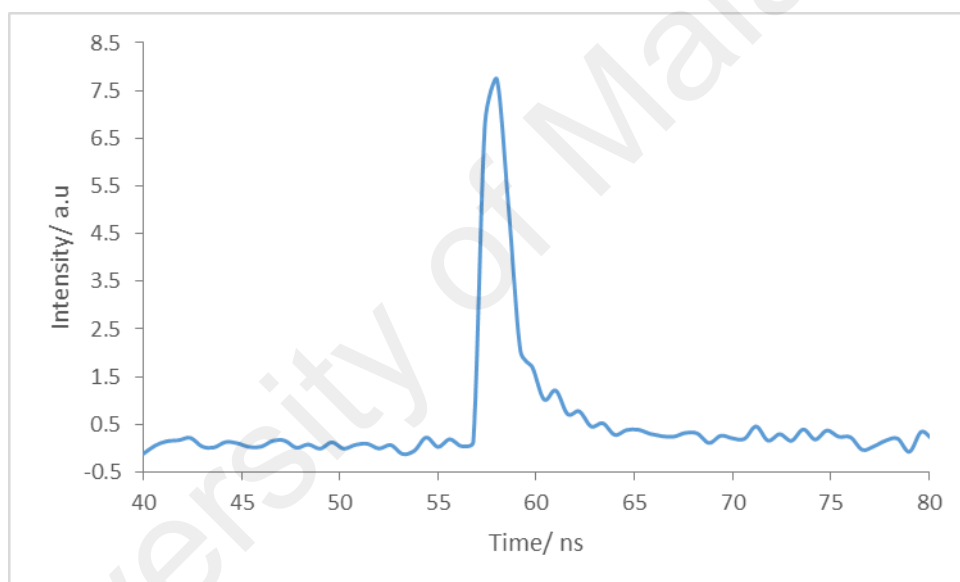


(b)

**Figure 4.103** Fluorescence spectra of **Complex 13** after excitation at: (a) 372 nm, and (b) 574 nm



(a)



(b)

**Figure 4.104** Fluorescence decay of **Complex 13** at  $\lambda_{emission}$  (a) 410 nm, (b) 592 nm

Its **CV** was recorded anodically in chloroform at a scan rate  $50 \text{ mV s}^{-1}$  in the potential range of +1.0 V to -1.0 V. The voltammogram (**Figure 4.105**) shows an anodic peak at +0.44 V assigned to the oxidation of [Co(II)] to [Co(III)] and a cathodic peak at -0.38 V assigned to the reduction of [Co(III)] to [Co(II)]. The  $\Delta E_p$  was 820 mV, indicating a quasireversible redox reaction ( $\Delta E_p > 59 \text{ mV}$  at  $30 \text{ }^\circ\text{C}$ ) and its  $I_{pc}/I_{pa}$  ratio was 0.7, indicating the reduced complex was chemically unstable. The HOMO and

LUMO of the complex was 0.30 V and -0.18 V, respectively. Hence, its  $E_e$  value was 0.48 eV.

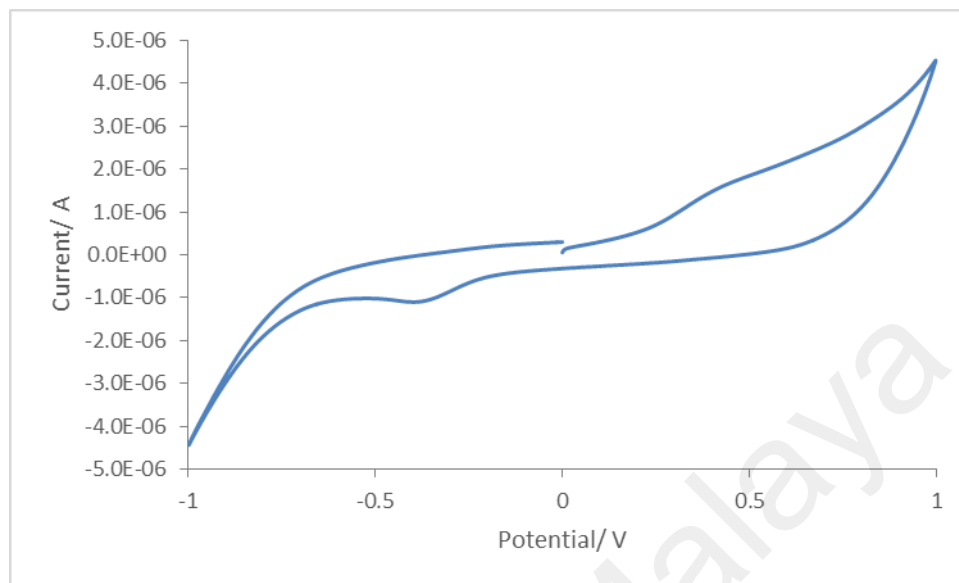


**Figure 4.105** Cyclic voltammogram for **Complex 13**

*(c) Magnetic properties*

Its  $\mu_{eff}$  value, calculated as before from  $FM = 864.88 \text{ g mol}^{-1}$ ,  $\chi_g = 2.64 \times 10^{-5} \text{ cm}^3 \text{ g}^{-1}$ ,  $\chi_m = 2.28 \times 10^{-2} \text{ cm}^3 \text{ mol}^{-1}$ ,  $\chi_{dia} = -4.71 \times 10^{-4} \text{ cm}^3 \text{ mol}^{-1}$ , and  $\chi_m^{corr} = 2.33 \times 10^{-2} \text{ cm}^3 \text{ mol}^{-1}$ , was 7.44 BM at 298 K. The value was slightly higher than expected spin only value of 6.93 BM for a dinuclear Co(II) complex (six unpaired electrons), suggesting a weak ferromagnetic interaction between the Co(II) centres.

*(d) Thermal properties*

Its TGA trace (**Figure 4.106**) shows an initial weight loss of 4.4% from about 50 °C to 251 °C due to evaporation of three lattice  $\text{H}_2\text{O}$  (calculated, 6.25%). The next weight loss of 81.9% from 251 °C to 594 °C was assigned to decomposition of  $\text{L3}^{2-}$  and two  $\text{CH}_3\text{COO}^-$  ions (calculated, 80.1%). The amount of residue at temperatures above 594 °C was 13.7%, which is in a good agreement with the calculated value of 17.3 % (assuming pure CoO). Hence, the complex was thermally stable up to 251 °C.

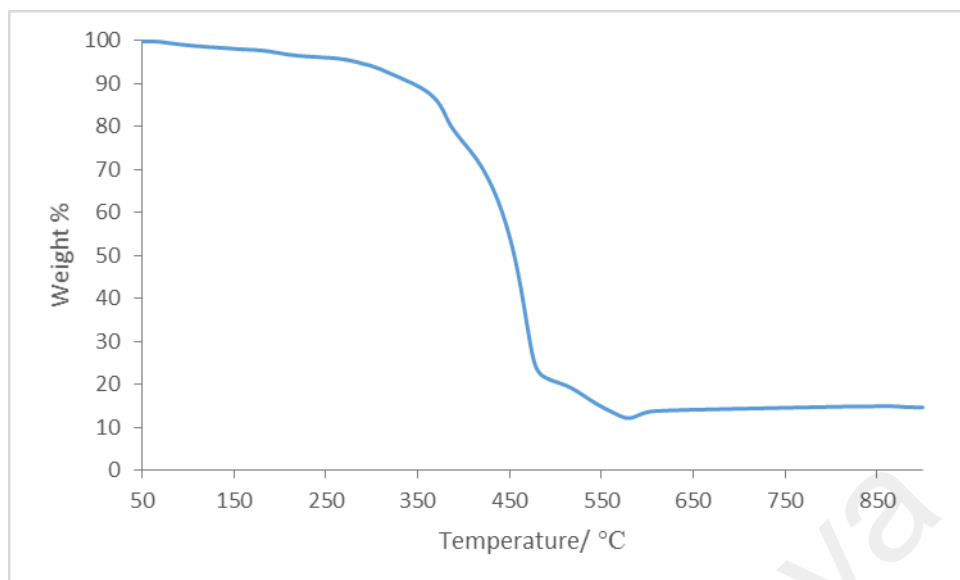


**Figure 4.106** TGA of **Complex 13**

*(e) Mesomorphic properties*

Its DSC spectrum (**Figure 4.107**) was recorded for heating-cooling cycle from 25 °C to 220 °C. On heating there were three endothermic peaks at 84.6 °C ( $\Delta H = +2.3 \text{ kJ mol}^{-1}$ ), 99.8 °C ( $\Delta H = +7.4 \text{ kJ mol}^{-1}$ ), and 123.7 °C ( $\Delta H = +1.5 \text{ kJ mol}^{-1}$ ), assigned as the breaking of weak bonds. On cooling, there were no peaks.

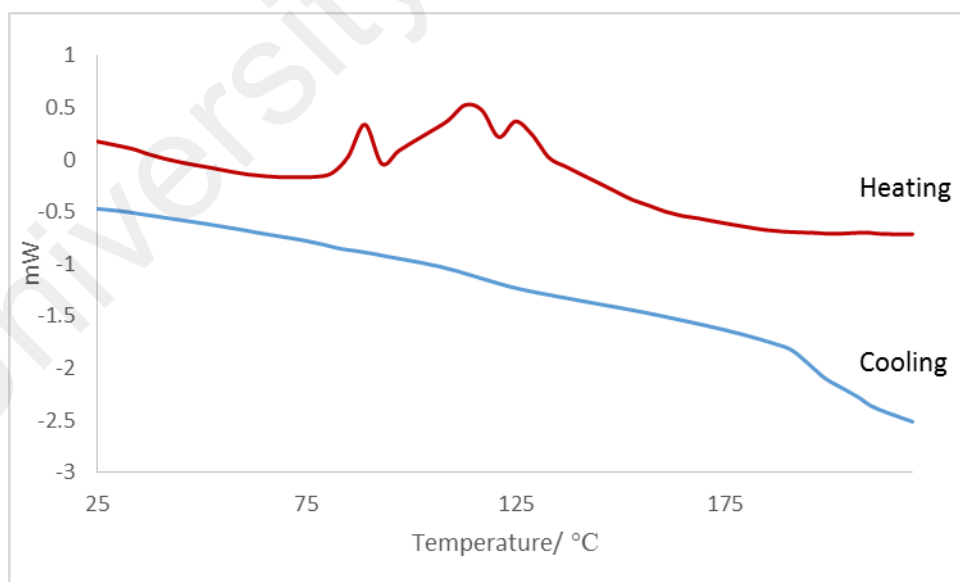


**Figure 4.107** DSC of **Complex 13**

Viewed under **OPM**, which was recorded for heating-cooling cycle from 25 °C to 220 °C, the complex did not show any optical textures. Hence, **Complex 13** did not exhibit mesomorphism.

#### 4.4.5 $[Fe(CH_3COO)(HL3)(H_2O)_2].3H_2O$

The Fe(II) complex of H<sub>2</sub>L3 was also synthesised by the one-pot method involving H<sub>2</sub>N(CH<sub>2</sub>)<sub>8</sub>NH<sub>2</sub>, 3,5-di(*tert*-butyl)-2-hydroxybenzaldehyde and [Fe(CH<sub>3</sub>COO)<sub>2</sub>] in ethanol. The product was a dark brown reddish powder, and the yield was 67.4%. It was soluble in chloroform and THF, and insoluble in other common organic solvents.

##### (a) Structural deduction

Based on the same instrumental analyses, it is proposed that the structural formula of the complex was [Fe(CH<sub>3</sub>COO)(HL3)(H<sub>2</sub>O)<sub>2</sub>].3H<sub>2</sub>O, which is similar to **Complex 4** ([Fe(CH<sub>3</sub>COO)(HL1)]) and **9** ([Fe(CH<sub>3</sub>COO)(HL2)].3H<sub>2</sub>O). Hence, it was mononuclear and the Schiff base (H<sub>2</sub>L3) was only partially deprotonated.

The results from the **elemental analyses** (61.39% C, 9.22% H, 4.31% N) were in good agreement with the chemical formula FeC<sub>40</sub>H<sub>72</sub>N<sub>2</sub>O<sub>9</sub> (780.85 g mol<sup>-1</sup>; 61.53% C, 9.29% H, 3.59% N).

Its **FTIR** spectrum (**Figure 4.108**) shows peaks for the expected functional groups and bonds at similar wavenumbers (3212 cm<sup>-1</sup>, 2939 cm<sup>-1</sup>, 2860 cm<sup>-1</sup>, 1610 cm<sup>-1</sup>, 1548 cm<sup>-1</sup>, and 1408 cm<sup>-1</sup>) as the corresponding metal complexes. From the latter peaks, the  $\Delta\nu_{COO}$  value was 140 cm<sup>-1</sup>, suggesting chelating binding mode for CH<sub>3</sub>COO<sup>-</sup> ion.

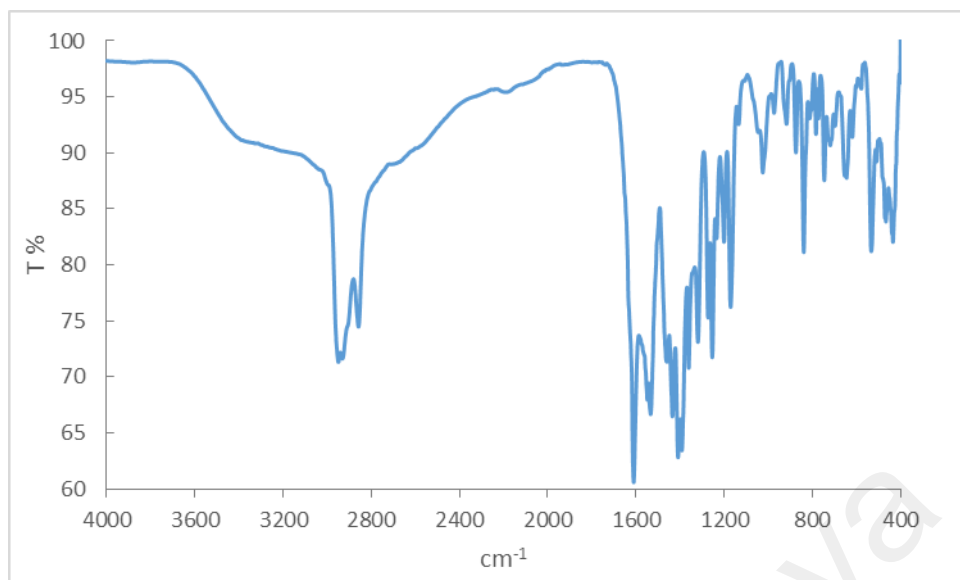


**Figure 4.108** FTIR spectrum for **Complex 14**

Its **UV-visible** spectrum (**Figure 4.109**), recorded in chloroform, shows MLCT bands at 328 nm ( $\epsilon_{\max} = 9406 \text{ M}^{-1} \text{ cm}^{-1}$ ), 454 nm ( $\epsilon_{\max} = 1872 \text{ M}^{-1} \text{ cm}^{-1}$ ) and 532 nm ( $\epsilon_{\max} = 2293 \text{ M}^{-1} \text{ cm}^{-1}$ ), and no *d-d* band up to 900 nm. This suggests that the complex has a high spin Fe(II) atom.

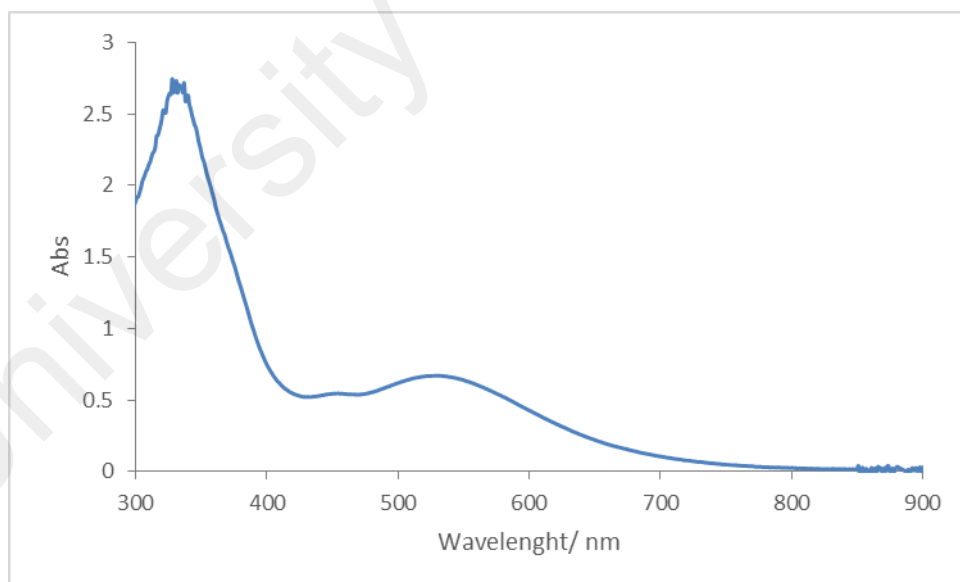


**Figure 4.109** UV-visible spectrum of **Complex 14**

Combining the results of elemental analyses and FTIR and UV-visible spectroscopies, the proposed structural formula for the complex is shown in **Figure 4.110**.

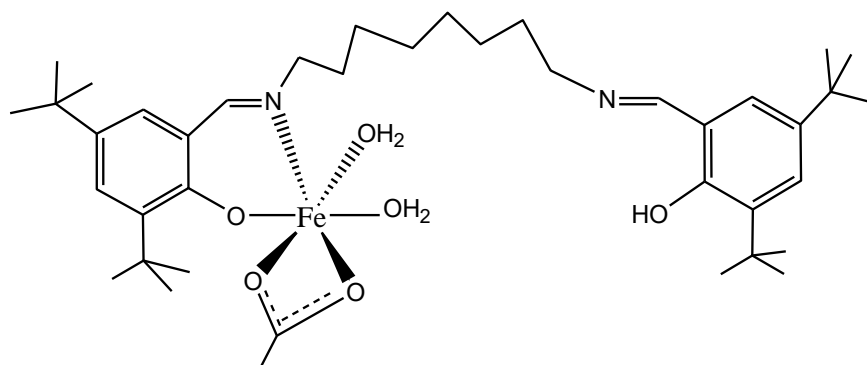


**Figure 4.110** Proposed structure for **Complex 14** (lattice H<sub>2</sub>O molecules are not shown)

(b) *Determination of bandgaps*

Its  $E_o$  value, calculated as before from its UV-vis spectrum, was 1.94 eV ( $\lambda = 640$  nm).

Its **fluorescence** spectrum (**Figure 4.111**) was recorded in chloroform. Upon excitation at 532 nm (MLCT band), it shows an emission peak at 549 nm. Hence, its Stokes shift was 17 nm. Additionally, its  $E_o$ , was 2.22 eV ( $\lambda = 558$  nm).

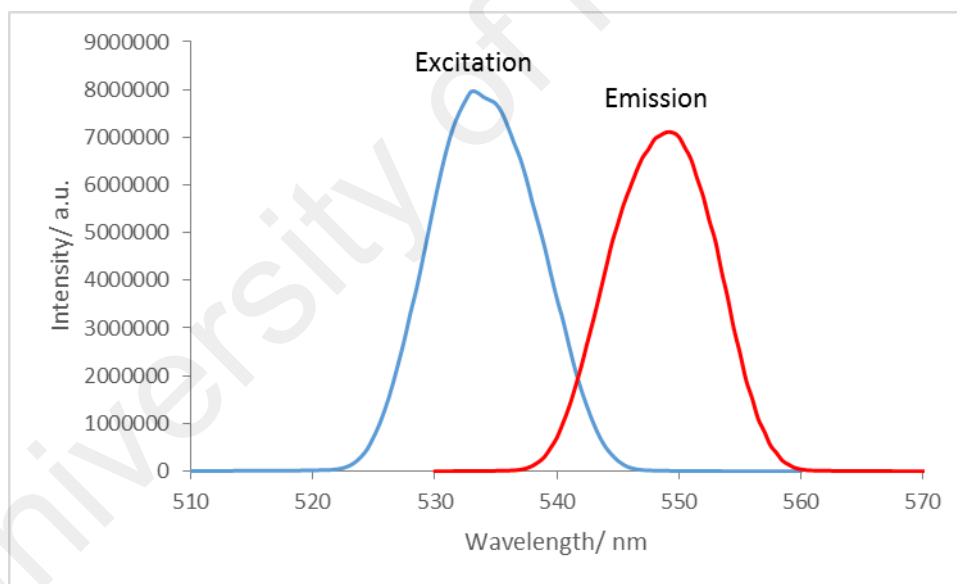


**Figure 4.111** Fluorescence spectrum of **Complex 14** after excitation at 532 nm

Its  $\tau$  value, calculated from its decay curve (**Figure 4.112**) was 0.7 ns

( $\lambda_{emission} = 549$  nm).

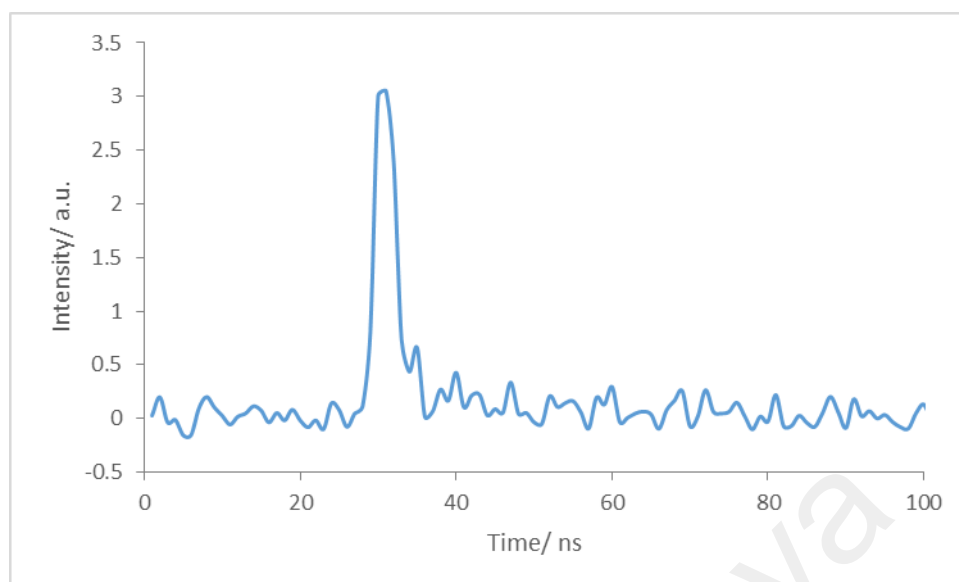


**Figure 4.112** Fluorescence decay of **Complex 14** at  $\lambda_{emission} = 549$  nm

Its CV (**Figure 4.113**) was recorded anodically in chloroform at a scan rate  $50 \text{ mV s}^{-1}$  in the potential range of  $+1.5 \text{ V}$  to  $-1.5 \text{ V}$ . The voltammogram does not show any peaks. Hence, its electrochemical band gap cannot be calculated.

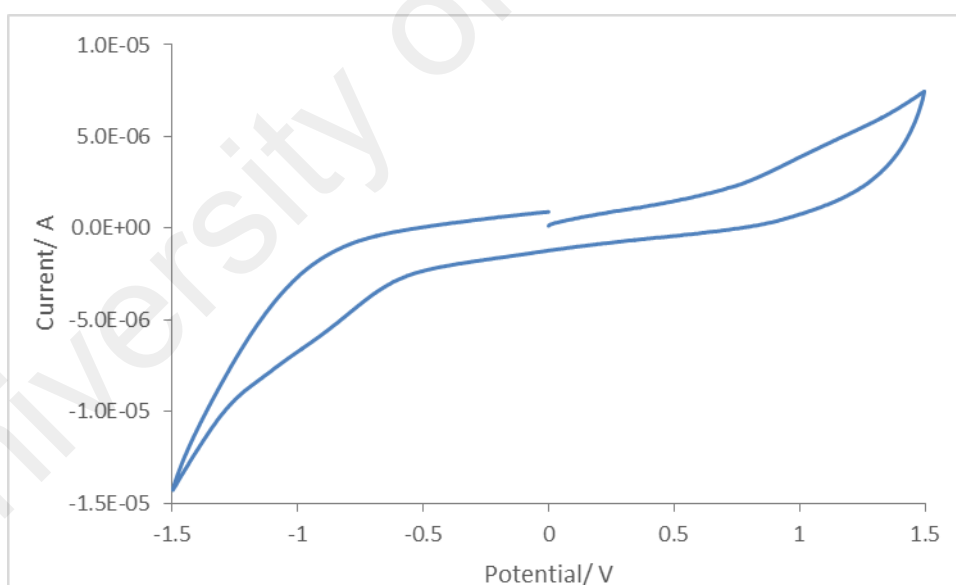


**Figure 4.113** Cyclic voltammogram for **Complex 14**

*(c) Magnetic properties*

Its  $\chi_m^{corr}T$  value, calculated as before from the values of  $FM = 780.85 \text{ g mol}^{-1}$ ,  $\chi_g = 1.07 \times 10^{-5} \text{ cm}^3 \text{ g}^{-1}$ ,  $\chi_m = 8.32 \times 10^{-3} \text{ cm}^3 \text{ mol}^{-1}$ ,  $\chi_{dia} = -4.56 \times 10^{-4} \text{ cm}^3 \text{ mol}^{-1}$ , and  $\chi_m^{corr} = 8.78 \times 10^{-3} \text{ cm}^3 \text{ mol}^{-1}$ , was  $2.6 \text{ cm}^3 \text{ K mol}^{-1}$  at  $298 \text{ K}$ . From this, it may be inferred

that this complex was made up of 87% HS and 13% LS Fe(II) at room temperature, in agreement with the data from UV-vis spectroscopy.

*(d) Thermal properties*

Its TGA trace (**Figure 4.114**) shows an initial weight loss of 2.3% from about 50 °C to 192 °C due to loss of lattice H<sub>2</sub>O molecules (calculated, 6.9%). The lower than calculated value suggests loss of lattice H<sub>2</sub>O molecules on storage. The next weight loss of 6.5% from 192 °C to 285 °C was due to the evaporation of coordinated H<sub>2</sub>O molecules (calculated, 6.9%). The final weight loss of 83.1% (285 °C to 793 °C) was due to the decomposition of HL<sup>3-</sup> and CH<sub>3</sub>COO<sup>-</sup> ions (calculated, 81.4%). The amount of residue at temperatures above 793 °C was 8.1%, which is in a good agreement with the calculated 9.2% (assuming pure FeO) [99]. Hence, the complex was thermally stable up to 192 °C.

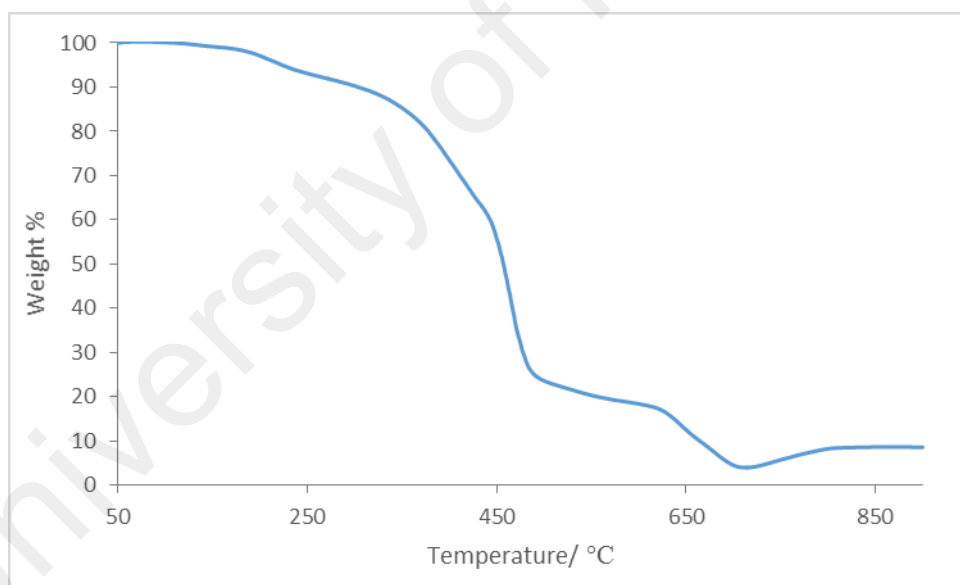


**Figure 4.114** TGA of Complex 14

*(e) Mesomorphic properties*

Its DSC spectrum (**Figure 4.115**) was recorded for heating-cooling cycle from 25 °C to 250 °C. On heating there were three endothermic peaks at 138.13 °C ( $\Delta H = +1.0 \text{ kJ mol}^{-1}$ ), 154.9 °C ( $\Delta H = +0.3 \text{ kJ mol}^{-1}$ ), 176.2 °C ( $\Delta H = +17.0 \text{ kJ mol}^{-1}$ )

assigned as evaporation of water molecules, crystal-to-crystal transition, and breaking of H-bond, respectively. On cooling, there were no peaks.

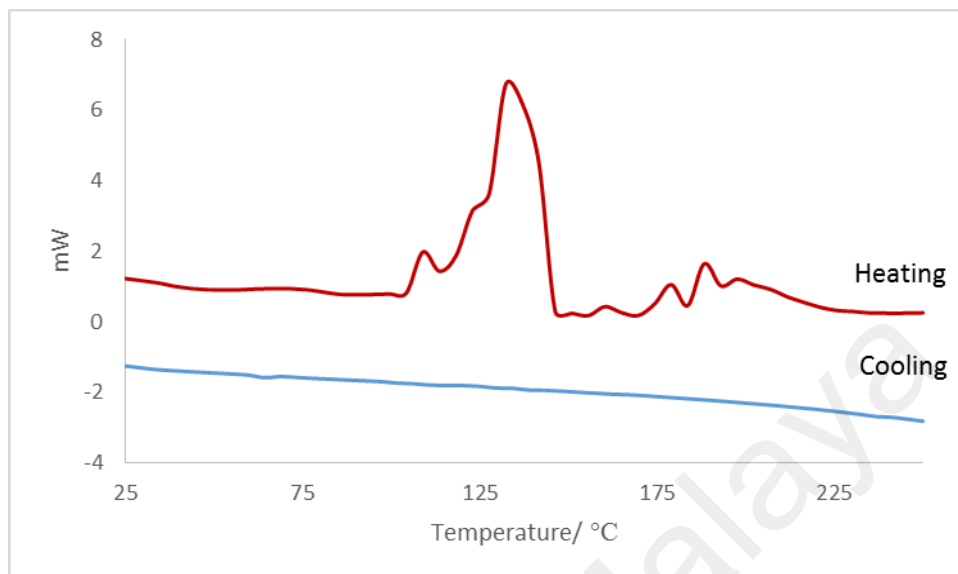


**Figure 4.115** DSC of **Complex 14**

Viewed under **OPM**, which was recorded for heating-cooling cycle from 25 °C to 250 °C, the complex did not show any optical textures. Hence, **Complex 14** did not exhibit mesomorphism.

#### **4.4.6** $[Mn(HL3)_2(H_2O)_2]$

The Mn(II) complex of H<sub>2</sub>L3 was also synthesised by the one-pot method involving the reaction of H<sub>2</sub>N(CH<sub>2</sub>)<sub>8</sub>NH<sub>2</sub>, 3,5-di(*tert*-butyl)-2-hydroxybenzaldehyde and [Mn(CH<sub>3</sub>COO)<sub>2</sub>].4H<sub>2</sub>O in ethanol. The product was a dark brown powder (**Complex 15**), and the yield was 29.6%. It was soluble in chloroform and insoluble in other organic solvents.

##### *a) Structural deduction*

Based on the instrumental data discussed below, the structural formula of the complex is [Mn(HL3)<sub>2</sub>(H<sub>2</sub>O)<sub>2</sub>]. Hence, it was mononuclear and the Schiff base (H<sub>2</sub>L3) was only partially deprotonated.

The results from the **elemental analyses** (73.19% C, 9.65% H, 3.76% N) were in good agreement with the chemical formula  $\text{MnC}_7\text{H}_{12}\text{N}_4\text{O}_6$  (1242.74 g mol<sup>-1</sup>; 73.45% C, 9.89% H, 4.51% N).

Its **FTIR** spectrum (**Figure 4.116**) shows peaks for the expected functional groups and bonds at similar wavenumbers (3419 cm<sup>-1</sup>, 2952 cm<sup>-1</sup>, 2859 cm<sup>-1</sup> and 1616 cm<sup>-1</sup>) as the corresponding metal complexes.

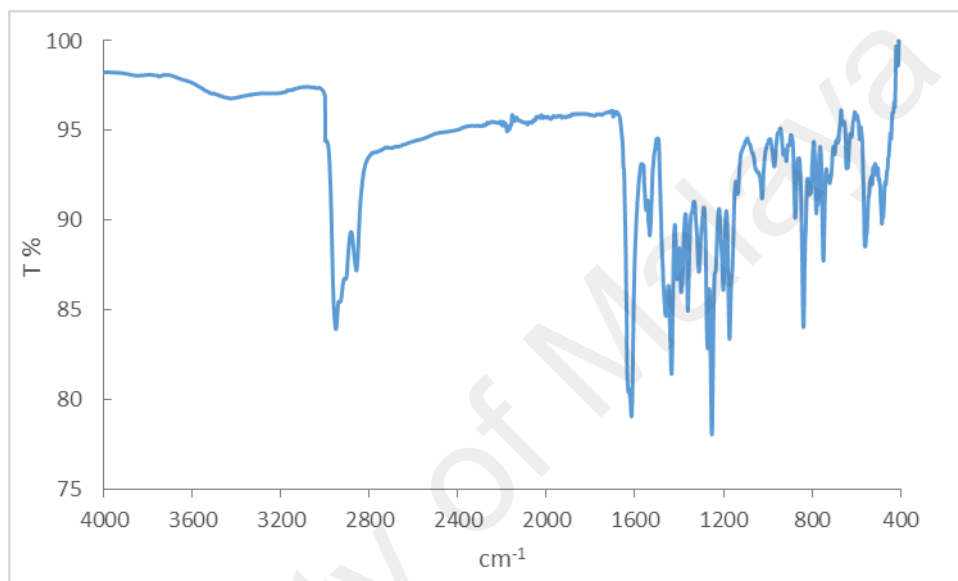


**Figure 4.116** FTIR spectrum for **Complex 15**

Its **UV-visible** spectrum was recorded in chloroform (**Figure 4.117**). The spectrum shows two *d-d* bands at 701 nm ( $\epsilon_{\text{max}} = 361 \text{ M}^{-1} \text{ cm}^{-1}$ ) and 562 nm ( $\epsilon_{\text{max}} = 511 \text{ M}^{-1} \text{ cm}^{-1}$ ), and a MLCT band at 417 nm ( $\epsilon_{\text{max}} = 4431 \text{ M}^{-1} \text{ cm}^{-1}$ ). These suggest that the geometry of Mn(II) in the complex was octahedral [109].

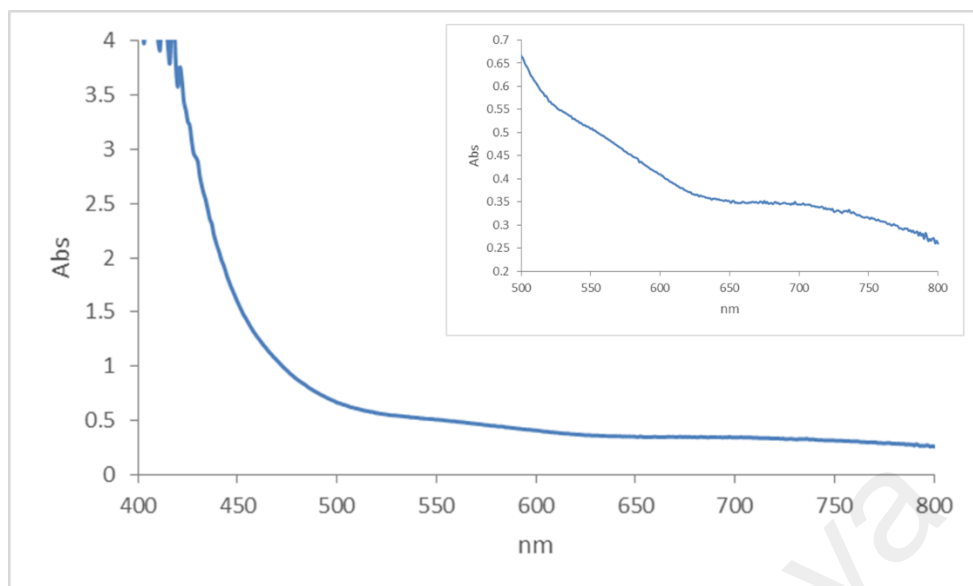


**Figure 4.117** UV-visible spectrum of **Complex 15**

Combining the results of elemental analyses and FTIR and UV-visible spectroscopies, the proposed structural formula of the complex is shown in **Figure 4.118**.

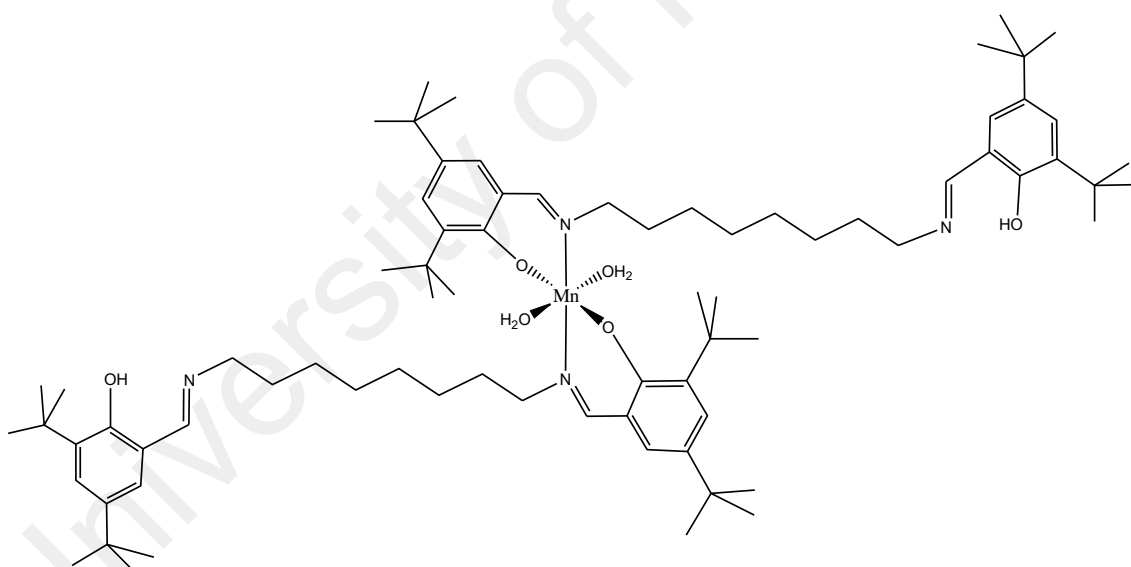


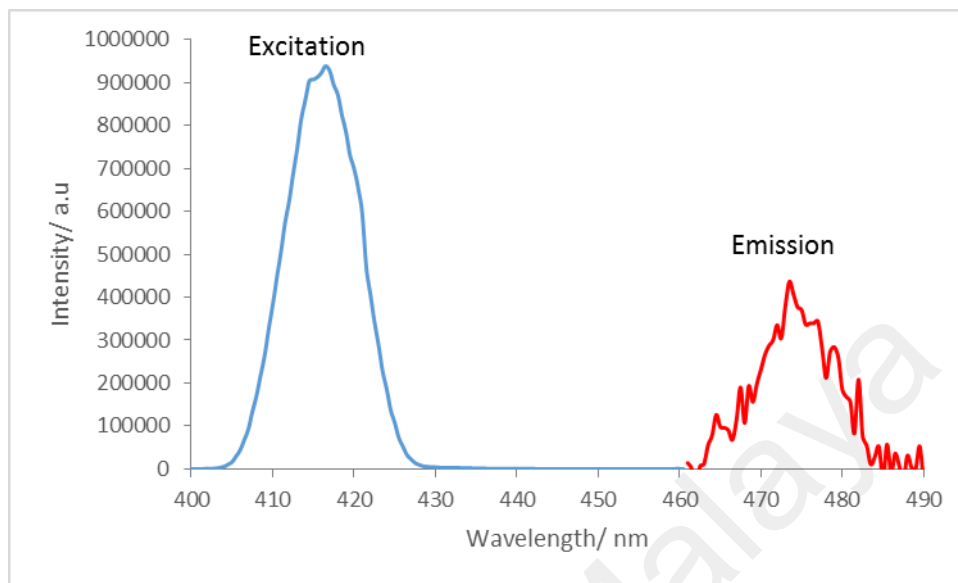
**Figure 4.118** Proposed structure for **Complex 15**

(b) *Determination of bandgaps*

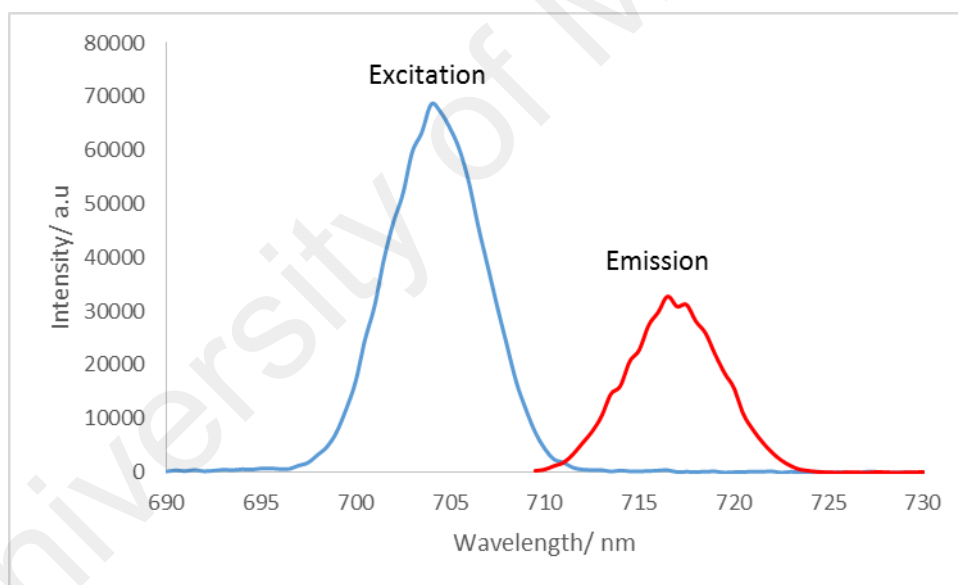
Its  $E_o$  value, calculated as before from its UV-vis spectrum, was 2.62 eV ( $\lambda = 474$  nm).

Its **fluorescence** spectra (**Figure 4.119**) were recorded in chloroform. Upon excitation at 416 nm (MLCT band), it shows an emission peak at 473 nm, while upon

excitation at 704 nm (*d-d* band), it shows an emission peak at 717 nm. Hence, its Stokes shifts were 57 nm and 13 nm, respectively. Additionally, its  $E_o$  was 2.55 eV ( $\lambda = 486$  nm).



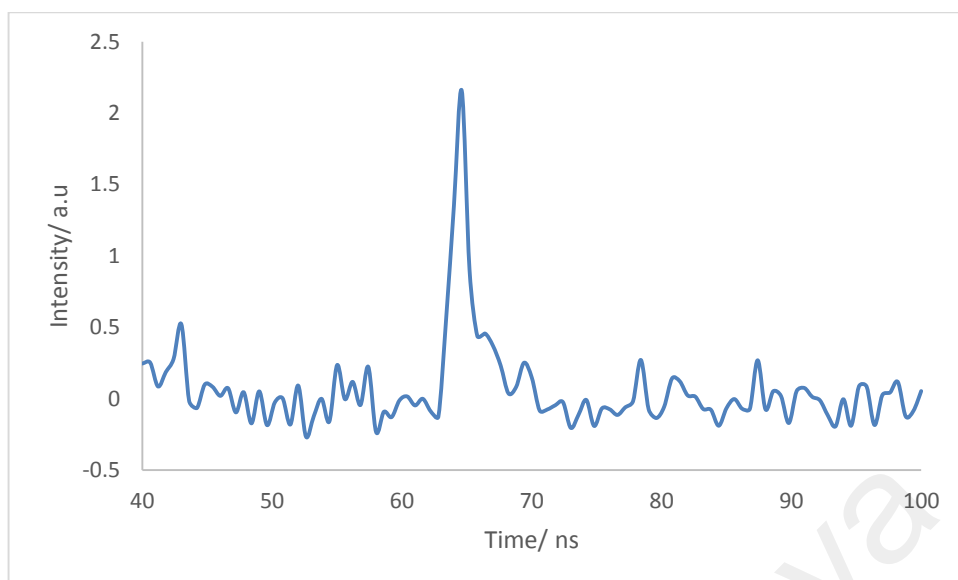
(a)



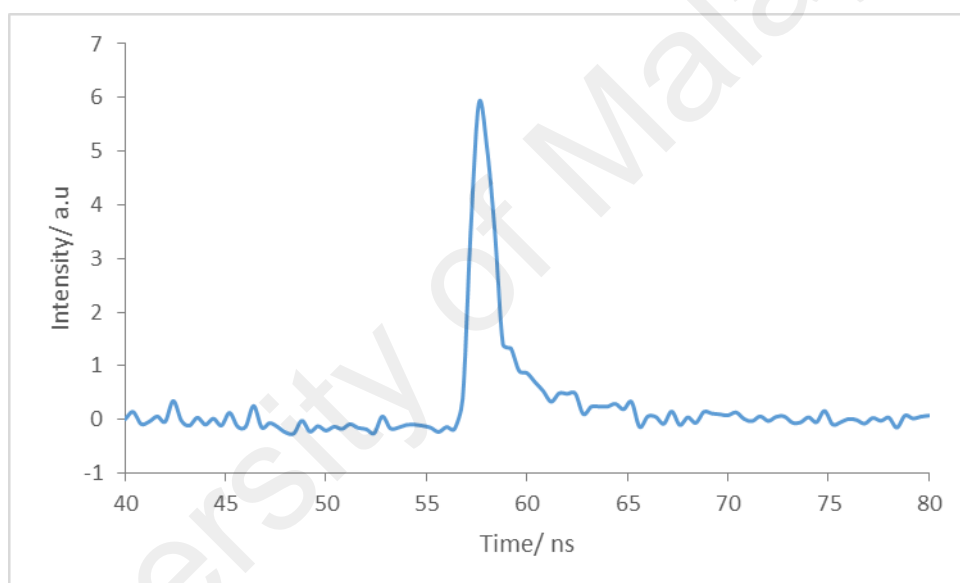
(b)

**Figure 4.119** Fluorescence spectra of **Complex 15** upon excitation at: (a) 416 nm, and (b) 704 nm

Its  $\tau$  value, calculated from its decay curve (**Figure 4.120**) was 1.7 ns ( $\lambda_{emission} = 473$  nm) and 1.2 ns ( $\lambda_{emission} = 717$  nm).



(a)



(b)

**Figure 4.120** Fluorescence decay of **Complex 15** at  $\lambda_{emission}$ : (a) 473 nm, and (b) 717 nm

Its CV was recorded anodically in chloroform at a scan rate  $50 \text{ mV s}^{-1}$  in the potential range of +1.5 V to -1.5 V. The voltammogram (**Figure 4.121**) shows an anodic peak at +0.44 V assigned to the oxidation of [Mn(II)] to [Mn(III)] and a cathodic peak at -1.20 V assigned to the reduction of [Mn(III)] to [Mn(II)]. The  $\Delta E_p$  was 1640 mV, indicating a quasireversible redox reaction ( $\Delta E_p > 59 \text{ mV}$  at  $30 \text{ }^\circ\text{C}$ ) and its  $I_{pc}/I_{pa}$  ratio is 0.2 indicating the oxidised complex was chemically unstable. The HOMO and LUMO of

the complex is 0.25 V and -0.75 V, respectively. Hence, the  $E_e$  value of the complex was 1.0 eV.

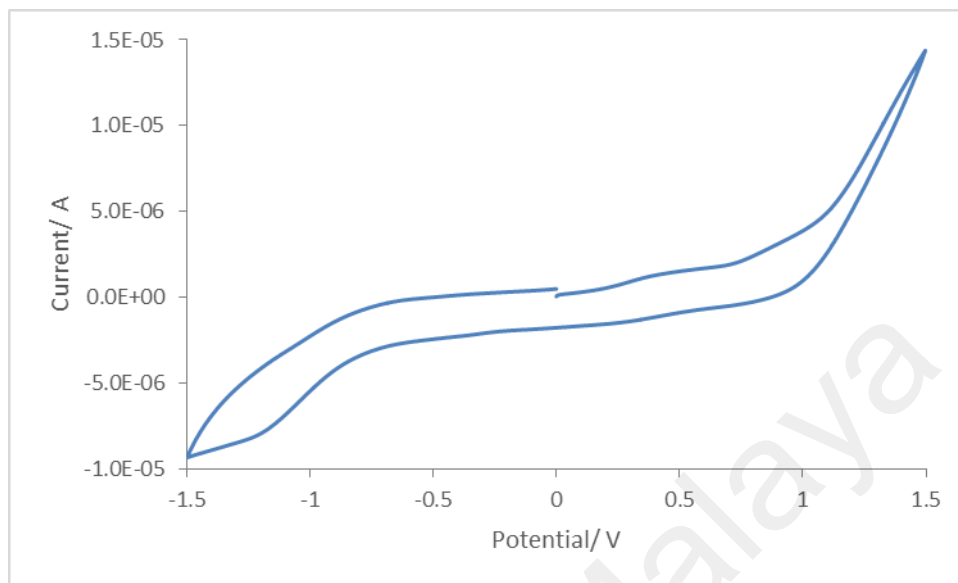


**Figure 4.121** Cyclic voltammogram for **Complex 15**

*(c) Magnetic properties*

Its  $\chi_m^{corr}T$  value, calculated as before from the values of FM = 1242.74 g mol<sup>-1</sup>,  $\chi_g = 0.841 \times 10^{-5}$  cm<sup>3</sup> g<sup>-1</sup>,  $\chi_m = 1.02 \times 10^{-2}$  cm<sup>3</sup> mol<sup>-1</sup>,  $\chi_{dia} = -7.70 \times 10^{-4}$  cm<sup>3</sup> mol<sup>-1</sup>, and  $\chi_m^{corr} = 1.12 \times 10^{-2}$  cm<sup>3</sup> mol<sup>-1</sup>, was 3.34 cm<sup>3</sup> K mol<sup>-1</sup>. From this, it may be inferred that this complex was made up of 74% HS and 26% LS Mn(II) at room temperature.

*(d) Thermal properties*

Its TGA trace (**Figure 4.122**) shows a gradual weight loss of 91.3% from 279 °C to 766 °C due to evaporation of two coordinated H<sub>2</sub>O molecules and decomposition of two HL3<sup>-</sup> ligands (calculated, 95.6%). The amount of residue at temperature 766 °C was 8.7%, which is in a good agreement with the calculated 6.4% (assuming pure Mn<sub>2</sub>O<sub>3</sub>). Hence, the complex was thermally stable up to 279 °C.

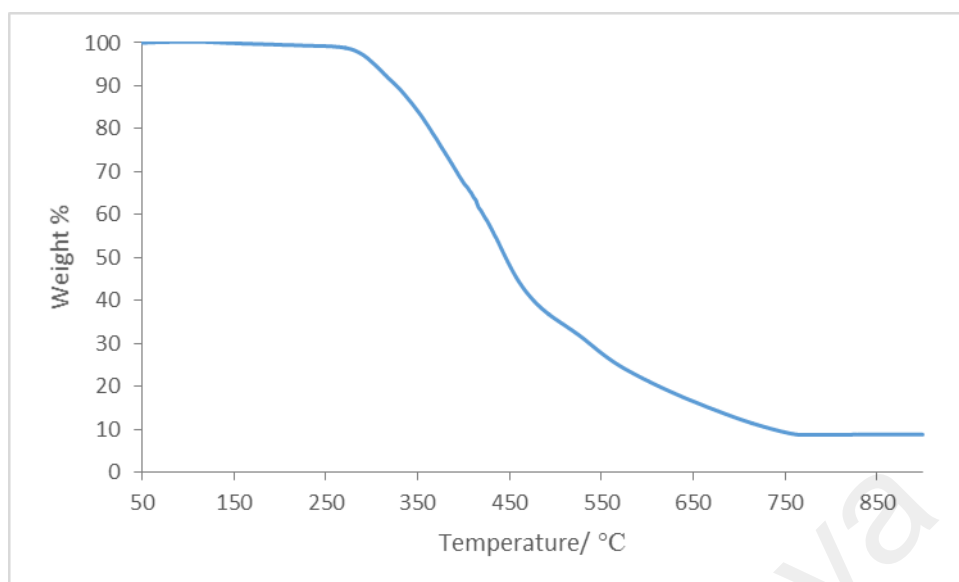


**Figure 4.122** TGA of **Complex 15**

*(e) Mesomorphic properties*

Its DSC spectrum (**Figure 4.123**) was recorded for heating-cooling cycle from 25 °C to 250 °C. On heating, there were three overlapping endothermic peaks at 90.5 °C ( $\Delta H = +5.9 \text{ kJ mol}^{-1}$ ), 165.8 °C ( $\Delta H = +1.7 \text{ kJ mol}^{-1}$ ) and 200.8 °C ( $\Delta H = +3.8 \text{ kJ mol}^{-1}$ ), assigned as the breaking of weak bonds. On cooling, there were no peaks.

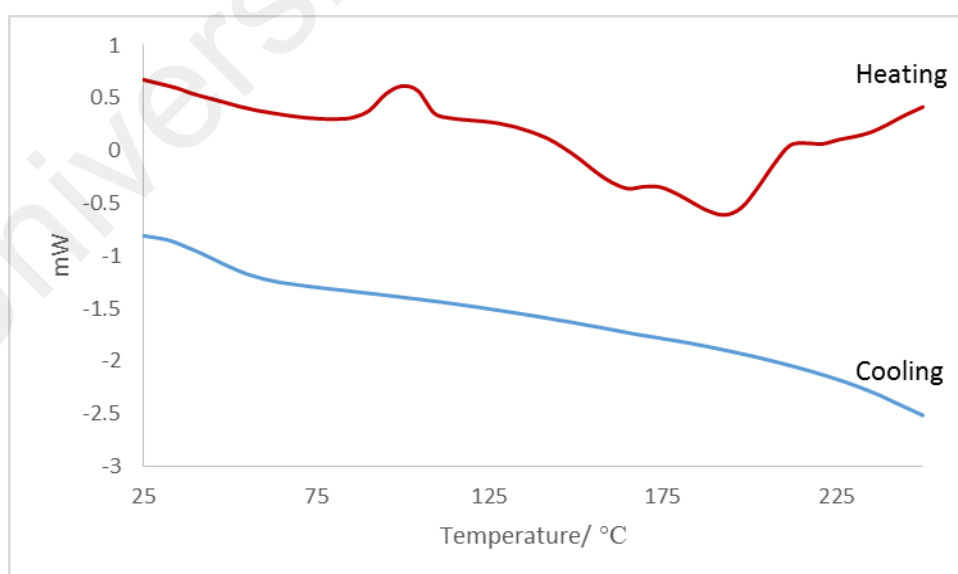


**Figure 4.123** DSC of **Complex 15**

Viewed under **OPM**, which was recorded for heating-cooling cycle from 25 °C to 250 °C, the complex did not show any optical textures. Hence, **Complex 15** did not exhibit mesomorphism.

#### **4.4.7 Summary**

The analytical results for **Complexes 11-15** are summarised in **Table 4.9**. All complexes, except for **Complex 13**, were mononuclear. **Complex 13** was dinuclear. All complexes were paramagnetic.

The optical bandgaps (from the CT absorption bands and emission bands) for all complexes were similar (1.94 eV– 2.85 eV). Hence, these complexes were semiconductors and have potential as solar cell materials [49].

Except for **Complex 13**, the lifetimes of all excited complexes were similar (0.7 ns to 1.7 ns). The lifetime for **Complex 13** was the longest at 3.9 ns. These lifetimes were sufficiently long to allow for electronic injection from absorbed dyes into nanocrystalline TiO<sub>2</sub>. The Stokes shift values for all complexes were in the range of 21-90 nm (CT transition) and 3-17 nm (*d-d* transition).

All complexes were thermally stable. Their decomposition temperatures range from 251 °C to 285 °C. Finally, all complexes did not exhibit mesomorphism.

**Table 4.9** Analytical results for metal(II) complexes of  $H_2L3$

Complex		11	12	13	14	15
Chemical Formula		$[Cu(L3)]$	$[Ni_2(L3)]$	$[Co_2(CH_3COO)_2(L3)].3H_2O$	$[Fe(CH_3COO)(HL3)(H_2O)_2].3H_2O$	$[Mn_2(HL3)(H_2O)_2]$
CH <sub>3</sub> COO mode		-	-	chelating		-
Geometry		square pyramidal	square planar	distorted tetrahedral	octahedral	octahedral
E <sub>o</sub> (eV)	absorption	2.29	2.67	2.85	1.94	2.62
	emission	2.39	2.89	3.00	2.22	2.55
	electrochemical	-	-	0.48	-	1.0
Stokes Shift (nm) CT, <i>d-d</i>		90, 6	21, 3	37, 18	17	57, 13
τ (ns)		1.3, 1.0	1.0	3.9, 3.2	0.7	1.7, 1.2
CV		redox inactive		redox active	redox inactive	redox active
μ <sub>eff</sub> (B.M.)		1.78	0.97	7.44	87% HS, 13LS	74% HS, 26% LS
T <sub>dec</sub> (°C)		280	283	251	285	279
Mesomorphism		Non-mesomorphic				

## 4.5 Cyclam and its Metal(II) Palmitate Complexes

### 4.5.1 $[\text{Ni}(\text{CH}_3(\text{CH}_2)_{14}\text{COO})(\text{cyclam})(\text{H}_2\text{O})](\text{CH}_3(\text{CH}_2)_{14}\text{COO})\cdot 4\text{H}_2\text{O}$

$[\text{Ni}(\text{CH}_3(\text{CH}_2)_{14}\text{COO})_2(\text{H}_2\text{O})_2]$  and cyclam reacted in ethanol to form brown crystals (**Complex 16**) in good yield (56.0 %). It was soluble in methanol, ethanol, and chloroform, but insoluble in other organic solvents.

#### (a) Structural deduction

The structural formula of **Complex 16** was ascertained by elemental analyses and IR spectroscopy, and confirmed by X-ray crystallography.

The results from the **elemental analyses** (58.38% C, 10.99% H, 7.21% N) were in good agreement with the chemical formula  $\text{NiC}_{42}\text{H}_{96}\text{N}_4\text{O}_9$  (58.66% C, 11.25% H, 6.52% N).

Its **FTIR** spectrum (**Figure 4.124**) shows a broad peak at  $3381\text{ cm}^{-1}$  for OH group, two peaks at  $2915\text{ cm}^{-1}$  and  $2850\text{ cm}^{-1}$  for  $\text{CH}_2$  ( $\nu_{\text{as}}$ ) and  $\text{CH}_2$  ( $\nu_{\text{s}}$ ), and peaks for  $\nu_{\text{asym}}\text{COO}$  at  $1650$  and  $1558\text{ cm}^{-1}$ , and  $\nu_{\text{sym}}\text{COO}$  at  $1391\text{ cm}^{-1}$ . Accordingly, from the latter peaks, the  $\Delta\nu_{\text{COO}}$  value were  $259\text{ cm}^{-1}$  and  $167\text{ cm}^{-1}$ , suggesting the presence of both monodentate  $\text{CH}_3(\text{CH}_2)_{14}\text{COO}^-$  ligand and  $\text{CH}_3(\text{CH}_2)_{14}\text{COO}^-$  ion, respectively.

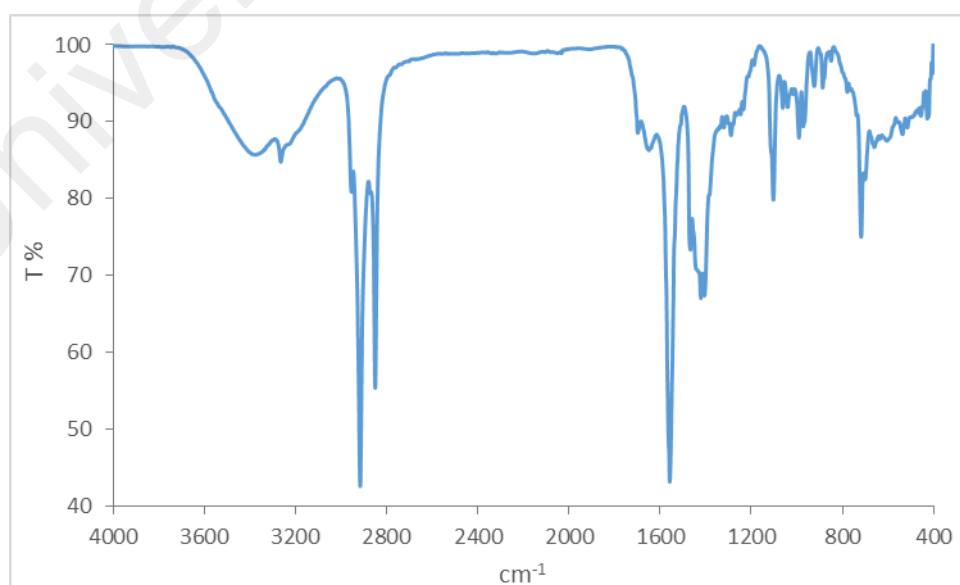


**Figure 4.124** The FTIR spectrum of **Complex 16**

The crystallographic and structure refinement data for **Complex 16** is given in **Table 4.10** and selected bond lengths and angles are given in **Table 4.11**. The molecular structure and the packing diagram are shown in **Figures 4.125** and **Figures 4.126**, respectively. The molecular structure shows that the complex was made up of  $[\text{Ni}(\text{CH}_3(\text{CH}_2)_{14}\text{COO})(\text{cyclam})(\text{H}_2\text{O})]^+$  cation,  $\text{CH}_3(\text{CH}_2)_{14}\text{COO}^-$  anion and four lattice  $\text{H}_2\text{O}$ . The Ni(II) atom was coordinated to cyclam through its four *aza*-N atoms of cyclam, one O atom of  $\text{CH}_3(\text{CH}_2)_{14}\text{COO}^-$  ion and one O atom of  $\text{H}_2\text{O}$  ligands ( $\text{NiN}_4\text{O}_2$  chromophore).

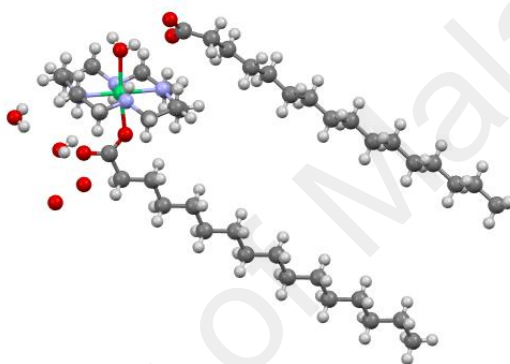


**Figure 4.125** An ORTEP presentation of **Complex 16** along *b*-axis. The probability level was 30%.

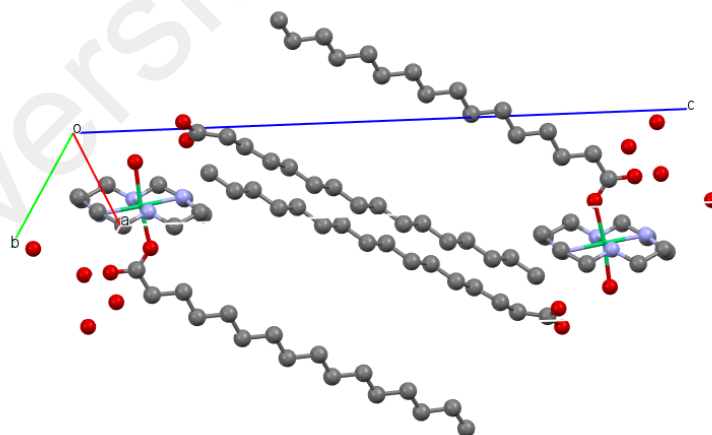


**Figure 4.126** The packing diagram viewed along the *b*-axis (H atoms are omitted for clarity).

**Table 4.10** Crystal data and structure refinement for **Complex 16**

Chemical formula	C <sub>42</sub> H <sub>92</sub> N <sub>4</sub> NiO <sub>9</sub>
Formula weight (g mol <sup>-1</sup> )	855.90
Temperature (K)	293(2)
Wavelength(Å)	0.71073
Crystal system, space group	Triclinic, <i>P</i> -1
Unit cell dimension	$a$ (Å) = 8.7722(4) (4) $\alpha$ (°) = 90.283(3) $b$ (Å) = 9.3242(4) $\beta$ (°) = 97.177(3) $c$ (Å) = 32.2381(11) $\gamma$ (°) = 113.61(4)
Volume (Å <sup>3</sup> )	2392.70(18)
Z, Calculated density (g cm <sup>-3</sup> )	2, 1.188
Absorption coefficient (mm <sup>-1</sup> )	0.458
<i>F</i> (000)	944
Theta range for data collection (°)	2.870 - 25.990
Index ranges	-10 ≤ <i>h</i> ≤ 10; -11 ≤ <i>k</i> ≤ 11; -39 ≤ <i>l</i> ≤ 39
Reflections collected	22203
Independent reflections	9401 (0.0278)
Data/restraints/parameters	9401/3/546
Goodness-of-fit on <i>F</i> <sup>2</sup>	0.890
Final <i>R</i> indices	R1 = 0.0626,
[ <i>I</i> ≥ 2.0σ( <i>I</i> )]	wR2 = 0.1609
<i>R</i> indices (all data)	R1 = 0.0722, wR2 = 0.1708
Δρ <sub>max</sub> , Δρ <sub>min</sub> (e Å <sup>-3</sup> )	1.785, -1.082

**Table 4.11** Selected bond lengths (Å) and angles (°) for **Complex 16**

Bond length			
N(1)-Ni(01)	2.063(3)	N(4)-Ni(01)	2.096(2)
N(2)-Ni(01)	2.063(2)	O(1)-Ni(01)	2.156(2)
N(3)-Ni(01)	2.056(2)	O(2)-Ni(01)	2.1183(19)
Angles			
C(10)-N(1)-Ni(01)	116.29(19)	N(3)-Ni(01)-N(1)	179.08(10)
C(1)-N(1)-Ni(01)	106.06(18)	N(3)-Ni(01)-N(2)	95.29(10)
Ni(01)-N(1)-H(1)	105(2)	N(1)-Ni(01)-N(2)	85.24(10)
C(2)-N(2)-Ni(01)	106.02(17)	N(3)-Ni(01)-N(4)	85.28(9)
C(3)-N(2)-Ni(01)	115.84(18)	N(1)-Ni(01)-N(4)	94.18(10)
Ni(01)-N(2)-H(2)	99(2)	N(2)-Ni(01)-N(4)	178.85(9)
C(6)-N(3)-Ni(01)	106.19(18)	N(3)-Ni(01)-O(2)	88.61(9)
C(5)-N(3)-Ni(01)	116.5(2)	N(1)-Ni(01)-O(2)	92.10(9)
Ni(01)-N(3)-H(3)	108(2)	N(2)-Ni(01)-O(2)	94.65(9)
C(7)-N(4)-Ni(01)	105.29(17)	N(4)-Ni(01)-O(2)	86.36(9)
C(8)-N(4)-Ni(01)	114.61(18)	N(3)-Ni(01)-O(1)	91.58(10)
Ni(01)-N(4)-H(4)	108(2)	N(1)-Ni(01)-O(1)	87.67(10)
Ni(01)-O(1)-H(1C)	133(4)	N(2)-Ni(01)-O(1)	91.03(9)
Ni(01)-O(1)-H(1D)	113(3)	N(4)-Ni(01)-O(1)	87.95(9)
C(11)-O(2)-Ni(01)	135.26(18)	O(2)-Ni(01)-O(1)	174.28(8)

Its **UV-visible** spectrum (**Figure 4.127**), in methanol, shows a *d-d* band at 441 nm ( $\epsilon_{\max} = 338 \text{ M}^{-1} \text{ cm}^{-1}$ ) assigned to  ${}^3\text{A}_{2g}(\text{F})$  to  ${}^3\text{T}_{1g}(\text{P})$  transition, suggesting an octahedral geometry at Ni(II) centre [112,113]. Another possible peak at around 750 nm and 500 nm may not be observed because it is towards the NIR region. Hence, its crystal structure, which shows octahedral geometry, was maintained in solution.

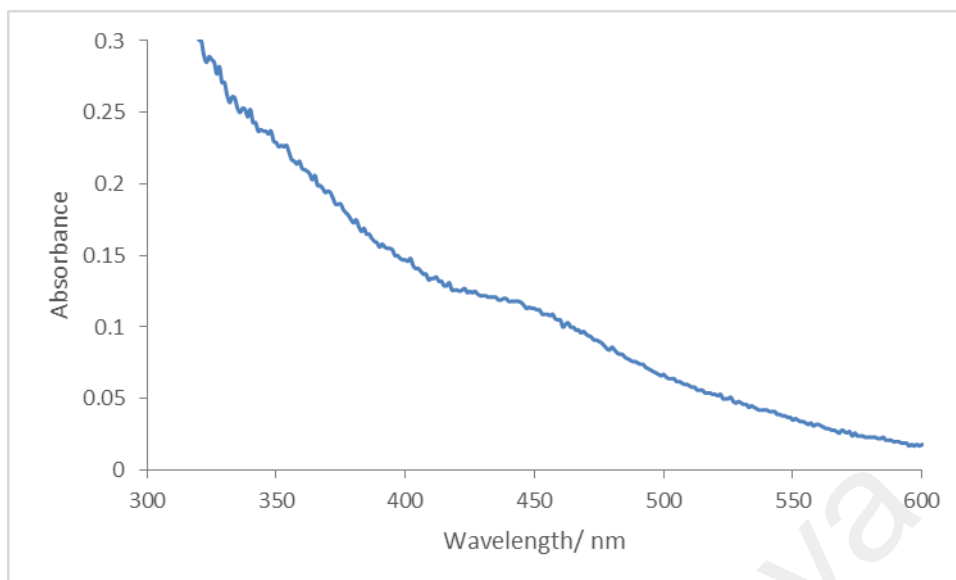


**Figure 4.127** UV-visible spectrum of **Complex 16**

*(b) Determination of bandgaps*

Its  $E_o$  value, calculated as before from the UV-vis spectrum, was 3.6 eV (356 nm).

Its CV scan was recorded anodically in chloroform at a scan rate of  $50 \text{ mV s}^{-1}$  in the potential range of +1.0 V to -1.0 V. The voltammogram (**Figure 4.128**) shows an anodic peak at +0.51 V and a cathodic peak at +0.40 V assigned to the oxidation of [Ni(II)] to [Ni(III)] and reduction [Ni(III)] to [Ni(II)], respectively. The  $\Delta E_p$  was 110 mV and its  $I_{pc}/I_{pa}$  ratio is 0.4, indicating a quasireversible redox reaction and chemically unstable oxidised complex. This value is similar with complex  $[\text{Ni}^{\text{II}}\text{L}^2]^{2+}$  where L is cyclam-pyridine, reported by Sanae El Ghachtouli in 2005 ( $\Delta E_p = 100 \text{ mV}$ ) [17]. The HOMO and LUMO values was 4.70 V and 5.01 V, respectively. Hence, its  $E_e$  value was 0.31 eV.

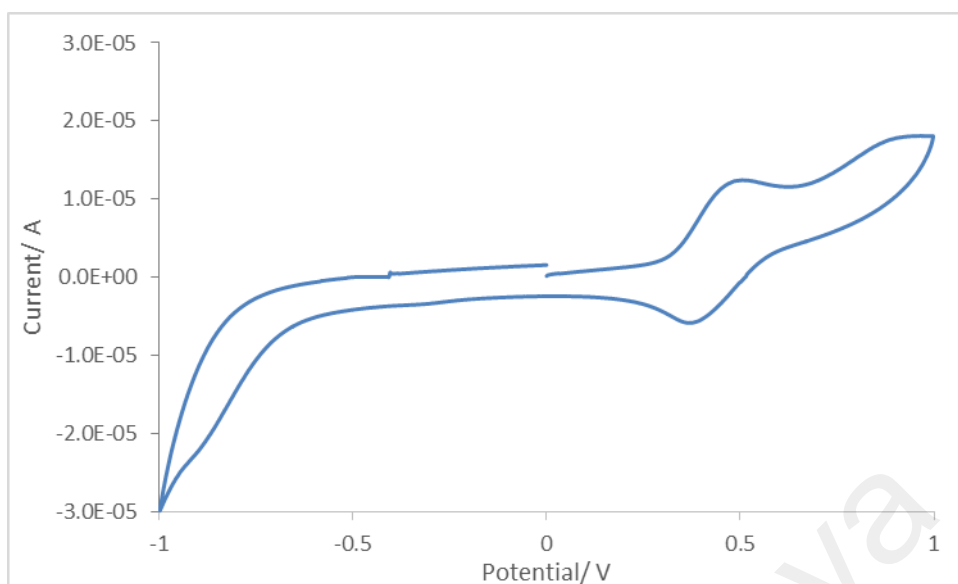


**Figure 4.128** Cyclic voltammogram of **Complex 16**

*(c) Magnetic properties*

Its  $\mu_{\text{eff}}$  value, calculated as previously done from the values of  $\text{FM} = 859.93 \text{ g mol}^{-1}$ ,  $\chi_{\text{g}} = 3.63 \times 10^{-6} \text{ cm}^3 \text{ g}^{-1}$ ,  $\chi_{\text{m}} = 3.12 \times 10^{-3} \text{ cm}^3 \text{ mol}^{-1}$ ,  $\chi_{\text{dia}} = -5.86 \times 10^{-4} \text{ cm}^3 \text{ mol}^{-1}$  and  $\chi_{\text{m}}^{\text{corr}} = 3.71 \times 10^{-3} \text{ cm}^3 \text{ mol}^{-1}$ , was 2.93 BM. The value is in good agreement with the spin-only value of 2.83 B.M. for a mononuclear nickel(II) complex (two unpaired electrons).

*(d) Thermal properties*

The TGA trace (**Figure 4.129**) shows an initial weight loss of 7.7% (calculated, 8.4%) from about 50 °C to 150 °C due to evaporation of lattice  $\text{H}_2\text{O}$ . This was followed by a major weight loss of 80.9% (calculated, 84.8%) from 243 °C to 615 °C due to evaporation of coordinated  $\text{H}_2\text{O}$  and decomposition of  $\text{CH}_3(\text{CH}_2)_{14}\text{COO}^-$  ion and cyclam. The amount of residue at temperatures above 615 °C was 11.4% (calculated, 8.7%, assuming pure NiO). Hence,  $T_{\text{dec}}$  for **Complex 16** was 243 °C.

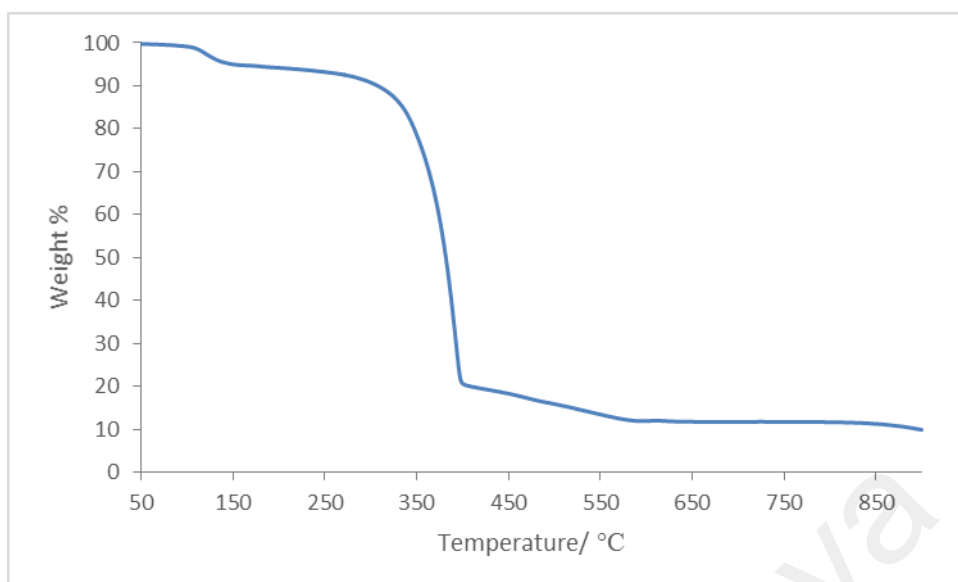


**Figure 4.129** TGA trace of **Complex 16**

*(e) Mesomorphic properties*

Its DSC spectrum (**Figure 4.130**) was recorded for one heating-cooling cycle in the temperature range 25 °C to 150 °C. On heating, there were two endothermic peaks at 56.1 °C ( $\Delta H = +10.6 \text{ kJ mol}^{-1}$ ) and 71.2 °C ( $\Delta H = +49.0 \text{ kJ mol}^{-1}$ ), assigned to the breaking of H-bonds and crystal-to-mesophase transition, respectively. On cooling from its isotropic liquid phase at 150 °C, there was an exothermic peak at 54.0 °C ( $\Delta H = -66.5 \text{ kJ mol}^{-1}$ ) assigned to the mesophase-to-crystal transition.

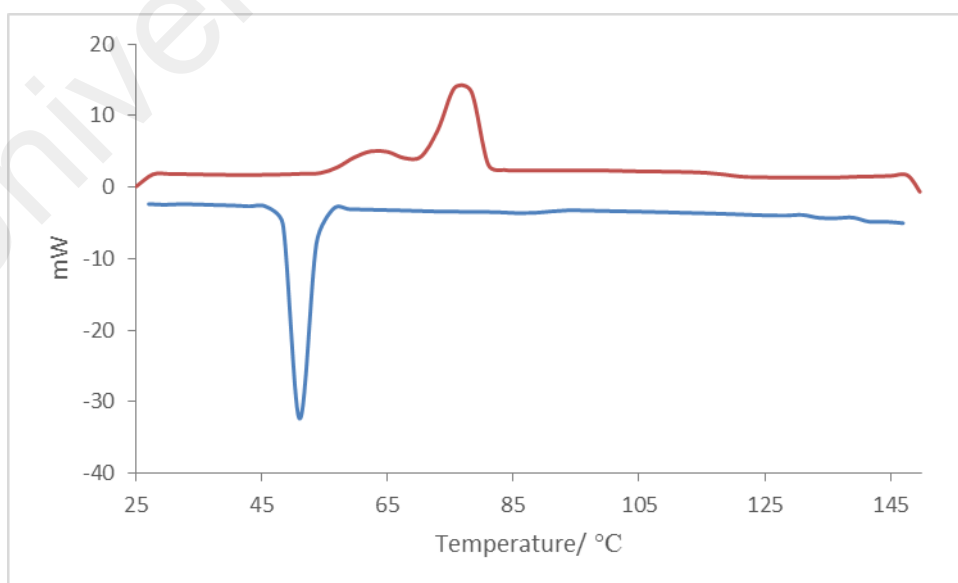


**Figure 4.130** DSC of **Complex 16**

Viewed under OPM, recorded for a heating-cooling cycle from 25 °C to 145 °C, **Complex 16** melted at 70 °C, and separated into a colourless fluid region and a dark red ‘solid’ region which did not clear completely at 150 °C (**Figure 4.131 (a)**). On cooling, an optical texture was observed at 66.4 °C within the colourless region (**Figure 4.131 (b)**).

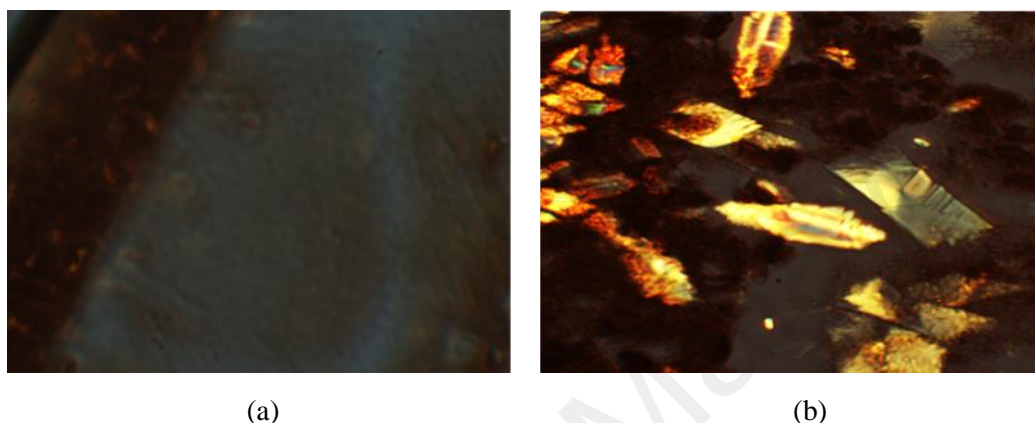


**Figure 4.131** Photomicrograph of **Complex 16** on: (a) heating at 150 °C; and (b) cooling at 66.4 °C

#### 4.5.2 $[Co(CH_3(CH_2)_{14}COO)_2(cyclam)] \cdot (CH_3(CH_2)_{14}COOH)_2$

$[Co(CH_3(CH_2)_{14}COO)_2(H_2O)_2]$  and cyclam reacted in ethanol to form dark purple crystals (**Complex 17**) in good yield (55.9%). It was soluble in methanol, ethanol, and chloroform, but insoluble in other organic solvents.

##### (a) Structural deduction

Based on the instrumental analyses, it was proposed that the structural formula of **Complex 17** is  $[Co(CH_3(CH_2)_{14}COO)_2(cyclam)] \cdot 2CH_3(CH_2)_{14}COOH$ . It was noted that this structure is different from its corresponding Ni(II),  $[Ni(CH_3(CH_2)_{14}COO)(cyclam)(H_2O)](CH_3(CH_2)_{14}COO) \cdot 4H_2O$ .

The results from the **elemental analyses** (68.86% C, 12.59% H, 4.50% N) were in good agreement with the chemical formula  $CoC_{74}H_{149}N_4O_8$  (69.33% C, 11.72% H, 5.37% N).

Its FTIR spectrum (Figure 4.132) shows peaks for the expected functional groups and bonds at wavenumbers ( $2914\text{ cm}^{-1}$ ,  $2849\text{ cm}^{-1}$ ,  $1584\text{ cm}^{-1}$ ,  $1471\text{ cm}^{-1}$ , and  $1383\text{ cm}^{-1}$ ) as the corresponding Ni(II) complexes. From the latter peaks, the  $\Delta\nu$  value was  $201\text{ cm}^{-1}$ , suggesting a monodentate binding mode for  $\text{CH}_3(\text{CH}_2)_{14}\text{COO}^-$ .

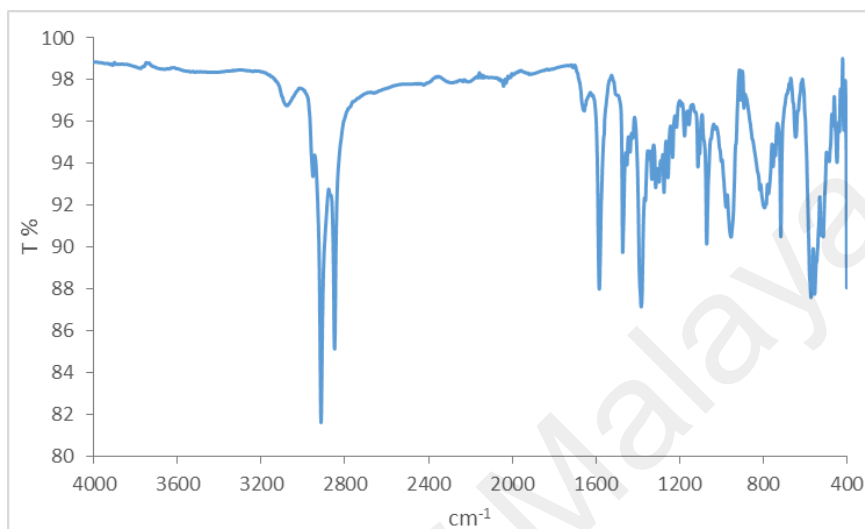
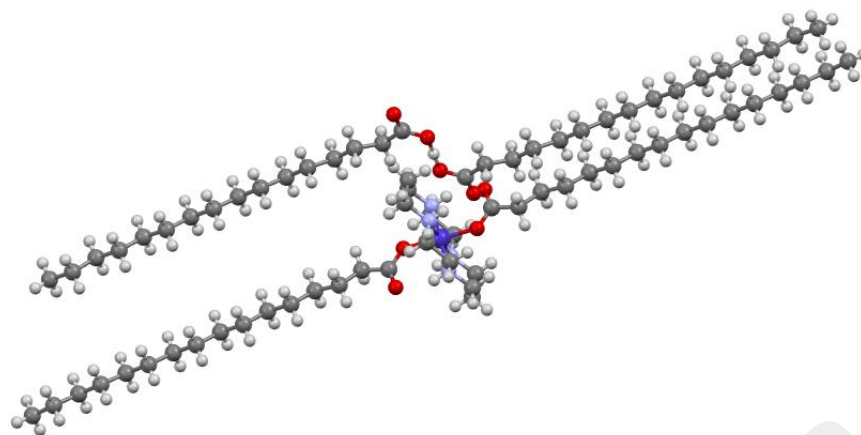
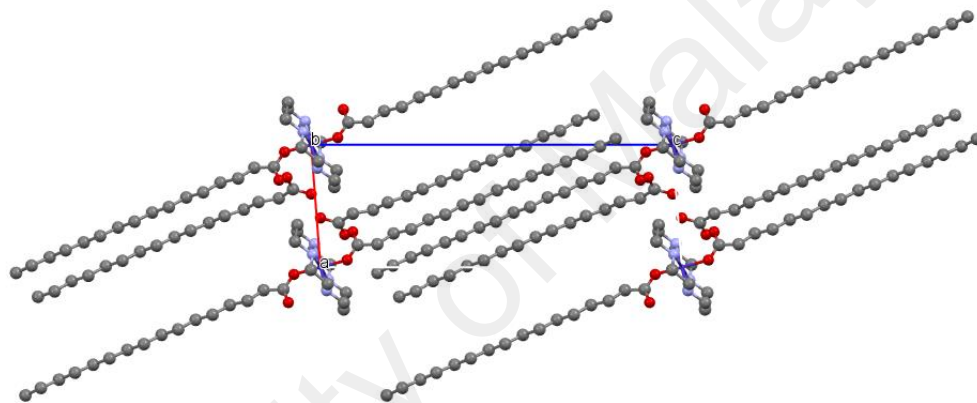


Figure 4.132 The FTIR spectrum of Complex 17

The crystallographic and structure refinement data for the crystals is given in Table 4.12, and selected bond lengths and angles are given in Table 4.13. The molecular structure (Figure 4.133) shows that the complex was made up of  $[\text{Co}(\text{CH}_3(\text{CH}_2)_{14}\text{CO}_2)_2(\text{cyclam})]^+$  cation, and  $\text{CH}_3(\text{CH}_2)_{14}\text{COO}^-$  anion. The Co(II) atom was coordinated to cyclam through the four *aza*-N atoms of cyclam and two O atoms of two  $\text{CH}_3(\text{CH}_2)_{14}\text{COO}^-$  ligands ( $\text{CoN}_4\text{O}_2$  chromophore). The packing diagram of the molecules in the structure is shown in Figure 4.134.



**Figure 4.133** An ORTEP presentation of **Complex 17** along *b*-axis. The probability level is 50%.



**Figure 4.134** The packing diagram of **Complex 17**, viewed along the *b*-axis (H atoms are omitted for clarity).

**Table 4.12** Crystal data and structure refinement for **Complex 17**

Chemical formula	$C_{74}H_{149}N_4CoO_8$
Formula weight (g mol <sup>-1</sup> )	1281.89
Temperature (K)	293(2)
Wavelength(Å)	0.71073
Crystal system, space group	Triclinic, <i>P</i> -1
Unit cell dimension	$a$ (Å) = 8.3533(4) $\alpha$ (°) = 83.334(4) $b$ (Å) = 9.1249(4) $\beta$ (°) = 85.390(4) $c$ (Å) = 24.7421(11) $\gamma$ (°) = 87.674(4)
Volume (Å <sup>3</sup> )	1866.18(15)
Z, Calculated density (g cm <sup>-3</sup> )	1, 1.141
Absorption coefficient (mm <sup>-1</sup> )	0.284
$F(000)$	712
Theta range for data collection (°)	2.852 - 26.000
Index ranges	$-9 \leq h \leq 10$ , $-11 \leq k \leq 11$ , $-30 \leq l \leq 29$
Reflections collected	16995
Independent reflections	7329 (0.0371)
Data/restraints/parameters	7329/0/404
Goodness-of-fit on $F^2$	1.087
Final $R$ indices	$R1 = 0.0404$
$[I \geq 2.0\sigma(I)]$	$wR2 = 0.1032$
$R$ indices (all data)	$R1 = 0.0461$ , $wR2 = 0.1076$
$\Delta\rho_{\max}$ , $\Delta\rho_{\min}$ (e Å <sup>-3</sup> )	0.760, -0.310

**Table 4.13** Selected bond lengths (Å) and angles (°) for **Complex 17**.

Bond length			
N(1)-Co(1)	1.9780(11)	Co(1)-O(1)#1	1.9097(10)
N(2)-Co(1)	1.9672(13)	Co(1)-N(2)#1	1.9672(13)
O(1)-Co(1)	1.9098(10)	Co(1)-N(1)#1	1.9780(11)
Angle			
C(1)-N(1)-Co(1)	119.03(9)	O(1)-Co(1)-N(2)	90.94(5)
C(4)-N(1)-Co(1)	107.12(9)	N(2)#1-Co(1)-N(2)	180.0
Co(1)-N(1)-H(1C)	101.8(11)	O(1)#1-Co(1)-N(1)#1	84.38(5)
C(1)-N(1)-Co(1)	119.03(9)	O(1)-Co(1)-N(1)#1	95.62(5)
C(4)-N(1)-Co(1)	107.12(9)	N(2)#1-Co(1)-N(1)#1	93.80(5)
C(5)-N(2)-Co(1)	108.12(9)	N(2)-Co(1)-N(1)#1	86.20(5)
C(3)-N(2)-Co(1)	118.34(9)	O(1)#1-Co(1)-N(1)	95.63(5)
Co(1)-N(2)-H(2C)	104.3(12)	O(1)-Co(1)-N(1)	84.38(5)
C(6)-O(1)-Co(1)	132.90(9)	N(2)#1-Co(1)-N(1)	86.21(5)
O(1)#1-Co(1)-O(1)	180.0	N(2)-Co(1)-N(1)	93.79(5)
O(1)#1-Co(1)-N(2)#1	90.94(5)	N(1)#1-Co(1)-N(1)	180.0
O(1)-Co(1)-N(2)#1	89.06(5)		

Its **UV-visible** spectrum was recorded in chloroform (**Figure 4.135**). The spectrum shows a *d-d* band at 547 nm ( $\epsilon_{\max} = 156 \text{ M}^{-1} \text{ cm}^{-1}$ ), shoulders at 450 nm ( $\epsilon_{\max} = 156 \text{ M}^{-1} \text{ cm}^{-1}$ ) and 384 nm ( $\epsilon_{\max} = 184 \text{ M}^{-1} \text{ cm}^{-1}$ ), assigned to  ${}^4\text{T}_{1g}(\text{F}) \rightarrow {}^4\text{T}_{2g}(\text{F})$ ,  ${}^4\text{T}_{1g}(\text{F}) \rightarrow {}^4\text{T}_{1g}(\text{P})$  and  ${}^4\text{T}_{1g}(\text{F}) \rightarrow {}^4\text{A}_{2g}(\text{F})$  transitions, respectively. Hence, suggesting a octahedral geometry at Co(II) centre and the crystal structure geometry was maintained in solution.

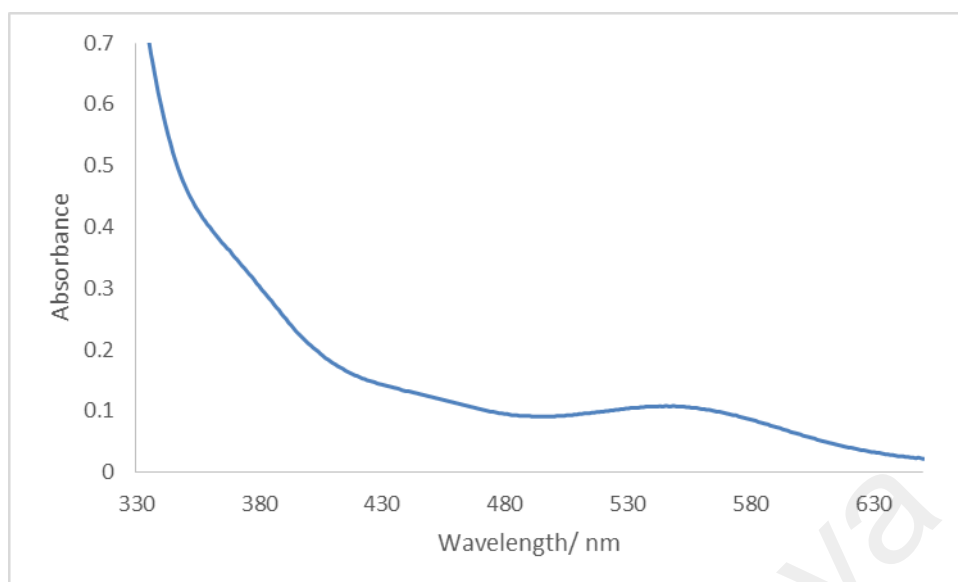


**Figure 4.135** UV-visible spectrum of **Complex 17**

*(b) Determination of bandgaps*

Its  $E_o$  value, calculated as before from the UV-vis spectrum, was 3.31 eV (375 nm).

Its **CV** was recorded anodically in chloroform at a scan rate  $50 \text{ mV s}^{-1}$  in the potential range of -1.5 V to +1.5 V. The voltammogram (**Figure 4.136**) shows an anodic peak at +1.12 V and a cathodic peak at -0.82 V, assigned to the oxidation of [Co(II)] to [Co(III)] and reduction [Co(III)] to [Co(II)] respectively. The  $\Delta E_p$  was 1940 mV, indicating a quasireversible redox reaction ( $\Delta E_p > 59 \text{ mV}$  at  $30 \text{ }^\circ\text{C}$ ) and its  $I_{pc}/I_{pa}$  ratio is 1.5 indicating that the oxidised complex was chemically unstable. The HOMO and LUMO of the complex is 5.25 V and 4.73 V, respectively. Hence, the redox process was quasireversible, and its  $E_e$  value was 0.52 eV.

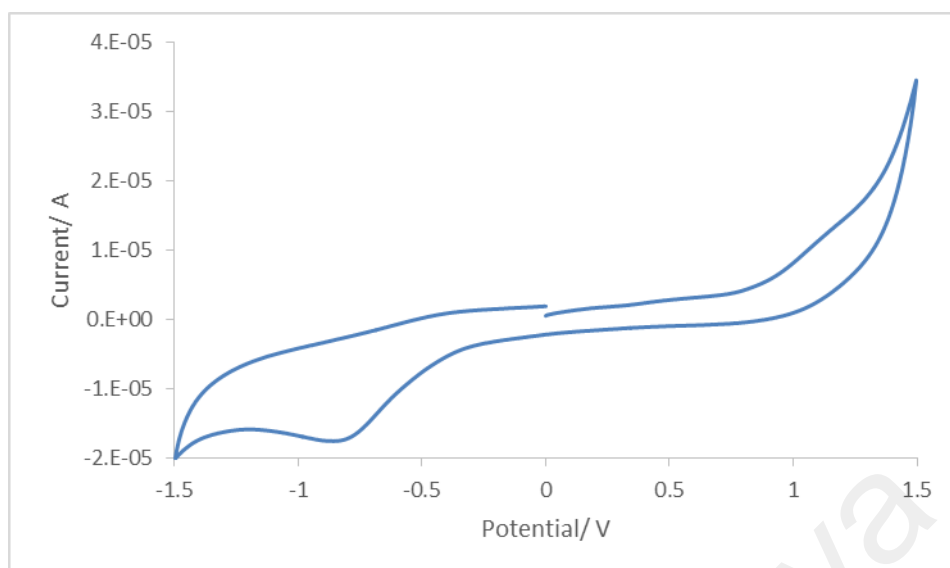


**Figure 4.136** Cyclic voltammogram of **Complex 17**

*(c) Magnetic properties*

Its  $\chi_m^{corr}T$  value, calculated as before using the following data: FM = 1281.93 g mol<sup>-1</sup>,  $\chi_g = 1.98 \times 10^{-6}$  cm<sup>3</sup> g<sup>-1</sup>,  $\chi_m = 2.54 \times 10^{-3}$  cm<sup>3</sup> mol<sup>-1</sup>,  $\chi_{dia} = -8.65 \times 10^{-4}$  cm<sup>3</sup> mol<sup>-1</sup> and  $\chi_m^{corr} = 3.40 \times 10^{-3}$  cm<sup>3</sup> mol<sup>-1</sup> was 1.01 cm<sup>3</sup> K mol<sup>-1</sup>. The theoretical value for a high spin (HS) Co(II) complex ( $S = 3$ ) is 1.876 cm<sup>3</sup> K mol<sup>-1</sup>, and for a low spin (LS) Co(II) complex ( $S = 1$ ) is 0.375 cm<sup>3</sup> K mol<sup>-1</sup>. From this, it may be inferred that this complex was made up of 42% HS and 58% LS Co(II) at room temperature (298 K).

*(d) Thermal properties*

Its TGA trace (**Figure 4.137**) shows an initial weight loss of 6.8% (calculated, 6.6%) from about 50 °C to 157 °C due to evaporation of lattice H<sub>2</sub>O molecules that may be absorbed during storage. This was followed by a major weight loss of 85.2% (calculated 89.2%) from 157 °C to 615 °C due decomposition of CH<sub>3</sub>(CH<sub>2</sub>)<sub>14</sub>COO<sup>-</sup> ion and cyclam. The amount of residue at temperatures above 714 °C was 8.0% (calculated, 5.5%, assuming pure CoO). Hence, T<sub>dec</sub> for **Complex 17** was 157 °C.

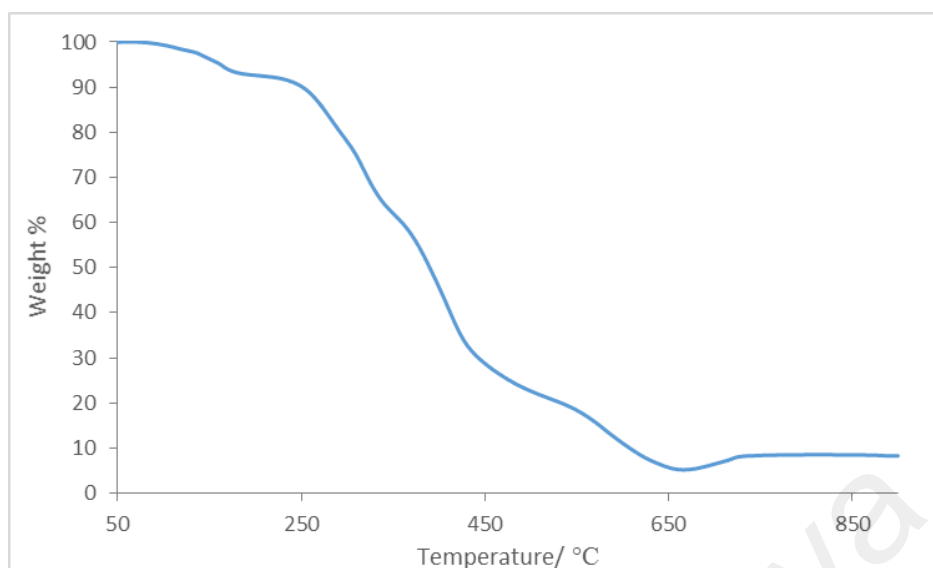


**Figure 4.137** TGA trace of **Complex 17**

*(e) Mesomorphic properties*

Its DSC spectrum (**Figure 4.138**) was recorded for one heating-cooling cycle in the temperature range of 25 °C to 150 °C. On heating, there were three endothermic peaks at 87.4 °C ( $\Delta H = +144.9 \text{ kJ mol}^{-1}$ ), 118.0 °C ( $\Delta H = +2.4 \text{ kJ mol}^{-1}$ ) and 137.2 °C ( $\Delta H = +69.4 \text{ kJ mol}^{-1}$ ) assigned to its melting temperature, the breaking of H-bond and Co-OOC(CH<sub>2</sub>)<sub>14</sub>CH<sub>3</sub> bond. On cooling, there were two exothermic peaks at 78.9 °C ( $\Delta H = -5.7 \text{ kJ mol}^{-1}$ ) and 71.1 °C ( $\Delta H = 79.8 \text{ kJ mol}^{-1}$ ), assigned to the isotropic to mesophase (I-to-M) and mesophase to crystal (M-to-Cr) phase transition.

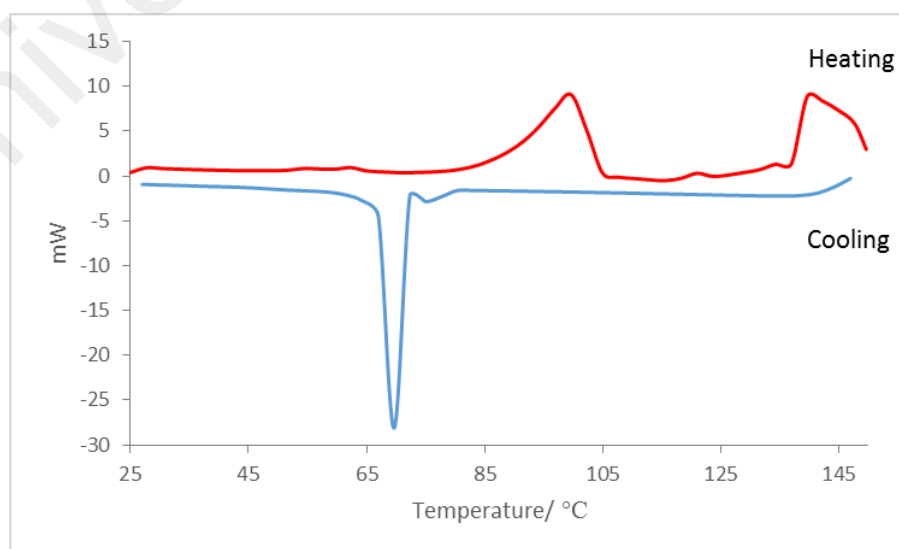


**Figure 4.138** DSC of **Complex 17**

Viewed under POM, which were recorded for one heating-cooling cycle from 25 °C to 122 °C, the sample was observed to start melting at 118.9 °C and clear to the isotropic liquid at 121.5 °C. On cooling from the isotropic liquid phase, an optical texture (cholesteric phase) was observed at 70.2 °C (**Figure 4.139(b)**) which became brighter on further cooling to 61.0 °C (**Figure 4.139(c)**).

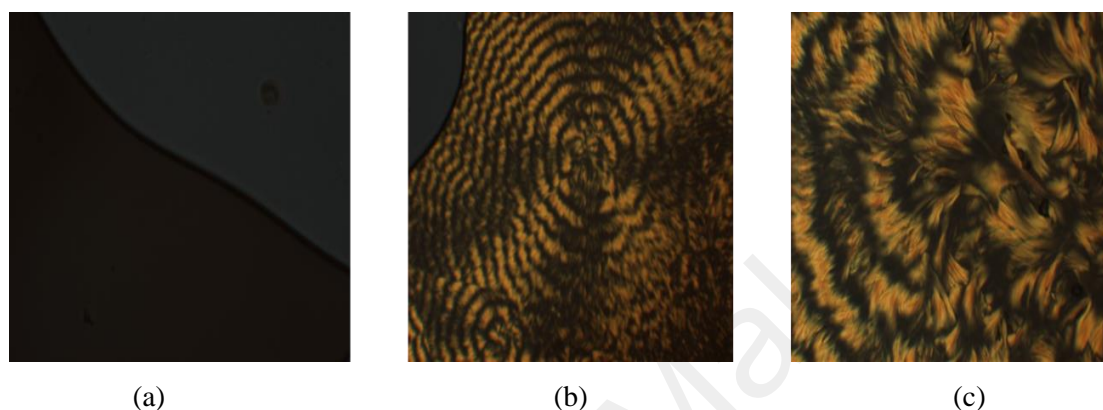


**Figure 4.139** Photomicrographs of **Complex 17** on: (a) heating at 122 °C; (b) cooling at 70.2 °C; and (c) further cooling at 61.0 °C

#### 4.5.3 $[Fe(CH_3(CH_2)_{14}COO)(OH)(cyclam)].H_2O.CH_3CH_2OH$

$[Fe(CH_3(CH_2)_{14}COO)_2(H_2O)_2]$  and cyclam were reacted in ethanol to form an orange powder (**Complex 18**) in good yield (52.4 %). It was soluble in water, methanol, ethanol, and chloroform, but insoluble in other organic solvents.

##### (a) Structural deduction

The structure of **Complex 18** was deduced based on the combined results of the elemental analyses, FTIR, and UV-visible spectroscopies.

The results from the **elemental analyses** (57.44% C, 11.27% H, 8.96% N) were in good agreement with the chemical formula  $FeC_{28}H_{64}N_4O_5$  (592.86 g mol<sup>-1</sup>; 56.74% C, 10.88% H, 9.45% N).

Its **FTIR** spectrum (**Figure 4.140**) shows peaks for the expected functional groups and bonds at wavenumbers (3380 cm<sup>-1</sup>, 2916 cm<sup>-1</sup>, 2850 cm<sup>-1</sup>, 1656 cm<sup>-1</sup>, 1560 and 1419 cm<sup>-1</sup>) similar to the corresponding Ni(II) and Co(II) complexes. From the latter

peaks, the  $\Delta\nu$  value was  $141\text{ cm}^{-1}$ , suggesting monodentate binding mode for  $\text{CH}_3(\text{CH}_2)_{14}\text{COO}^-$  ion.

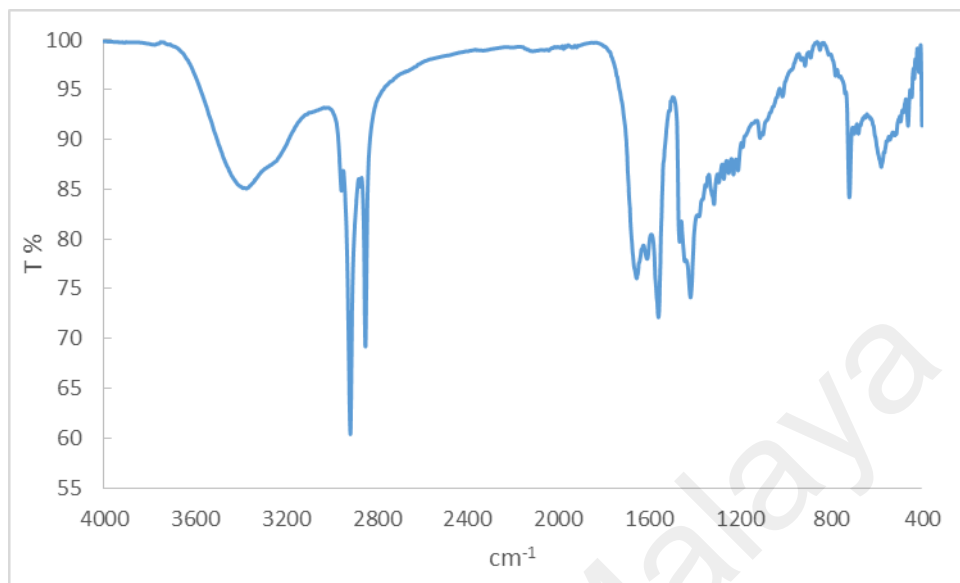


**Figure 4.140** The FTIR spectrum of **Complex 18**

Its **UV-visible** spectrum was recorded in water (**Figure 4.141**). The spectrum shows a *d-d* band (shoulder) at 440 nm ( $\epsilon_{\text{max}} = 409\text{ M}^{-1}\text{ cm}^{-1}$ ) assigned to  ${}^1\text{A}_{1g} \rightarrow {}^1\text{T}_{1g}$  transition, suggesting octahedral geometry at centre of low spin Fe(II). Additionally, MLCT band was observed at 314 nm ( $\epsilon_{\text{max}} = 3933\text{ M}^{-1}\text{ cm}^{-1}$ ).

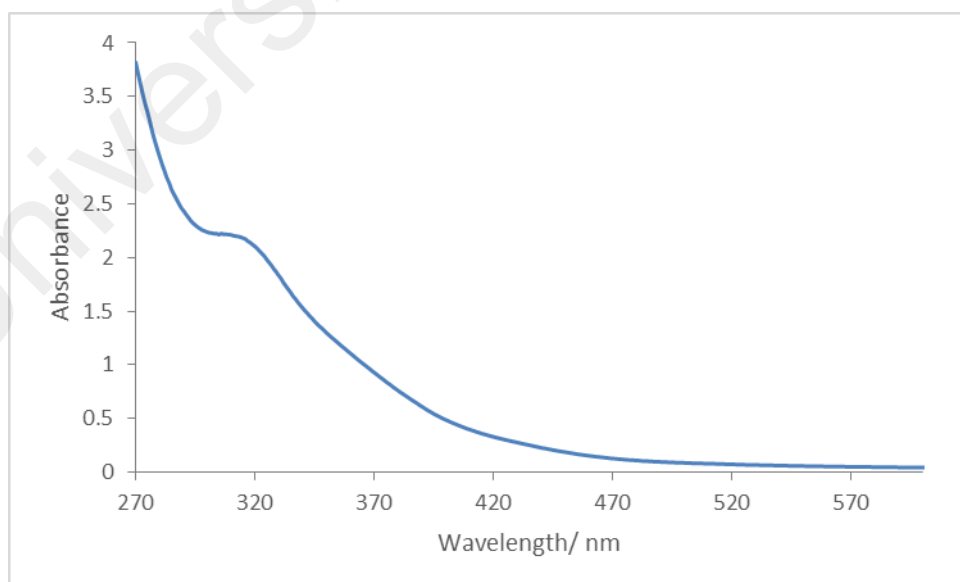


**Figure 4.141** UV-visible spectrum of **Complex 18**

Combining the results of elemental analyses and FTIR and UV-visible spectroscopies, the proposed structural formula for **Complex 18** is  $[\text{Fe}(\text{CH}_3(\text{CH}_2)_{14}\text{COO})(\text{OH})(\text{cyclam})]\cdot\text{H}_2\text{O}\cdot\text{CH}_3\text{CH}_2\text{OH}$  (**Figure 4.142**).

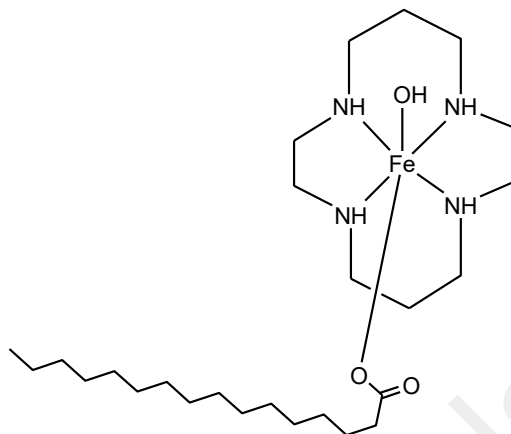


**Figure 4.142** Proposed structure for **Complex 18** (lattice  $\text{H}_2\text{O}$  and  $\text{CH}_3\text{CH}_2\text{OH}$  are omitted).

(b) *Determination of bandgaps*

Its  $E_o$  value, calculated as before from the UV-vis spectrum, was 2.9 eV ( $\lambda_{\text{onset}} = 430$  nm).

Its CV scan was recorded anodically in water at a scan rate  $50 \text{ mV s}^{-1}$  in the potential range of +1.5 V to -1.5 V. The voltammogram (**Figure 4.143**) shows an anodic peak at +1.14 V and a cathodic peak at -0.82 V, assigned to the oxidation of  $[\text{Fe}(\text{II})]$  to  $[\text{Fe}(\text{III})]$  and reduction  $[\text{Fe}(\text{III})]$  to  $[\text{Fe}(\text{II})]$ , respectively. The  $\Delta E_p$  was 1960 mV, indicating a quasireversible redox reaction ( $\Delta E_p > 59 \text{ mV}$  at  $30^\circ\text{C}$ ) and its  $I_{pc}/I_{pa}$  ratio is 1.6 indicating the oxidised complex was chemically unstable. The HOMO and LUMO of the complex is 5.36 V and 3.96 V, respectively. Hence, its  $E_e$  value was 1.40 eV.

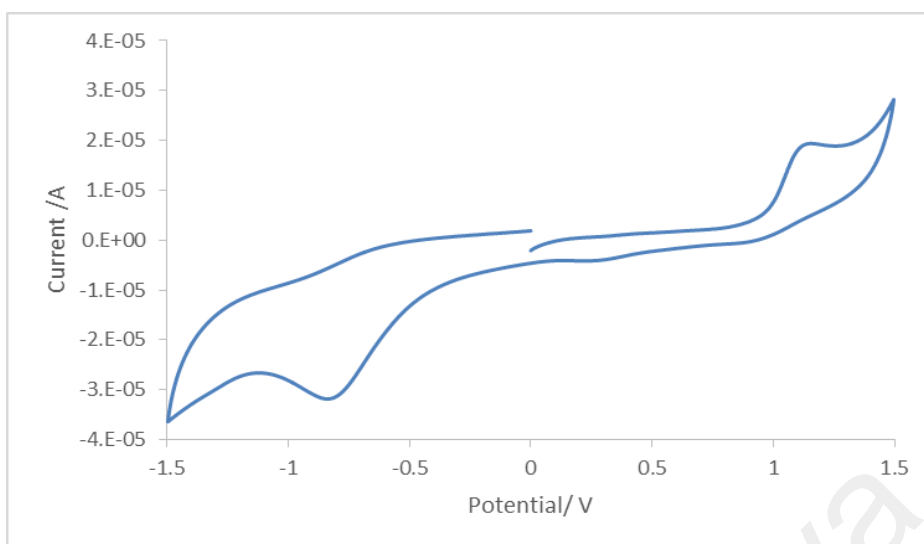


**Figure 4.143** Cyclic voltammogram of **Complex 18**

*(c) Magnetic properties*

Its  $\chi_m^{corr}T$  value, calculated as previously done using the following data:  $FM = 592.68 \text{ g mol}^{-1}$ ,  $\chi_g = 0.84 \times 10^{-6} \text{ cm}^3 \text{ g}^{-1}$ ,  $\chi_m = 5.00 \times 10^{-3} \text{ cm}^3 \text{ mol}^{-1}$ ,  $\chi_{dia} = -3.78 \times 10^{-4} \text{ cm}^3 \text{ mol}^{-1}$ , and  $\chi_m^{corr} = 5.38 \times 10^{-3} \text{ cm}^3 \text{ mol}^{-1}$ , was  $1.60 \text{ cm}^3 \text{ K mol}^{-1}$ . From this, it may be inferred that this complex was made up of 53% HS and 47% LS Fe(II) at room temperature.

*(d) Thermal properties*

The TGA trace (**Figure 4.144**) shows an initial weight loss of 6.2% (calculated, 10.8%) from  $50 \text{ }^\circ\text{C}$  to  $168 \text{ }^\circ\text{C}$  due to evaporation of lattice  $\text{H}_2\text{O}$  and  $\text{CH}_3\text{CH}_2\text{OH}$ . The lower than calculated value suggests loss of lattice  $\text{H}_2\text{O}$  molecules during storage. This was followed by a major weight loss of 83.8% (calculated, 82.8%) from  $168 \text{ }^\circ\text{C}$  to  $771 \text{ }^\circ\text{C}$  due to evaporation of coordinated  $\text{H}_2\text{O}$ , and decomposition of  $\text{CH}_3(\text{CH}_2)_{14}\text{COO}^-$  ion and cyclam. The amount of residue at temperatures above  $771 \text{ }^\circ\text{C}$  was 10.0% (calculated 12.1%, assuming pure FeO). Hence,  $T_{dec}$  for **Complex 18** was  $186 \text{ }^\circ\text{C}$ .

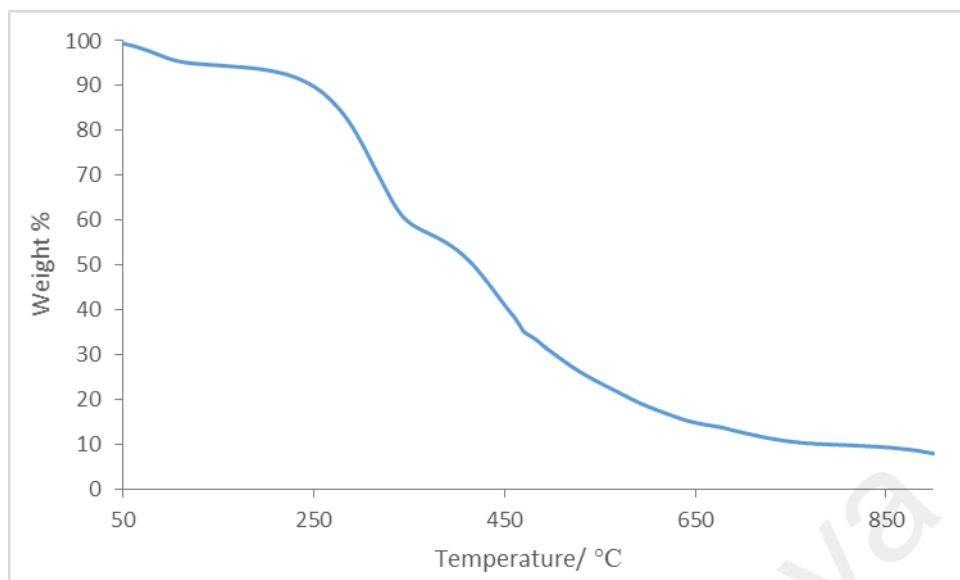


**Figure 4.144** TGA trace of **Complex 18**

*(e) Mesomorphic properties*

The DSC scan of **Complex 18** (**Figure 4.145**) was recorded for one heating-cooling cycle from 25 °C to 150 °C. On heating, there were two endothermic peaks at 78.2 °C ( $\Delta H = +20.1 \text{ kJ mol}^{-1}$ ) and at 139.5 °C ( $\Delta H = +9.7 \text{ kJ mol}^{-1}$ ), assigned to breaking of Fe-OH and Fe-OH<sub>2</sub> bond. On cooling from 150 °C, there were two exothermic peaks at 45.9 °C ( $\Delta H = -6.1 \text{ kJ mol}^{-1}$ ) and 31.4 °C ( $\Delta H = -2.7 \text{ kJ mol}^{-1}$ ) assigned to formation of H-bond to H<sub>2</sub>O.

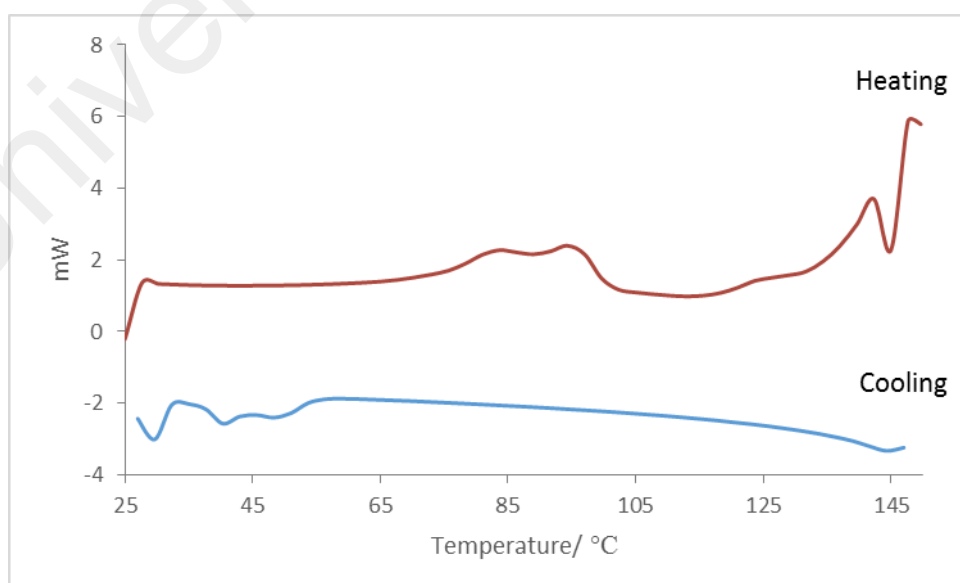


**Figure 4.145** DSC of **Complex 18**

Viewed under **OPM**, which was recorded for heating-cooling cycle from 25 °C to 115 °C, the complex was did not show any optical textures. Hence, **Complex 18** did not exhibit mesomorphism.

#### 4.5.4 [Mn(CH<sub>3</sub>(CH<sub>2</sub>)<sub>14</sub>COO)(OH)<sub>2</sub>(NH<sub>3</sub>)<sub>2</sub>(H<sub>2</sub>O)]

[Mn(CH<sub>3</sub>(CH<sub>2</sub>)<sub>14</sub>COO)<sub>2</sub>(H<sub>2</sub>O)<sub>2</sub>] and cyclam reacted in ethanol to form a black powder (**Complex 19**) in good yield (83.7 %). It was soluble in methanol and ethanol, but insoluble in other organic solvents.

##### (a) Structural deduction

Based on the instrumental data discussed below, the structural formula of **Complex 19** is [Mn(CH<sub>3</sub>(CH<sub>2</sub>)<sub>14</sub>COO)(OH)<sub>2</sub>(NH<sub>3</sub>)<sub>2</sub>(H<sub>2</sub>O)], which was not the expected complex. It suggests that Mn(II) was oxidized to Mn(III), and cyclam reduced to NH<sub>3</sub> during synthesis. Currently, similar redox reaction could not be found in the literature.

The results from the **elemental analyses** (47.70% C, 9.23% H, 7.57% N) were in good agreement with the chemical formula MnC<sub>16</sub>H<sub>41</sub>N<sub>2</sub>O<sub>5</sub> (396.45 g mol<sup>-1</sup>; 48.47% C, 10.42% H, 7.07% N).

Its **FTIR** spectrum (**Figure 4.146**) shows peaks for the expected functional groups and bonds at wavenumbers (3365 cm<sup>-1</sup>, 3259 cm<sup>-1</sup>, 2915 cm<sup>-1</sup>, 2850 cm<sup>-1</sup>, 1657 cm<sup>-1</sup>, 1395 cm<sup>-1</sup>, cm<sup>-1</sup>) as the corresponding metal complexes. From the latter peaks, the Δν<sub>COO</sub> value was 262 cm<sup>-1</sup>, suggesting monodentate binding mode for CH<sub>3</sub>(CH<sub>2</sub>)<sub>14</sub>COO<sup>-</sup> ion.

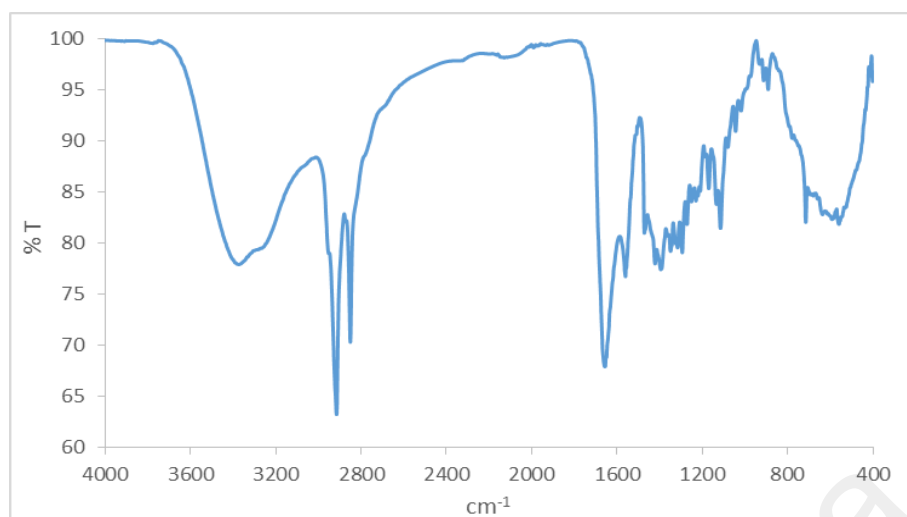


**Figure 4.146** The FTIR spectrum of **Complex 19**

Its **UV-visible** spectrum was recorded in methanol (**Figure 4.147**). The spectrum show a *d-d* band (shoulders) at 408 nm ( $\epsilon_{\max} = 795 \text{ M}^{-1} \text{ cm}^{-1}$ ) and 531 nm ( $\epsilon_{\max} = 270 \text{ M}^{-1} \text{ cm}^{-1}$ ). These suggest an octahedral geometry at the Mn(III) centre. Also observed is an intense LMCT band at 306 nm ( $\epsilon_{\max} = 1654 \text{ M}^{-1} \text{ cm}^{-1}$ ),

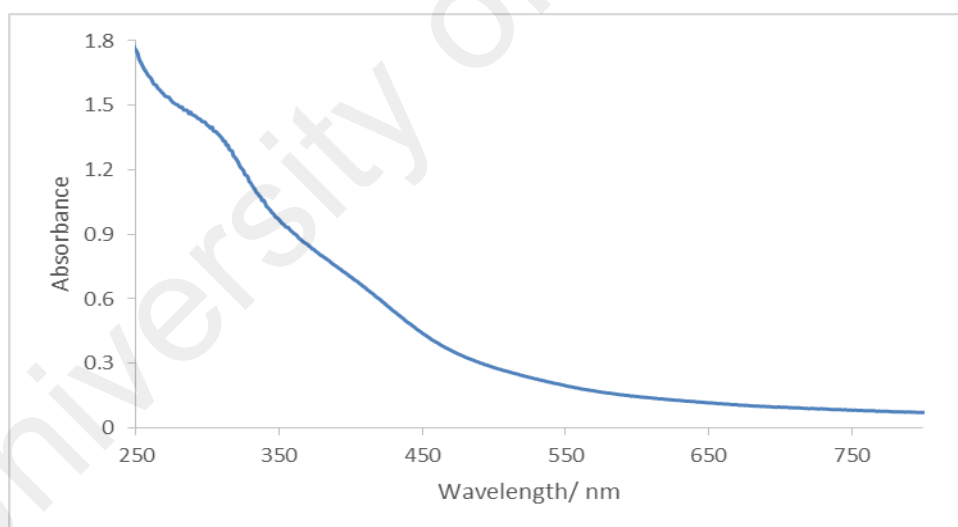


**Figure 4.147** UV-visible spectrum of **Complex 19**

*(b) Determination of bandgaps*

Its  $E_o$  value, calculated as before from the UV-vis spectrum, was 2.84 eV (437 nm).

Its **CV** scan was recorded cathodically in water at a scan rate  $50 \text{ mV s}^{-1}$  in the potential range of  $-1.5 \text{ V}$  to  $+1.5 \text{ V}$ . The voltammogram (**Figure 4.148**) shows a cathodic peak at  $-0.88 \text{ V}$  and an anodic peak at  $+0.62 \text{ V}$ , assigned to the reduction of [Mn(III)] to

[Mn(II)] and oxidation [Mn(II)] to [Mn(III)], respectively. The  $\Delta E_p$  was 1500 mV, indicating a quasireversible redox reaction ( $\Delta E_p > 59$  mV at 30 °C) and its  $I_{pa}/I_{pc}$  ratio is 0.27 indicating the oxidised complex was chemically unstable. The HOMO and LUMO of the complex is 3.88 V and 4.79 V, respectively. Hence, the redox process was quasireversible and its  $E_e$  value was 0.91 eV.

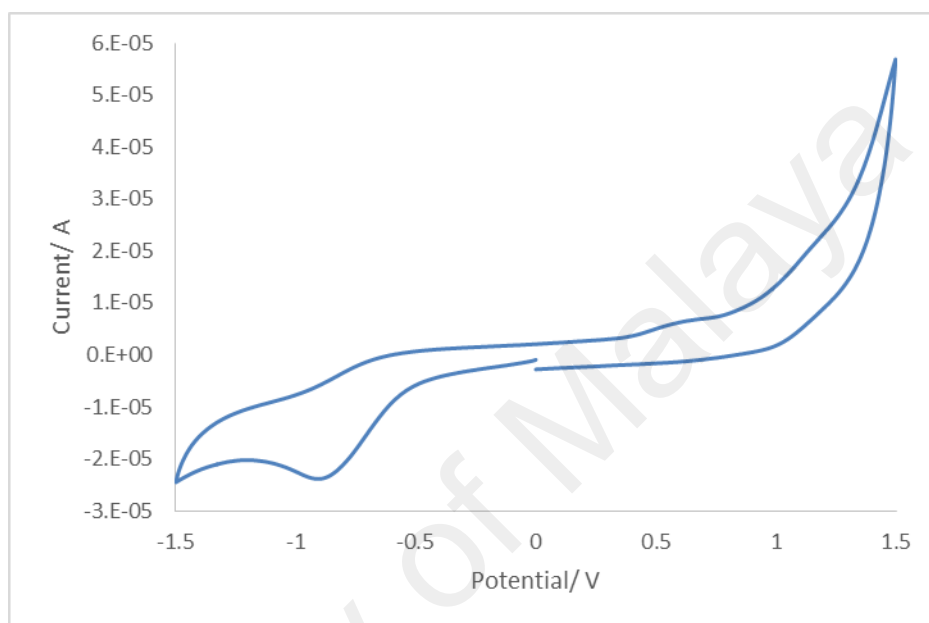


**Figure 4.148** Cyclic voltammogram of **Complex 19**

(c) *Magnetic properties*

Its  $\chi_m^{corr}T$  value, calculated as previously done using the following data: FM = 396.45 g mol<sup>-1</sup>,  $\chi_g = 1.36 \times 10^{-5}$  cm<sup>3</sup> g<sup>-1</sup>,  $\chi_m = 5.38 \times 10^{-3}$  cm<sup>3</sup> mol<sup>-1</sup>,  $\chi_{dia} = -2.19 \times 10^{-4}$  cm<sup>3</sup> mol<sup>-1</sup>, and  $\chi_m^{corr} = 5.60 \times 10^{-3}$  cm<sup>3</sup> mol<sup>-1</sup>, was 1.67 cm<sup>3</sup> K mol<sup>-1</sup>. The theoretical value for a high spin (HS) Mn(III) complex ( $S = 2$ ) is 3.001 cm<sup>3</sup> K mol<sup>-1</sup>, and for a low spin (LS) Mn(III) complex ( $S = 1$ ) is 1.000 cm<sup>3</sup> K mol<sup>-1</sup>. From this, it may be inferred that this complex was made up of 67% HS and 33% LS Mn(III) at room temperature.

*(d) Thermal properties*

The TGA trace (**Figure 4.149**) shows an initial weight loss of 5.0% (calculated, 4.5%) from 50 °C to 140 °C due to evaporation of water. This was followed by a major weight loss of 82.1% (calculated, 81.6%) from 140 °C to 653 °C due to evaporation of NH<sub>3</sub> and decomposition of OH<sup>-</sup> and CH<sub>3</sub>(CH<sub>2</sub>)<sub>14</sub>COO<sup>-</sup> ions. The amount of residue at temperatures above 653 °C was 12.9% (calculated, 17.9%, assuming pure MnO. Hence, T<sub>dec</sub> for **Complex 19** was 140 °C.

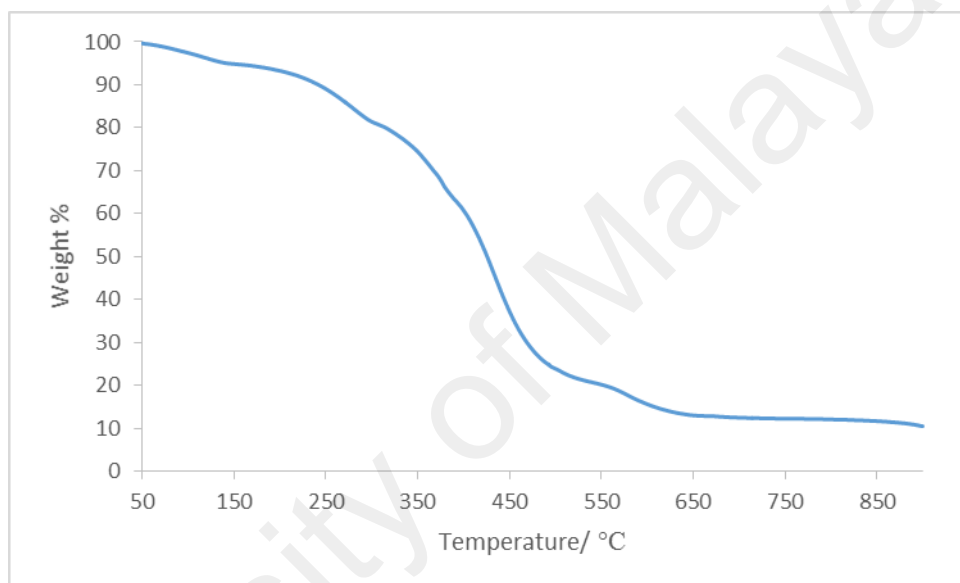


**Figure 4.149** TGA trace of **Complex 19**

*(e) Mesomorphic properties*

Its DSC scan (**Figure 4.150**) was recorded for one heating-cooling cycle from 25 °C to 120 °C. On heating, there was a broad endothermic peak at 81.6 °C ( $\Delta H = +16.5 \text{ kJ mol}^{-1}$ ) assigned to the breaking of H-bond. On cooling from 120 °C, there was an exothermic peak at 103 °C ( $\Delta H = -20.9 \text{ kJ mol}^{-1}$ ) and assigned to formation of H-bond.

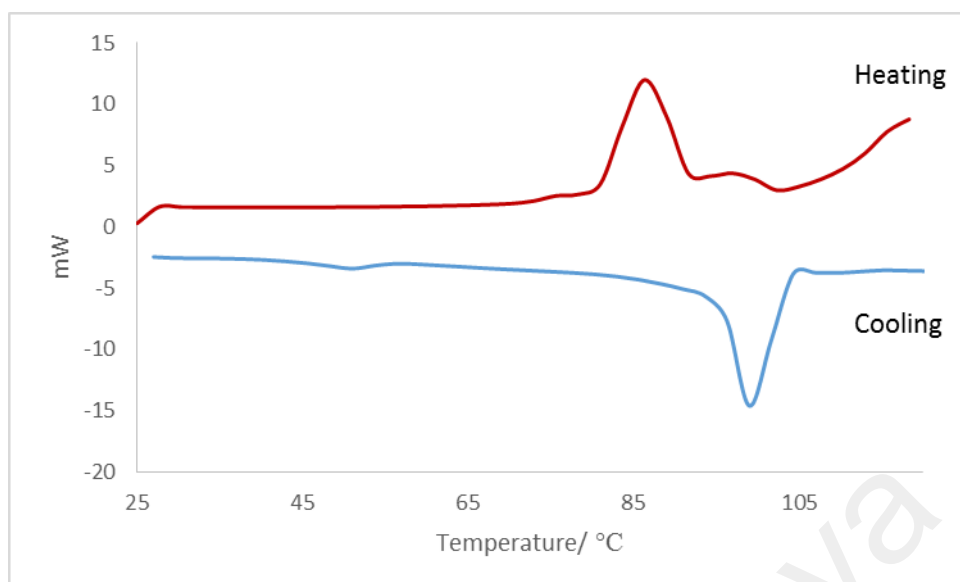


**Figure 4.150** DSC of **Complex 19**

Viewed under **OPM**, which was recorded for heating-cooling cycle from 25 °C to 120 °C, the complex did not show any optical textures. Hence, **Complex 19** did not exhibit mesomorphism.

#### **4.5.5 Summary**

The analytical results for **Complex 16-19** are summarised in **Table 4.14**. All complexes were mononuclear and paramagnetic.

The optical bandgaps from the CT absorption bands for all complexes were similar (2.84 eV– 3.60 eV), while for electrochemical bandgap is in the range 0.31 eV and 1.40 eV. Hence, these complexes were semiconductors and potentials as photovoltaic and solar cells materials.

All complexes were thermally stable. Their decomposition temperatures range from 140 °C to 243 °C. Finally, only **Complexes 16** and **17** were mesomorphic.

**Table 4.14** Analytical results for metal(II) complexes of cyclam

Complex		16	17	18	19
Chemical Formula		[Ni(R)(cyclam)(H <sub>2</sub> O)](R).4H <sub>2</sub> O	[Co(R) <sub>2</sub> (cyclam)].2RH	[Fe(R)(cyclam)(OH)].H <sub>2</sub> O.CH <sub>3</sub> CH <sub>2</sub> OH	[Mn(R)(OH) <sub>2</sub> (NH <sub>3</sub> ) <sub>2</sub> (H <sub>2</sub> O)]
CH <sub>3</sub> COO mode		monodentate			
Geometry		octahedral			
E <sub>o</sub> (eV)	absorption	3.60	3.31	2.90	2.84
	electrochemical	0.31	0.52	1.40	0.91
CV		Redox active			
μ <sub>eff</sub> (B.M.)		2.93	2.81 (34% HS, 66% LS)	3.60 (53% HS, 47% LS)	3.68 (67% HS, 33% LS)
T <sub>dec</sub> (°C)		243	157	186	140
Mesomorphism		mesomorphic		Non-mesomorphic	

R= CH<sub>3</sub>(CH<sub>2</sub>)<sub>14</sub>COO

## 4.6 Mixed-Metal Complexes

In this research, attempts were made to prepare mixed-metal complexes of general formula  $[\text{CuM}(\text{CH}_3\text{COO})_2(\text{Ln})]$ , where  $M = \text{Ni(II)}$ ,  $\text{Co(II)}$ ,  $\text{Fe(II)}$ , and  $\text{Mn(II)}$ , and  $n = 1$ , 2, and 3. However, only complex with  $M = \text{Co(II)}$  was successfully, as discussed below.

### 4.6.1 $[\text{CuCo}(\text{CH}_3\text{COO})_2(\text{HL1})_2(\text{H}_2\text{O})]$

The Cu(II)-Co(II) mixed metal complex of H<sub>2</sub>L1 was synthesised using the one-pot reaction from the reaction of H<sub>2</sub>N(CH<sub>2</sub>)<sub>8</sub>NH<sub>2</sub>, 2-hydroxybenzaldehyde,  $[\text{Cu}(\text{CH}_3\text{COO})_2] \cdot \text{H}_2\text{O}$  and  $[\text{Co}(\text{CH}_3\text{COO})_2] \cdot 4\text{H}_2\text{O}$  in ethanol. The product was a khaki green powder (**Complex 20**) and the yield was 75.2%. It was soluble in DMSO, DMF, and THF, but insoluble in water and other common organic solvents.

#### (a) Structural deduction

Based on the combined results of the elemental analyses and FTIR and UV-visible spectroscopies presented below, it is proposed that the structural formula of **Complex 20** was  $[\text{CuCo}(\text{CH}_3\text{COO})_2(\text{HL1})_2(\text{H}_2\text{O})]$ .

The results of the **elemental analyses** (59.90% C, 6.18% H, 5.68% N) were in good agreement with the chemical formula  $\text{CuCoC}_{48}\text{H}_{62}\text{N}_4\text{O}_9$  (FW, 961.51 g mol<sup>-1</sup>; 59.96% C, 6.50% H, 5.83 % N).

Its **FTIR** spectrum (**Figure 4.151**) shows a small broad peak at 3377 cm<sup>-1</sup> for H<sub>2</sub>O, two peaks for CH<sub>2</sub> (ν<sub>asym</sub>) and CH<sub>2</sub> (ν<sub>sym</sub>) at 2921 cm<sup>-1</sup> and 2851 cm<sup>-1</sup>, respectively, a strong peak for C=N at 1620 cm<sup>-1</sup>, a strong peak at 1538 cm<sup>-1</sup> for COO<sub>asym</sub>, and a peak at 1446 cm<sup>-1</sup> for COO<sub>sym</sub>. From the latter peaks, the Δ value was 92 cm<sup>-1</sup>, suggesting a chelating binding mode for CH<sub>3</sub>COO<sup>-</sup> ligand.

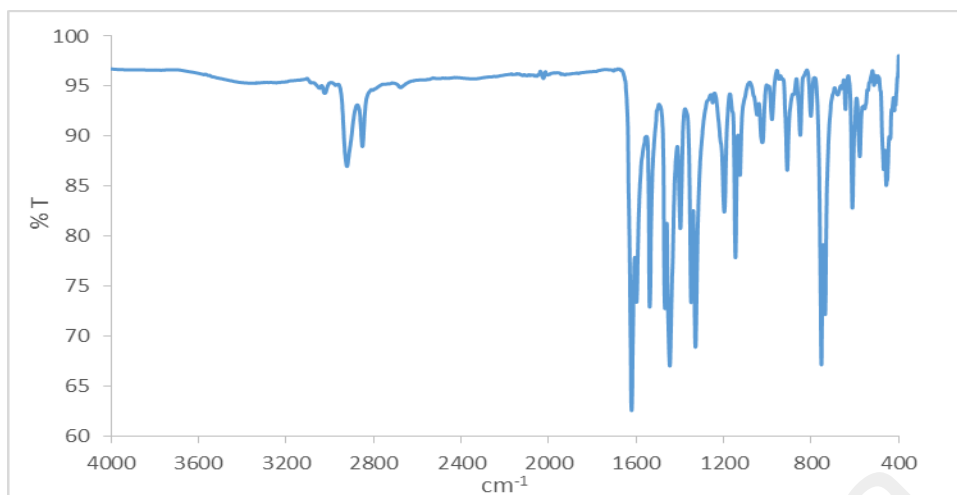


**Figure 4.151** FTIR spectrum for **Complex 20**

Its **UV-visible** spectrum, recorded in chloroform (**Figure 4.152**), shows *d-d* bands at 640 nm ( $\epsilon_{\max} = 153 \text{ M}^{-1} \text{ cm}^{-1}$ ) and 461 nm ( $\epsilon_{\max} = 545 \text{ M}^{-1} \text{ cm}^{-1}$ ), and MLCT bands at 369 nm ( $\epsilon_{\max} = 5749 \text{ M}^{-1} \text{ cm}^{-1}$ ) and 307 nm ( $\epsilon_{\max} = 5446 \text{ M}^{-1} \text{ cm}^{-1}$ ). These suggest a tetrahedral geometry at each Cu(II) and Co(II) centre for this complex.

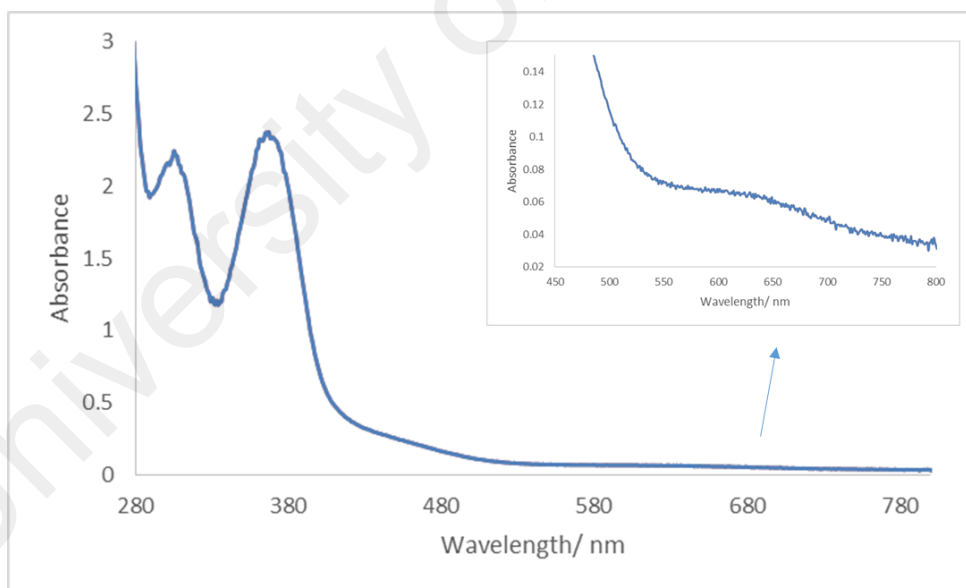


**Figure 4.152** UV-visible spectrum of **Complex 20**

(b) *Determination of bandgaps*

Its  $E_g$  value, calculated as before from its UV-vis spectrum, was 2.95 eV ( $\lambda_{\text{onset}} = 421 \text{ nm}$ ).

Its CV scan was recorded cathodically in chloroform at a scan rate  $50 \text{ mV s}^{-1}$  in the potential range of  $-1.5.0 \text{ V}$  to  $+1.5 \text{ V}$ . However, its voltammogram (**Figure 4.153**) did not show any redox peaks. Hence, its electrochemical band gap cannot be calculated.

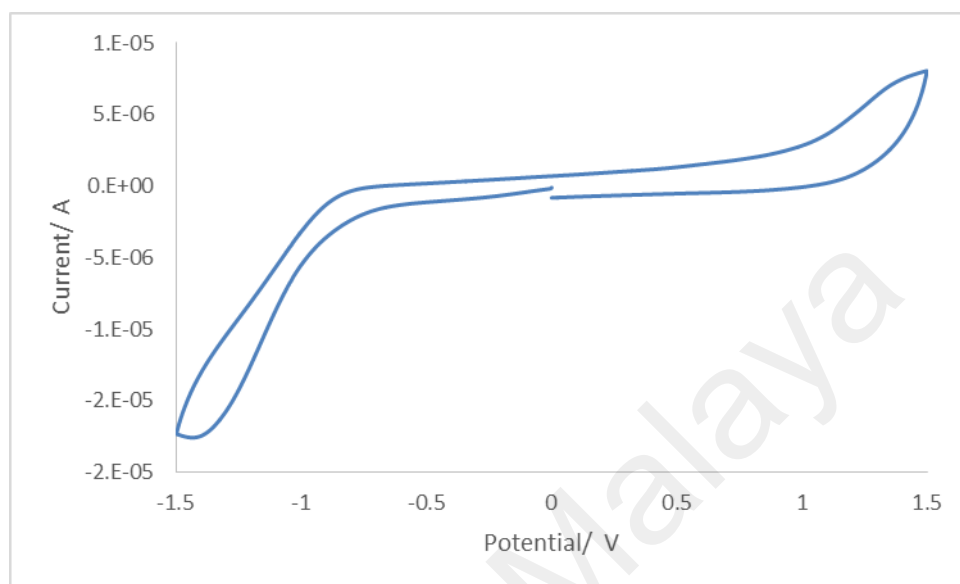


**Figure 4.153** Cyclic voltammogram for **Complex 20**

*(c) Magnetic properties*

Its  $\mu_{\text{eff}}$  value, calculated as previously done from the values of  $\text{FM} = 961.51 \text{ g mol}^{-1}$ ,  $\chi_{\text{g}} = 6.92 \times 10^{-6} \text{ cm}^3 \text{ g}^{-1}$ ,  $\chi_{\text{m}} = 6.65 \times 10^{-3} \text{ cm}^3 \text{ mol}^{-1}$ ,  $\chi_{\text{dia}} = -4.16 \times 10^{-4} \text{ cm}^3 \text{ mol}^{-1}$ , and  $\chi_{\text{m}}^{\text{corr}} = 7.07 \times 10^{-3} \text{ cm}^3 \text{ mol}^{-1}$ , was 4.13 B.M. This is lower than the expected value 5.60 B.M for 4 unpaired electron (1 unpaired electron from Cu(II) and 3 unpaired electron from Co(II)), suggesting a weak ferromagnetic interaction between Cu(II) and Co(II) centers.

*(d) Thermal properties*

Its TGA trace (**Figure 4.154**) shows an initial weight loss of 1.8% from about  $142 \text{ }^{\circ}\text{C}$  to  $222 \text{ }^{\circ}\text{C}$  due to the evaporation of coordinated  $\text{H}_2\text{O}$  (calculated, 1.9%). The next weight loss of 79.3% from  $222 \text{ }^{\circ}\text{C}$  to  $676 \text{ }^{\circ}\text{C}$  is assigned to decomposition of two  $\text{HL1}^-$  and two  $\text{CH}_3\text{COO}^-$  ions (calculated, 86.4%). The amount of residue at temperatures above  $676 \text{ }^{\circ}\text{C}$

was 18.9%, which is in a good agreement with the calculated value of 16.1%, assuming pure CuO and CoO. Accordingly,  $T_{\text{dec}}$  for **Complex 20** was 142 °C.

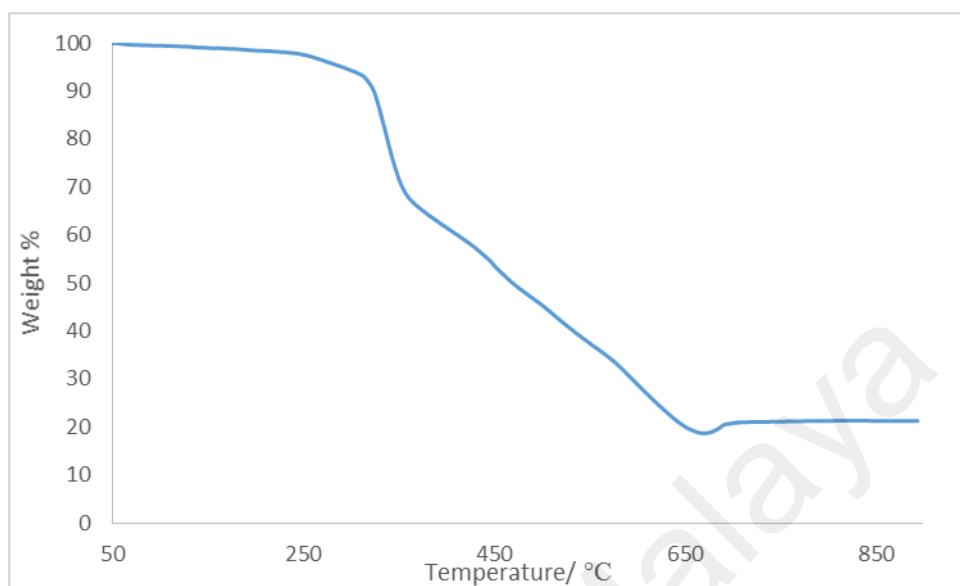


**Figure 4.154** TGA of **Complex 20**

*(e) Mesomorphic properties*

Its DSC spectrum (**Figure 4.155**) was recorded for a heating-cooling cycle from 25 °C to 200 °C. On heating, there was an endothermic peak at 177.8 °C ( $\Delta H = +49.52 \text{ kJ mol}^{-1}$ ) assigned as the melting temperature of the complex. However, there was no peak on cooling from this temperature.

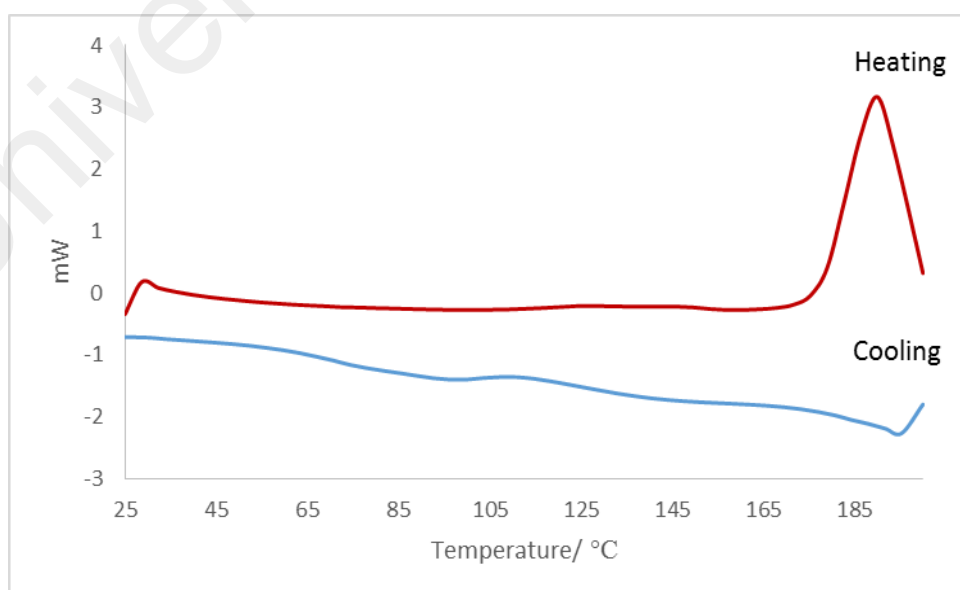


**Figure 4.155** DSC of **Complex 20**

Viewed under **OPM**, which was recorded for a heating-cooling cycle from 25 °C to 200 °C, the complex did not show any optical textures. Hence, **Complex 20** did not exhibit mesomorphism.

#### 4.6.2 [CuCo(CH<sub>3</sub>COO)<sub>2</sub>(L2)].2H<sub>2</sub>O

The Cu(II)-Co(II) complex of H<sub>2</sub>L2 was synthesised using the one-pot reaction from the reaction of NH<sub>2</sub>(CH<sub>2</sub>)<sub>8</sub>NH<sub>2</sub>, 2,4-dihydroxybenzaldehyde, [Cu(CH<sub>3</sub>COO)<sub>2</sub>].H<sub>2</sub>O and [Co(CH<sub>3</sub>COO)<sub>2</sub>].4H<sub>2</sub>O in ethanol. The product was a khaki green powder (**Complex 21**), and its yield was 71.5%. It was soluble in DMSO, DMF, and THF, but insoluble in water and other common organic solvents.

##### (a) Structural deduction

Based on the combined results of the elemental analyses and FTIR and UV-visible spectroscopies presented below, it is proposed that the structural formula of **Complex 21** was [CuCo(CH<sub>3</sub>COO)<sub>2</sub>(L2)].2H<sub>2</sub>O, which was similar as **Complex 8** ([Co<sub>2</sub>(CH<sub>3</sub>COO)<sub>2</sub>(L2)].H<sub>2</sub>O).

The results from the **elemental analyses** (48.05% C, 5.50% H, 4.41% N) were in good agreement with the chemical formula CuCoC<sub>26</sub>H<sub>36</sub>N<sub>2</sub>O<sub>10</sub> (FM, 695.05 g mol<sup>-1</sup>; 47.38% C, 5.51% H, 4.25% N).

Its **FTIR** spectrum (**Figure 4.156**) shows peaks at similar wavenumbers (in cm<sup>-1</sup>) as previously discussed complexes (3194, 2927, 2858, 1598, 1553 and 1444) and may be similarly assigned. From the latter two peaks, the Δ value was 109 cm<sup>-1</sup>, suggesting a chelating binding mode for CH<sub>3</sub>COO<sup>-</sup> ligand.

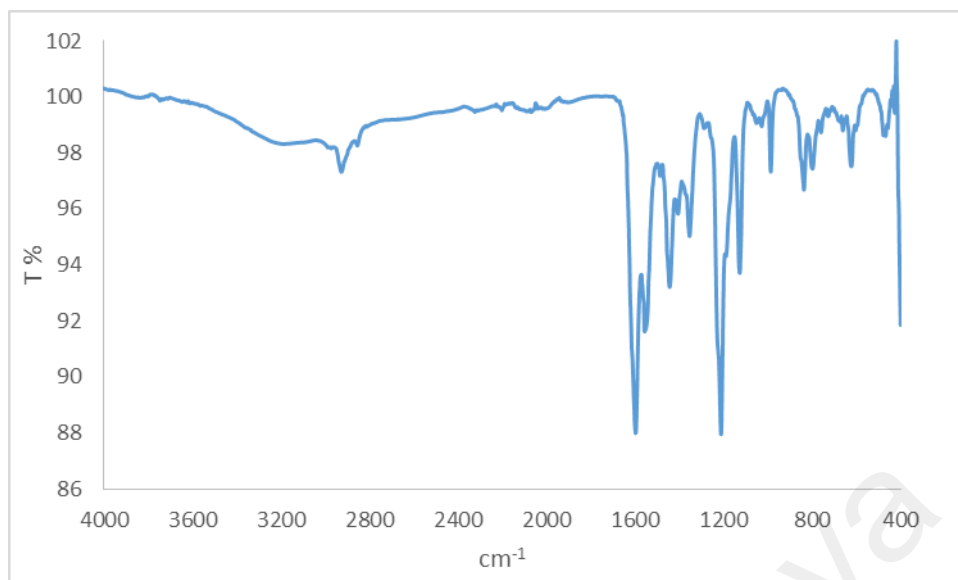


**Figure 4.156** FTIR spectrum for **Complex 21**

Its **UV-visible** spectrum, recorded in DMSO (**Figure 4.157**), shows *d-d* bands at 614 nm ( $\epsilon_{\max} = 76 \text{ M}^{-1} \text{ cm}^{-1}$ ) and 436 nm ( $\epsilon_{\max} = 598 \text{ M}^{-1} \text{ cm}^{-1}$ ). These suggest a tetrahedral geometry at each Cu(II) and Co(II) centre for this complex.

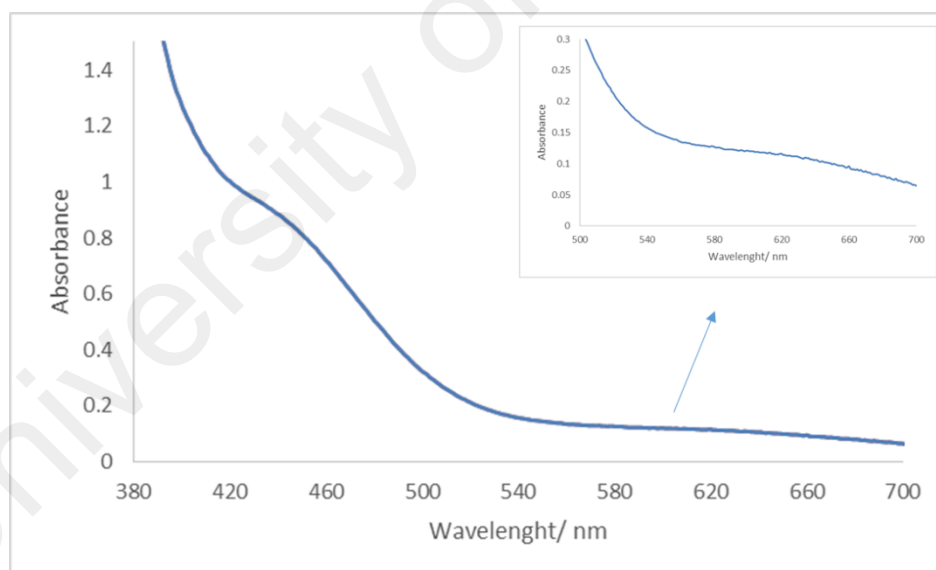


**Figure 4.157** UV-visible spectrum of **Complex 21**

*(b) Determination of bandgaps*

Its  $E_o$  value, calculated as before from its UV-vis spectrum, was 3.06 eV ( $\lambda_{\text{onset}} = 405 \text{ nm}$ ).

Its **CV** scan was recorded cathodically in chloroform at a scan rate  $50 \text{ mV s}^{-1}$  in the potential range of  $-2.0 \text{ V}$  to  $+2.0 \text{ V}$ . The voltammogram (**Figure 4.158**) shows an anodic

peak at -0.98 V assigned to the oxidation of [Co(II)] to [Cu(III)], but no corresponding cathodic peak, indicating an irreversible redox process. Hence, its electrochemical band gap cannot be calculated. The voltammogram (**Figure 4.158**) shows an anodic peak at +1.47 V assigned to the oxidation of the ligand and no corresponding cathodic. No redox peaks were observed for Cu(II) and Co(II), hence its electrochemical band gap cannot be calculated.

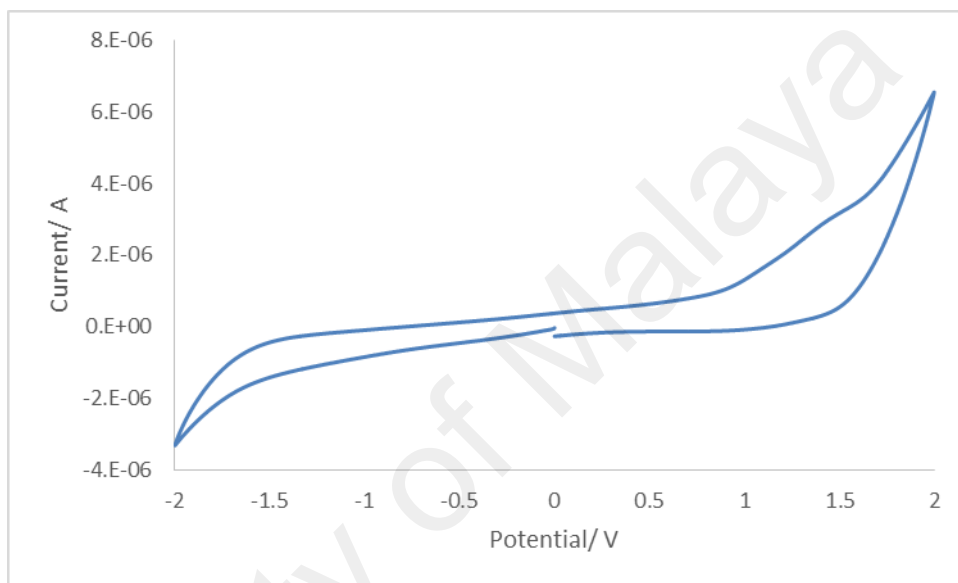


**Figure 4.158** Cyclic voltammogram for **Complex 21**

(c) *Magnetic properties*

Its  $\mu_{\text{eff}}$  value, calculated as previously done from the values of  $FM = 659.05 \text{ g mol}^{-1}$ ,  $\chi_{\text{g}} = 1.61 \times 10^{-5} \text{ cm}^3 \text{ g}^{-1}$ ,  $\chi_{\text{m}} = 1.06 \times 10^{-2} \text{ cm}^3 \text{ mol}^{-1}$ ,  $\chi_{\text{dia}} = -2.40 \times 10^{-4} \text{ cm}^3 \text{ mol}^{-1}$ , and  $\chi_{\text{m}}^{\text{corr}} = 1.08 \times 10^{-2} \text{ cm}^3 \text{ mol}^{-1}$  was 5.07 B.M. Comparing with **Complex 20**, it may be inferred that the presence of OH group at *para* position in **Complex 21** led to geometrical distortion through the formation of H-bonds, and a more stronger ferromagnetic interaction between Cu(II) and Co(II) centres.

(d) *Thermal properties*

Its TGA trace (**Figure 4.159**) shows an initial weight loss of 5.6% from about 50 °C to 151 °C due to the evaporation of lattice H<sub>2</sub>O (calculated, 5.5%). The next weight loss of

72.4% from 194 °C to 796 °C is assigned to decomposition of  $L2^{2-}$  and two  $CH_3COO^-$  ions (calculated, 75.9%). The amount of residue at temperatures above 796 °C was 22.0%, which is in a good agreement with the calculated value of 23.4%, assuming pure CuO and CoO. Accordingly,  $T_{dec}$  for **Complex 21** was 194 °C.

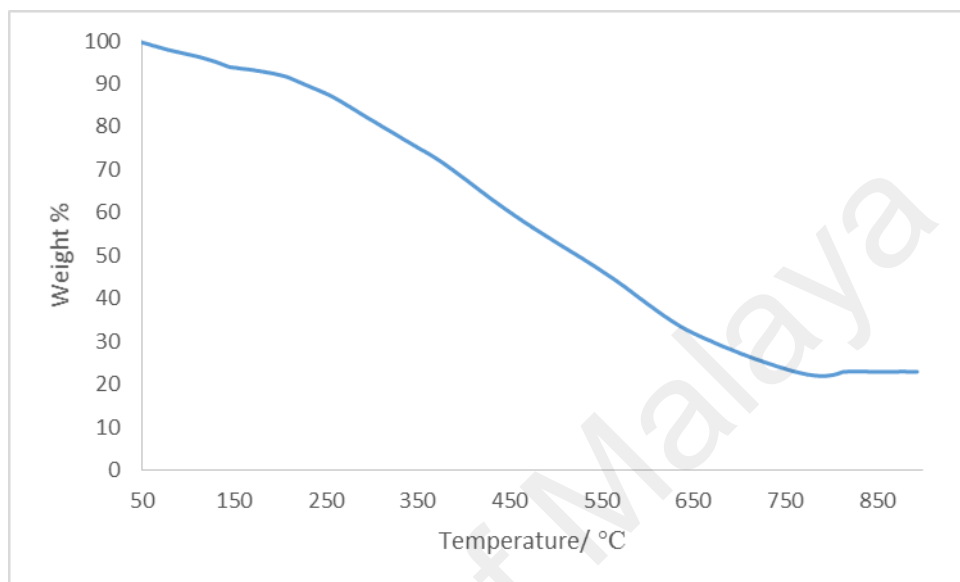


**Figure 4.159** TGA of **Complex 21**

*(e) Mesomorphic properties*

Its DSC spectrum (**Figure 4.160**) was recorded for heating-cooling cycle from 25 °C to 160 °C. On heating, there was an endothermic peak at 140.8 °C ( $\Delta H = +48.7 \text{ kJ mol}^{-1}$ ), assigned as its melting temperature. However, there was no peak on cooling from this temperature.

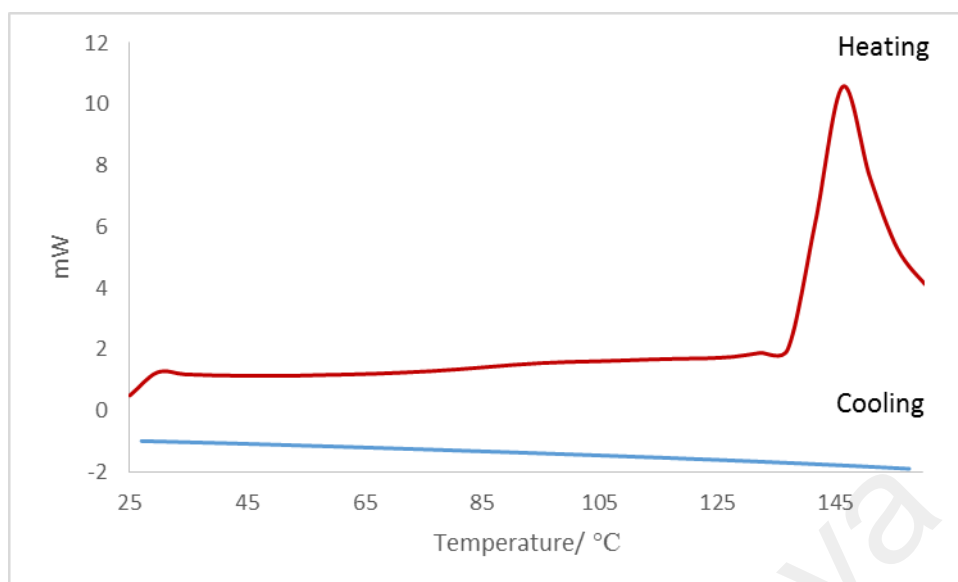


**Figure 4.160** DSC of **Complex 21**

Viewed under **OPM**, which was recorded for heating-cooling cycle from 25 °C to 160 °C, the complex did not show any optical textures. Hence, **Complex 21** did not exhibit mesomorphism.

#### 4.6.3 $[\text{CuCo}(\text{CH}_3\text{COO})_2(\text{HL3})_2]$

The Cu(II)-Co(II) complex of H<sub>2</sub>L3 was synthesised using the one-pot reaction from the reaction of NH<sub>2</sub>(CH<sub>2</sub>)<sub>8</sub>NH<sub>2</sub>, 3,5-di(*tert*-butyl)-2-hydroxybenzaldehyde, [Cu(CH<sub>3</sub>COO)<sub>2</sub>].H<sub>2</sub>O and [Co(CH<sub>3</sub>COO)<sub>2</sub>].4H<sub>2</sub>O in ethanol. The product was a dark brown powder (**Complex 22**) and the yield was 40.6%. It was soluble in chloroform and insoluble in water and other common organic solvents.

##### (a) Structural deduction

Based on the combined results of the elemental analyses and FTIR and UV-visible spectroscopies presented below, it is proposed that the structural formula of **Complex 22** was  $[\text{CuCo}(\text{CH}_3\text{COO})_2(\text{HL3})_2]$ , which was similar to **Complex 20**  $[\text{CuCo}(\text{CH}_3\text{COO})_2(\text{HL1})_2].2\text{H}_2\text{O}$ .

The results from the **elemental analyses** (68.69% C, 8.98% H, 3.95% N) were in good agreement with the chemical formula  $\text{CuCoC}_{80}\text{H}_{124}\text{N}_4\text{O}_8$  (FM, 1392.34 g mol<sup>-1</sup>; 69.01% C, 8.98% H, 4.02% N).

Its **FTIR** spectrum (**Figure 4.161**) shows peaks at similar wavenumbers (in cm<sup>-1</sup>) as previously discussed complexes (2950 cm<sup>-1</sup>, 2859 cm<sup>-1</sup>, 1617 cm<sup>-1</sup>, 1531 cm<sup>-1</sup> and 1434 cm<sup>-1</sup>) and may be similarly assigned. From the latter two peaks, the  $\Delta$  value was 97 cm<sup>-1</sup>, suggesting a chelating binding mode for  $\text{CH}_3\text{COO}^-$  ligand.

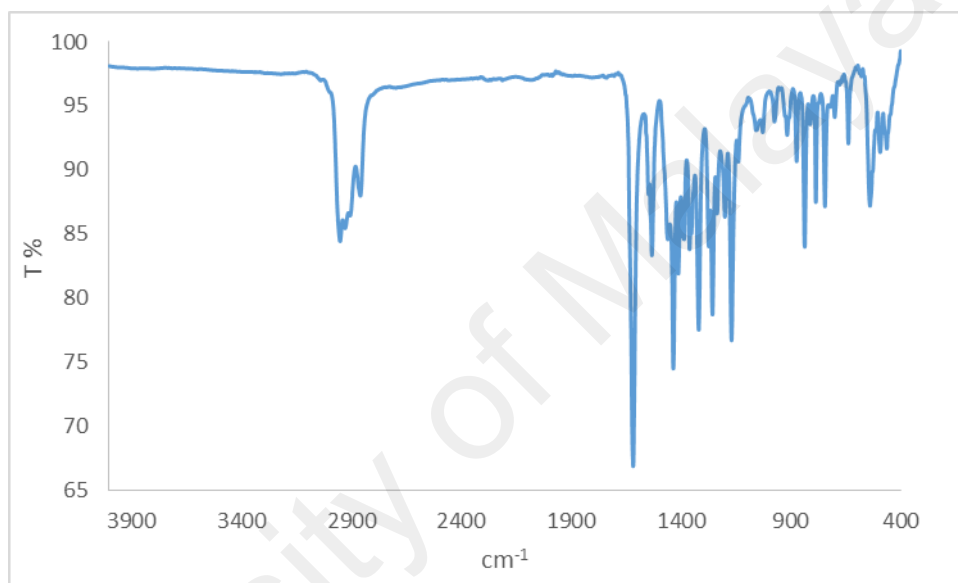


**Figure 4.161** FTIR spectrum for **Complex 22**

Its **UV-visible** spectrum, recorded in chloroform (**Figure 4.162**), shows a *d-d* band at 663 nm ( $\epsilon_{\text{max}} = 498 \text{ M}^{-1} \text{ cm}^{-1}$ ) and MLCT band at 497 nm ( $\epsilon_{\text{max}} = 1408 \text{ M}^{-1} \text{ cm}^{-1}$ ). This suggests a tetrahedral geometry at each Cu(II) and Co(II) centre in this complex.

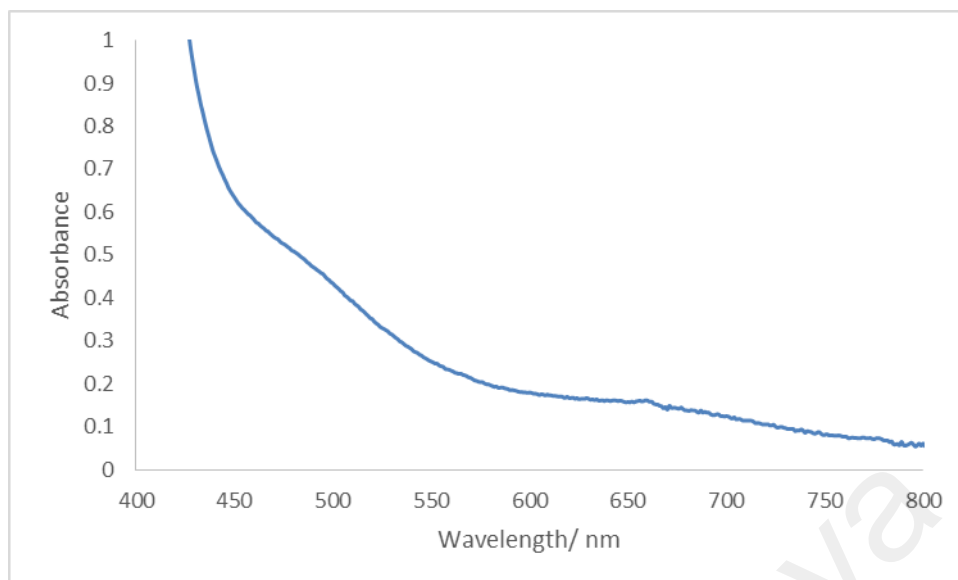


**Figure 4.162** UV-visible spectrum of **Complex 22**

*(b) Determination of bandgaps*

Its  $E_o$  value, calculated as before from its UV-vis spectrum, was 2.08 eV ( $\lambda_{\text{onset}} = 595$  nm).

Its CV scan was recorded anodically in chloroform at a scan rate  $50 \text{ mV s}^{-1}$  in the potential range of -1.5 V to +1.5 V. The voltammogram (**Figure 4.163**) shows a cathodic peaks at -0.87 V, assigned to a reduction of Cu(II)Co(II) to Cu(I)Co(II) and an anodic peak at +1.15 V, assigned to an oxidation of Cu(I)Co(II) to Cu(II)Co(III). Another two cathodic peak was observed at +0.59 V, assigned to reduction of Cu(II)Co(III) to Cu(II)Co(II). The  $\Delta E_p$  value for Cu(II) was 2020 mV and for Co(II) was 180 mV. The  $I_{pa}/I_{pc}$  ratio for Cu(II) was 1.3 and for Co(II) is 0.8, indicating a quasireversible redox reaction ( $\Delta E_p > 59$  mV at  $30^\circ\text{C}$ ) and chemically unstable reduced Cu(I) and oxidised Co(III) complex. The HOMO and LUMO values was 5.44 V and 3.73 V, respectively. Hence, its  $E_e$  value was 1.71 eV.

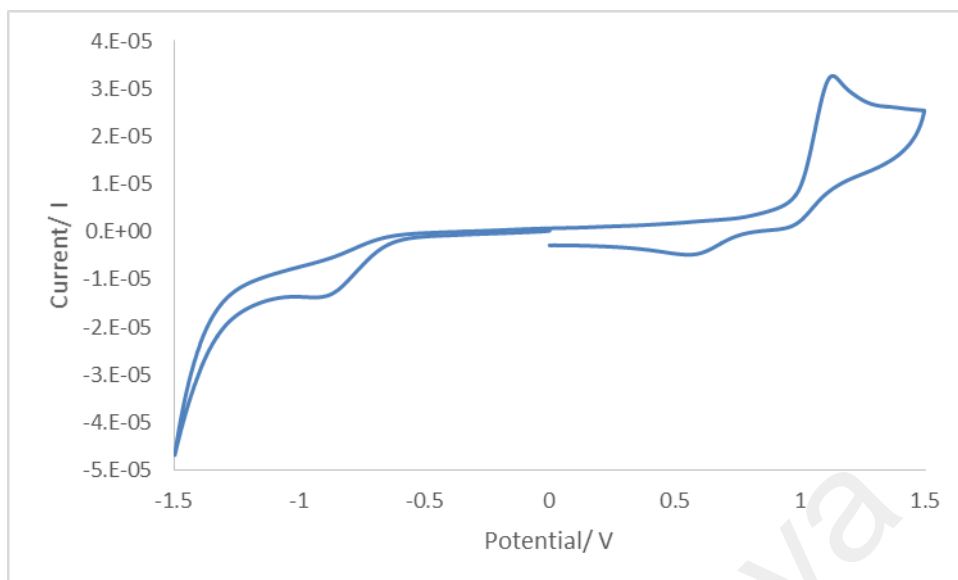


**Figure 4.163** Cyclic voltammogram for **Complex 22**

*(c) Magnetic properties*

Its  $\mu_{\text{eff}}$  value, calculated as previously done from the values of  $\text{FM} = 1392.34 \text{ g mol}^{-1}$ ,  $\chi_{\text{g}} = 5.87 \times 10^{-6} \text{ cm}^3 \text{ g}^{-1}$ ,  $\chi_{\text{m}} = 8.18 \times 10^{-3} \text{ cm}^3 \text{ mol}^{-1}$ ,  $\chi_{\text{dia}} = -7.82 \times 10^{-4} \text{ cm}^3 \text{ mol}^{-1}$ , and  $\chi_{\text{m}}^{\text{corr}} = 8.96 \times 10^{-3} \text{ cm}^3 \text{ mol}^{-1}$ , was 4.64 B.M. This is lower than the expected values 5.60 B.M and may similarly explained as **Complex 20**.

*(d) Thermal properties*

Its **TGA** trace (**Figure 4.164**) shows an initial weight loss of 86.3% from about 251 °C to 645 °C due to decomposition of two  $\text{HL3}^-$  and two  $\text{CH}_3\text{COO}^-$  ions (calculated, 91.2%). The amount of residue at temperatures above 645 °C was 13.7%, which is in a good agreement with the calculated value of 11.1%, assuming pure CuO and CoO. Accordingly,  $T_{\text{dec}}$  for **Complex 22** was 251 °C.

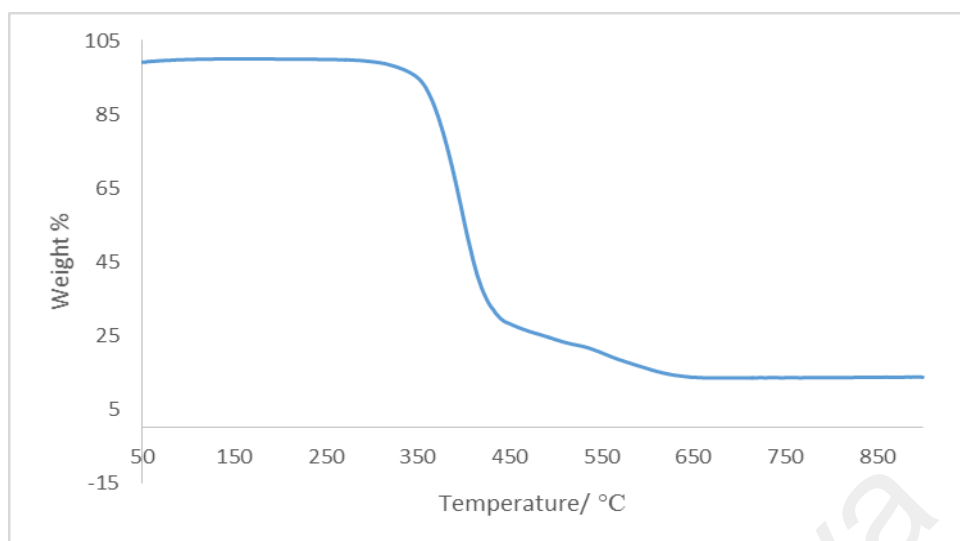


**Figure 4.164** TGA of **Complex 22**

*(e) Mesomorphic properties*

Its DSC spectrum (**Figure 4.165**) was recorded for heating-cooling cycle from 25 °C to 180 °C. On heating, there was an endothermic peak at 153.42 °C ( $\Delta H = +9.7 \text{ kJ mol}^{-1}$ ), assigned as the breaking of H-bond. However, there was no peak on cooling from this temperature.

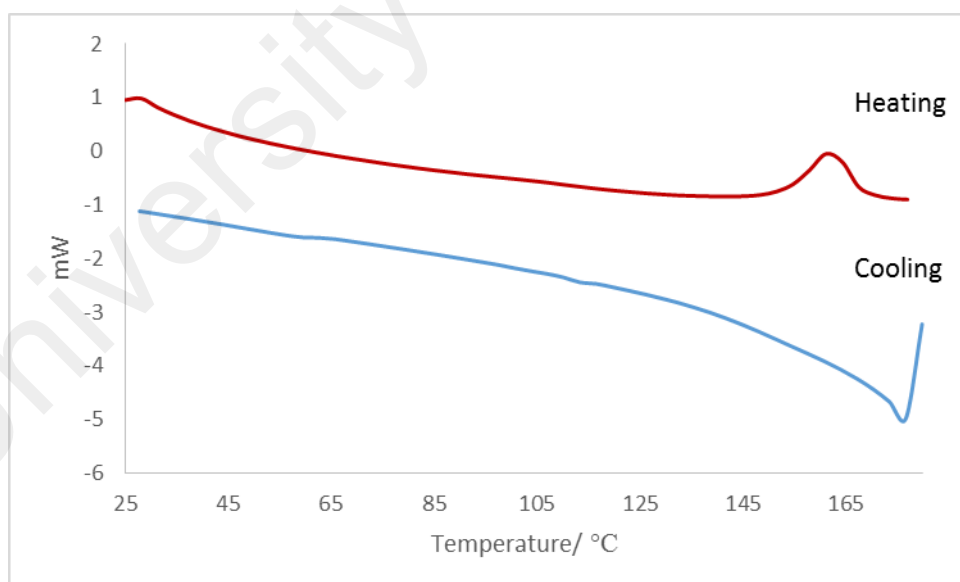


**Figure 4.165** DSC of **Complex 22**

Viewed under **OPM**, which was recorded for heating-cooling cycle from 25 °C to 200 °C, the complex did not show any optical textures (**Figure 4.166**). Hence, **Complex 22** did not exhibit mesomorphism.



**Figure 4.166** Photomicrograph of **Complex 22**: (a) on heating at 200 °C; and (b) on cooling at 62 °C

#### **4.6.4 Summary**

The analytical data for **Complexes 20-22** are summarised in **Table 4.15**. All complexes were dinuclear and paramagnetic.

The optical bandgaps from the CT absorption bands for all complexes were in the range of 2.08 eV– 3.06 eV. Hence, these complexes were semiconductors and potentials as photovoltaic and solar cells materials.

All complexes were thermally stable. Their decomposition temperatures range from 142 °C to 251 °C. Finally, all complexes were not mesomorphic.

**Table 4.15** Analytical results for heterometallic complexes

<b>Complex</b>		<b>20</b>	<b>21</b>	<b>22</b>
<b>Chemical Formula</b>		[CuCo(CH <sub>3</sub> COO) <sub>2</sub> (HL1) <sub>2</sub> (H <sub>2</sub> O)]	[CuCo(CH <sub>3</sub> COO) <sub>2</sub> (L2)].2H <sub>2</sub> O	[CuCo(CH <sub>3</sub> COO) <sub>2</sub> (HL3) <sub>2</sub> ]
<b>CH<sub>3</sub>COO mode</b>		chelating		
<b>Geometry</b>		tetrahedral		
<b>E<sub>o</sub></b> <b>(eV)</b>	<b>absorption</b>	2.95	3.06	2.08
	<b>emission</b>	-	-	-
<b>CV</b>		Redox inactive		
<b>μ<sub>eff</sub> (B.M.)</b>		4.13	5.07	4.64
<b>T<sub>dec</sub> (°C)</b>		142	151	251
<b>Mesomorphism</b>		Non-mesomorphic		

## CHAPTER 5 CONCLUSIONS AND SUGGESTIONS FOR FUTURE WORKS

### 5.1 Conclusions

Three new Schiff bases ( $H_2L1$ ,  $H_2L2$  and  $H_2L3$ ) were successfully obtained from the condensation reactions of 1,8-diaminooctane with 2-hydroxybenzaldehyde, 2,4-dihydroxybenzaldehyde, and 3,5-di(*tert*-butyl)benzaldehyde, respectively. All ligands were obtained in good yields (88.5% - 90.2%). The structural formulae of these ligands are shown in **Figure 5.1**.

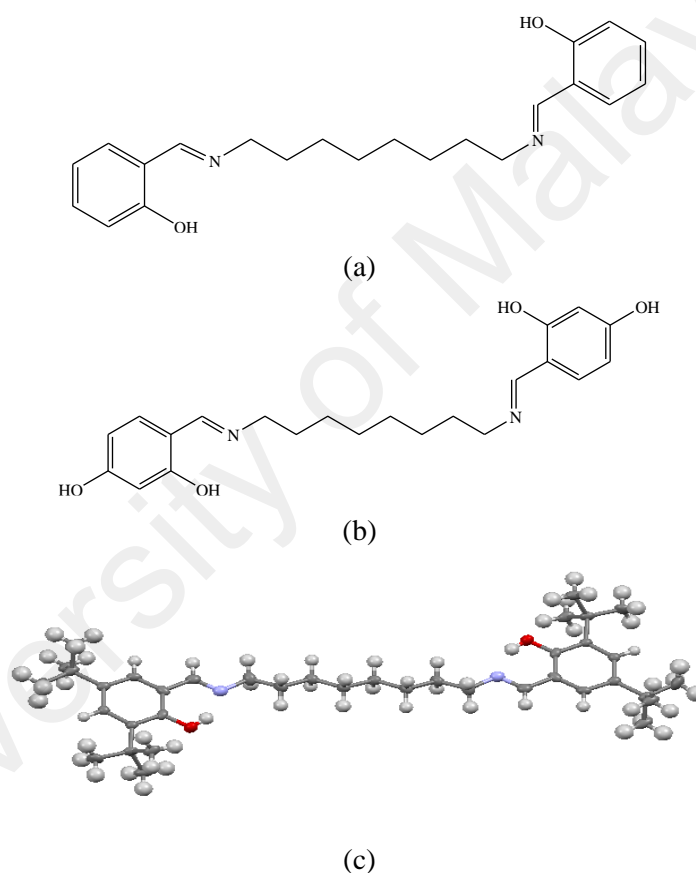


**Figure 5.1** Structure formula of Schiff bases (a)  $H_2L1$ , (b)  $H_2L2$  and (c)  $H_2L3$

Fifteen homometallic complexes of Cu(II), Ni(II), Co(II), Fe(II) and Mn(II) and three heterometallic complexes of Cu(II)Co(II) with each ligand were successfully obtained by one-pot reaction. Another four complexes of Ni(II), Co(II), Fe(II) and Mn(II) with cyclam also prepared by step-wise reaction. All complexes were obtained in good yields. The structure, band gap, redox, lifetime, thermal and mesomorphic properties of

these complexes were determined. The chemical formula of these complexes are shown in **Table 5.1**.

**Table 5.1** Chemical formulae of complexes

Complex	Chemical formula
1	[Cu(L1)] <sub>2</sub> .H <sub>2</sub> O
2	[Ni <sub>2</sub> (CH <sub>3</sub> COO) <sub>2</sub> (L1)].3H <sub>2</sub> O
3	[Co <sub>2</sub> (CH <sub>3</sub> COO) <sub>2</sub> (L1)].2H <sub>2</sub> O
4	[Fe(CH <sub>3</sub> COO)(L1)]
5	[Mn <sub>2</sub> (CH <sub>3</sub> COO) <sub>2</sub> (L1)(H <sub>2</sub> O) <sub>4</sub> ].2H <sub>2</sub> O
6	[Cu(CH <sub>3</sub> COO)(HL2)(H <sub>2</sub> O)].H <sub>2</sub> O
7	[Ni <sub>2</sub> (CH <sub>3</sub> COO) <sub>2</sub> (L2)].3H <sub>2</sub> O
8	[Co <sub>2</sub> (CH <sub>3</sub> COO) <sub>2</sub> (L2)].2H <sub>2</sub> O
9	[Fe(CH <sub>3</sub> COO)(HL2)]
10	[Mn <sub>2</sub> (CH <sub>3</sub> COO) <sub>2</sub> (L2)(H <sub>2</sub> O) <sub>4</sub> ].2H <sub>2</sub> O
11	[Cu(L3)]
12	[Ni <sub>2</sub> (L3)]
13	[Co <sub>2</sub> (CH <sub>3</sub> COO) <sub>2</sub> (L3)].3H <sub>2</sub> O
14	[Fe(CH <sub>3</sub> COO)(HL3)(H <sub>2</sub> O) <sub>2</sub> ].3H <sub>2</sub> O
15	[Mn <sub>2</sub> (HL3)(H <sub>2</sub> O) <sub>2</sub> ]
16	[Ni(CH <sub>3</sub> (CH <sub>2</sub> ) <sub>14</sub> COO)(cyclam)(H <sub>2</sub> O)](CH <sub>3</sub> (CH <sub>2</sub> ) <sub>14</sub> COO).4H <sub>2</sub> O
17	[Co(CH <sub>3</sub> (CH <sub>2</sub> ) <sub>14</sub> COO) <sub>2</sub> (cyclam)].2CH <sub>3</sub> (CH <sub>2</sub> ) <sub>14</sub> COOH
18	[Fe(CH <sub>3</sub> (CH <sub>2</sub> ) <sub>14</sub> COO)(cyclam)(OH)].H <sub>2</sub> O CH <sub>3</sub> CH <sub>2</sub> OH.
19	[Mn(CH <sub>3</sub> (CH <sub>2</sub> ) <sub>14</sub> COO)(OH)(NH <sub>3</sub> )(H <sub>2</sub> O)]
20	[CuCo(CH <sub>3</sub> COO) <sub>2</sub> (HL1) <sub>2</sub> (H <sub>2</sub> O)]
21	[CuCo(CH <sub>3</sub> COO) <sub>2</sub> (L2)].2H <sub>2</sub> O
22	[CuCo(CH <sub>3</sub> COO) <sub>2</sub> (HL3) <sub>2</sub> ]

All complexes with **H<sub>2</sub>L1** were paramagnetic. **Complex 1** was dimeric complex, **4** was mononuclear, while **Complexes 2, 3** and **5** were dinuclear. The optical bandgaps for all complexes were similar (2.81 eV – 3.61 eV). Only **Complex 2** was redox active

(electrochemical band gap was 0.1 eV). Except for **Complex 5**, the lifetimes of all excited complexes were similar (0.7 ns to 1.3 ns). The lifetime for **Complex 5** was the longest at 2.4 ns. These complexes were thermally stable ( $T_{\text{dec}} = 134\text{ }^{\circ}\text{C}$  to  $307\text{ }^{\circ}\text{C}$ ) and only **Complex 5** was mesomorphic.

All complexes with **H<sub>2</sub>L<sub>2</sub>** were paramagnetic. **Complexes 6, 9** and **10** were mononuclear, while **Complexes 7** and **8** were dinuclear. The optical bandgaps from absorption spectroscopy were similar (2.29 eV– 3.10 eV) for all complexes, while the bandgaps from emission spectroscopy and cyclic voltammetry only can be calculated for **Complex 6** (2.41 eV and 0.71 eV, respectively). Accordingly, only the lifetime of **Complex 6** can be determined (1.9 eV for the CT band and 2.0 eV for *d-d* band). All complexes were thermally stable ( $197\text{ }^{\circ}\text{C}$  to  $234\text{ }^{\circ}\text{C}$ ), but were not mesomorphic.

All complexes with **H<sub>2</sub>L<sub>3</sub>** ligand were mononuclear and paramagnetic except for **Complex 13** (dinuclear) and **Complex 12** (diamagnetic). The optical bandgaps for all complexes were similar (1.94 eV– 2.85 eV). Except for **Complex 13**, the lifetimes of all excited complexes were similar (0.7 ns to 1.7 ns). The lifetime for **Complex 13** was the longest at 3.9 eV. All complexes were thermally stable. Their decomposition temperatures range from  $251\text{ }^{\circ}\text{C}$  to  $285\text{ }^{\circ}\text{C}$ , but these complexes were not mesomorphic.

All Carboxylate complexes of Ni(II), Co(II), Fe(II) and Mn(II) with cyclam as co-ligand were mononuclear and paramagnetic. The optical bandgaps for all complexes were similar (2.84 eV– 3.60 eV), while for electrochemical bandgaps were in the range 0.31 eV and 1.40 eV. All complexes were thermally stable. Their decomposition temperatures range from  $140\text{ }^{\circ}\text{C}$  to  $243\text{ }^{\circ}\text{C}$ . However, only **Complexes 16** and **17** were mesomorphic.

All heterometallic complexes were dinuclear and paramagnetic. The optical bandgaps for all complexes were in the range of 2.08 eV– 3.06 eV, and there were redox

inactive. All complexes were thermally stable (142 °C to 251 °C) but were not mesomorphic.

## 5.2 Suggestions for Future Works

The chemical and structural formulas of these materials should be further ascertained by either forming crystals and the molecular structures investigated by single-crystal X-ray diffraction, or by molecular modelling. A shorter linear chain and branched-chain amino group can be used to obtain single crystals.

A study of similar complexes with lower band gaps may be undertaken, using conjugated polymeric organic ligands, mixed valence complexes and other mixed-metal complexes.

Their magnetic properties should be further studied by using SQUID magnetometer to investigate their spin crossover properties.

Most of the Schiff base complexes were not mesomorphic as their C=N bonds were hydrolysed on heating. A possible solution to this problem is to design complexes with lower melting temperatures, such as using long linear alkyl or alkyloxy chain or branched alkyl chains substituted at the aromatic rings.

Lastly, it would be interesting to study the thermoelectric behaviour of these complexes by measuring their electrical conductivities at different temperatures.

## REFERENCES

- [1] Peumans, P., Yakimov, A., & Forrest, S. R. (2003). Small molecular weight organic thin-film photodetectors and solar cells. *Journal of Applied Physics*, 93(7), 3693-3723.
- [2] Wong, H., Lam, L., Cheng, K., Man, K., Chan, W., Kwong, C., & Djurišić, A. (2004). Low-band-gap, sublimable rhenium(I) diimine complex for efficient bulk heterojunction photovoltaic devices. *Applied Physics Letters*, 84(14), 2557-2559.
- [3] Lindoy, L. (1971). Metal-ion control in the synthesis of Schiff base complexes. *Quarterly Reviews, Chemical Society*, 25(3), 379-391.
- [4] Kasumov, V. T., & Köksal, F. (2005). Synthesis, spectroscopy, and electrochemistry of copper(II) complexes with N,N'-bis(3,5-di-*t*-butylsalicylideneimine)polymethylenediamine ligands. *Spectrochimica Acta Part A: Molecular and Biomolecular Spectroscopy*, 61(1-2), 225-231.
- [5] Holm, R., Everett, G., & Chakravorty, A. (1966). Metal complexes of Schiff bases and  $\beta$ -ketoamines. *Progress in Inorganic Chemistry, Volume 7*, 83-214.
- [6] Hobday, M. D., & Smith, T. (1973). N, N'-ethylenebis (salicylideneiminato) transition metal ion chelates. *Coordination Chemistry Reviews*, 9(3), 311-337.
- [7] Mukherjee, P., Biswas, C., Drew, M. G., & Ghosh, A. (2007). Structural variations in Ni(II) complexes of salen type di-Schiff base ligands. *Polyhedron*, 26(13), 3121-3128.
- [8] Yamada, S. (1999). Advancement in stereochemical aspects of Schiff base metal complexes. *Coordination Chemistry Reviews*, 190, 537-555.
- [9] Konsler, R. G., Karl, J., & Jacobsen, E. N. (1998). Cooperative asymmetric catalysis with dimeric salen complexes. *Journal of the American Chemical Society*, 120(41), 10780-10781.
- [10] Pletcher, D., & Thompson, H. (1999). A microelectrode study of the catalysis of alkyl halide reduction by Co(II)(salen). *Journal of Electroanalytical Chemistry*, 464(2), 168-175.

- [11] Oriol, L., & Serrano, J. L. (1995). Metallomesogenic polymers. *Advanced Materials*, 7(4), 348-369.
- [12] Aazam, E., El Husseiny, A., & Al-Amri, H. (2012). Synthesis and photoluminescent properties of a Schiff-base ligand and its mononuclear Zn(II), Cd(II), Cu(II), Ni(II) and Pd(II) metal complexes. *Arabian Journal of Chemistry*, 5(1), 45-53.
- [13] Meyer, M., Dahaoui-Gindrey, V., Lecomte, C., & Guillard, R. (1998). Conformations and coordination schemes of carboxylate and carbamoyl derivatives of the tetraazamacrocycles cyclen and cyclam, and the relation to their protonation states. *Coordination Chemistry Reviews*, 178, 1313-1405.
- [14] Parker, D. (1990). Tumour targeting with radiolabelled macrocycle-antibody conjugates. *Chemical Society Reviews*, 19(3), 271-291.
- [15] Jurisson, S., Berning, D., Jia, W., & Ma, D. (1993). Coordination compounds in nuclear medicine. *Chemical Reviews*, 93(3), 1137-1156.
- [16] Alexander, V. (1995). Design and synthesis of macrocyclic ligands and their complexes of lanthanides and actinides. *Chemical Reviews*, 95(2), 273-342.
- [17] El Ghachtouli, S., Cadiou, C., Déchamps-Olivier, I., Chuburu, F., Aplincourt, M., Patinec, & Roisnel, T. (2006). Nickel(II) complexes of cyclen-and cyclam-pyridine: topological reorganisations induced by electron transfer. *New Journal of Chemistry*, 30(3), 392-398.
- [18] Cuenot, F., Meyer, M., Bucaille, A., & Guillard, R. (2005). A molecular approach to remove lead from drinking water. *Journal of Molecular Liquids*, 118(1), 89-99.
- [19] Barbette, F., Rascalou, F., Chollet, H., Babouhot, J., Denat, F., & Guillard, R. (2004). Extraction of uranyl ions from aqueous solutions using silica-gel-bound macrocycles for alpha contaminated waste water treatment. *Analytica Chimica Acta*, 502(2), 179-187.
- [20] Collinson, S. R., & Fenton, D. E. (1996). Metal complexes of bibracchial Schiff base macrocycles. *Coordination Chemistry Reviews*, 148, 19-40.

- [21] Kumar, S., Dhar, D. N., & Saxena, P. (2009). Applications of metal complexes of Schiff bases—a review. *Journal of Scientific and Industrial Research*, 68(3), 181-187.
- [22] Nishinaga, A., Yamada, T., Fujisawa, H., Ishizaki, K., Ihara, H., & Matsuura, T. (1988). Catalysis of cobalt-Schiff base complexes in oxygenation of alkenes: on the mechanism of ketonization. *Journal of Molecular Catalysis*, 48(2), 249-264.
- [23] Sreekala, R., Yusuff, K. & Mohammed (1999). Catalytic activity of mixed ligand five coordinate Co (II) complexes of a polymer bound Schiff base, Catal (Pap Natl Symp),(1994) 507-510. Paper presented at the *Chemical Abstracts*.
- [24] Joshi, K., & Pancholi, A. (2000). Synthesis, characterization and antibacterial activity of complexes of Schiff bases derived from 2-amino-5-methyl-4-phenyl thiazole and heterocyclic ketone/b-diketone. *Oriental Journal Of Chemistry*, 16(2), 287-290.
- [25] Sirajuddin, M., Ali, S., Shah, F. A., Ahmad, M., & Tahir, M. N. (2014). Potential bioactive Vanillin–Schiff base di-and tri-organotin(IV) complexes of 4-((3, 5-dimethylphenylimino) methyl)-2-methoxyphenol: synthesis, characterization and biological screenings. *Journal of the Iranian Chemical Society*, 11(2), 297-313.
- [26] Norbani Abdullah, Yanti Yana Halid, JiaTi, T., & Afiq Azil. (2016). Crystal Structures and Mesomorphic Properties of Schiff Base Homologs and Derivative, and Magnetic Properties of their Dimeric and Dinuclear Copper(II) Complexes. *Molecular Crystals and Liquid Crystals*, 624(1), 132-143.
- [27] Abdullah, N., Lo, K. M., Tajuddin, H. A., Tee, J. T., & Ng, S. W. (2008). 2, 2'-[Nonane-1,9-diylbis(nitrilomethylidyne)]diphenol. *Acta Crystallographica Section E: Structure Reports Online*, 64(12), 2494-2494.
- [28] Khalaji, A. D., Nikookar, M., & Das, D. (2014). Co(III), Ni(II), and Cu(II) complexes of bidentate N, O-donor Schiff base ligand derived from 4-methoxy-2-nitroaniline and salicylaldehyde. *Journal of Thermal Analysis and Calorimetry*, 115(1), 409-417.

- [29] Raman, N., Ravichandran, S., & Thangaraja, C. (2004). Copper(II), cobalt(II), nickel(II) and zinc(II) complexes of Schiff base derived from benzil-2,4-dinitrophenylhydrazone with aniline. *Journal of Chemical Sciences*, 116(4), 215-219.
- [30] Katwal, R., Kaur, H., & Kapur, B. K. (2013). Applications of copper—Schiff's base complexes: a review. *Scientific Review & Chemical Communications*, 3(1), 1-15.
- [31] Supuran, C., Barboiu, M., Luca, C., Pop, E., Brewster, M., & Dinculescu, A. (1996). Carbonic anhydrase activators. Part 14. Syntheses of mono and bis pyridinium salt derivatives of 2-amino-5-(2-aminoethyl)- and 2-amino-5-(3-aminopropyl)-1, 3, 4-thiadiazole and their interaction with isozyme II. *European Journal Of Medicinal Chemistry*, 31(7), 597-606.
- [32] Niederhoffer, E. C., Timmons, J. H., & Martell, A. E. (1984). Thermodynamics of oxygen binding in natural and synthetic dioxygen complexes. *Chemical Reviews*, 84(2), 137-203.
- [33] Tisato, F., Refosco, F., & Bandoli, G. (1994). Structural survey of technetium complexes. *Coordination Chemistry Reviews*, 135, 325-397.
- [34] Balamurugan, R., Palaniandavar, M., & Halcrow, M. A. (2006). Copper(II) complexes of sterically hindered Schiff base ligands: synthesis, structure, spectra and electrochemistry. *Polyhedron*, 25(5), 1077-1088.
- [35] Ourari, A., Derafa, W., & Aggoun, D. (2015). A novel copper(II) complex with an unsymmetrical tridentate-schiff base: synthesis, crystal structure, electrochemical, morphological and electrocatalytic behaviors toward electroreduction of alkyl and aryl halides. *Royal Society of Chemistry Advances*, 5(101), 82894-82905.
- [36] Sarkar, B., Drew, M. G., Estrader, M., Diaz, C., & Ghosh, A. (2008). Cu(II) acetate complexes involving N,N,O donor Schiff base ligands: Mono-atomic oxygen bridged dimers and alternating chains of the dimers and Cu<sub>2</sub>(OAc)<sub>4</sub>. *Polyhedron*, 27(12), 2625-2633.

- [37] Cozzi, P. G. (2004). Metal–Salen Schiff base complexes in catalysis: practical aspects. *Chemical Society Reviews*, 33(7), 410-421.
- [38] Chohan, Z. H., Praveen, M., & Ghaffar, A. (1998). Synthesis, characterisation and biological role of anions (Nitrate, Sulphate, Oxalate and Acetate) in Co(II), Cu(II) and Ni(II) metal chelates of some Schiff base derived Amino Acids. *Synthesis And Reactivity In Inorganic And Metal-Organic Chemistry*, 28(10), 1673-1687.
- [39] Lv, J., Liu, T., Cai, S., Wang, X., Liu, L., & Wang, Y. (2006). Synthesis, structure and biological activity of cobalt(II) and copper(II) complexes of valine-derived Schiff bases. *Journal of inorganic biochemistry*, 100(11), 1888-1896.
- [40] Sasaki, M., Manseki, K., Horiuchi, H., Kumagai, M., Sakamoto, M., Sakiyama, H., & Okawa, H. (2000). Synthesis, structure, and magnetic properties of discrete d-f heterodinuclear complexes designed from tetrahedrally distorted [Cu(salabza)] (H<sub>2</sub>salabza = N,N'-bis(salicylidene)-2-aminobenzylamine) and [Ln(hfac)<sub>3</sub>] (Hhfac = 1,1,1,5,5,5-hexafluoroacetylacetone, Ln = Gd or Lu). *Journal of the Chemical Society, Dalton Transactions*(3), 259-263. doi: 10.1039/A907423F
- [41] Nathan, L. C., Koehne, J. E., Gilmore, J. M., Hannibal, K. A., Dewhurst, W. E., & Mai, T. D. (2003). The X-ray structures of a series of copper(II) complexes with tetradentate Schiff base ligands derived from salicylaldehyde and polymethylenediamines of varying chain length. *Polyhedron*, 22(6), 887-894. doi: 10.1016/S0277-5387(03)00029-9
- [42] Canpolat, E., Kaya, M., & Yazıcı, A. (2005). Mononuclear Chelates Derived from Substituted Schiff Base Ligands: Synthesis and Characterization of a New 3-Methoxysalicylidene-p-Aminoacetophenoneoxime and its Complexes with Co(II), Ni(II), Cu(II), and Zn(II). *Spectroscopy Letters*, 38(1), 35-45.
- [43] Hundekar, A., & Sen, D. (1984). Preparation and characterization of metal-complexes of n-acetyl-n-aryloxyferrocenyl hydrazides. *Indian Journal of Chemistry Section A - Inorganic Physical Theoretical & Analytical Chemistry*, 23(6), 477-479.

- [44] Konstantinović, S. S., Radovanović, B. C., Cakić, Ž., & Vasić, V. M. (2003). Synthesis and characterization of Co(II), Ni(II), Cu(II) and Zn(II) complexes with 3-salicylidenehydrazono-2-indolinone. *Journal of the Serbian Chemical Society*, 68(8-9), 641-647.
- [45] Salavati-Niasari, M., & Amiri, A. (2005). Synthesis and characterization of alumina-supported Mn(II), Co(II), Ni(II) and Cu(II) complexes of bis(salicylaldiminato) hydrazone as catalysts for oxidation of cyclohexene with tert-butylhydroperoxide. *Applied Catalysis A: General*, 290(1), 46-53.
- [46] Gómez-Saiz, P., García-Tojal, J., Maestro, M. A., Mahía, J., Arnáiz, F. J., & Rojo, T. (2002). Synthesis, crystal structure and spectroscopic properties of copper(II) complexes derived from 2-methylamino-5-pyridin-2-yl-1,3,4-oxadiazole. *Polyhedron*, 21(22), 2257-2263.
- [47] Vafazadeh, R., Hayeri, V., & Willis, A. C. (2010). Synthesis, crystal structure and electronic properties of bis(N-2-bromophenyl-salicydenaminato)copper(II) complex. *Polyhedron*, 29(7), 1810-1814.
- [48] Emara, A. A., Ali, A. M., El-Asmy, A. F., & Ragab, E.-S. M. (2014). Investigation of the oxygen affinity of manganese(II), cobalt(II) and nickel(II) complexes with some tetradentate Schiff bases. *Journal of Saudi Chemical Society*, 18(6), 762-773.
- [49] Yousef, T., El-Reash, G. A., El-Gammal, O., & Bedier, R. (2013). Synthesis, characterization, optical band gap, in vitro antimicrobial activity and DNA cleavage studies of some metal complexes of pyridyl thiosemicarbazone. *Journal of Molecular Structure*, 1035, 307-317.
- [50] SÖNMEZ, M. (2001). Synthesis and characterization of copper(II), nickel(II), cadmium(II), cobalt(II) and zinc(II) complexes with 2-benzoyl-3-hydroxy-1-naphthylamino-3-phenyl-2-propen-1-on. *Turkish Journal of Chemistry*, 25(2), 181-185.
- [51] Banerjee, A., Guha, A., Adhikary, J., Khan, A., Manna, K., Dey, S., Das, D. (2013). Dinuclear cobalt(II) complexes of Schiff-base compartmental ligands:

Syntheses, crystal structure and bio-relevant catalytic activities. *Polyhedron*, 60, 102-109.

- [52] Li, J.-z., Li, S.-x., Xie, F., Zhou, B., Zeng, W., & Qin, S.-y. (2006). Dioxygen affinities and catalytic epoxidation performance of mono-Schiff base transition-metal complexes with aza-crown or morpholino pendants. *Transition Metal Chemistry*, 31(8), 1066-1070.
- [53] Zeyrek, C., Elmali, A., & Elerman, Y. (2005). Synthesis and Crystal Structures of a New  $\mu$ -Bis(tetradentate) Schiff Base Ligand and its Mononuclear Iron(III) Complex: Iron(III) Induced Imidazolidine Ring Hydrolysis of Binucleating Schiff Base Ligand. *Zeitschrift für Naturforschung B*, 60(5), 520-526.
- [54] Nishida, Y., Kino, K., & Kida, S. (1987). X-Ray structural study of [Fe(saltrien)] X (X = Br.2H<sub>2</sub>O, BPh<sub>4</sub> or PF<sub>6</sub>). Origin of unusual magnetic behaviour of the spin-crossover complex [Fe(saltrien)](PF<sub>6</sub>). *Journal of the Chemical Society, Dalton Transactions*(8), 1957-1961.
- [55] Abdullah, N., Azil, A., Marlina, A., & Noor, N. L. M. (2014). Magnetic, Photophysical and Thermal Properties of Complexes of Iron(II) with Structurally Different Schiff Bases. *Asian Journal of Chemistry*, 26(24).
- [56] Pouralimardan, O., Chamayou, A.-C., Janiak, C., & Hosseini-Monfared, H. (2007). Hydrazone Schiff base-manganese(II) complexes: Synthesis, crystal structure and catalytic reactivity. *Inorganica Chimica Acta*, 360(5), 1599-1608.
- [57] Raman, N., Raja, Y. P., & Kulandaisamy, A. (2001). Synthesis and characterisation of Cu(II), Ni(II), Mn(II), Zn(II) and VO(II) Schiff base complexes derived from *o*-phenylenediamine and acetoacetanilide. *Journal of Chemical Sciences*, 113(3), 183-189.
- [58] Füzzerová, S., Kotek, J., Císařová, I., Hermann, P., Binnemans, K., & Lukeš, I. (2005). Cyclam (1,4,8,11-tetraazacyclotetradecane) with one methylphosphonate pendant arm: a new ligand for selective copper(II) binding. *Dalton transactions*(17), 2908-2915.

- [59] Mohan, S., & Prakash, R. (2010). Novel conducting polymer functionalized with metal–cyclam complex and its sensor application: Development of azidothymidine drug sensor. *Talanta*, 81(1), 449-454.
- [60] Korbakov, N., Timmerman, P., Lidich, N., Urbach, B., Sa'ar, A., & Yitzchaik, S. (2008). Acetylcholine detection at micromolar concentrations with the use of an artificial receptor-based fluorescence switch. *Langmuir*, 24(6), 2580-2587.
- [61] Nigam, P., Mohan, S., Kundu, S., & Prakash, R. (2009). Trace analysis of cefotaxime at carbon paste electrode modified with novel Schiff base Zn(II) complex. *Talanta*, 77(4), 1426-1431.
- [62] Prakash, R., Kandoi, S., & Srivastava, R. C. (2002). Electrochemical and spectroscopic studies of metal cyclam complexes with thiocyanate. Evidence for mixed ligand complex formation. *Transition Metal Chemistry*, 27(6), 598-603.
- [63] Gasser, G., Belousoff, M. J., Bond, A. M., & Spiccia, L. (2007). Binding of Nitrate to a Cu<sup>II</sup>-Cyclen Complex Bearing a Ferrocenyl Pendant: Synthesis, Solid-State X-ray Structure, and Solution-Phase Electrochemical and Spectrophotometric Studies. *Inorganic Chemistry*, 46(10), 3876-3888.
- [64] Vorotyntsev, M. A., & Vasilyeva, S. V. (2008). Metallocene-containing conjugated polymers. *Advances in Colloid and Interface Science*, 139(1), 97-149.
- [65] Yilmaz, I., Arslan, S., Guney, S., & Becerik, I. (2007). Synthesis, electro-spectroelectrochemical characterization and electrocatalytic behavior towards dioxygen reduction of a new water-soluble cobalt phthalocyanine containing naphthoxy-4-sulfonic acid sodium salt. *Electrochimica Acta*, 52(24), 6611-6621.
- [66] Lindoy, L. F. (1989). *The Chemistry of Macrocyclic Ligand Complexes: Cambridge University Press, Cambridge.*
- [67] Sanders, J., Atwood, J., Davies, J., Mac Nicol, D., & Vogel, F. (1996). *Comprehensive Supramolecular Chemistry, Vol. 9, Elsevier, Amsterdam.* 131-164.
- [68] Parker, D. (1996). *Macrocyclic Synthesis: A Practical Approach (Vol. 2): Oxford University Press, Oxford.*

- [69] Barefield, E. K. (2010). Coordination chemistry of N-tetraalkylated cyclam ligands—A status report. *Coordination Chemistry Reviews*, 254(15), 1607-1627.
- [70] Tajidi, N. S. A., Abdullah, N., & Arifin, Z. (2011). Diaqua (1,4,8,11-tetraazacyclotetradecane- $\kappa^4, N^1, N^4, N^8, N^{11}$ )copper(II) didodecanoate dihydrate. *Acta Crystallographica Section E: Structure Reports Online*, 67, M588.
- [71] Lindoy, L. F., Mahinay, M. S., Skelton, B. W., & White, A. H. (2003). Ligand assembly and metal ion complexation: syntheses and X-ray structures of Ni(II) and Cu(II) benzoate and 4-tert-butylbenzoate complexes of cyclam. *Journal Coordination Chemistry*, 56(14), 1203-1213.
- [72] He, Y., Zhao, G., Peng, B., & Li, Y. (2010). High-Yield Synthesis and Electrochemical and Photovoltaic Properties of Indene-C70 Bisadduct. *Advanced Functional Materials*, 20(19), 3383-3389.
- [73] Theivasanthi, T., & Alagar, M. (2013). Lead Nanopowder as Advanced Semiconductor, An Insight. *Research and Application of Material*, 1(4), 36-43.
- [74] Paris, J., & Brandt, W. W. (1959). Charge transfer luminescence of a ruthenium(II) chelate. *Journal of the American Chemical Society*, 81(18), 5001-5002.
- [75] Dharma, J., Pisal, A., & Shelton, C. (2009). Simple method of measuring the band gap energy value of TiO<sub>2</sub> in the powder form using a UV/Vis/NIR spectrometer. *Application Note Shelton, CT: PerkinElmer*.
- [76] Turan, N., Gündüz, B., Körkoca, H., Adigüzel, R., Çolak, N., & Buldurun, K. (2014). Study of Structure and Spectral Characteristics of the Zinc(II) and Copper(II) Complexes With 5,5-Dimethyl-2-(2-(3-nitrophenyl)hydrazono)cyclohexane-1,3-dione and Their Effects on Optical Properties and the Developing of the Energy Band Gap and Investigation of Antibacterial Activity. *Journal of the Mexican Chemical Society*, 58(1), 65-75.
- [77] Yousef, T., El-Reash, G. A., El-Gammal, O., & Bedier, R. (2012). Co(II), Cu(II), Cd(II), Fe(III) and U(VI) complexes containing a NSNO donor ligand: synthesis,

characterization, optical band gap, in vitro antimicrobial and DNA cleavage studies. *Journal of Molecular Structure*, 1029, 149-160.

- [78] Lakowicz, J. R. *Principles of Fluorescence Spectroscopy* (3rd ed.). USA: Springer.
- [79] Zhang, X.-F., Zhang, J., & Liu, L. (2014). Fluorescence Properties of Twenty Fluorescein Derivatives: Lifetime, Quantum Yield, Absorption and Emission Spectra. *Journal of Fluorescence*, 24(3), 819-826.
- [80] Theivasanthi, T., & Alagar, M. (2013). Lead Nanopowder as Advanced Semi-Conductor, An Insight. *Research and Application of Material*, 1(14), 36-43.
- [81] Zanello, P. (2003). Inorganic Electrochemistry: Theory, Practice and Applications: *Royal Society of Chemistry*.
- [82] Bredas, J., Silbey, R., Boudreaux, D., & Chance, R. (1983). Chain-length dependence of electronic and electrochemical properties of conjugated systems: polyacetylene, polyphenylene, polythiophene, and polypyrrole. *Journal of the American Chemical Society*, 105(22), 6555-6559.
- [83] Abdullah, N., & Mohamadin, M. I. (2012). Mixed-Valence Low Bandgap Photovoltaic Material:  $[\text{Cu(II)Cu(I)(R)}_3(\text{RH})_2(\text{L})_4]\cdot\text{CH}_3\text{COCH}_3$  ( $\text{R} = \text{C}_6\text{H}_5\text{COO}$ ;  $\text{L} = \text{CH}_3\text{COCH}_2\text{C}(\text{OH})(\text{CH}_3)_2$ ). *Advanced Materials Research*, 347, 738-741.
- [84] Attard, G., & Cullum, P. (1990). Thermotropic mesomorphism in a branched chain copper(II) carboxylate and its pyrazine complex. *Liquid Crystals*, 8(3), 299-309.
- [85] Jha, N., & Ray, I. P. (2000). Magnetic studies on Co(II) and Ni(II) complexes of hydroxamic acid. *Asian Journal of Chemistry*, 12(3), 703.
- [86] Giroud-Godquin, A. M. (1998). My 20 years of research in the chemistry of metal containing liquid crystals. *Coordination Chemistry Reviews*, 178, 1485-1499.
- [87] Bhattacharjee, C. R., Datta, C., Das, G., Chakrabarty, R., & Mondal, P. (2012). Induction of photoluminescence and columnar mesomorphism in hemi-disc salphen type Schiff bases via nickel(II) coordination. *Polyhedron*, 33(1), 417-424.

- [88] Rezvani, Z., Ghanea, M. A., Nejati, K., & Baghaei, S. A. (2009). Syntheses and mesomorphic properties of new oxygen-bridged dicopper complex homologous derived from azo-containing salicylaldimine Schiff base ligands. *Polyhedron*, 28(14), 2913-2918.
- [89] Ueno, K., & Martell, A. E. (1956). Infrared Studies on Synthetic Oxygen Carriers. *The Journal of Physical Chemistry*, 60(9), 1270-1275.
- [90] Prabhuswamy, M., Dinesha, Pampa, K., Kumar, S. M., Nagaraja, G., & Lokanath, N. (2014). Synthesis, Crystal Structure and Characterization of (Z)-2-N'-hydroxyisonicotinamide. *Molecular Crystals and Liquid Crystals*, 593(1), 243-252.
- [91] Kato, M., Jonassen, H. B., & Fanning, J. C. (1964). Copper(II) complexes with subnormal magnetic moments. *Chemical Reviews*, 64(2), 99-128.
- [92] Abdullah, N., Al-Hakem, Y., Abdullah, N., Samsudin, H., & Tajidi, N. S. A. (2014). Room-temperature magnetic liquid complexes of 2-hexyldecanoato ligand with Cu(II), Ni(II) and Co(II) ions. *Asian Journal of Chemistry*, 26(4), 987.
- [93] Kozlevčar, B. (2008). Structural analysis of a series of copper(II) coordination compounds and correlation with their magnetic properties. *Croatica Chemica Acta*, 81(2), 369-379.
- [94] Deacon, G., & Phillips, R. (1980). Relationships between the carbon-oxygen stretching frequencies of carboxylato complexes and the type of carboxylate coordination. *Coordination Chemistry Reviews*, 33(3), 227-250.
- [95] Kaya, M., Yenikaya, C., Colak, A. T., & Colak, F. (2008). Synthesis, spectral, thermal and biological studies of Co(III) and binuclear Ni(II) complexes with a novel amine-imine-oxime ligand. *Russian Journal of General Chemistry*, 78(9), 1808-1815.
- [96] Czakis-Sulikowska, D., & Czyłkowska, A. (2003). Complexes of Mn(II), Co(II), Ni(II) and Cu(II) with 4, 4'-bipyridine and dichloroacetates. *Journal of Thermal Analysis and Calorimetry*, 71(2), 395-405.

- [97] Czakis-Sulikowska, D., Malinowska, A., & Radwańska-Doczekalska, J. (2000). Synthesis, properties and thermal decomposition of bipyridine-oxalato complexes with Mn(II), Co(II), Ni(II) and Cu(II). *Polish Journal of Chemistry*, 74(5), 607-614.
- [98] Khan, O. (1993). *Molecular Magnetism*, VCH Publisher, Inc., USA.
- [99] Sun, Z.-L. (2005). Characteristics of thermal decomposition products of rare earth, alkali earth metal and transition metal p-toluenesulfonates. *Journal of Thermal Analysis and Calorimetry*, 79(3), 731-735.
- [100] Czakis-Sulikowska, D., Czyłkowska, A., & Radwańska-Doczekalska, J. (2000). Synthesis and thermal properties of 4,4'-bipyridine adducts of Mn(II), Co(II), Ni(II) and Cu(II) monochloroacetate. *Journal of Thermal Analysis and Calorimetry*, 63(2), 387-395.
- [101] Lai, Y.-C., & Tsai, Y.-C. (2012). An efficient 3C-silicon carbide/titania nanocomposite photoelectrode for dye-sensitized solar cell. *Chemical Communications*, 48(53), 6696-6698.
- [102] Ferrere, S. (2002). New photosensitizers based upon  $[\text{Fe}^{\text{II}}(\text{L})_2(\text{CN})_2]$  and  $[\text{Fe}^{\text{II}}\text{L}_3]$ , where L is substituted 2,2'-bipyridine. *Inorganica Chimica Acta*, 329(1), 79-92.
- [103] Hatzidimitriou, A., & Bolos, C. A. (1998). The effect of chelate rings on the structure of copper(II) compounds with triamine derivatives. The crystal structure of  $[\text{Cu}(\text{dptSS})\text{Cl}_2]$ . *Polyhedron*, 17(10), 1779-1785.
- [104] Mehrotra, R., & Singh, J. (1984). Synthesis, spectroscopic, and magnetic studies of new alkoxy and allied bimetallic derivatives of nickel(II) with aluminium. *Canadian Journal of Chemistry*, 62(6), 1003-1007.
- [105] Czakis-Sulikowska, D., Czyłkowska, A., & Malinowska, A. (2002). Thermal and other properties of new 4,4'-bipyridine-trichloroacetato complexes of Mn(II), Ni(II) and Zn(II). *Journal of Thermal Analysis and Calorimetry*, 67(3), 667-678.
- [106] Bhatt, V. D. R., S. R. (2012). Preparation and Properties of Dinuclear Schiff Base Complexes from Salicylaldehyde and 2-Aminophenol Complexes of Cu(II), Co(II) and Ni(II). *Chemical Sciences Journal*, 2012, 1.

- [107] Saha, N. C., Butcher, R. J., Chaudhuri, S., & Saha, N. (2003). Synthesis and spectroscopic characterisation of cobalt(III) and nickel(II) complexes with 5-methyl-3-formylpyrazole-N(4)-dibutylthiosemicarbazone (HMPzNBu<sub>2</sub>): X-ray crystallography of [Co(MPzNBu<sub>2</sub>)<sub>2</sub>]NO<sub>3</sub>.H<sub>2</sub>O (I) and [Ni(HMPzNBu<sub>2</sub>)<sub>2</sub>](ClO<sub>4</sub>)<sub>2</sub> (II). *Polyhedron*, 22(3), 383-390.
- [108] Holah, D., & Coucouvanis, D. (1975). Synthesis and characterization of a new series of first row element tetrahedral mercaptide complexes. *Journal of the American Chemical Society*, 97(23), 6917-6919.
- [109] Thimmaiah, K., Lloyd, W., & Chandrappa, G. (1985). Stereochemistry and fungitoxicity of complexes of p-anisaldehydethiosemicarbazone with Mn(II), Fe(II), Co(II) and Ni(II). *Inorganica Chimica Acta*, 106(2), 81-83.
- [110] Ferenc, W., Walków-Dziewulska, A., & Sadowski, P. (2005). Thermal, spectral and magnetic properties of 3,5-dimethoxybenzoates of Co(II), Ni(II) and Cu(II). *Journal of Thermal Analysis and Calorimetry*, 82(2), 365-371.
- [111] Kalanithi, M., Kodimunthiri, D., Rajarajan, M., & Tharmaraj, P. (2011). Synthesis, characterization and biological activity of some new VO(IV), Co(II), Ni(II), Cu(II) and Zn(II) complexes of chromone based NNO Schiff base derived from 2-aminothiazole. *Spectrochimica Acta Part A: Molecular and Biomolecular Spectroscopy*, 82(1), 290-298.
- [112] Kulkarni, A. D., Patil, S. A., & Badami, P. S. (2009). Electrochemical properties of some transition metal complexes: synthesis, characterization and in-vitro antimicrobial studies of Co(II), Ni(II), Cu(II), Mn(II) and Fe(III) complexes. *International Journal of Electrochemical Science*, 4(5), 717-729.
- [113] Melson, G. A., Crawford, N. P., & Geddes, B. J. (1970). Thiocarboxylates of nickel(II). *Inorganic chemistry*, 9(5), 1123-1126.